LATE QUATERNARY STRATIGRAPHIC AND TECTONIC EVOLUTION OF THE NORTHEASTERN AEGEAN SEA

EKREM BURSIN İSLER

Late Quaternary Stratigraphic and Tectonic Evolution of

the Northeastern Aegean Sea

by

©Ekrem Bursin İşler

A thesis submitted to the School of Graduate Studies

in partial fulfilment of the requirements for the degree of

Master of Science

Earth Science Department

Memorial University of Newfoundland

March 2005

Abstract

The late Quaternary–Recent stratigraphic and tectonic evolution of the NE Aegean Sea, between the Islands of Bozcaada and Lesbos and the Biga Peninsula, is examined using ~1600 km of seismic reflection and side scan profiles and six cores collected during cruises in 1998, 2000, 2002, and 2003.

Detailed examination of the seismic reflection profiles showed that several vertically stacked depositional sequences developed within three NE-SW trending basins. These depositional sequences exhibit oblique- to complex oblique-sigmoid internal seismic reflection configuration and are separated from one another by shelf-crossing unconformities. The chronology of the depositional sequences is constrained by seven radiocarbon and two U/Th dates on *in situ* shell samples extracted from five cores. Sedimentation rates calculated by using these dates range between 19 cm/kyr and 30 cm/kyr. The ages and the stacked architecture of the depositional sequences, together with the correlations with the oxygen isotopic stages and global sea-level curve reveal that these seaward-prograded delta sequences were developed in a sufficiently rapidly subsiding shelf environment during successive global eustatic sea-level falls associated with late Quaternary glaciations. The progradation of the depositional sequences decelerated and eventually halted shortly after the subsequent major transgressions during which the shelf-crossing unconformities were generated. The terrigenous materials transported throughout the development of the depositional sequences originated from the Tuzla, Karamenderes, and Dümbek rivers draining the

Biga Peninsula.

Seismic reflection profiles showed no evidence for a major E–W-trending fault system, suggesting that the western continuation of the central strand of the North Anatolian Transform Fault does not exit into the Aegean Sea at Ezine. Detailed mapping of the seismic data showed that two major faults, A_1 and β_8, constitute the main fault system in the study area. The Baba Burnu Basin is bounded by these two faults, and is interpreted to develop either as a rhomboidal pull-apart basin or as a half-graben. In the case of being a pull-apart basin, the faults A_1 and β_8 represent the seaward extension of the southern strand of the North Anatolian Transform Fault where it initially runs $\sim$ NW-SE (i.e., fault A_1) and then deflects toward NE-SW (i.e., β_8) forming a releasing bend. It then continues further southwest along fault β_8 and extends as far as the North Skyros Basin. In the case of being a half-graben, the central strand of the North Anatolian Transform Fault continues west in an ENE-WSW direction in the Gulf of Edremit and then it deviates toward southwest off the Island of Lesbos.

Acknowledgments

Table of contents

List of Figures

List of Tables

CHAPTER 1

1. Introduction

The aim of this study is to delineate the Quaternary tectonic and kinematic framework of the northeastern portion of the Aegean Sea and to establish first-order correlations with structures observed in northwestern Turkey. The data base consists of high resolution seismic-reflection profiles and cores that will be used in conjunction with geological maps of western Turkey, Global Positioning System data and earthquake data including fault plane solutions. Details of the objectives are listed at the end of Chapter 1.

1.1. Plate Tectonic Framework

The Eastern Mediterranean Sea represents the last remnants of the Tethys Ocean which has been consumed during the Cenozoic along a series of north-dipping subduction zones that developed across the collisional margin between the African and Eurasian plates (Şengör and Yılmaz, 1981). The present-day tectonic framework of the region is controlled by the northeast-directed motion of the African Plate, the north-directed motion of the Arabian-Syrian Microplate relative to the Eurasian Plate, and the re-shuffling of smaller microplates and continental fragments (Fig. 1.1). The collisional boundary north of the African Plate is characterized by a zone of subduction along two arcuate arcs: the Hellenic and Cyprus arcs (Fig. 1.1). The Pliny-Strabo trenches in the

EURASIAN PLATE

Black Sea

0   100   200
Scale (km)

SGFZ

NATF

TÇFZ

YEFZ

AFZ

KTJ

AEGEAN-ANATOLIAN
MICROPLATE

TFZ

YGFZ

EATF

EFZ

Aegean Sea

HA

PT

ST

FR

CA

AFZ

Mediterranean Sea

AFRICAN PLATE

DSTF

ARABIAN-SYRIAN
MICROPLATE

Scale
15 mm/yr

42°N
40°N
38°N
36°N
34°N
32°N

20°E   24°E   28°E   32°E   36°E   40°E
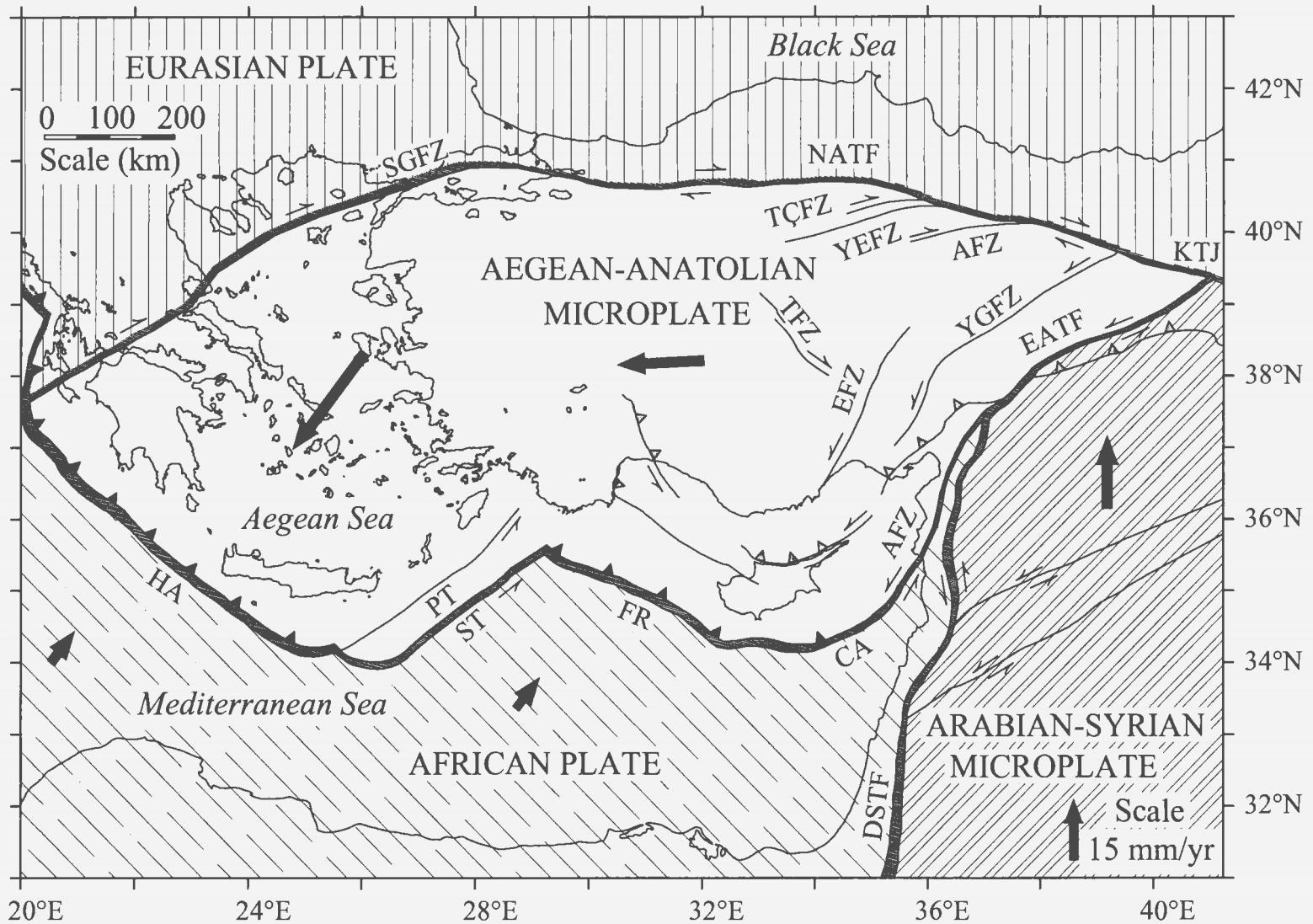
Figure 1.1. Simplified plate tectonic map of the Eastern Mediterranean showing the Aegean-Anatolian Microplate and major tectonic elements (modified from Aksu et al., 1992; McClusky, 2000). NATF- North Anatolian Transform Fault, EATF- East Anatolian Transform Fault, DSTF- Dead Sea Transform Fault, YGFZ- Yakapınar-Göksun Fault Zone, EFZ- Ecemiş Fault Zone, AFZ- Almus Fault Zone, TÇFZ- Taşova-Çorum Fault Zone, YEFZ- Yağmurlu-Ezinepazarı Fault Zone, TFZ- Tuzgölü Fault Zone, SGFZ- Saros- Ganiköy Fault Zone, HA- Hellenic Arc, PT- Pliny Trench, ST- Strabo Trench, FR- Florence Rise, CA- Cyprus Arc, AFZ- Amanos Fault Zone, KTJ- Karlıova Triple Junction. Heavy lines with filled triangles show the active subduction zones with triangles on the overriding plate. Lines with stippled triangles show major thrust faults with symbols on the hanging wall. Line with stippled triangles on the Arabian-Syrian Microplate constitutes western portion of the Bitlis-Zagros suture zone. Large arrows show the relative movement and the rates of movement of the African Plate and the Arabian-Syrian and Aegean-Anatolian microplates. Half arrows represent strike-slip faults with arrows showing the directions of relative displacement. The southwest rotation of the Aegean segment of the Aegean-Anatolian Microplate is clearly visible. Whether there are two or one microplate is still debated in the literature (e.g. McKenzie, 1972 and Reilinger et al., 1997a).

west and the Tartus Ridge and Amanos Fault Zone in the east are regions of the Eastern

Mediterranean where structures are oriented parallel to the African Plate vector, thus

exhibit prominent sinistral strike-slip displacements. The Aegean-Anatolian Microplate

is situated immediately north of the Hellenic and Cyprus arcs. Just east of the

Mediterranean, the African Plate abuts the Arabian-Syrian Microplate at the sinistral

Dead Sea Transform Fault which accommodates the north-directed motion of the

Arabian-Syrian Microplate (Fig. 1.1). The African Plate meets the Arabian-Syrian and

Aegean-Anatolian microplates at a complicated triple junction in southeastern Turkey,

near the town of Kahramanmaraş, whereas the Eurasian Plate meets the Arabian-Syrian

and Aegean-Anatolian microplates in eastern Turkey near the town of Karlıova (Fig. 1.1).

The pervasive collision between the Arabian-Syrian Microplate and the eastern

segment of the Aegean-Anatolian Microplate since the middle Miocene (Dewey and

Şengör, 1979; Şengör, 1979; Dewey et al., 1986 Philip et al., 1989) and the subsequent

suturing along the Bitlis-Zagros zone in the late Miocene (Şengör and Yılmaz, 1981)

resulted in the prominent west-directed tectonic escape of the Aegean-Anatolian

Microplate during the Pliocene-Quaternary (McKenzie, 1978; Dewey and Şengör, 1979;

Jackson, 1994; Martinod et al., 2000). This westward escape occurs along two large,

crustal-scale strike-slip faults: the dextral North Anatolian Transform Fault and the

sinistral East Anatolian Transform Fault (Fig. 1.1; McKenzie, 1978). Data from GPS

(Global Positioning System) stations in Turkey clearly document that the eastern portion

of the Aegean-Anatolian Microplate is moving westward at velocities of ~20–24 mm yr^{-1},

whereas the western segment of the microplate is moving in a southwesterly direction at a rate of ~30±2 mm yr^{-1} (Fig. 1.1; Ambraseys, 1970; Jackson and McKenzie, 1988b; Reilinger et al., 1997; McClusky et al., 2000). Internal deformation within the eastern and central part of the Anatolian-Aegean Microplate is estimated to be less than 2 mm yr^{-1} (Reilinger et al., 1997). The southwesterly rotation of the Aegean segment of the microplate is caused by its hard boundary with the southern Eurasian Plate in western Greece (Reilinger et al., 1997). Here, the microplate swings towards the rheologically least-resistant zone: the Hellenic Arc, where the present-day convergence is nearly orthogonal to the African Plate vector.

The North Anatolian Transform Fault and associated structures along the northern boundary of the microplate extends from the Karlıova Triple Junction in the east to the Gulf of Corinth in the west, with a total length of ~1500 km (Fig. 1.1; Barka and Kadinsky-Cade, 1988; Nalbant et al., 1998). The eastern portion of the Aegean-Anatolian Microplate is dissected by several large sinistral and/or dextral strike-slip splays of the North Anatolian Transform Fault, such as the Yağmurlu-Ezinepazarı Fault Zone, Taşova-Çorum Fault Zone, Almus Fault Zone, and Yakapınar-Göksun Fault Zone (Fig. 1.1; Şaroğlu et al., 1992; Bozkurt and Koçyiğit, 1996). Along the northwestern portion of the microplate, the North Anatolian Transform Fault splits into three main branches west of the town of Mudurnu, at longitude ~31°E: the northern, middle, and southern branches. Each branch displays a horse-tail of secondary dextral strike-slip faults (Fig. 1.2).

The present-day Hellenic Arc represents the "free" edge of the escape zone and
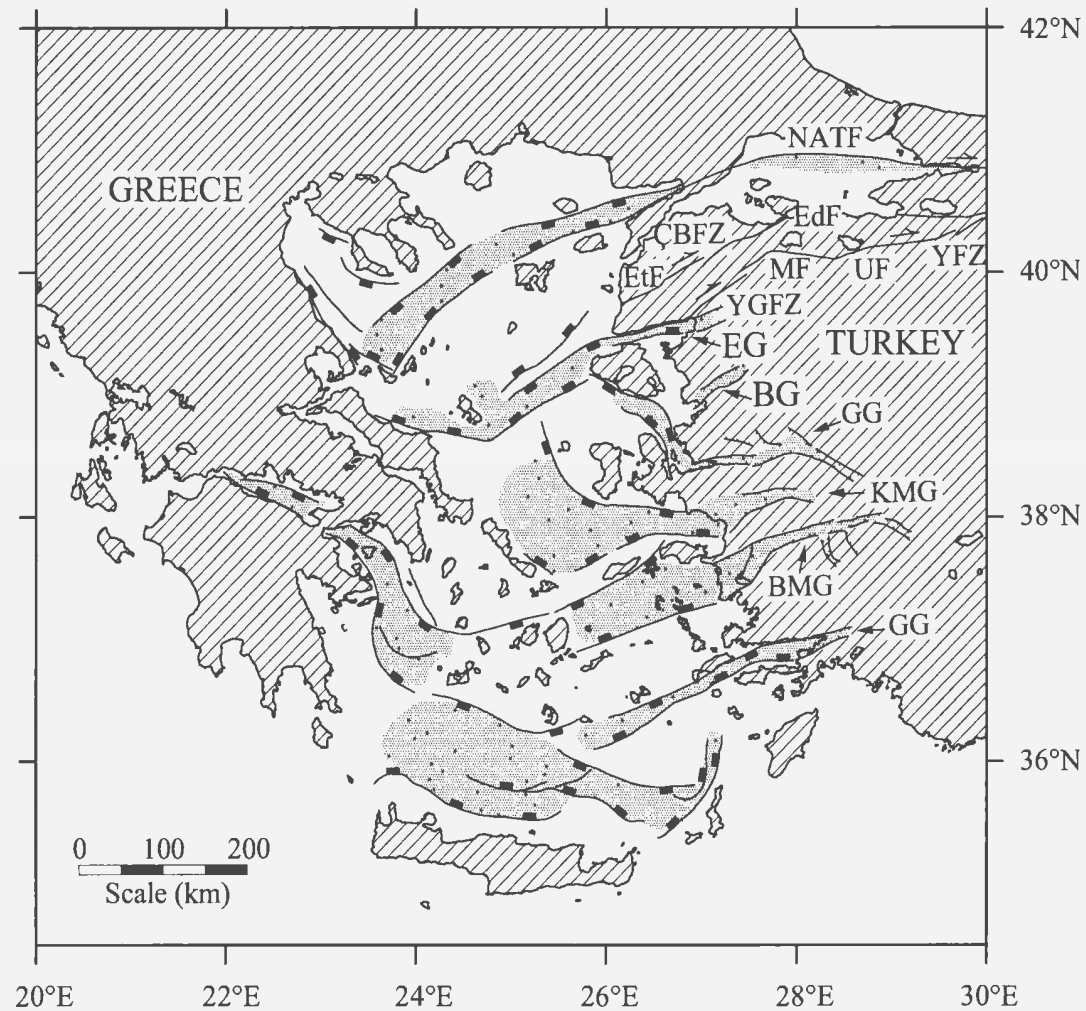
Figure 1.2. Tectonic map of western Turkey and the Aegean Sea showing the splays of the North Anatolian Transform Fault and major E-W-trending graben (modified from IGME, 1989; Mascle and Martin, 1990; Taymaz et al., 1991; Okay et al., 1999; Barka and Kadinsky-cade, 1988; Yaltırak et al., 1996). NATF- North Anatolian Transform Fault, YFZ- Yalova Fault Zone, UF- Ulubat Fault, MF- Manyas Fault, ÇBFZ- Çan-Biga Fault Zone, YGFZ- Yenice-Gönen Fault Zone, EdF- Edincik Fault, EtF- Etili Fault, EG- Edremit Graben, BG- Bakırçay Graben, GG- Gediz Graben, KMG- Küçük Menderes Graben, BMG- Büyük Menderes Graben, GG- Gökova Graben.

the southern edge of the Aegean Sea. This arc actively contributes to the extensional regime that has dominated the Aegean region since the late Serravallian–early Tortonian (Meulenkamp et al., 1988). The subduction at the Hellenic Arc commenced in the early Miocene, but the roll-back process (Royden, 1993) which gave rise to the extensional regime in the back-arc region only started after the subducting slab gained sufficient length and density (Meulenkamp et al., 1988). The north-directed subduction of the African Plate beneath the Aegean segment of the Aegean-Anatolian Microplate, together with the west-directed motion of the eastern segment of the Aegean-Anatolian Microplate, created a prominent N–S extension which resulted in the development of a number of E–W-trending horsts and intervening graben. It is notable that all major rivers draining western Anatolia flow within these graben. Palynological studies of sediments from the E–W-trending Büyük Menderes graben show that the N–S extensional regime in western Turkey probably started as early as the latest Oligocene–early Miocene (Seyitoğlu and Scott, 1992a).

1.2. Bathymetry of the Aegean Sea and environs

The Aegean Sea is a shallow inland sea situated in the northeastern Mediterranean Sea between mainland Turkey in the east and Greece in the west. It is connected to the Black Sea via the Straits of Dardanelles and Bosphorus and the small land-locked Marmara Sea. The Aegean Sea is naturally divided into three morphological regions (Fig. 1.3): the northern Aegean Sea, including the North Aegean Trough; the central Aegean

Figure 1.3. Map of the Aegean Sea showing its three divided regions (see the inset), major basins (stippled), the Aegean Volcanic Arc (Cyclades), Cretan Trough and major rivers draining into the Aegean Sea. NAT- North Aegean Trough, NSB- North Skiros Basin, SSB- South Skiros Basin, LB- Lesvos Basin, KB- Kaloyeroi Basin, NIB- North Ikaria Basin, SIB- South Ikaria Basin, MB- Myrtoon Basin, KB- Karpathos Basin. SLR- Sporades-Limnos Ridge, ELR- Eyboaea-Lesbos Ridge, ACR- Andros-Chios Ridge, NAS- North Aegean Sea, CAS- Central Aegean Sea, SAS- South Aegean Sea.

plateaux and basins; and the southern Aegean Sea including the Cretan Trough. Although the shelves surrounding the Aegean Sea are generally 5–25 km wide, they widen considerably to ~ 65–75 km off the mouths of major rivers such as the Meriç, Nestos, Strymon, Axios, Aliakmon and Peneios rivers (Fig. 1.3). Here, the shelf-to-slope transitions are marked by the topset-to- foreset transitions of drowned deltas which last prograded during the sea-level lowstand of the last glacial maximum (Aksu et al., 1987).

The dominant bathymetric feature in the northern portion of the Aegean Sea is the North Aegean Trough (Fig. 1.3). It forms a narrow and arcuate, 800–1000 m-deep bathymetric depression which extends from the Gelibolu Peninsula with a WSW trend, swinging to a more southwesterly trend and widening toward the west. The North Aegean Trough comprises a number of interconnected deep depocentres, including the Saros and Sporades Basins (Fig. 1.3).

The central Aegean Sea is characterized by a series of shallower (400–600 m), generally NE-trending broad depressions, including the North and South Skiros, Lesbos, Kaloyeroi, North and South Ikaria Basins and their intervening 100–200 m-deep shoals and banks, including Sporades-Limnos, Eyboaea-Lesbos, Andros-Chios Ridges and associated islands (Fig. 1.3). To the northeast, the Sporades-Limnos Ridge extends toward a very shallow (<100 m-deep) broad platform south of the Strait of Dardanelles (Fig. 1.3).

The southern Aegean Sea is separated from the central Aegean Sea by the arcuate Cyclades, a convex-southward shallow volcanic arc dotted by numerous islands and

shoals extending from the southern tip of Evvoia Island to southwestern Turkey (Fig. 1.3). A large, and 1000–2000 m-deep, generally E–W-trending depression, the Cretan Trough, occupies the southernmost portion of the Aegean Sea immediately north of Crete. Two smaller Myrtoon and Karpathos basins occur in the northwestern and northeastern portions of the Cretan Trough, respectively.

1.3. Structural Framework of the Aegean Sea and environs

The Aegean Sea, including the coastal regions of Greece and western Turkey, are the most seismically active regions of the Aegean-Anatolian Microplate (Fig. 1.4). This region is characterized by a predominantly extensional/transtensional tectonic regime, as indicated by fault-plane solutions of recent earthquakes (McKenzie, 1978; Taymaz et al., 1991), GPS slip vectors (Reilinger et al., 1997; Straub et al., 1997; McClusky et al., 2000) and regional structural maps (Mascle and Martin, 1990; Saatçılar et al., 1999).

1.3.1. Seismicity and Fault-Plane Solutions

The large, crustal-scale faults that bound the Aegean-Anatolian Microplate can be readily identified by earthquakes with <70 km focal depths (Fig. 1.4). Similarly, the southern boundary of the microplate, particularly the Hellenic Arc and to a lesser extent the Cyprus Arc, can easily be distinguished by a narrow belt created by earthquake epicenters at <70 km and >70 km depth. The seismicity map further shows that very few earthquakes with focal depth >70 km have occurred on land, except for the triple junction
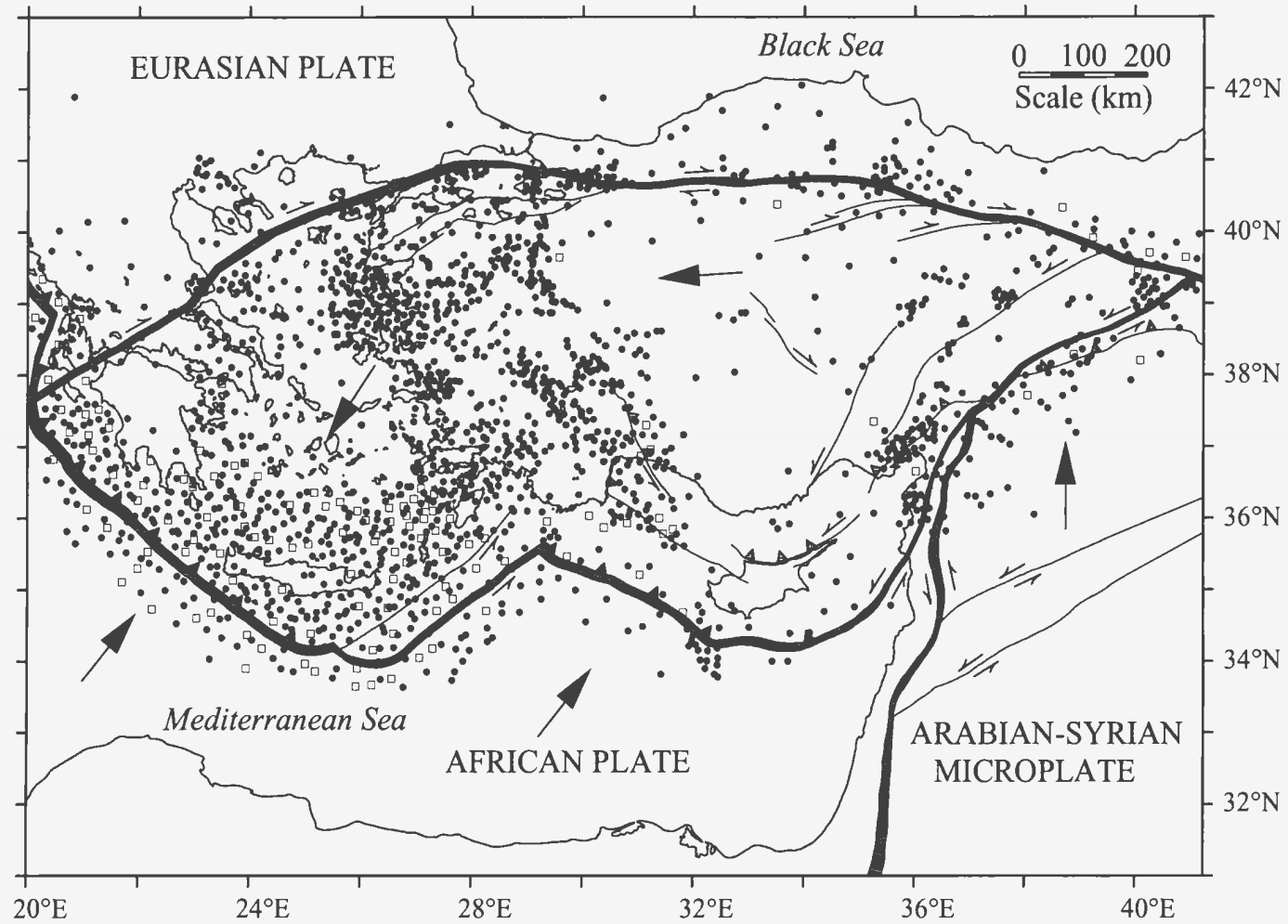
Figure 1.4. Map showing the distribution of the epicentres of large earthquakes (magnitude>4) in the Eastern Mediterranean (from Kandilli Observatory and Earthquake Research Institute- KOERI, and International Bathymetric Chart of the Mediterranean - Seismicity- IBCM-S). Filled circles and open squares represent epicentres with focal depths of <70 km and >70 km, respectively. Heavy lines with filled triangles show the active subduction zone. Lines with stippled triangles show major thrust faults with symbols on the hanging wall. Large arrows show the relative movement of the African Plate and Arabian-Syrian and Aegean-Anatolian microplates. Half arrows represent strike-slip faults with arrows showing the directions of relative displacement.

near Karlıova where the North Anatolian and East Anatolian transform faults meet (Fig. 1.1; Şengör, 1979).

Earthquakes with focal depths <70 km cluster along the E–W-trending North Anatolian and East Anatolian transform faults. Several large earthquakes have occurred along the North Anatolian Transform Fault during the last 60 years. For example, the 1939 Erzincan earthquake (M=7.9 to 8.0) created 350 km of ground rupture. Similarly, large earthquakes such as the 1942 Erbaa-Niksar (M=7.1), 1943 Tosya (M=7.6), 1944 Bolu-Gerede (M=7.3), 1957 Abant (M=7.0), 1967 Mudurnu (M=7.1), 1992 Erzincan (M=6.8),1999 Kocaeli (M=7.4), and 1999 Düzce earthquakes have produced more than 1000 km of cumulative surface rupture along the North Anatolian Transform Fault. The East Anatolian Transform Fault is also seismically active with numerous large earthquakes, such as the 1971 Bingöl (M=6.8) and 1986 Sürgü (M=6.0) earthquakes (Pamir and Ketin, 1941; Ketin, 1968; Ambraseys, 1970; McKenzie, 1970; Tokay, 1973; Dewey, 1976; Koçyiğit, 1988, 1989, and 1990; Barka et al., 2000; Wright et al., 2000; Bozkurt, 2001).

Earthquakes with focal depths of <70 km and small to moderate magnitudes demonstrate the coherent crustal character of the central region of the Aegean-Anatolian Microplate. Within this area, only occasional historical and recent earthquakes have been recorded, such as the 1717 and 1835 Ecemiş, 1914 Gemerek (M=5.6), 1938 Kırşehir (M=6.8), 1940 Erciyes (M=5.3), and 1996 Mecitözü-Çorum (M=5.6) earthquakes. The majority of these earthquakes have been concentrated along sinistral splays of the North

Anatolian Transform Fault (Paréjas and Pamir, 1939; Ketin, 1968; Eyidoğan et al.,1991; Kalafat and Pınar, 1998).

Western Turkey, west of 31°E, and the region of the Aegean Sea experience intense normal-slip and dextral strike-slip fault activity associated with the counterclockwise rotation of the microplate. This tectonic activity is manifested by swarms of low-magnitude earthquakes, forming major E–W-trending zones defining the E–W-trending graben, such as the Edremit, Bakırçay, Gediz, Küçük Menderes, Büyük Menderes and Gökova graben (Fig. 1.2; Bozkurt, 2001). Within these graben, several historical to recent, moderate–large magnitude earthquakes have been recorded, such as the 1653 and 1899 Menderes, 1919 Soma (M=6.9), 1928 Torbalı (M=6.3), 1933 Gökova (M=6.5), 1939 Dikili-Bergama (M=6.8), 1956 Söke-Balat (M=7.1), 1965 Salihli (M=5.8), 1965 Honaz (M=5.3), 1969 Demirci (M=5.9), 1969 Alaşehir (M=6.5), 1970 Gediz (M=7.2), and 1986 Çubukdağ (M=5.5) earthquakes (Ergin et al., 1967; Ambraseys and Finkel, 1987; Eyidoğan, 1988; Ambraseys, 1988; Eyidoğan et al., 1991; Westaway, 1993; Taymaz, 1993; Nalbant et al., 1998; Altunel, 1998).

In northwestern Turkey (i.e., the Marmara region) low-magnitude earthquakes define well-defined linear seismic zones along three major strands of the North Anatolian Transform Fault. The first seismic zone traces the northern strand and has an E–W trend as it extends across the Marmara Sea. The exact position of the northern strand in the Marmara Sea is not well imaged, but is suggested to form an arcuate zone within the northern segment of the Marmara Sea beneath the deep central basins (Aksu et al., 2000).

Towards the west, this fault zone enters the Gulf of Saros in the northeastern Aegean Sea. The other two seismic zones delineate the central and southern strands of the North Anatolian Transform Fault. They display an ENE trend in the east progressively becoming NE and NNE as they cross the Biga Peninsula and eventually enter the Aegean Sea at Ezine and the Gulf of Edremit, respectively (Barka and Kadinsky-Cade, 1988).

Seismicity maps of earthquake activity together with fault-plane mechanisms provide more reliable data on the nature of deformation and the most recent neotectonic activity in the region. The fault-plane-solution map of major earthquakes clearly demonstrates the intense normal- and strike-slip activity in the Aegean Sea (Fig. 1.5; Appendix A). Along the North Anatolian and East Anatolian transform faults, the fault-plane mechanisms reveal pure strike-slip solutions which are consistent with the field studies and GPS results. Moreover, fault-plane mechanisms indicate a progressive increase in the compressional component associated with the dominant strike-slip fault activity along the North Anatolian and East Anatolian transform faults toward the triple junction near Karlıova (Fig. 1.5).

In western Turkey, fault-plane mechanisms clearly illustrate the dominance of extensional deformation corresponding to the major graben systems. In northwestern Turkey (i.e., the Marmara region), fault-plane solutions demonstrate that normal- and strike-slip fault activity is dominant as the North Anatolian Transform Fault trifurcates west of Adapazarı. The fault-plane solutions in the Aegean Sea exhibit the presence of a dominantly strike-slip regime with a significant dip-slip component. However,
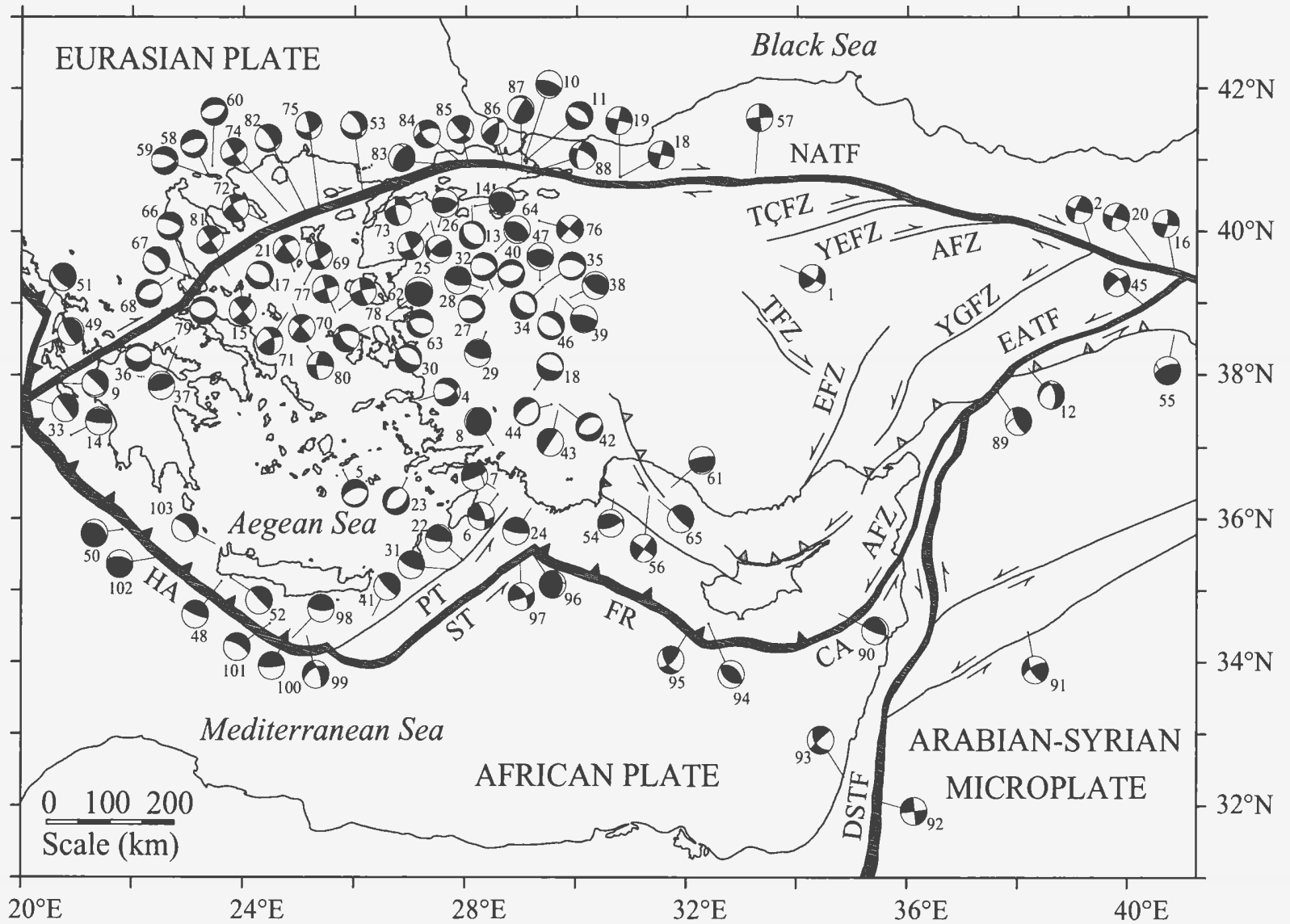
Figure 1.5. Map showing the fault-plane solutions of selected earthquakes (lower hemisphere projection) from several authors (McKenzie, 1972, 1978; Dziewonski et al., 1981; Jackson and McKenzie, 1984; Taymaz et al., 1991; Gürbüz et al., 2000; USGS PDE). Compressional quadrants are shaded. Numbers identify earthquakes reported in Appendix A. NATF- North Anatolian Transform Fault, EATF- East Anatolian Transform Fault, DSTF- Dead Sea Transform Fault, YGFZ- Yakapınar-Göksun Fault Zone, EFZ- Ecemiş Fault Zone, AFZ- Almus Fault Zone, TÇFZ- Taşova-Çorum Fault Zone, YEFZ- Yağmurlu-Ezinepazarı Fault Zone, TFZ- Tuzgölü Fault Zone, HA- Hellenic Arc, PT- Pliny Trench, ST- Strabo Trench, FR- Florence Rise, CA- Cyprus Arc, AFZ- Amanos Fault Zone. Heavy lines with filled triangles show the active subduction zone. Lines with stippled triangles show thrust faults with symbols on the hanging wall. Half arrows represent strike-slip faults with arrows showing the directions of relative displacement. A typical strike-slip symbol is found at 40°N at the extreme right of the map (no. 16), whereas a typical dip-slip symbol is immediately below at 38°N (no. 55).

extensional forces ought to be more effective than they appear to be on these lower hemisphere projections of the focal mechanisms to account for the deep basins in the North Aegean Trough, Gulf of Edremit, and Skyros Basin of the Aegean Sea.

1.3.2. GPS-based Motions

GPS is a constellation of 24 Earth-orbiting satellites which can be used for precise geodetic position measurements. These measurements provide constraints on rheological models of the continental lithosphere, the forces responsible for active deformation when applied to crustal plates, and the deformations where such plates interact (e.g., McClusky et al., 2000).

The GPS velocity field relative to an arbitrarily fixed Eurasian Plate clearly shows the counterclockwise rotation of Turkey, south of the North Anatolian Transform Fault, and the progressive west–southwest increase in the velocity of the microplate towards the Hellenic Arc (Fig. 1.6).

Reilinger et al. (1997) and McClusky et al. (2000) have derived two Euler vectors (i.e., rotation pole and rate) using (1) only the stations located in central Anatolia and (2) the stations located all around Turkey. They showed that Euler vectors display negligible differences in pole locations indicating that the region south of the North Anatolian Transform Fault moves west-southwest as a coherent unit. However, based on evidence for different velocities and the significant difference in earthquake focal mechanisms between the Aegean and Anatolian microplates, McKenzie (1970), Jackson and
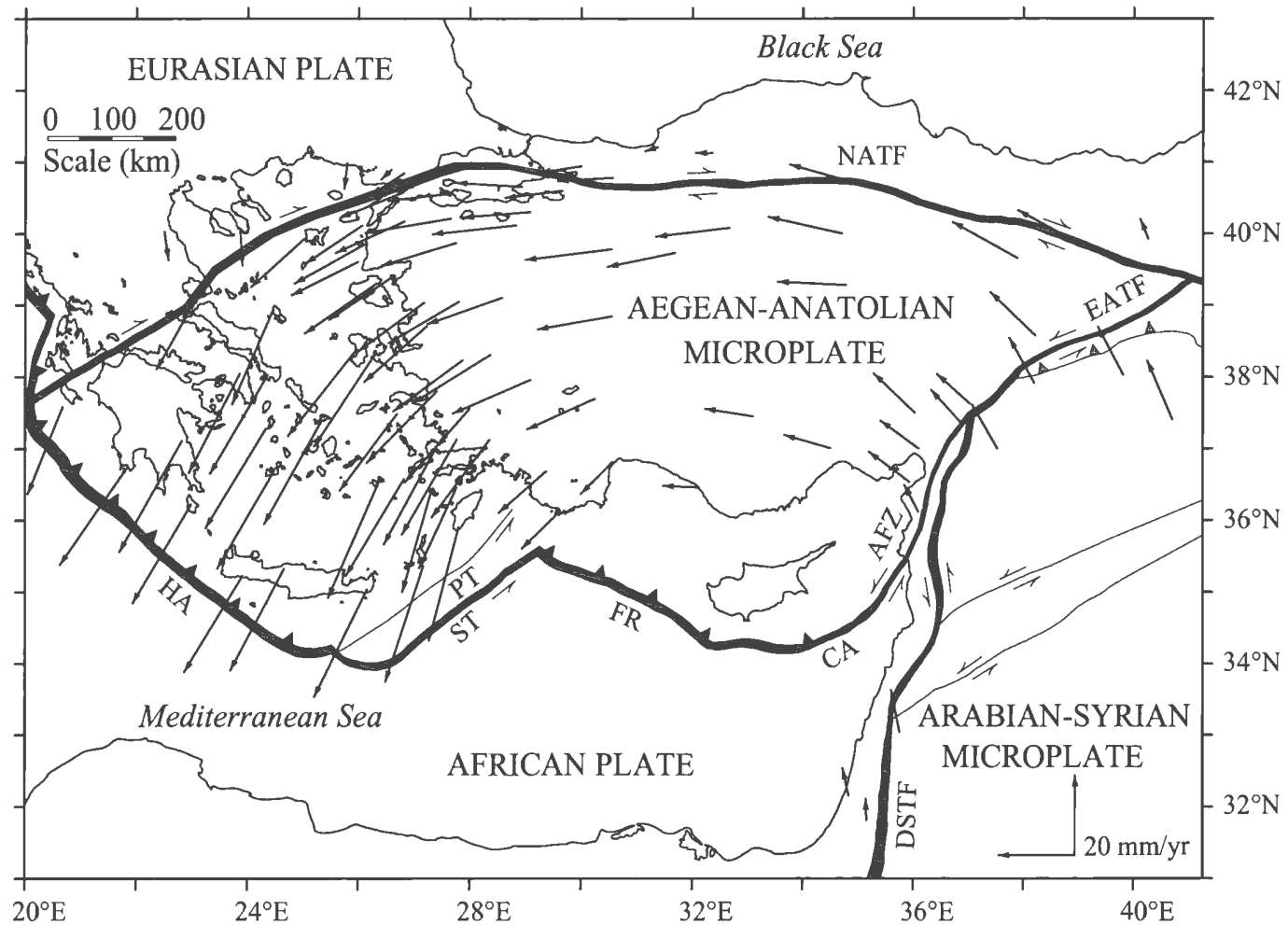
Figure 1.6. Map showing the Global Positioning System (GPS) horizontal velocities of the Aegean-Anatolian Microplate with respect to a Eurasia-fixed reference frame for the period 1988-1997 (modified from McClusky et al., 2000). These velocities are plotted as vectors with scale printed at lower right (each station is at the tail of the arrow). NATF- North Anatolian Transform Fault, EATF- East Anatolian Transform Fault, DSTF- Dead Sea Transform Fault, HA- Hellenic Arc, PT- Pliny Trench, ST- Strabo Trench, FR- Florence Rise, CA- Cyprus Arc, AFZ- Amanos Fault Zone. Heavy lines with filled triangles show the active subduction zone. Lines with stippled triangles show thrust faults with symbols on the hanging wall. Half arrows represent strike-slip faults with arrows showing the directions of relative displacement.

McKenzie (1988), and Jackson (1992) postulated the existence of a N–S extension zone

that separates the western Aegean half from the eastern Anatolian half of the microplate.

In reality, there is no distinct boundary between the Aegean and Anatolian parts of the

microplate; instead, a diffuse N–S-trending zone extending from the Anaximander

Mountains to the Gulf of İzmit was postulated to divide the microplate (McKenzie,1972).

This interpretation contrasts with the single plate hypothesis of Reilinger et al.(1997a)

and Oral et al.(1995) for the Aegean-Anatolian Microplate. They point to internal

deformation in the western part of the microplate to explain the east-west contrasts.

Figure 1.7 displays the residual velocities for GPS stations after removing the

coherent plate motion in a reference frame fixed to the eastern Anatolian segment of the

microplate. Figure 1.7 not only illustrates the negligible internal deformation (<2 mm yr^{-1}) of central Anatolia east of 31° E, but also lends support to the two-microplate

hypothesis of McKenzie (1972) and Barka and Reilinger (1997) by demonstrating the

noticeable differences in velocities of the stations located in the western Aegean part and

the eastern Anatolian part of the microplate.

Many authors have derived Euler vectors for the Anatolian Microplate and the

Eurasian Plate (e.g., Jackson and McKenzie, 1984; Taymaz et al., 1991; Westaway,

1994a; Reilinger et al., 1997; McClusky et al., 2000). An Euler vector (a rotation vector)

is a combination of spreading rates, transform-fault azimuths and earthquake slip vectors

which allows the prediction of relative plate motions. Positive rotation rate (e.g. 0.64°

Myr^{-1}) implies counterclockwise rotation of the related plate. Jackson and McKenzie
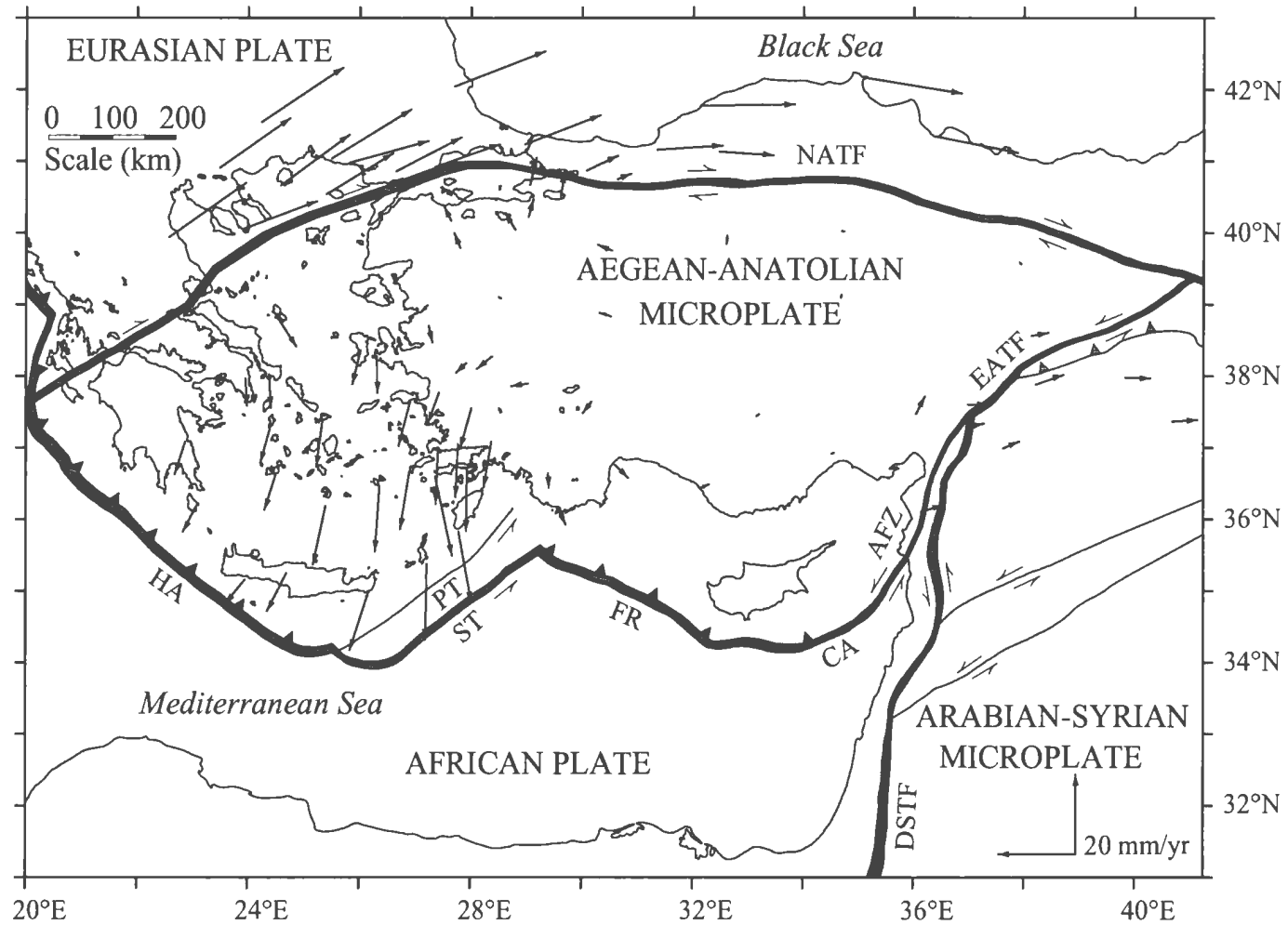
Figure 1.7. Map showing the Global Positioning System (GPS) horizontal velocities of the Aegean-Anatolian Microplate with respect to an Anatolia-fixed reference frame for the period 1988-1997 (modified from McClusky et al., 2000). NATF- North Anatolian Transform Fault, EATF- East Anatolian Transform Fault, DSTF- Dead Sea Transform Fault, HA- Hellenic Arc, PT- Pliny Trench, ST- Strabo Trench, FR- Florence Rise, CA- Cyprus Arc, AFZ- Amanos Fault Zone. Heavy lines with filled triangles show the active subduction zone. Lines with stippled triangles show thrust faults with symbols on the hanging wall. Half arrows represent strike-slip faults with arrows showing the directions of relative displacement.

(1984) have derived an Euler vector using the earthquake-slip vectors along the dextral North Anatolian Transform Fault (14.6° N, 34° E, 0.64° Myr^{-1}). Taymaz et al. (1991) have derived an Euler vector (14.6°N, 34°E, 0.78° Myr^{-1}) close to that of Jackson and McKenzie (1984), but with a minor difference in rotation rate. However, Westaway (1994), Reilinger et al. (1997), and McClusky et al. (2000) have derived Euler vectors (31°N, 35.5° E, 0.83±0.1° Myr^{-1}; 29.2±0.8°N, 32.9±0.4°E, 1.3±0.1° Myr^{-1}; 30.7±0.8°N, 32.6±0.4°E, 1.2±0.1° Myr^{-1}, respectively) that display a ~15° northward shift from the previously obtained rotation poles of Jackson and McKenzie (1984) and Taymaz et al. (1991). This north-shifted pole location indicates a smaller radius for the counterclockwise rotation of the Aegean-Anatolian Microplate.

Many authors have estimated slip rates for the North Anatolian and East Anatolian Transform Faults. Based on Euler vectors for the Anatolian Microplate, McClusky et al. (2000) and Reilinger et al. (1997) have obtained slip rates for the North Anatolian Transform Fault of 24±1 mm yr^{-1}, and 30±2 mm yr^{-1}, respectively, and for the East Anatolian Transform Fault of 9±1 mm yr^{-1} and 15±3 mm yr^{-1}, respectively. Straub and Kahle (1994, 1995) have used independent GPS data spanning the western end of the North Anatolian Transform Fault in the Marmara region and estimated a slip rate of 20±3 mm yr^{-1} for the area. Taymaz et al. (1991) and Westaway (1994a), based on the seismic moments of earthquakes on the East Anatolian Transform Fault, have obtained slip rates of 6–10 mm yr^{-1}. These estimated slip rates are internally consistent except for those calculated by Reilinger et al. (1997) who used limited GPS data from 1988–1994.

1.4. Structural architecture

1.4.1. Marine

Interpretation of regional multi-channel seismic reflection profiles (Mascle and Martin, 1990) shows that the upper crustal structural framework of the Aegean Sea is characterized by a series of relatively deep NE–SW-trending and E–W-trending horst-graben structures in the north and south, respectively. Comparison of the structural and bathymetric maps (Institute of Geology and Mineral Exploration-IGME, 1989; Mascle and Martin, 1990) shows that most of the graben structures are associated with bathymetric troughs whereas horsts are represented by linear shallow ridges and associated small islands in the Aegean Sea, collectively suggesting that the present-day physiography of the region is largely a result of active tectonism (Fig. 1.3).

Multi-channel seismic reflection profiles show that the flanks of the graben are bounded by large faults with notable NW- and SE-directed normal-sense dip separations and listric fault geometries (e.g., Mascle and Martin, 1990). The Plio–Quaternary strata within these graben display large growth wedges concentrated along one of the master faults, producing an asymmetric half-graben architecture. Recent studies of seismicity (Saatçılar et al., 1999) and earthquake fault-plane solutions reveal that a large proportion of these faults have a pronounced dextral strike-slip component (McKenzie, 1978; Taymaz et al., 1991). Local marine studies show that many of the master faults bounding these graben can be readily traced landward on to mainland Turkey where they are

mapped as prominent splays of the North Anatolian Transform Fault (Armijo et al., 1999).

Seismic reflection profiles show that the Saros Trough is an ENE-trending half graben bounded by normal faults (Mascle and Martin, 1990). A number of fault-plane solutions reveal that these master faults also display a significant dextral strike-slip component (53, 75 and 82 in Fig. 1.5 and Appendix A). The northern master fault bounding the Saros Trough extends westward, linking with the Ganos-Gaziköy Fault Zone in the northern Gelibolu Peninsula (Ambraseys, 1970; Allen, 1975; Crampin and Evans, 1986; Okay et al., 1999; Gürbüz et al., 2000), which in turn extends farther eastward to connect with the northern strand of the North Anatolian Transform Fault beneath the Marmara Sea (Barka and Kadinsky-Cade, 1988; Yaltırak et al., 1996).

The Sporades Basin is a NE-trending asymmetric graben situated at the southwestern end of the North Aegean Trough. It is characterized by steep scarps along NE-trending master faults with significant normal-sense dip-slip at its northern and southern margins. A large SE-trending normal fault delineates its western margin (Brooks and Ferentinos, 1980; Lybéris, 1984; Le Pichon et al., 1984). Fault-plane solutions (Taymaz et al., 1991; McKenzie, 1978) show that motion on the master faults has a strong dextral strike-slip component (15, 72, 74, 81 in Fig. 1.5 and Appendix A).

The North Skiros Basin and its northeastern continuation, the Edremit Trough, define a narrow NE-trending graben system which is bounded by large faults with normal-sense dip-slip separations, forming steep escarpments on the sea floor (Mascle

and Martin, 1990). The northern fault zone of this basin defines the southern margin of the Sporades-Limnos Ridge and the Eyboaea-Lesbos Ridge (Fig. 1.3). However, fault-plane solutions of four seismic events (21, 69, 70 and 71 in Fig. 1.5 and Appendix A) show that the large basin-bounding faults also show significant dextral strike-slip with a trend varying from NE to ENE. Farther to the northeast, the Edremit Trough takes a more ENE trend and possibly links with the notable graben structure trending WSW from the Baba Burnu promontory of western Turkey (Taymaz et al., 1991).

Taymaz et al. (1991) postulate that the northern bounding fault (69 in Fig. 1.5 and Appendix A) of the North Skiros Basin, with a dominant right-lateral slip, extends northeast toward the Biga Peninsula and appears to connect with the fault that bounds the northern shores of the Edremit Graben. The NE to ENE changes in fault orientation and bathymetric trends from west to east toward the Turkish mainland broadly parallel the curvature of the North Aegean Trough in the north.

Compared to the north and central Aegean, there is little seismic activity in the southern Aegean. Fault-plane solutions indicate a dominantly extensional and compressional regimes in the areas north and south of Crete, respectively as a consequence of subduction along the Hellenic Arc (Fig. 1.5; McKenzie, 1978).

1.4.2. Onland

The northern branch of the North Anatolian Transform Fault extends with an E–W trend from Sapanca Lake toward the town of Gölcük. Farther to the west, it enters

the Marmara Sea and forms the main stem which links the North Anatolian Transform Fault with the Saros-Ganiköy Fault Zone (Fig. 1.1; see Yaltırak, 2002, for a review). The origin of the Marmara Sea and the nature of the main stem of the North Anatolian Transform Fault within the deep Marmara Sea basins are conjectural, and presently hotly debated (i.e., Barka and Kadinsky-Cade, 1988; Reilinger et al., 1997; Aksu et al., 2000; Yaltırak, 2002). A number of studies have suggested that several pull-apart basins and the associated releasing and constraining bends connect the North Anatolian Transform Fault to the Saros-Ganiköy Fault Zone in the western Marmara Sea (e.g., Barka and Kadinsky-Cade, 1988), whereas others have argued that a single, deeply-buried stem of the North Anatolian Transform Fault cuts across the Marmara Sea with an E–W trend, with the Marmara Sea defining a negative flower structure, or tulip structure (Aksu et al., 2000). Despite the controversy regarding the nature of the North Anatolian Transform Fault within the Marmara Sea, there is consensus that at the western end of the Marmara Sea this fault reaches the Gelibolu Peninsula near the town of Şarköy, and extends to the SW to connect with the Saros-Gaziköy–Ganos Fault system (Figs 1.1, 1.2). The latter shows a continuous, almost 100 km-long, rupture zone (Dewey and Şengör, 1979; Evans et al., 1985; Crampin and Evans, 1986; Jackson, 1994; Tüysüz, 1998).

The central branch of the North Anatolian Transform Fault extends west from the town of Gölcük, along the northern shores of the Bozburun Peninsula and enters the Marmara Sea ~ 15 km west of the town of Yalova, where it shows a ~ 70 km-long linear rupture zone (Fig. 1.2; Barka and Kadinsky-Cade, 1988).

The southern branch of the North Anatolian Transform Fault splays off the central branch in a SW direction west of the town of Mudurnu and runs parallel to the Yalova Fault Zone (Fig. 1.2). It extends westward with an E–W trend, passes through the Geyve Basin, then skirts the southern shore of Lake İznik, entering the Marmara Sea near the town of Gemlik (Fig. 1.2; Üçer et al.,1985; Barka and Kadinsky-Cade, 1988; Straub et al., 1995). This fault is postulated to extend into Bandırma Bay (Barka and Kadinsky-Cade, 1988; Gürbüz et al., 2000). A dextral strike-slip fault zone extends westward from Bandırma Bay, south of the Kapıdağ Peninsula and southwest toward the Biga Peninsula. From northeast to southwest this fault zone includes the Edincik Fault, Sarıköy Fault, Çan-Biga Fault Zone and Etili Fault (Fig. 1.2; Barka and Kadinsky-Cade, 1988; Şaroğlu et al., 1992). This fault system continues farther southwest and enters the Aegean Sea west of the town of Ezine (Fig. 1.2).

A major dextral strike-slip fault system separates from the southern branch of the North Anatolian Transform Fault near the town of İznik and extends toward the southwest. This fault zone links to the west with the Ulubat Fault which tracks the southeastern shores of Ulubat Lake (Fig. 1.2). Farther to the west, it links with the E–W-trending to WNW–ESE-trending Manyas Fault, south of Manyas Lake. Thereafter, this fault zone displays a sharp swing to the southwest and connects with the Yenice-Gönen Fault Zone. The latter is postulated to continue farther southwest, to connect with the large fault zone which defines the northern shores of Edremit Bay (Yılmaz et al., 2000), and to reach the Skiros Basin at its western extremity (Fig. 1.2; Nalbant et al.,1998; Barka

and Kadinsky-Cade, 1988).

1.5. Paleoceanography of the Aegean Sea

The Aegean Sea has a surface area of $\sim 2 \times 10^5$ km^2 and a volume of $\sim 74,104$ km^3. It constitutes one of the four prominent basins of the eastern Mediterranean Sea (Yüce, 1992). The Aegean Sea is connected to the Black Sea through the Straits of Dardanelles (50–60 m deep) and Bosphorus (30–45 m deep) and the intervening Marmara Sea (Fig. 1.3). It is connected to the eastern Mediterranean Sea via larger and deeper straits between the Peloponnesus (southern Greece), the islands of Crete and Rhodes, and southwestern Turkey.

The water exchange between the Black Sea and the eastern Mediterranean occurs through the Straits of Bosphorus and Dardanelles and the Marmara Sea as a two-layer flow (Latif et al., 1992; Özsoy et al., 1995; Polat and Tuğrul, 1996). The cooler (5°–15°C) and lower salinity (17–20‰) surface water leaves the Black Sea, then flows south and southwest through the straits with velocities of 10–30 cm s^{-1}. It has an annual outflow of ~ 300 km^3 across the Strait of Dardanelles into the northeast Aegean Sea, mostly occurring in late spring and summer as the result of maximum discharge of large rivers entering the Black Sea, such as the Dnieper, Dniester, Don, Danube and Bug (Özsoy et al., 1995). This water mass forms a 25–100 m-thick surface layer in the Black Sea and Marmara Sea as well as the north easternmost segment of the Aegean Sea. In the northern Aegean Sea, this lower-salinity and relatively cold surface water forms a

cyclonic gyre which is affected by the bottom topography, shoreline configurations, and the prevailing winds in the region (Yüce, 1991). The warmer (15°–20°C) and higher salinity (38–39‰) Mediterranean water flows along the eastern side of the Aegean Sea, enters the Strait of Dardanelles and moves northeast beneath the Black Sea surface water with velocities of 5–25 cm s^{-1}.

The prevailing winds in the region show notable seasonal variability and alter the flow path of the surface waters. During the winters, the northeasterly gales (Bora type) are the frequent winds in the northern Aegean Sea. These gales occur with outbreaks of continental polar or arctic air from the Black Sea and bring cold-dry winds into the area (Yüce, 1991). In summers, the persistent winds of the northern Aegean are known as the Etesians. These winds are primarily northeasterly monsoon-type winds, and result in upwelling and downwelling along the Turkish and Greek coasts, respectively.

The physical oceanography of the Aegean Sea is controlled mainly by the regional climate, the fresh-water discharge from major rivers draining southeastern Europe, and the seasonal variations in the Black Sea surface-water outflow through the Strait of Dardanelles. Based on the analysis of CTD data collected throughout the Aegean Sea during the summer, autumn, winter and spring, Yaşar (1994) distinguished three distinct water masses: surface, intermediate and bottom. The Aegean Sea surface water forms a 40–50 m-thick layer, with summer and winter temperatures of 21°–26°C and 10°–16°C, and salinities of 30.0–39.5‰ and 36.1–39.5‰, respectively. The steepest salinity gradient is observed in the northern Aegean Sea immediately west of the Strait of

Dardanelles. The Aegean Sea intermediate water is observed between ~40–300 m water depth. It exhibits small variations in salinity (39.0–39.1‰) and temperature (15°–18° to 11°–16°C) during summers and winters, respectively. The Aegean Sea bottom water occurs below 200–300 m depth and displays uniform temperature (13°–14°C) and salinity (39.1–39.2‰).

The Aegean Sea has experienced considerable sea-level fluctuations through glacial–interglacial cycles. During the glacial maximum, ca. 20,000 yr BP (years before present), the sea level stood at ~ −115 m (Aksu et al., 1987) and both the straits of Bosphorus and Dardanelles were subaerially exposed disrupting the water exchange between the Black Sea and the Aegean Sea (Yaltırak et al., 2002). In addition, most of the continental shelves and shallow channels in the Aegean Volcanic Arc (Cyclades) were also subaerially exposed, so the water exchange between the Mediterranean and the Aegean seas was considerably reduced (Fig. 1.8).

The global glacio-eustatic sea-level curve of Fairbanks (1989) suggests that the post- glacial sea-level rise started at ~14,000 yr BP. The sea level rose from its minimum height (–115 m) to ~ –80 m by ~12,000 BP. Between ~ 12,000 and 9,500 yr BP, the sea level rose from ~ –80 m to ~ –50 m and the sill in the Dardanelles was breached, reconnecting the Marmara Sea to the Aegean Sea (Yaltırak et al., 2002). Later, at ~10,000 to 10,500 yr BP, surface waters from the Black Sea first flowed into the Marmara Sea and Aegean Sea (Hiscott et al., 2002; Aksu et al., 2002). This interval corresponds to the cessation of delta progradation across the shallow shelves of the

Figure 1.8. Map showing the position of the shoreline in the Aegean Sea during the last glacial maximum (ca. 20,000-15,000 yr BP) when the sea level stood ~ 115 m below present level (dashed hachure). Also shown is the present-day coastline and major rivers draining into the Aegean Sea.

Aegean Sea (Aksu et al., 1995). The water level reached its present height by ~3000 yr BP.

1.6. Geology of the Biga Peninsula

The geology of the Biga Peninsula and the Island of Lesbos (Midilli) in the northeast Aegean Sea is summarized here because these rocks constitute the acoustic basement for the Quaternary successions studied for this thesis. Also, these rocks record the recent tectonic deformation in the northeastern segment of the Aegean Sea.

High-grade Paleozoic metamorphic rocks, such as in the core of the Kazdağ complex, constitute a significant portion of the geology of the Biga Peninsula and are composed of gneiss, amphibolite and marble (Fig. 1.9; Bingöl et al., 1975). The Miocene volcanic and sedimentary successions in the study area overlie the deeply eroded metamorphic terrain (Fig. 1.9; Siyako et al., 1989; Okay et al., 1990). Lower and middle Miocene successions in the Biga Peninsula, Edremit Bay and the Island of Lesbos are dominated by calc-alkaline volcanic rocks of the Doyran and Ezine formations, igneous rocks including andesites, dacites, rhyolites and welded tuffs, and to a lesser extent intrusive igneous rocks, such as large granodiorite plutons (Fig. 1.9; Ternek, 1964; Kalafatçıoğlu, 1964; Siyako et al., 1989; Institute of Geology and Mineral Exploration (IGME), 1989). Contemporaneous and intercalated with these volcanic rocks are the basal conglomerates of the Kızılyar Formation and the predominantly siliciclastic Çan, İlyasbaşı, Kızılyar and Küçükkuyu formations. The equivalent formation names on the
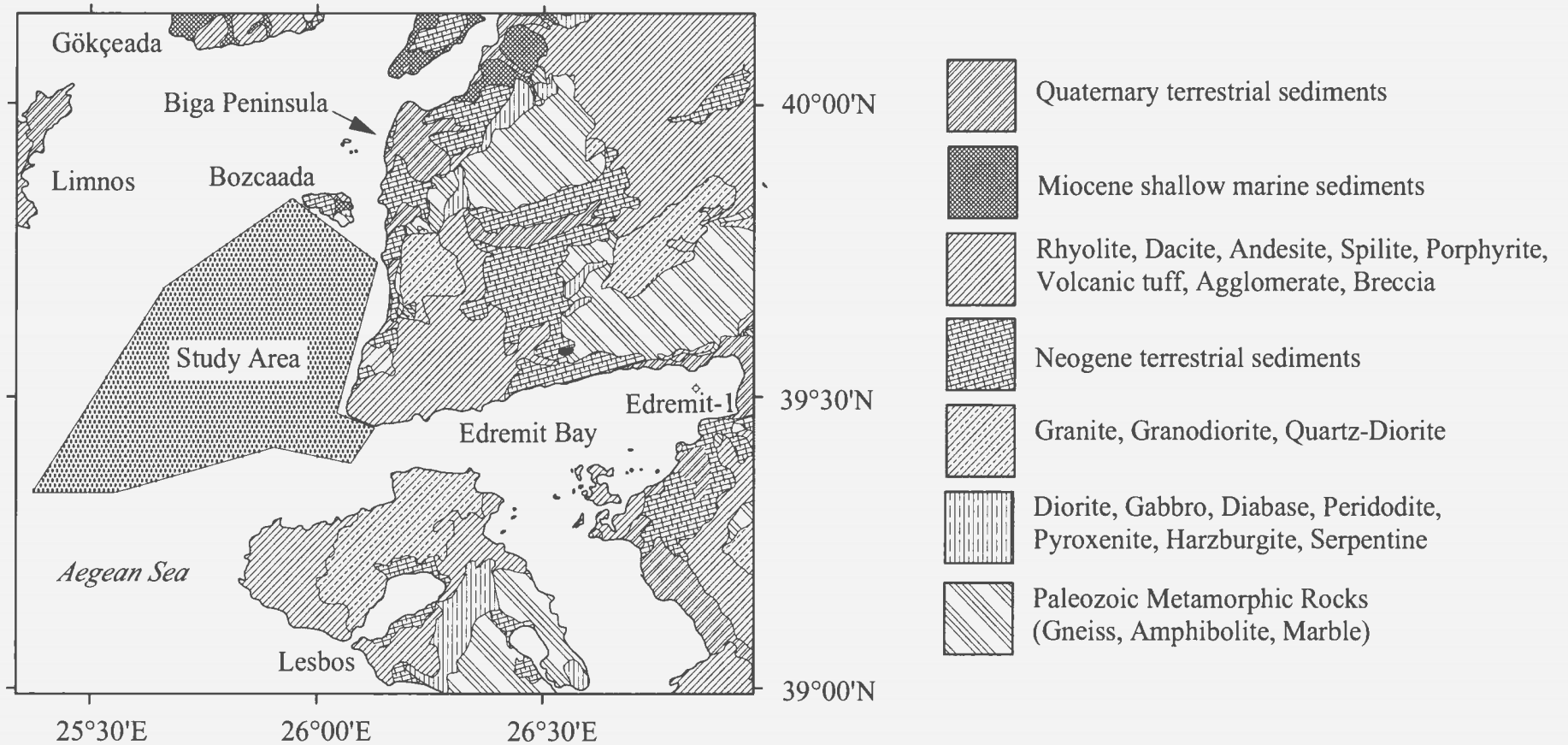
Figure 1.9. Simplified geological map of the Biga Peninsula and the Islands of Bozcaada, Gökçeada, Lesbos and Limnos (from Ternek, Kalafatçıoğlu, 1964; Institute of Geology and Mineral Exploration- IGME, 1989).

Island of Lesbos are summarized in Pe-Piper and Piper (2002).

The early–middle Miocene Çan Formation is composed of bituminous shales, siltstones, sandstones, tuffs and sporadic seams of coal. It is on average 250 m thick and unconformably rests on Miocene volcanic rocks (Fig. 1.10).

The upper Miocene İlyasbaşı Formation is ~500 m thick and consists of red to brown polygenic basal conglomerates, shales, calcareous shales, sandstones, tuffs, limestones and dolomitic limestones. It unconformably overlies the Küçükkuyu Formation south of Edremit Bay and the Doyran and Kızılyar formations and the Cretaceous Mélange east of the Baba Burnu promontory, southwest of the Biga Peninsula (Fig. 1.10). The Kızılyar Formation is characterized by red, poorly-sorted conglomerates and sandstones and has a maximum thickness of 100 m in the Edremit-1 exploration well. The Lower Miocene Küçükkuyu Formation unconformably overlies the Doyran Formation but elsewhere is a lateral equivalent of the Doyran Formation. It is composed of a basal conglomerate overlain by a thin turbidite succession, consisting dominantly of dark-coloured shales (İnci, 1984), separated from a 20–30 m-thick sandstone by a 40 m-thick yellow tuff layer (Fig. 1.10). These siliciclastic and volcaniclastic successions were deposited in small, isolated fault-bounded basins (Siyako et al., 1989).

Upper Miocene marine siliciclastic successions of the Gazhandere, Kirazlı and Alçıtepe formations overlie the lower–middle Miocene rocks across a major regionally erosional unconformity (Fig. 1.10; Siyako et al., 1989). The Gazhandere Formation is 50–100 m thick and consists of conglomerates, sandstones, shales and occasional thin

		Taştepe Basalt
Plio-Quaternary		
	Bayramiç Formation	
	Alçıtepe Formation	
	Kirazlı Formation	
	Gazhandere Formation	
Upper Miocene		Ezine Volcanics Andesite, basalt, tuff, agglomerate
	İlyasbaşı Fm	
?	Çan Formation	
Lower-Middle Miocene		
		Doyran Volcanics Andesite, basalt, agglomerate
	Küçükkuyu Formation	Kızılyar Formation
		B Tuff
Upper Eocene	Ceylan Formation	
		A Tuff
Middle Eocene	Soğucak Formation	
	Koyunbaba Formation	
Paleocene -Eocene		
Upper Cretaceous	Mélange	

Figure 1.10. Stratigraphic column showing the relationship between volcanic and sedimentary successions in Biga Peninsula (modified from Siyako et al., 1989).

limestone layers; laterally, it passes into the Kirazlı Formation (Fig. 1.10; Saltık,1974). The Kirazlı Formation (~100 m thick) is composed dominantly of cross-bedded and laminated sandstones and shales. The paleocurrent directions of these sedimentary structures indicate that the Miocene basins deepened toward the present-day Aegean and Marmara seas (Siyako et al., 1989). The shallow-marine Alçıtepe Formation is ~200 m thick and intercalates both with the Gazhandere and Kirazlı formations (Fig. 1.11). It consists of sandstones, conglomerates, shales, marls and includes oolitic limestone.

The Pliocene-Quaternary Gülpınar and Bayramiç formations overlie the Miocene siliciclastics and volcanoclastic successions as well as the metamorphic and volcanic series with a notable unconformity. The Gülpınar Formation is composed of lacustrine carbonates and intercalates with the Bayramiç Formation. The Bayramiç Formation consists of fluvial siliciclastics (shales, sandstones and conglomerates) and lacustrine carbonates (Figs. 1.10, 1.11; Siyako et al., 1989). The thicknesses of the Pliocene-Quaternary succession are highly variable in the study area, ranging from 200–300 m in small depressions and valleys in the Biga Peninsula to ~1500 m in Edremit Bay (Siyako et al., 1989). The Taştepe Basalt has a limited areal distribution, and is exclusively associated with young fault zones.

1.7. Objectives

Despite numerous studies on land in western Turkey and offshore in the northern Aegean Sea, the detailed stratigraphic architecture and tectonic framework of the
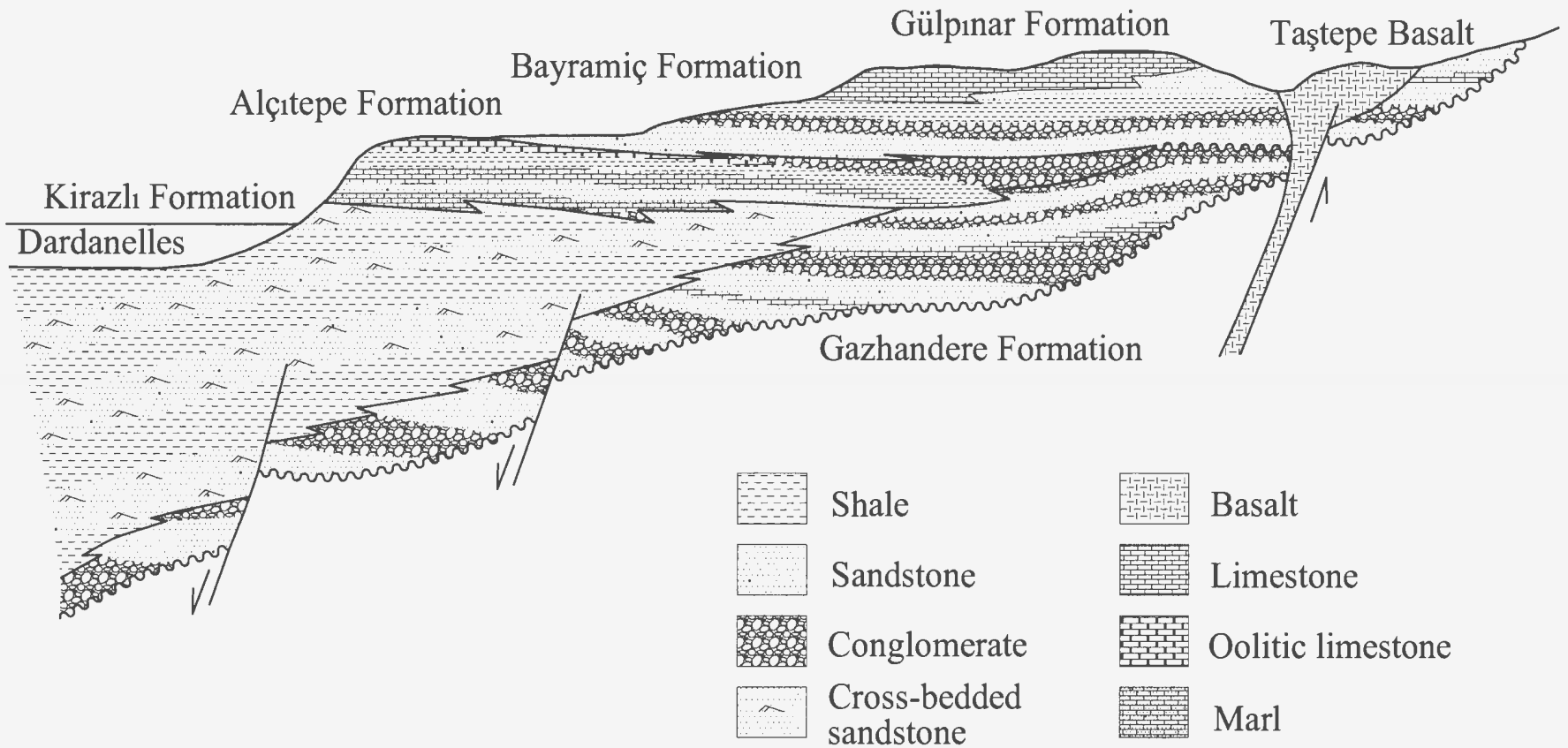
Figure 1.11. Schematic cross section showing the stratigraphic relationships of upper Miocene and Plio-Quaternary units of the Biga Peninsula (from Siyako et al., 1989).

northeastern Aegean Sea and its linkage with the North Anatolian Transform Fault system remain conjectural. For example, the western continuation of the western strands of the North Anatolian Transform Fault is not mapped and remains elusive. Similarly, the linkage between the North Anatolian Transform Fault and the prominent dextral strike-slip faults which bound the flanks of northern Aegean Sea basins remains undetermined. Therefore, the objectives of this thesis are:

(1) to delineate the structural architecture of the northeastern Aegean Sea through detailed interpretation and mapping of high resolution seismic-reflection profiles;

(2) to erect a broad seismic-stratigraphic architecture for the Quaternary successions in the NE Aegean Sea which will form the basis for a subsequent study of basin evolution within the context of oscillating glacio-eustatic sea-level variations and local tectonic subsidence in the NE Aegean Sea;

(3) to integrate this local tectonic framework with structures delineated in northwestern Turkey as well as elsewhere in the northern Aegean Sea using the earthquake focii locations, fault-plane solutions and detailed fault maps;

(4) to provide a linkage between the western strands of the North Anatolian Transform Fault and the NE-trending dextral strike-slip faults mapped in the North Skyros Basin, North Aegean Sea.

CHAPTER 2

2. Data Acquisition

2.1. Geophysical Data Acquisition

This thesis is based on detailed interpretation of ~1600 km of seismic reflection and side-scan sonar profiles and six cores collected from the northeastern Aegean Sea during cruises MAR-98 (1998), MAR-00 (2000) and MAR-02 (2002) using the research vessel *Koca Piri Reis* of the Institute of Marine Sciences and Technology (IMST), İzmir, Turkey (Fig. 2.1). All the seismic reflection profiles were collected in either a NE or a NW direction. Average line spacing is ~6 km. The orientation of most seismic profiles is nearly perpendicular to the major tectonic structures that are critical for tracing particular structural elements. This dense grid of seismic profiles provides the necessary data base for determination of the stratigraphic architecture and the structural framework of the study area. All navigational fixes were determined using the ship's GPS system. The bathymetry was recorded every 10 minutes using a 12 kHz echo-sounder.

In 1998, ~ 831 km of high-resolution Huntec deep tow system (DTS) and sparker profiles were acquired over a tight grid with ~ 5.5 km line spacing (Fig. 2.1). The Huntec DTS profiles were collected using a 500 joule multi-tip sparker source mounted on the tow fish;reflections were received using both a high-resolution single internal hydrophone and a 21-element, 6 m-long Benthos hydrophone streamer trailing behind the tow fish.
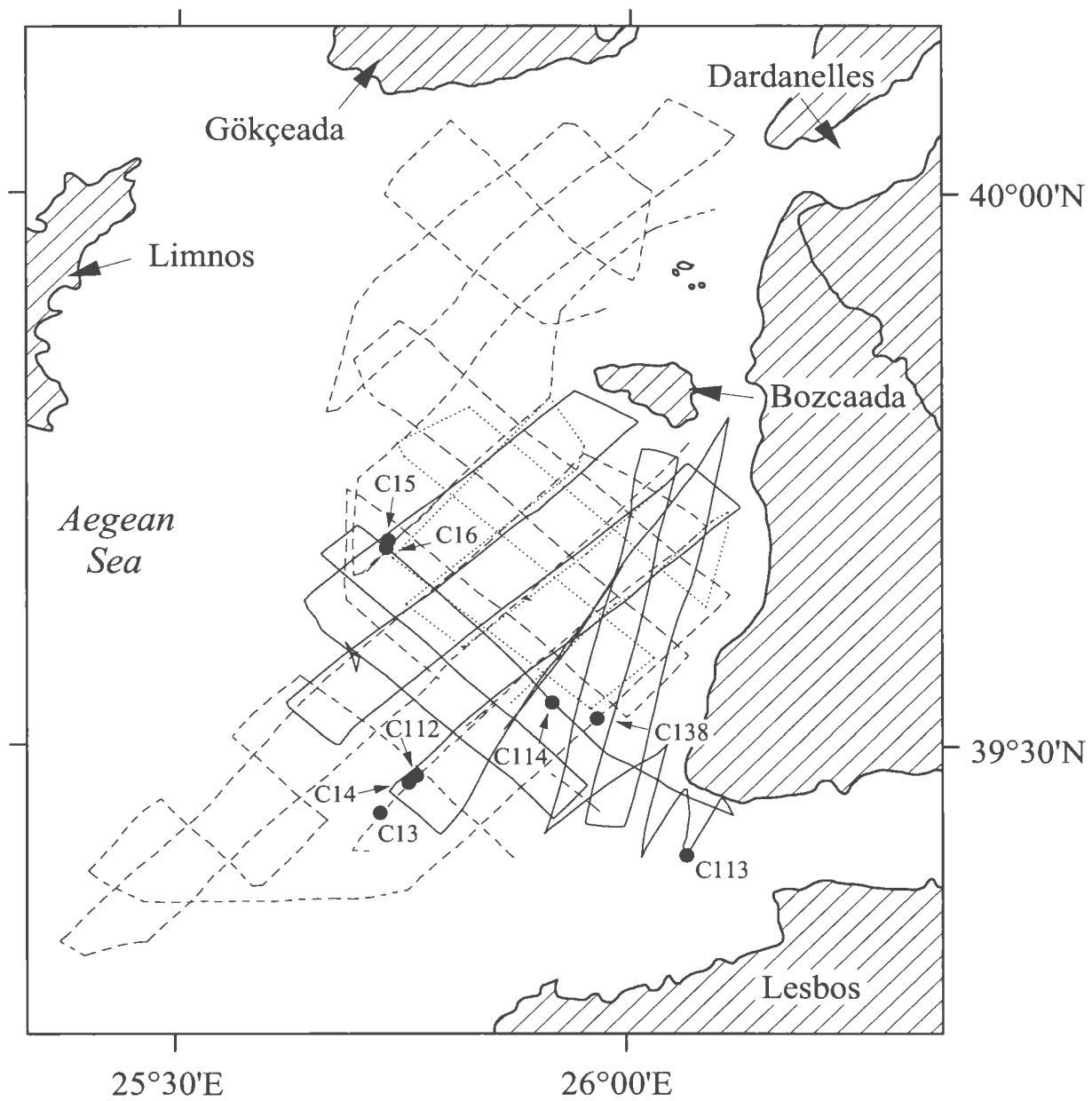
Figure 2.1. Location map of the study area showing the seismic lines and the core locations.

------------- MAR-98 (1998)

.... MAR-00 (2000)

——————— MAR-02 (2002)

The sparker data were collected using a 1580 joule multi-tip sparker source; reflections were received using a 50-element, 9 m-long Benthos hydrophone streamer and a 25-element, 6.7 m-long Nova Scotia Research Foundation Corporation (NSRFC) hydrophone streamer. The seismic data were analogue-recorded on reel-to-reel magnetic tapes using an 8-channel HP tape recorder. The sparker data were further displayed on two EPC 3200 analogue recorders, while the Huntec DTS data were displayed on two EPC 4600 recorders: one for the internal hydrophone and one for the external hydrophone streamer.

In 2000, ~ 227 km of side-scan sonar, high-resolution Huntec DTS and airgun seismic reflection profiles were collected on a grid with ~ 8 km line spacing (Fig. 2.1). The airgun profiles were collected using a 40 cubic inch (655 cm^3) sleeve airgun as source and reflections were received by a Benthos Mesh 25/50P 50-element, 7.6 m-long hydrophone streamer. These data were displayed using two separate EPC 9800 thermal recorders and analogue recorded on reel-to-reel tapes using an 8-channel HP tape recorder. The Huntec DTS profiles were collected using a 500 joule boomer source on the tow fish and reflections were received by a high-resolution single internal hydrophone and a 21-element 6 m-long Benthos hydrophone streamer on the tow fish. These data were displayed using two EPC 9800 thermal recorders and digitally recorded on DAT tapes using a CODA DA200 dual-trigger, 4-channel system. The side-scan sonar data were collected in conjunction with seismic reflection profiles using a Klein 590 system. The side-scan fish was towed at approximately 1/10 of the water depth and the range was

set at 125 m per channel (swath=250 m). The source frequency was set at 100 kHz and reflections from the seafloor were received using a Klein 595 Digital Graphic Sonar Recorder, and digitally recorded on DAT tapes using the CODA DA200 system.

In 2002, ~ 600 km of airgun reflection profiles were collected using a 40 cubic inch (655 cm^3) sleeve gun source over a grid with ~ 8 km line spacing; reflections were received using a Benthos Mesh 25/50 P 50-element, 7.6 m-long hydrophone streamer. The data were digitally recorded on DAT types using the CODA DA200 system and they were displayed on two EPC 9800 thermal recorders.

2.2. Core Collection and Stratigraphy

During the MAR-98 cruise, four short gravity cores were collected using a 4 m-long corer with 10 cm internal diameter and 400-kg weight, whereas during the MAR-02 and MAR-03 cruises seven ~4–10 m-long piston cores were taken using a Benthos piston corer (Fig. 2.1). Coordinates, water depths and core length are given in Table 2.1. Cores were stored upright onboard ship and were shipped to Memorial University of Newfoundland, where they were split, described and photographed. Sediment colour was determined using the "Rock-Color Chart" published by the Geological Society of America in 1984. Shells were extracted at several critical stratigraphic depths and have been U/Th and radiocarbon dated at Université du Québec à Montréal and Isotrace Laboratories, University of Toronto, respectively.

Cores (Cruise)	Coordinates		Water Depth	Core Length
	Lat N°	Long E°	(m)	(cm)
MAR98-13	39° 26.303'	25° 43.656'	430.9	165
MAR98-14	39° 28.032'	25° 45.638'	361.3	177
MAR98-15	39° 41.076'	25° 44.334'	118	21
MAR98-16	39° 40.760'	25° 44.191'	125.5	27
MAR02-112	39° 27.925'	25° 45.560'	361	879
MAR02-113	39° 24.184'	26° 04.121'	298	731
MAR02-114	39° 32.401'	25° 55.005'	189	458
MAR02-138	39° 31.312'	25° 58.000'	147	421

Table 2.1. Coordinates, water depth and length of cores collected from the NE Aegean

Sea. Cores are shown in Figure 2.1.

CHAPTER 3

3. Seismic Stratigraphy

3.1. Stratigraphic Architecture

Sequence stratigraphy is a powerful technique in the study of sedimentary successions. It allows the delineation of geographically extensive rock units that were deposited within a set of temporally related environments. In seismic stratigraphic analysis, the reflection profiles are divided into discrete packages referred to as depositional sequences, which are composed of relatively conformable reflections returned from genetically related strata bounded at their top and base by unconformities or their correlative conformities (Fig. 3.1; Mitchum et al., 1977).

Mitchum et al. (1977) introduced the terms 'lapout, truncation, baselap, onlap, downlap, and toplap' to delineate geometric relationships that define stratal architecture along discontinuities in seismic reflection profiles. Here, these terms are briefly described in order to clarify the techniques used during seismic stratigraphic interpretation. *Lapout* is the lateral termination of a reflector at its depositional limit due to non-deposition. *Truncation* is the termination of a reflector as a result of erosion, intersection of a fault plane or slump scar, or where a reflection abuts an igneous intrusion, rather than as a consequence of non-deposition. *Baselap* is the lapout of reflectors against an underlying reflector. Baselap can be divided into two subtypes:
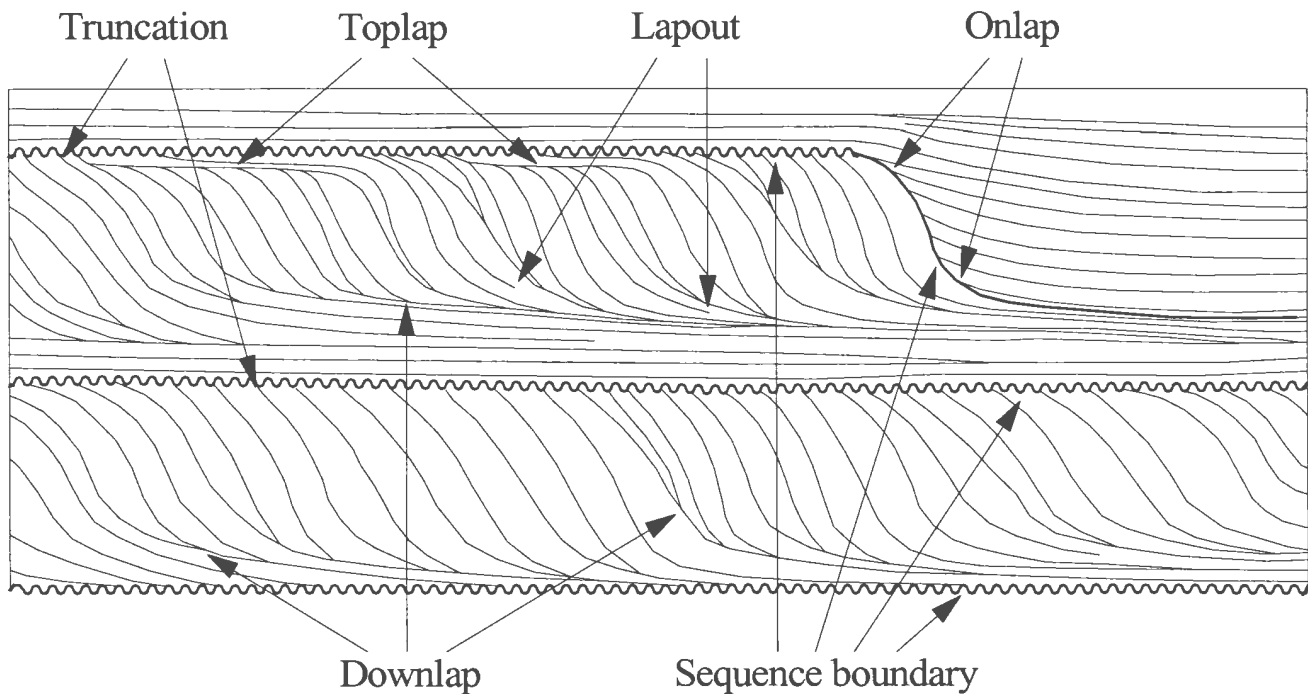
Figure 3.1. Schematic cross-section showing depositional sequences, sequence boundaries and typical internal reflection terminations.

downlap and onlap. *Downlap* is a baselap in which inclined seismic reflectors dip more steeply than the underlying surface, whereas onlap is a baselap in which the underlying surface dips more steeply than the inclined reflectors (Fig. 3.1). Toplap is the updip termination of an inclined reflector against an overlying near-horizontal surface (Fig. 3.1). In seismic reflection profiles, unconformities are identified by truncation and/or at downlap, onlap and toplap reflection terminations against widespread reflections.

In seismic profiles, reflection configurations which constitute the internal architecture of a depositional sequence can be further defined as parallel, subparallel, divergent, prograded, and chaotic based on geometric relationships between reflections (Figs. 3.2 and 3.3).

Parallel (even)

Subparallel

Divergent

Parallel

Chaotic
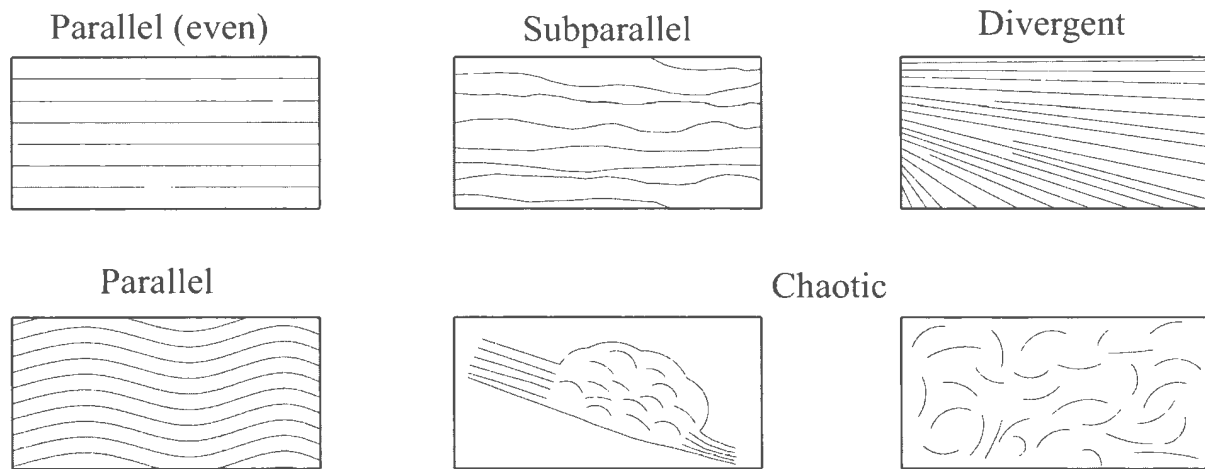
Figure 3.2. Types of reflection configurations (modified from Mitchum et al., 1977).

Sigmoid

Oblique parallel

Oblique

Shingled

Hummocky
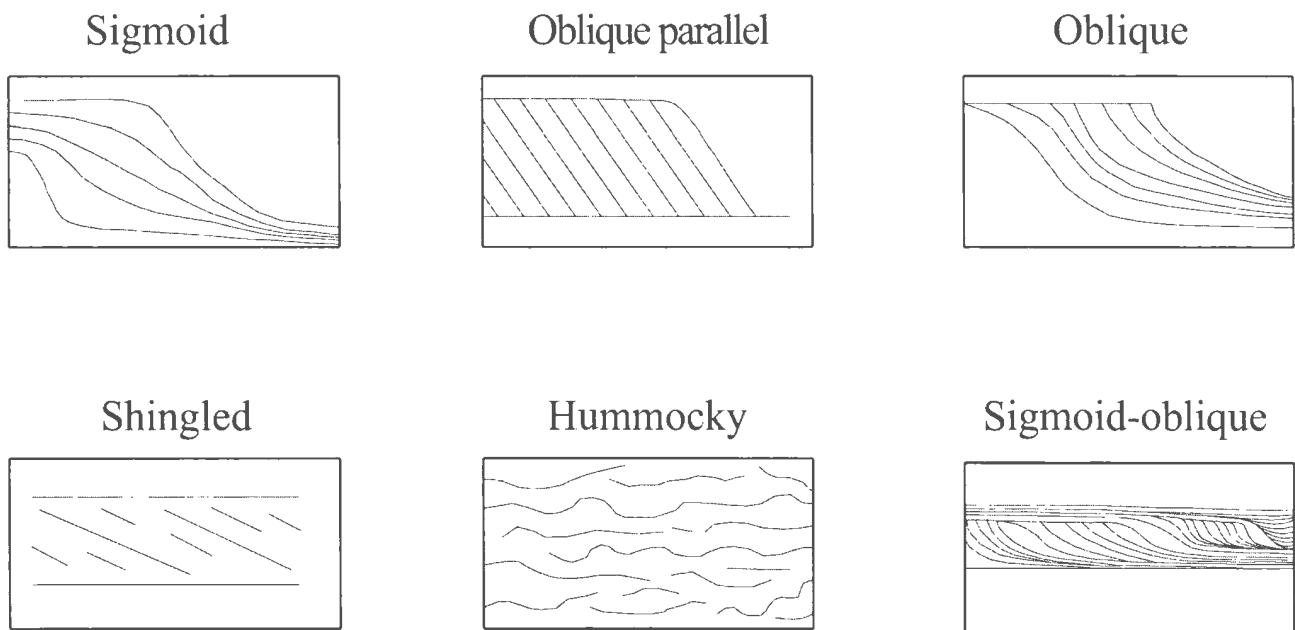
Sigmoid-oblique

Figure 3.3. Seismic reflection patterns of prograding clinoforms (modified from Mitchum et al., 1977).

Prograded reflection configurations can be further characterized as sigmoid, oblique, shingled, and hummocky progradational patterns on the basis of the degree of inclination of the clinoforms as well as the interplay between clinoform progradation and upbuilding observed within a depositional sequence (Fig. 3.3).

A clinoform surface can be divided into discrete topset, foreset, and bottomset segments, based on their dips and locations along the clinoform surface (Fig. 3.4; Myers and Milton, 1996).
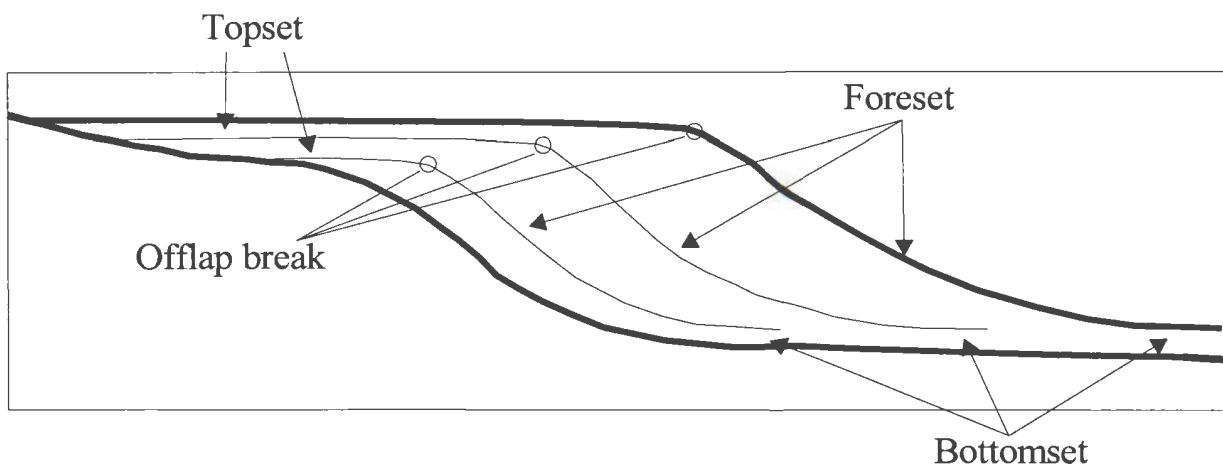
Figure 3.4. Typical clinoform surfaces with topset, foreset and bottomset segments (modified from Myers and Milton, 1996).

Topset and bottomset reflectors are characterized by low gradients (i.e., <0.1°) and constitute the upper and lower portions of a clinoform surface, respectively. A foreset

reflector is the downdip continuation of a topset reflector with gradients commonly >1°. The *offlap break* is defined as the transition point from low to steeper gradients at the top of a clinoform surface (i.e., topset-to-foreset transition; Fig. 3.4).

The following step-by-step method is used for the delineation of depositional sequences. The localities of all of the seismic reflection profiles presented below are shown in Figure 3.5. Initially, reflection terminations are identified in seismic profiles and marked with arrowheads. Later, distinctive seismic reflections, particularly those defining unconformities, are highlighted with a coloured pencil. The unconformities and their correlative conformities are traced as precisely as possible and are correlated to other seismic profiles at cross-overs. For the determination of unconformities, the immediately overlying prominent reflection is chosen instead of the seismic reflection against which the reflections appear to terminate updip. This method is utilized mainly because of the potential occurrence of an artificial reflection (ringing) which may possibly be produced when a strong reflection is developed at an erosional surface (Mitchum et al., 1977). The secondary reflection (ringing) camouflages the reflection terminations below the string reflection and gives the false impression that these reflections terminate against it rather than against the next overlying principal reflection (Fig. 3.6).

3.2. Seabed physiography of the study area

The study area is situated in the northeastern Aegean Sea, south of the Island of Bozcaada and west of the Biga Peninsula, and covers an area of ~2150 km^2 (Fig. 1.9).
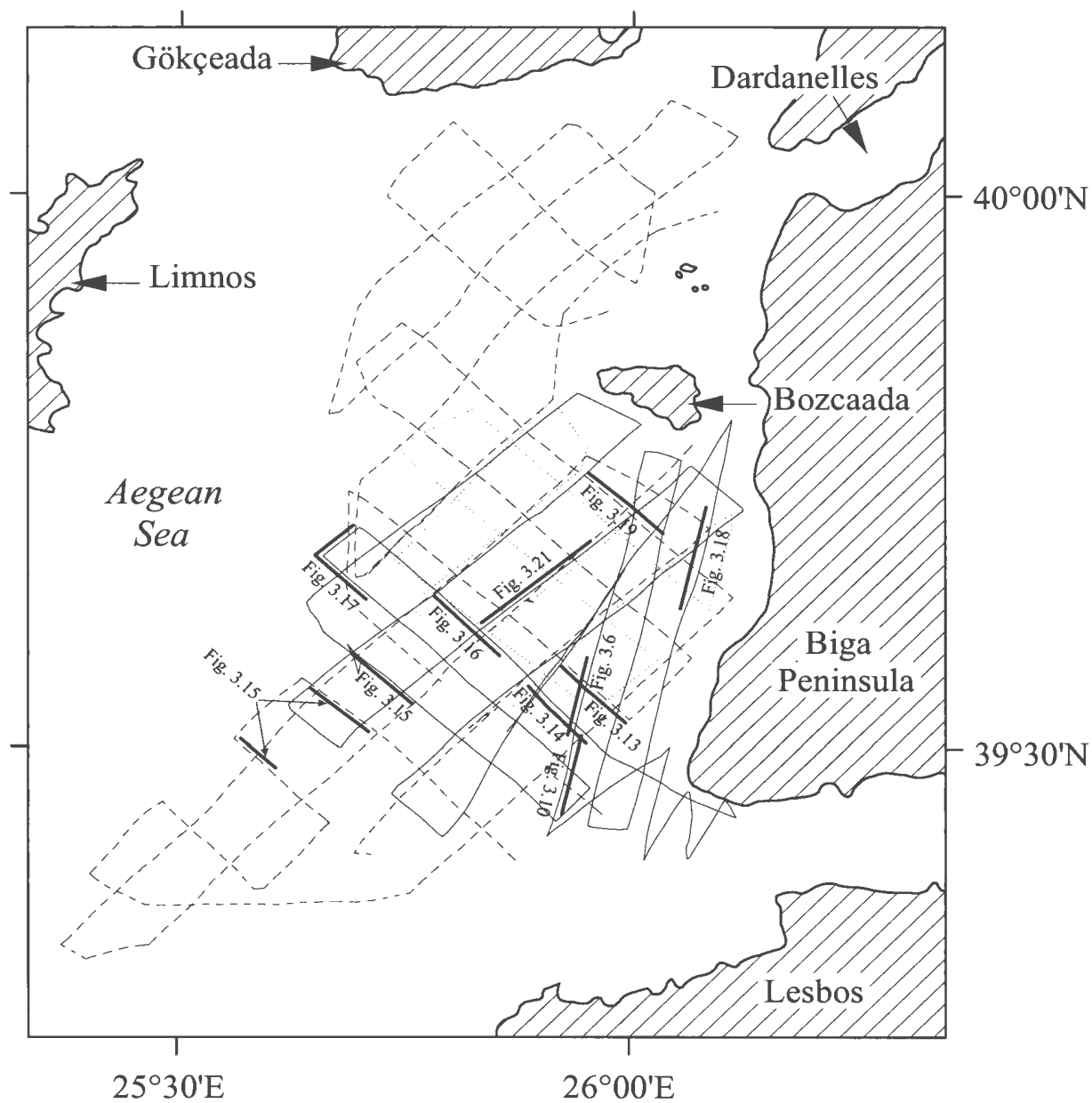
Figure 3.5. Map showing the locations of seismic profiles displayed in this chapter.

------------- MAR-98 (1998)

. . . . MAR-00 (2000)

——————— MAR-02 (2002)
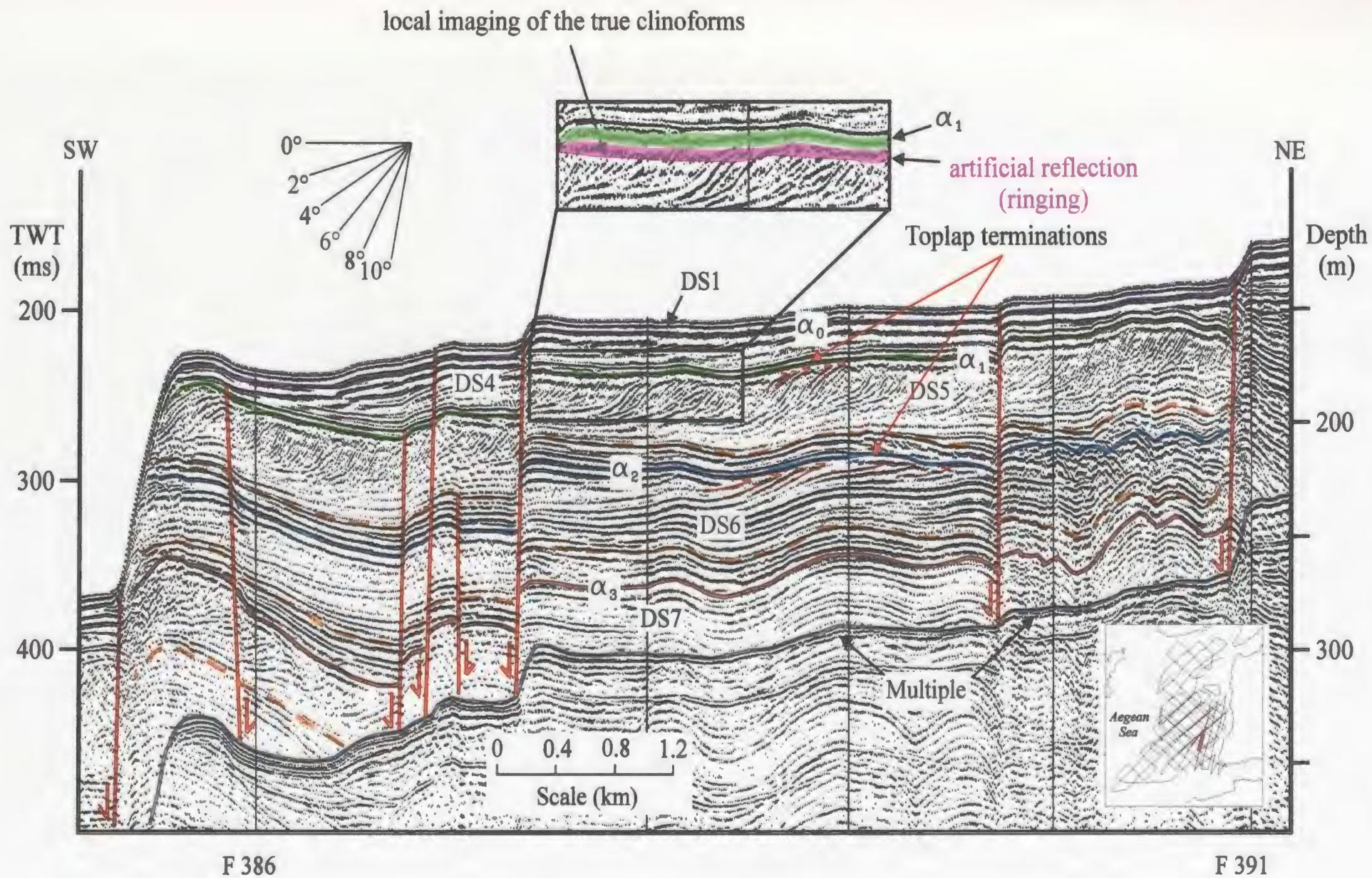
Figure 3.6. Northeast-southwest-trending seismic reflection profile from basin B1 with pronounced toplap terminations mostly at an artificial reflection. The unconformity (α_1) is actually not at this level, but rather at the next overlying prominent reflection (green). The artificial reflection is produced by ringing, and obscures the tops of the clinoforms

The dense grid of seismic lines has facilitated the construction of a detailed bathymetric map with isobaths drawn every 10 m (Fig. 3.7) and has permitted the preparation of a three-dimensional topography of the sea bed (Fig. 3.8).

The basemap used for the construction of the bathymetry map extends from 25° 22' E to 26° 07' E and 39° 23' N to 39° 50' N and includes parts of the Biga Peninsula, the Islands of Lesbos and Limnos, and all of the Island of Bozcaada (Fig. 1.9). It was generated in AutoCAD LT 2000i and its paper copies were printed for various mapping exercises. All depth data recorded during the cruises of the *Koca Piri Reis* in 1998, 2000 and 2002, were plotted onto the paper basemap and contoured by hand at 10m intervals. Additional bathymetry data surrounding the study area were compiled from the Institute of Geology and Mineral Exploration (1989) and integrated with the isobaths to obtain a complete bathymetry map of the area shown in the basemap. The final bathymetry map was digitized using a Summagraphics Microgrid II 4260 digitizing tablet driven by Autocad. This detailed bathymetry map is used to assist in the delineation of the tectono-stratigraphic evolution of the study area (see also Chapter 4). The elevations of the surrounding land were obtained from topographic maps (Erguvanlı and Ternek, 1947). A three-dimensional block diagram was constructed using the coordinates of all contour lines throughout the basemap. These data were imported into a Surfer worksheet and gridded using a 793×1189 gridded wire frame.

The detailed bathymetry map shows that the study area can be divided into two physiographic regions: a gently, southwest-sloping shelf to the north, and a westward-
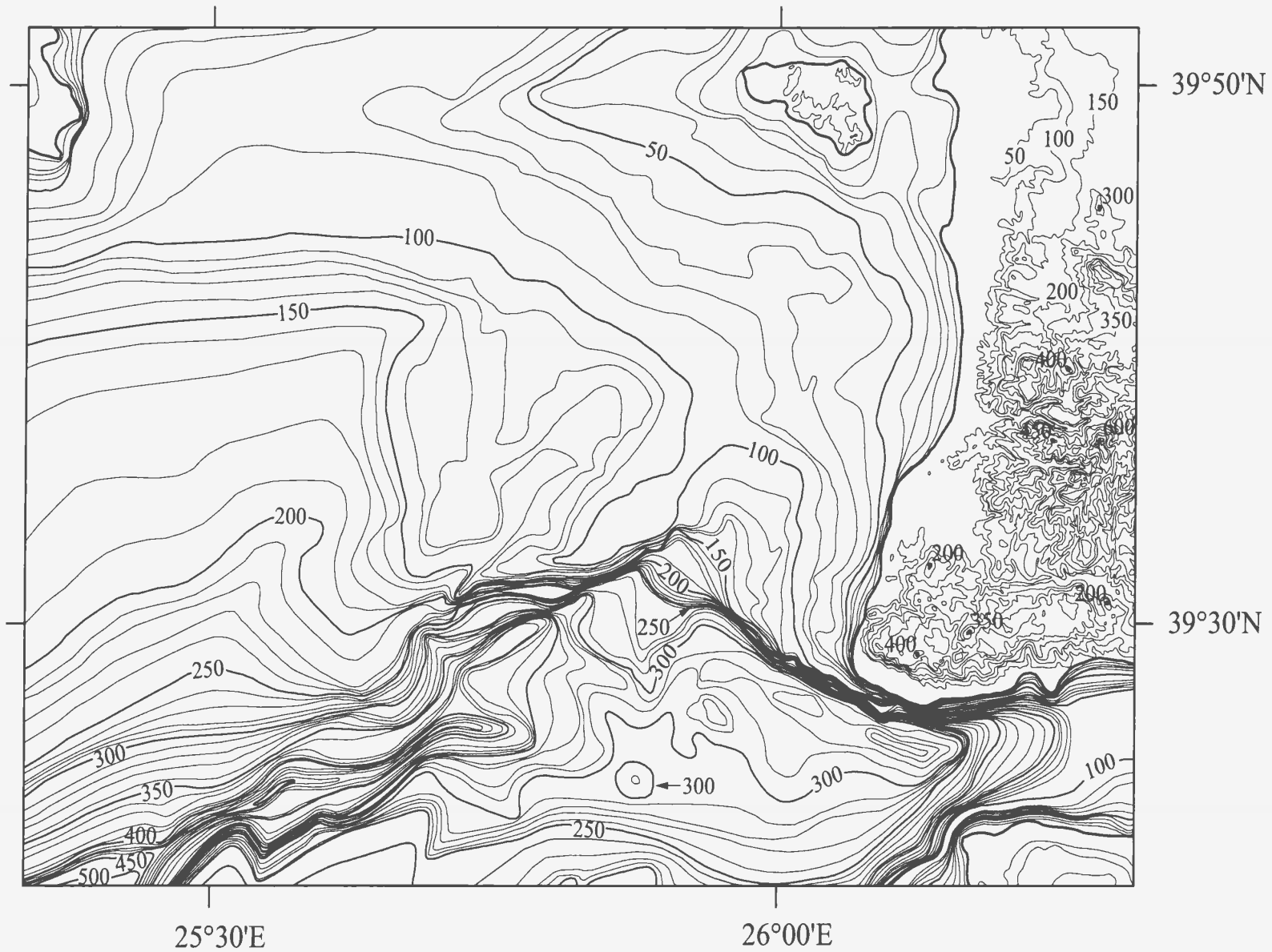
Figure 3.7. Bathymetric map of the study area with isobaths drawn at 10-m intervals. Onland contours at 50-m intervals are not all labelled because of their close spacing. The highest point on land has an elevation of 600 m. Offshore data are compiled from soundings obtained during cruises of the *Koca Piri Reis* in 1998, 2000 and 2002 as well as IGME (1989) and IOC (1981), whereas onshore topographic contours are from Erguvanlı and Ternek (1947).
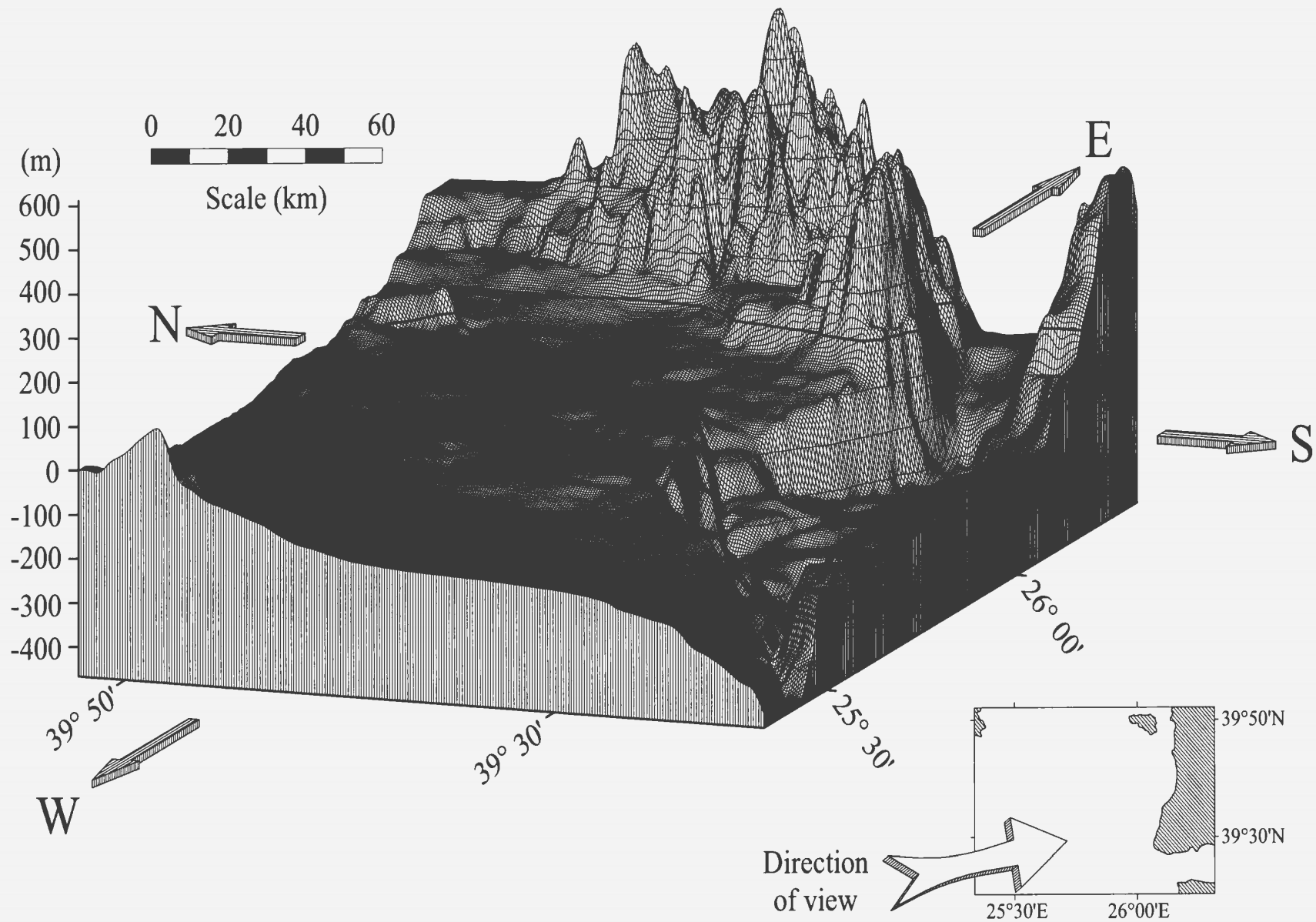
Figure 3.8. Three-dimensional block diagram of the study area showing morphological features of the sea bed. Prepared using digitized bathymetry in Surfer® for Windows by Golden Software, Inc. Thick contour shows the shoreline. Vertical exaggeration is 3.5 times. The slot-shaped depressions to the right is Edremit Bay.

deepening basinal area to the south.

In the shelf region, the seabed has a smooth to gently undulating morphology, which is clearly visible in the 3D block diagram (Fig. 3.8). Here, the seabed gradients are generally low varying from 0.1° to 1.8° in the depth ranges between 30–90 m, with higher gradients occurring along three NE–SW-trending basins referred to as B1, B2, B3 and situated within the eastern, central, and western portions of the study area, respectively (Figs. 3.8, 3.9).

The shelf break occurs at depths ranging between –120 m and –150 m. Seaward of the shelf, the basin slope is inclined at angles varying between 8° and 13°. The basinal area, occupying the southern portion of the study area, lies between the Biga Peninsula and the Island of Lesbos (Fig. 3.9). Here, the elevation difference between coastal hills and the seafloor is as high as 750 m. West of 26° 10' E, the basinal area hooks toward the northwest, after which it swings to the southwest, narrows dramatically and takes on an arcuate geometry (Figs. 3.8). At its southwestern end, it displays a canyon-like morphology with steep escarpments situated along both sides (Fig. 3.8). The sea-bed morphology of the basinal area, particularly adjacent to the slope, is highly corrugated (Figs. 3.8, 3.10). It deepens toward the west with average depths ranging between 200–350 m and 400–450 m in the eastern and western portions, respectively (Fig. 3.7).

3.3. Volume calculations

Total volume of the sediments stored in each depositional sequence and in each
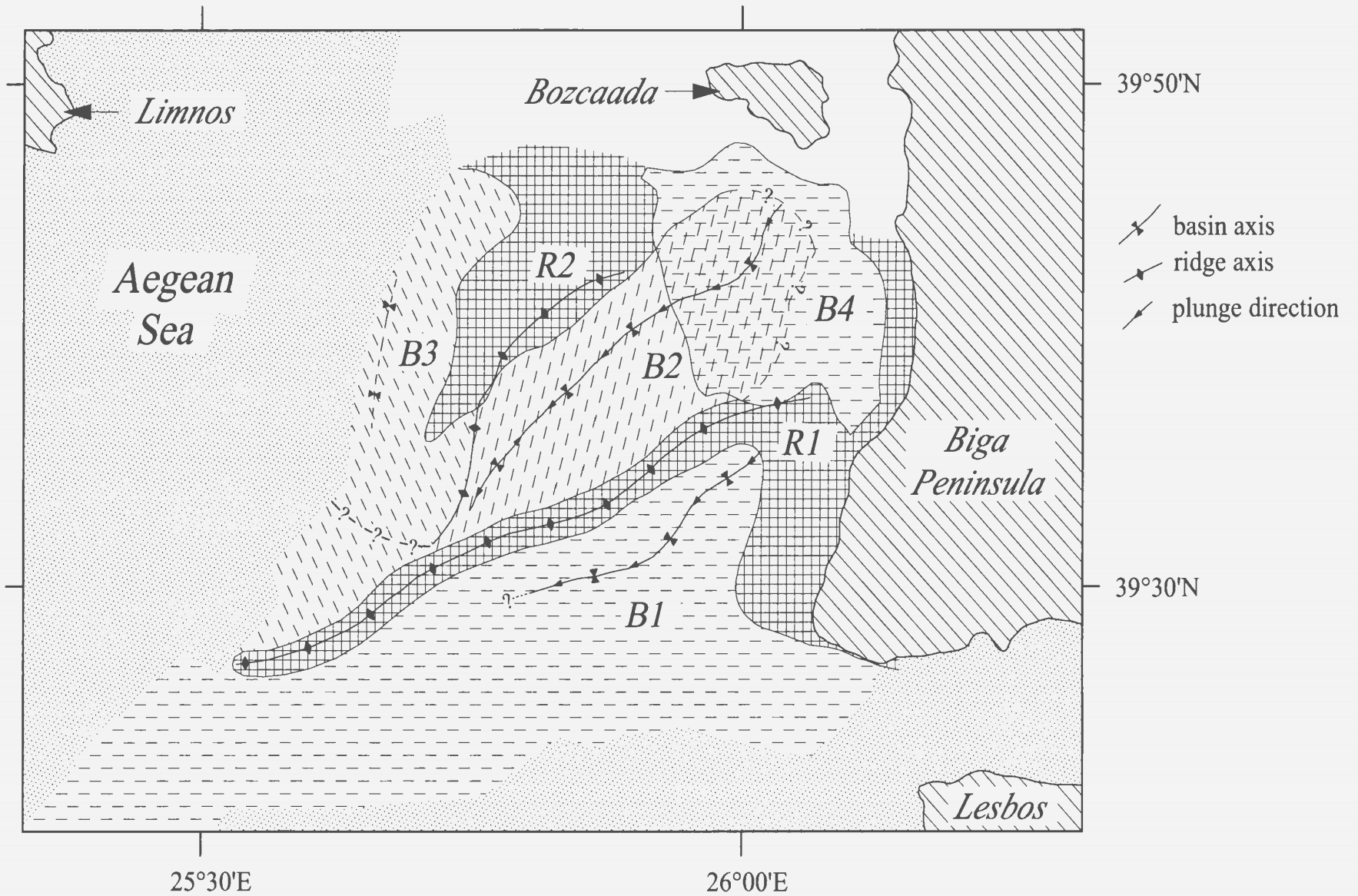
Figure 3.9. Map showing the locations of the three major sedimentary basins and intervening ridges mapped from seismic reflection profiles. Dotted areas are outside the seismic grid.
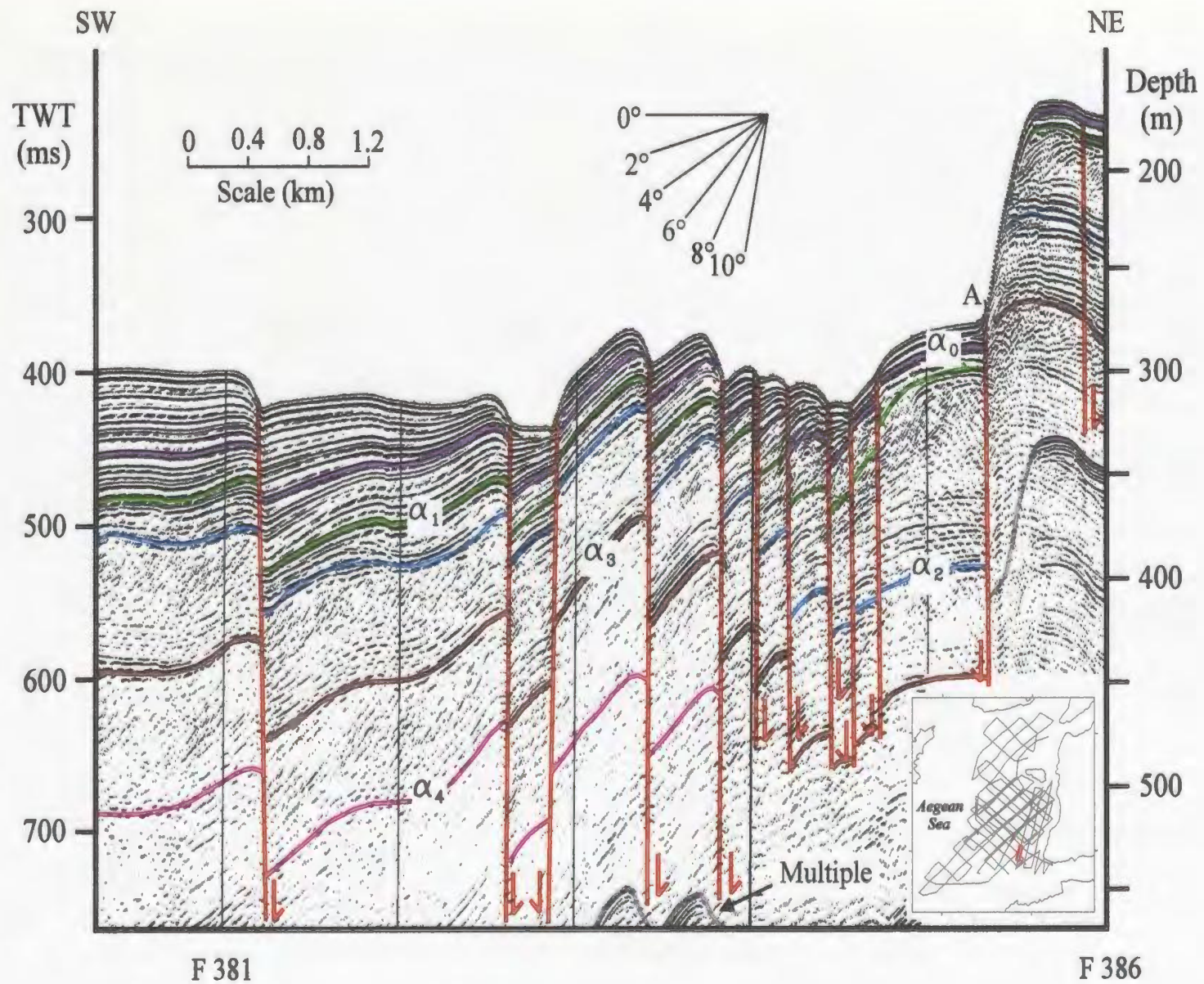
Figure 3.10. Seismic section showing the corrugated morphology of the seabed within the deeper portions of basin B1. See Figure 3.5 for location.

basin was calculated assuming an average acoustic velocity of 1500 m s^{-1} and using the areal distributions of each depositional sequence obtained from detailed isopach maps. The acoustic velocity is approximate due to the fact that sediments, at sub-seafloor depths of about 60 m, may transmit sound at velocities slightly higher than 1500 m s^{-1} (Aksu et al., 1999). However, the discrepancy between 1500 m s^{-1} and the actual velocity is small and has no serious impact on results. Throughout the study area, the interpreted depositional sequences are mostly within 75 m of the seafloor. Therefore, using 1500 m s^{-1} for thickness estimates of each depositional sequence is deemed reasonable. Masses of the sediments present in each depositional sequence were calculated using a grain density of 2.65 g cm^{-3} and an average porosity of 35% (average value in mixed sands and muds, from Hegarty et al., 1988; see Fig. 3.11). The yield of rivers that supplied these deltaic units would have been higher than the calculated masses, because ~ 40% of the load reaching a delta is dispersed well beyond the delta itself (Kukal, 1971, p.38). The calculated sediment volumes and, accordingly, the masses of sediment are only approximate because: (1) particularly in the northern portion of the central basin, most of the sequence boundaries (prominent unconformities) lie beneath the first multiple so accurate thickness measurement is impossible, and (2) the limited seismic coverage does not allow tracing of the 0 m contour line of most of the depositional sequences so that isopach maps are not complete. Calculated volumes and masses for each depositional sequence, and estimated river yields to account for these masses, are given in Table 3.1.
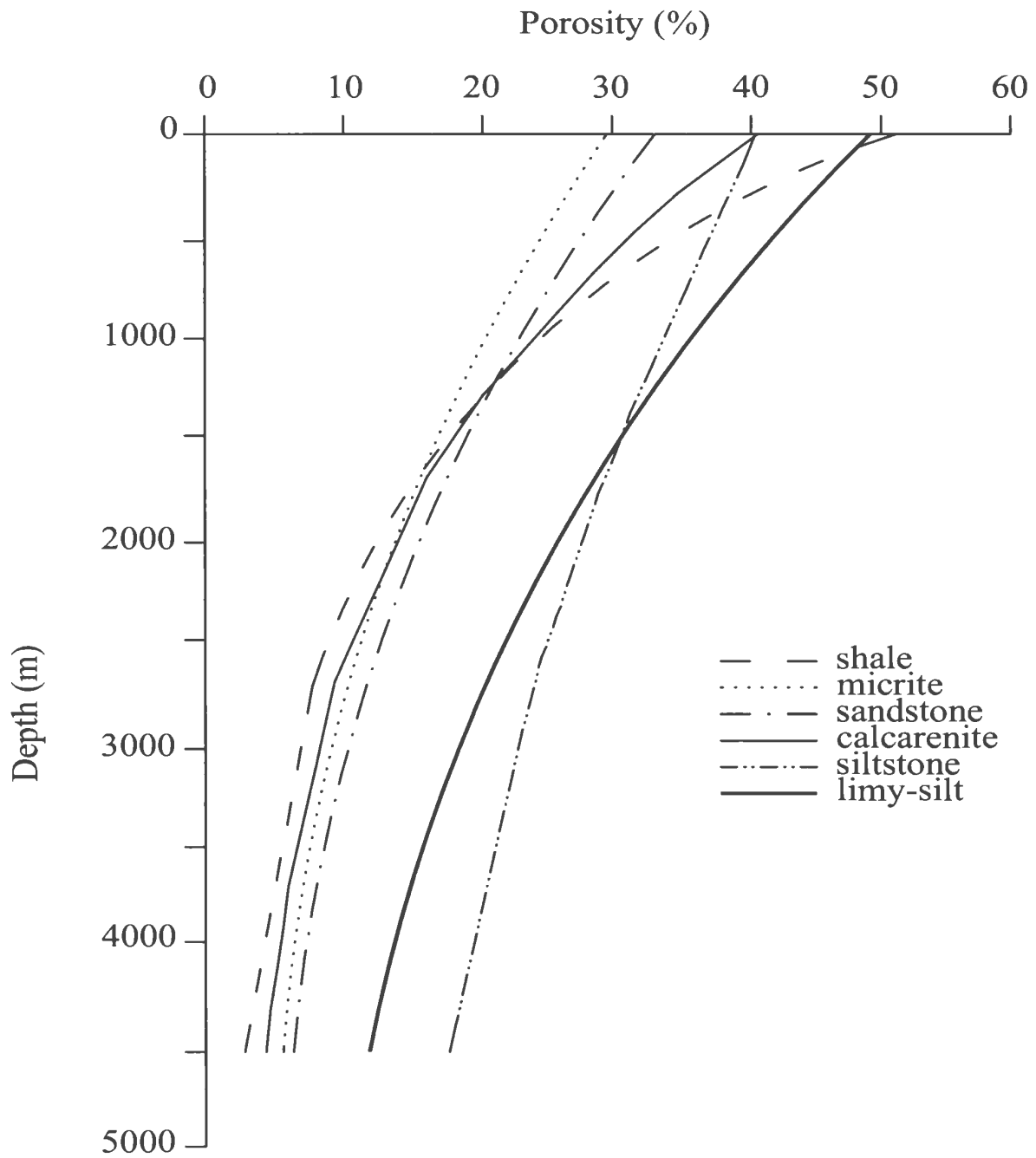
Figure 3.11. Lithology-dependent porosity curves determined from density and sonic well-log data showing porosity decreasing with depth (from Hegarty et al., 1988).

Depositional sequences	Solids volume (km^3)	Mass (t)	Estimated river yield (t)
DS2	20.3	2.1×10^{10}	3.5×10^{10}
DS3	11.5	1.17×10^{10}	1.98×10^{10}
DS4	25.9	2.93×10^{10}	4.46×10^{10}
DS5	38.2	4.05×10^{10}	6.58×10^{10}
DS6	37.8	4.01×10^{10}	6.51×10^{10}
Basin B1	50.5	5.42×10^{10}	8.69×10^{10}
Basin B2	51.2	5.53×10^{10}	8.82×10^{10}
Basin B3	19.5	2.12×10^{10}	3.36×10^{10}
Basin B4	11.5	1.19×10^{10}	1.98×10^{10}

Table 3.1. The volumes and solids masses for the depositional sequences from 2 to 6.

3.4. Stratigraphic architecture of the morphologic features in the study area

Based on the detailed examination of the seismic reflection profiles, three broadly NE–SW trending basins (B1, B2, B3), two intervening ridges (R1, R2), and structures attributed to delta progradation are recognized. Throughout the study area, the seismic successions are predominantly contained within these three basins (Figs. 3.9 and 3.12). On the basis of seismic stratigraphic methods described in Mitchum et al. (1977), the seismic successions (i.e., basin fill) are divided into nine discrete depositional sequences (DS1 through DS9). The depositional sequences are separated from one another by regional (α, α_{0-6}) and local (α') unconformities. Unconformities are correlated across the ridges into adjacent basins. In seismic profiles, some of the unconformities, particularly
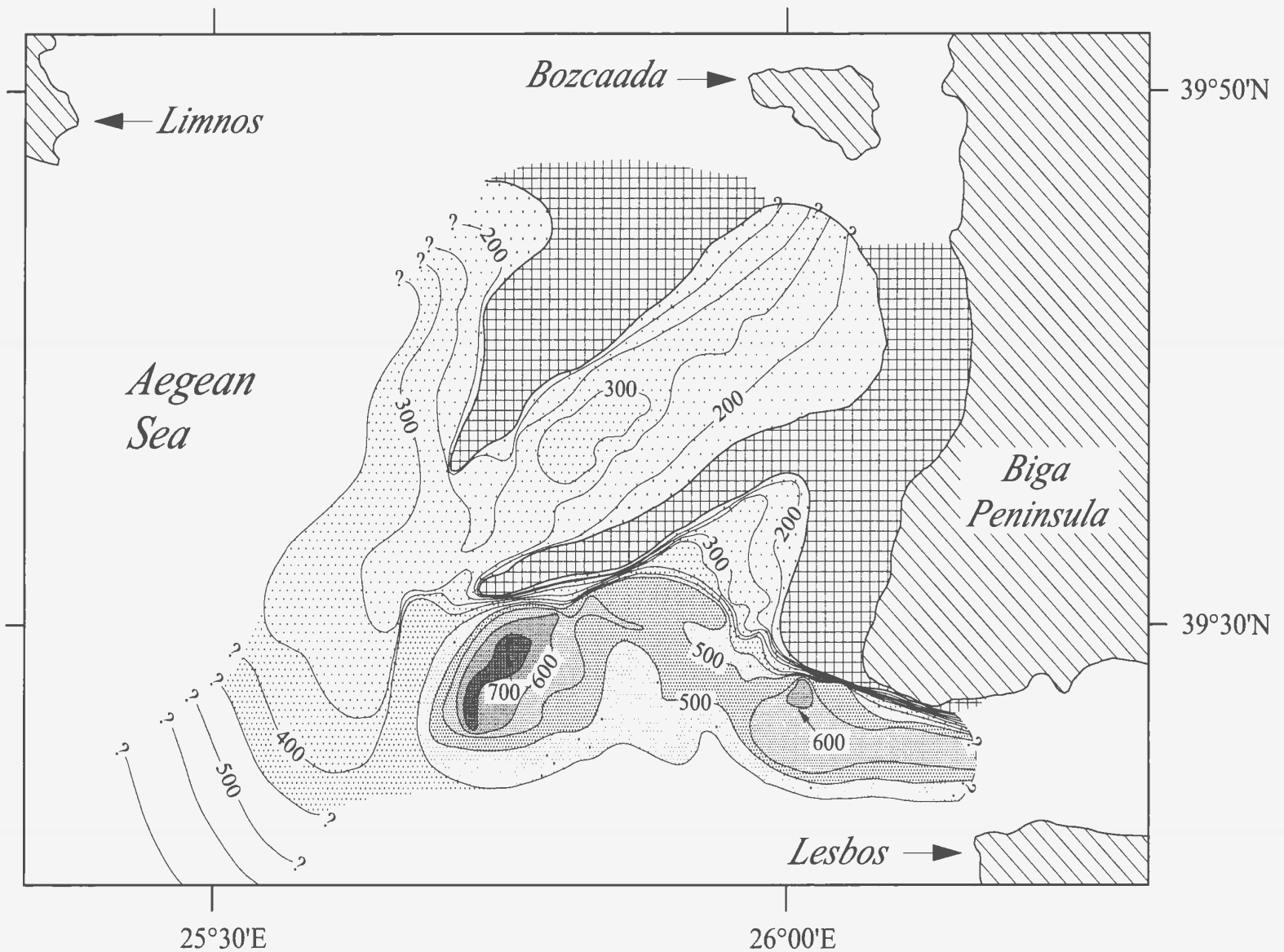
Figure 3.12. Time-structure map of the shelf-crossing unconformity, α_2, in ms (TWT). Squarely hatched areas are ridges.

in shallow regions of the shelf, lie under the first multiple. Where imaged, most of the unconformities mimic the morphology of the basin, while the others are either nearly horizontal or concave-upward surfaces. Detailed analysis of the age and spatial distribution of each unconformity can provide useful information regarding the tectonic and sedimentary evolution of the study area. The basins, ridges, unconformities, and depositional sequences will be described separately.

3.4.1. Basins

Basin B1

Basin B1 is a very large, triangular-shaped depocenter situated between ridge R1 and the Biga Peninsula (Fig. 3.9). The axis of the basin coincides with the modern seafloor depression and forms a relatively linear, broadly NE–SW-trending map trace. The seabed along the basin axis is gently inclined toward the south at an average angle of ~0.8°. In the northern portions of the study area, the basin exhibits an asymmetrical cross-sectional geometry (Fig. 3.13). Here, the depositional sequences within the basin show gradual thinning from 165 ms along the axis of the basin to <10 ms toward ridge R1 in the west and the shelf edge in the east; they are largely absent over the crests of the ridges. The thinning is accomplished by the convergence of reflections toward the ridges, as well as progressive west- and east-directed interstratal onlap associated with variable amount of erosion by the converging unconformities. In its central and southern portions, basin B1 loses its asymmetric cross-sectional geometry and becomes a broad depocenter,
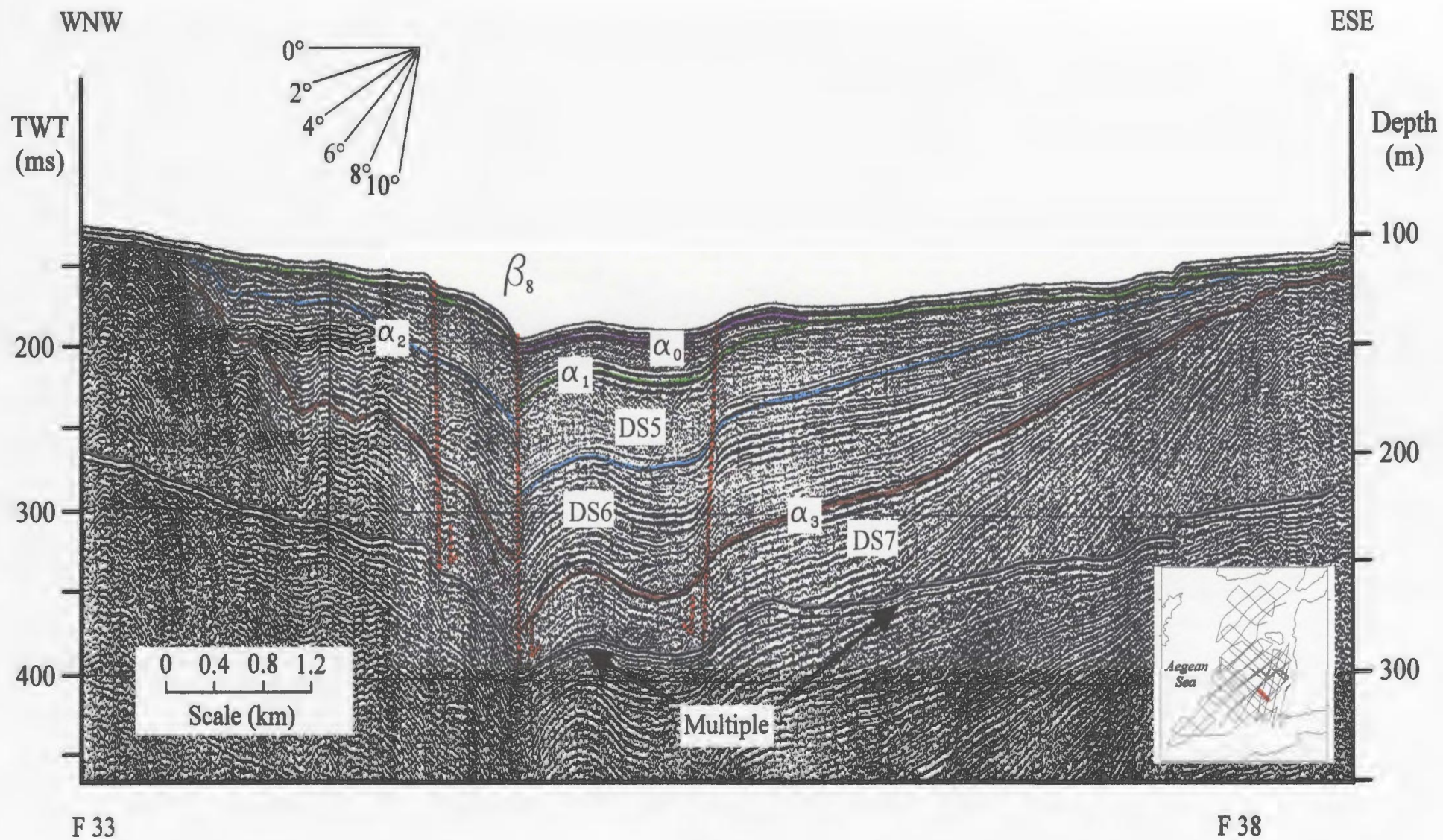
Figure 3.13. Northwest-southeast-trending seismic reflection profile from the northern portion of basin B1 showing the asymmetrical geometry of the basin and the positions of the unconformities.

extending farther southward beyond the limits of the study area (Fig. 3.14).

Basin B2

Basin B2 is a NE–SW-trending elongate depocenter situated between ridges R1 and R2 (Fig. 3.9). It extends with a relatively constant width of ~15 km in the northern and central portions, but narrows considerably to <4 km at its southern extension (Figs. 3.9 and 3.15). The axis of the basin forms a curvilinear map trace and the seafloor along the axis is gently inclined toward the south. The thickest basin fill occurs within the southern portion of the basin.

In the northern portion, basin B2 exhibits an asymmetrical cross-sectional geometry with a steeper western flank dipping SE at an angle of ~12° and a gentler eastern flank dipping NW at ~6°. Here, the depositional sequences are very attenuated and are, in places, entirely absent over the crests of the ridges. The depositional sequences show gradual thinning toward ridge R1 from ~130 ms along the axial trough to <10 ms over the crest of the ridge. The thinning is attained by the convergence of reflections toward the ridge, as well as progressive SE-directed interstratal onlap associated with minor amount of erosion along the converging unconformities. Along the steeper western flank of basin B2, the depositional sequences show abrupt thinning toward ridge R2.

In its central portion, basin B2 displays a symmetrical cross-sectional geometry (Fig. 3.16). The depositional sequences show gradual thinning from ~150 ms along the axis of the basin to 10 and 25 ms toward ridges R1 and R2, respectively. The sequences
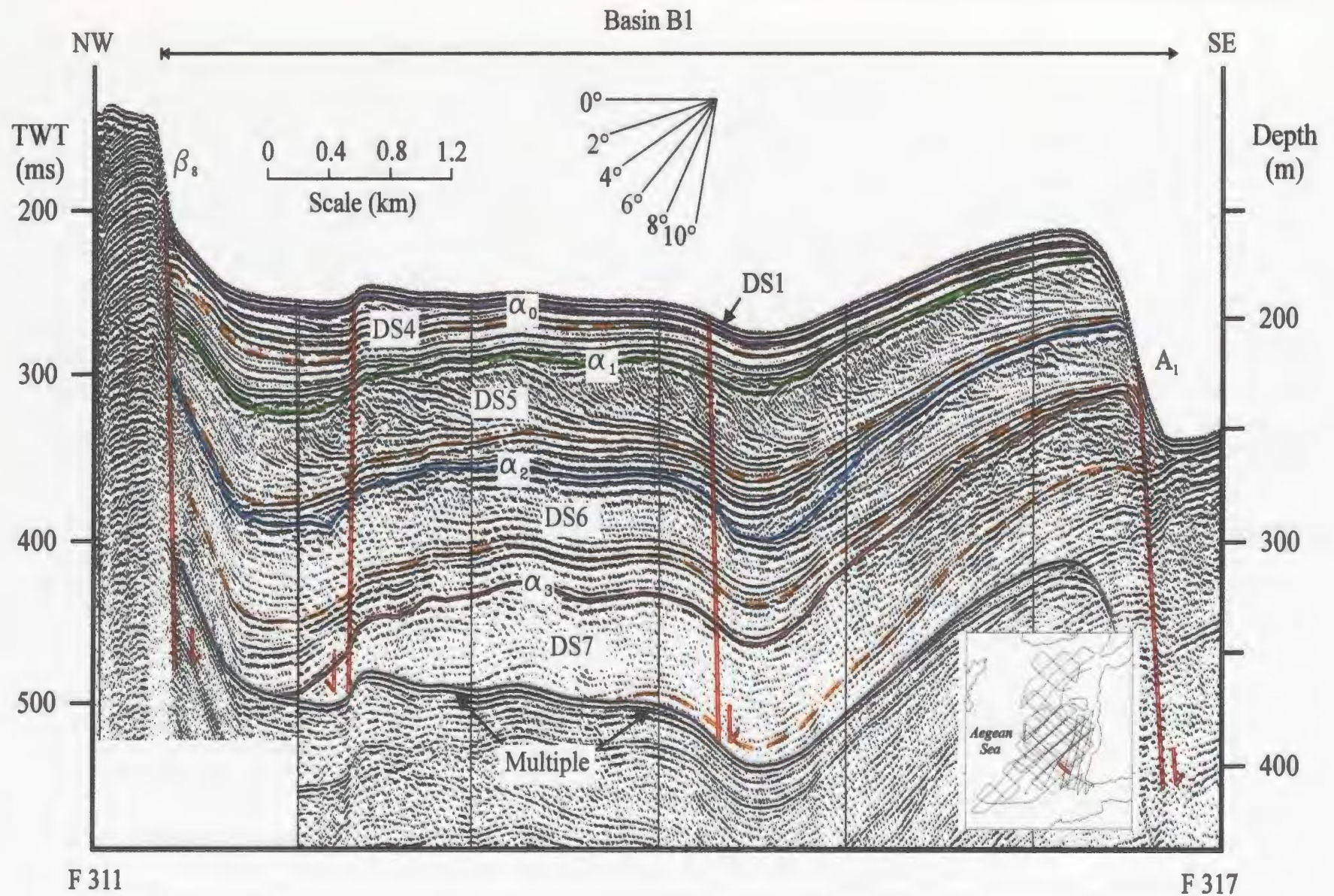
Figure 3.14. Sesimic reflection profile showing southern part of basin B1 where it reaches its maximum width.
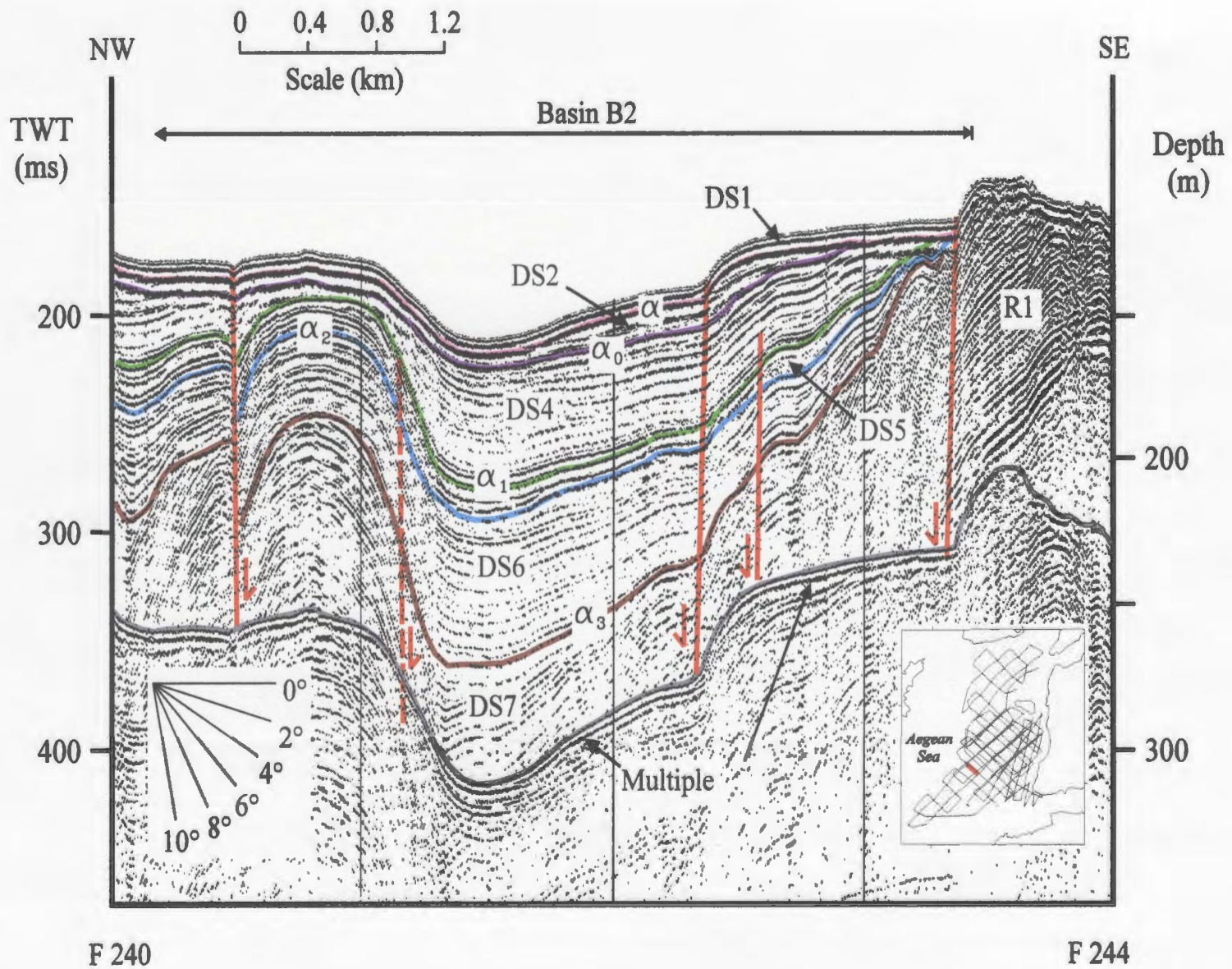
Figure 3.15. Seismic reflection profile showing basin B2 where it narrows noticeably at its southern end.
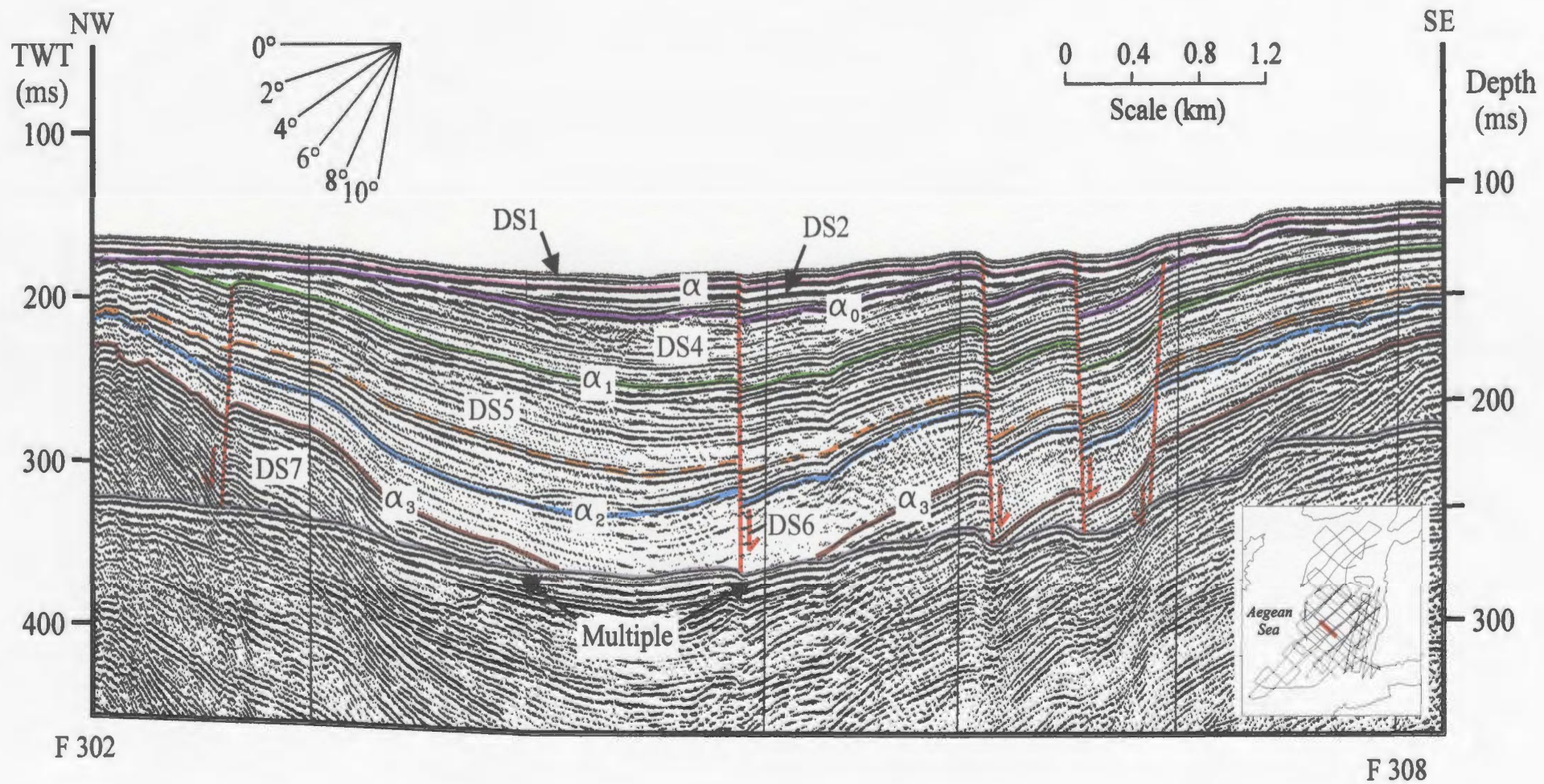
Figure 3.16. Seismic reflection profile showing relations between depositional sequences in the central part of basin B2.

are largely absent over the crests of the ridges. The thinning of the depositional sequences is accomplished by convergence of reflections toward the ridges, as well as progressive NW- and SE-directed interstratal onlap associated with variable amount of erosion by the converging unconformities.

In the southern portion, basin B2 exhibits an asymmetrical cross-sectional geometry across its width (Fig. 3.15). Here, the modern seafloor depression coincides with the axis of the depocenter. Along the eastern flank of the depocenter the depositional sequences show gradual thinning toward ridge R1 from ~80 ms along the axis of the basin to ~0 ms over the crest of the ridge. This thinning is achieved by the convergence of reflections toward the ridge, as well as progressive SE-directed interstratal onlap associated with variable amount of erosion by the converging unconformities. However, along the steeper western flank, the depositional sequences show abrupt thinning from 80 ms along the axial trough to 30 ms over the crest of the ridge where they drape over and extend further west.

Basin B3

Basin B3 occupies the westernmost part of the study area (Fig. 3.9). The basin fill gradually thins toward the SE (Fig. 3.17). The thinning of the depositional sequences is achieved by convergence of reflections toward the ridges, as well as progressive NE-directed interstratal onlap. The thickest sediment accumulation occurs along a NNE–SSW- trending trough. (Fig. 3.17). However, the basin extends beyond the study area so its overall geometry and morphology are unknown.
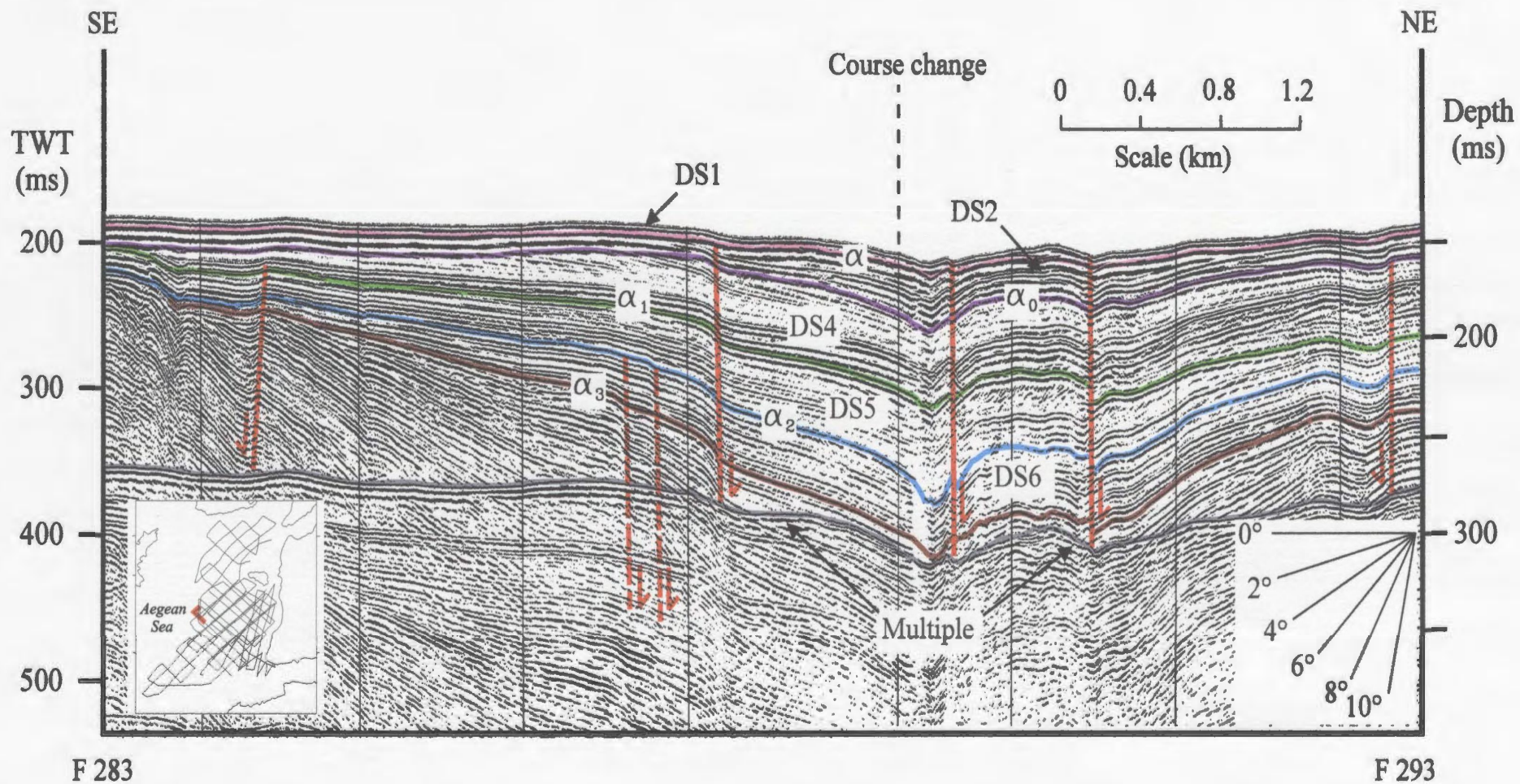
Figure 3.17. Seismic reflection profile showing the relations between DS1 through DS6 in basin B3.

3.4.2. Ridges

Seismic reflection profiles and isopach maps show that ridges R1 and R2 define broadly NE–SW trending and generally cylindrical anticlinal structures. The crestal hinge lines of these anticlines form curvilinear map traces (Fig. 3.9). Ridges R1 and R2 are largely defined by the shelf-crossing unconformity α. The ridges display different external geometries but exhibit relatively similar internal reflection configurations. They are predominantly blanketed by the depositional sequence 1 (see below), locally overstepped by the older depositional sequences, but rarely are exposed at the seafloor throughout the study area.

Ridge R1

Ridge R1 is an anticlinal structure which defines an arcuate narrow belt situated between basins B1 and B2 (Fig. 3.9). It exhibits an asymmetrical cross-sectional geometry with a long, gently northwesterly-dipping flank and shorter and steeper southeasterly-dipping flank. In the southern portion of the study area, ridge R1 appears as a cylindrical anticline, creating an ~70 ms-high expression on the sea floor. The internal architecture of the core of the ridge in the southern portion of the study area is characterized by highly disturbed, low–high amplitude reflections that give the core its corrugated and chaotic appearance. In the central and northern portions of the study area ridge R1 loses its cylindrical cross-sectional geometry and appears as a flat-topped anticlinal structure. Here, the internal architecture of the core of the ridge is defined by high-amplitude and

continuous NW-dipping reflections.

Ridge R2

Ridge R2 is an anticlinal structure situated between basins B2 and B3 (Fig. 3.9). Ridge R2 displays an asymmetrical cross-sectional geometry with a long, gently northwesterly-dipping flank and a shorter and steeper southeasterly-dipping flank. It is composed mainly of high amplitude, gently SE-dipping and continuous reflections with rare chaotic patches. The reflections below and near the crestal region of ridge R2 are highly disturbed and have a multi-crested low amplitude fold geometry. In the southern portions of the study area, the ridge is blanketed by a 20 to 25 ms-thick sedimentary succession consisting of depositional sequences 1 and 2. In the northern portions of the study area, it is mostly exposed on the seafloor, but it does not create a morphological expression at the seabed.

3.4.3. Channel-shaped structural features

Basin B4

Basin B4 is a relatively small, channel-fill structure situated in the northeastern portion of the study area, south of the Island of Bozcaada (Fig. 3.18). The axis of the basin forms a sinuous map trace trending in a NW–SE direction. The basin is widest in its central part and narrows down to 12 and 4 km at its southern and northern extensions, respectively. The basin exhibits an asymmetrical cross-sectional geometry with a steeper western flank dipping NE at angles ranging between 6° and 4°. The stratal units within
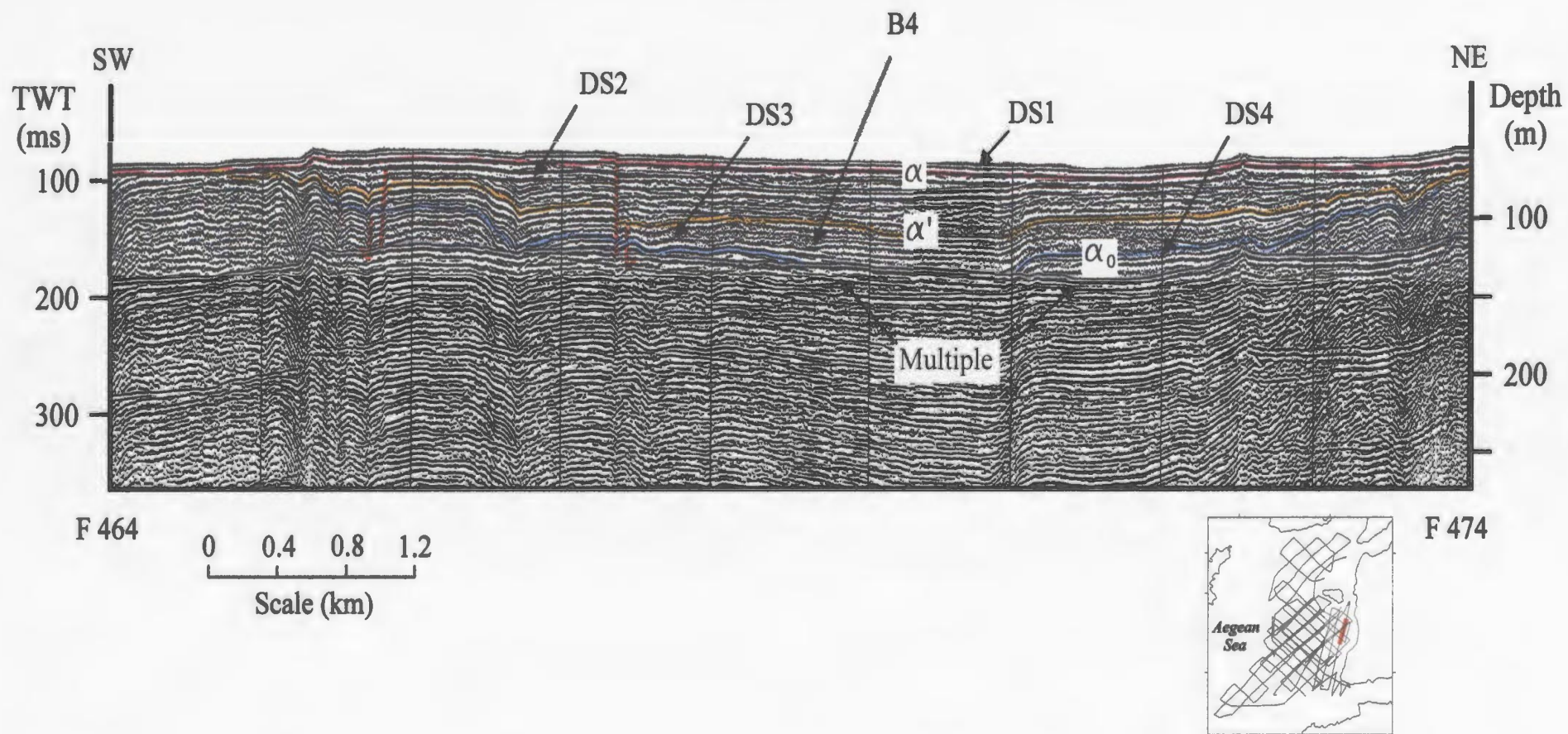
Figure. 3.18. Seismic section from the northeastern part of the study area showing basin B4.

basin B4 are thickest along the axis (~ 80 ms) and thin toward either side of the basin to <10 ms. The thinning is attained by the convergence of the reflections and progressive interstratal onlap.

Cut-and-fill structures

Within the study area, several superimposed cut-and-fill structures are imaged on the seismic reflection profiles (Figs. 3.19, 3.20). Close spacing of the parallel seismic lines permits the confident tracing of the cut-and-fill structures; however, long-distance correlation of the structures is not possible because older units in the southwestern portion of the study area being situated under the first multiple within northern portions. The cut-and-fill structures are confined within basin B2 and their long axes trend broadly parallel to the axis of the basin. From one crossing line seismic line to the next, the structures exhibit variable dimensions changing in depth from 10–50 m and in width from 300 m to as much as 900 m (Figs. 3.19, 3.20). It is certain that these structures were produced during sea-level lowstands when rivers incised older successions.

3.4.4. Widespread Unconformities

Unconformity α

Unconformity α is situated between depositional sequences 1 and 2. It is characterized by a moderate–high amplitude continuous reflection (Figs. 3.16, 3.17, 3.21). It appears as a horizontal, relatively undisturbed surface within the basins. It defines the top of the ridges throughout the study area. In basins B2 and B3, the units
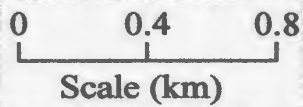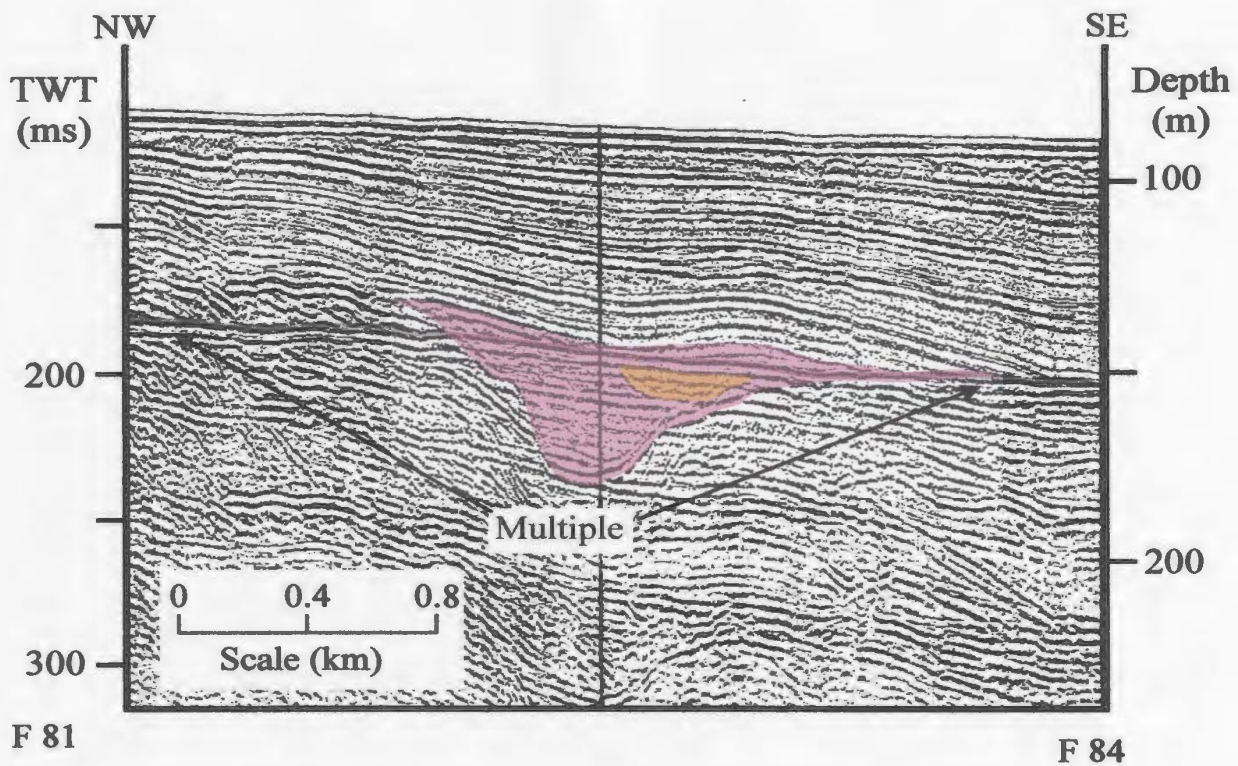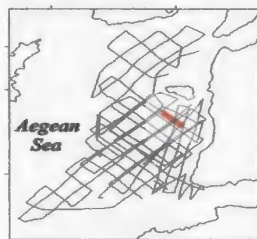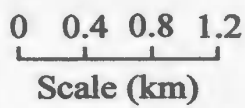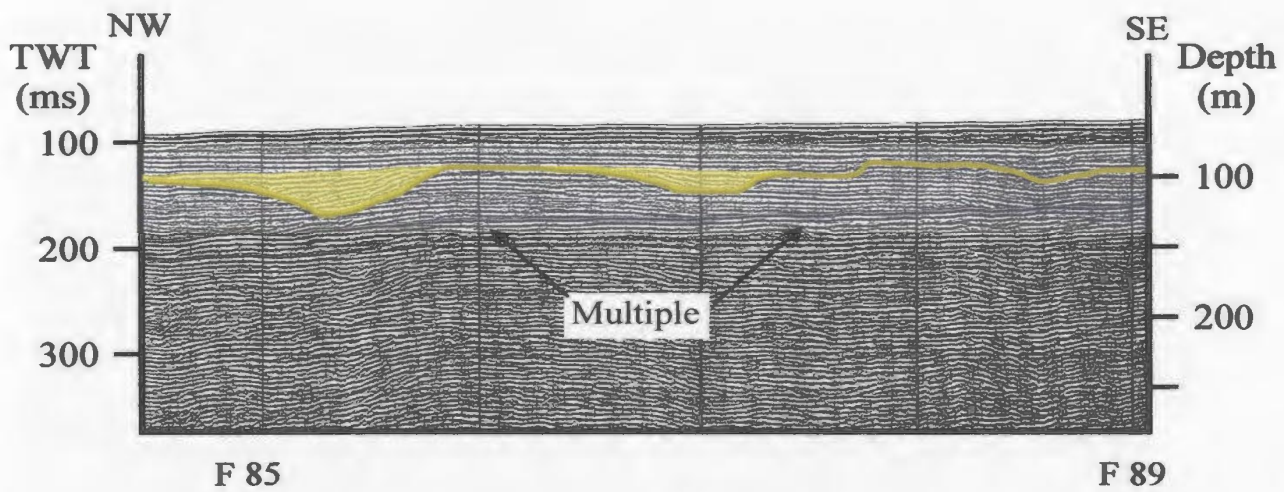
Figure. 3.19. Seismic profiles taken from the northern portion of basin B2 showing cut-and-fill structures.
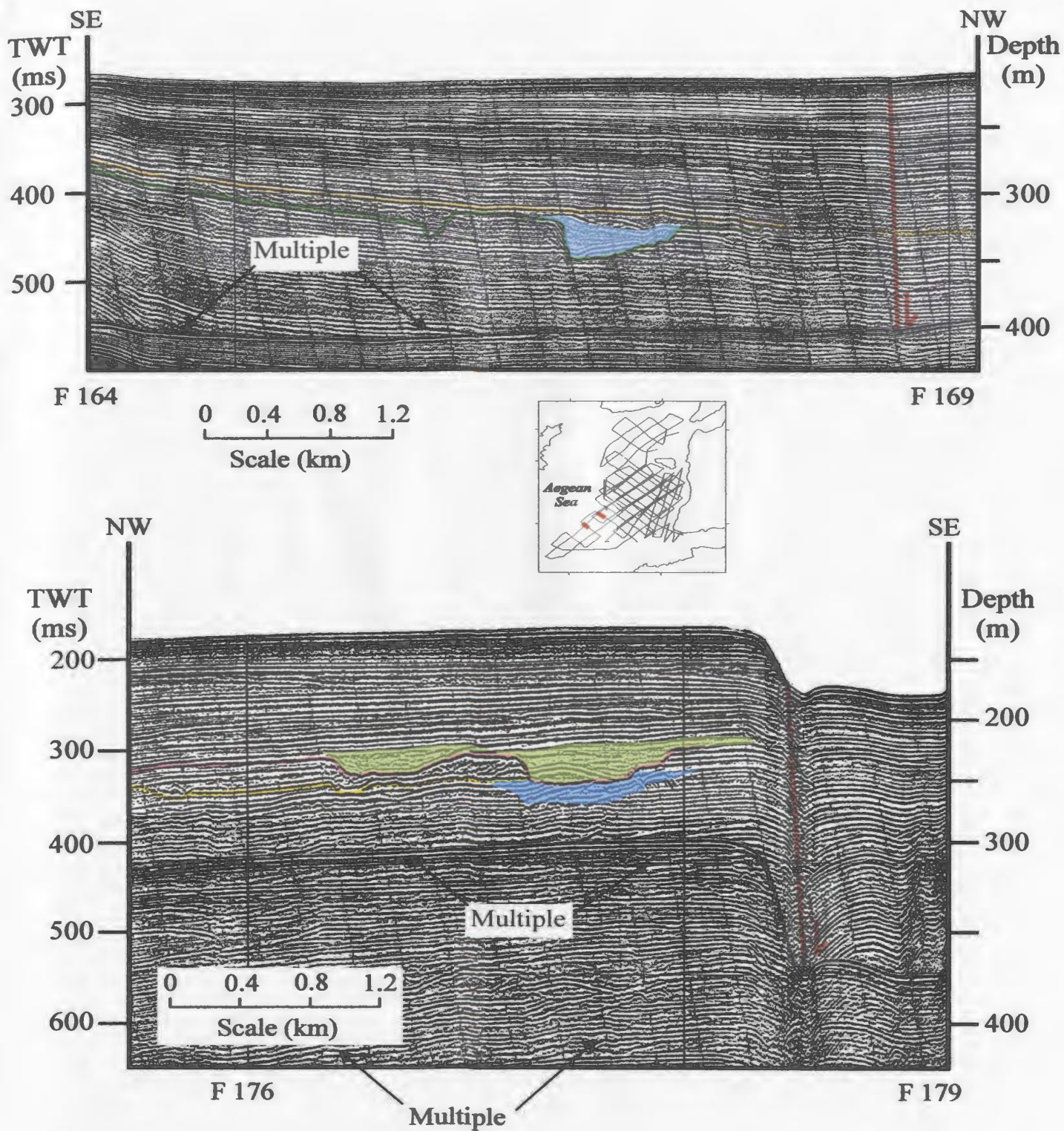
Figure. 3.20. Seismic profiles taken from two successive seismic lines showing superimposed cut-and-fill structures.
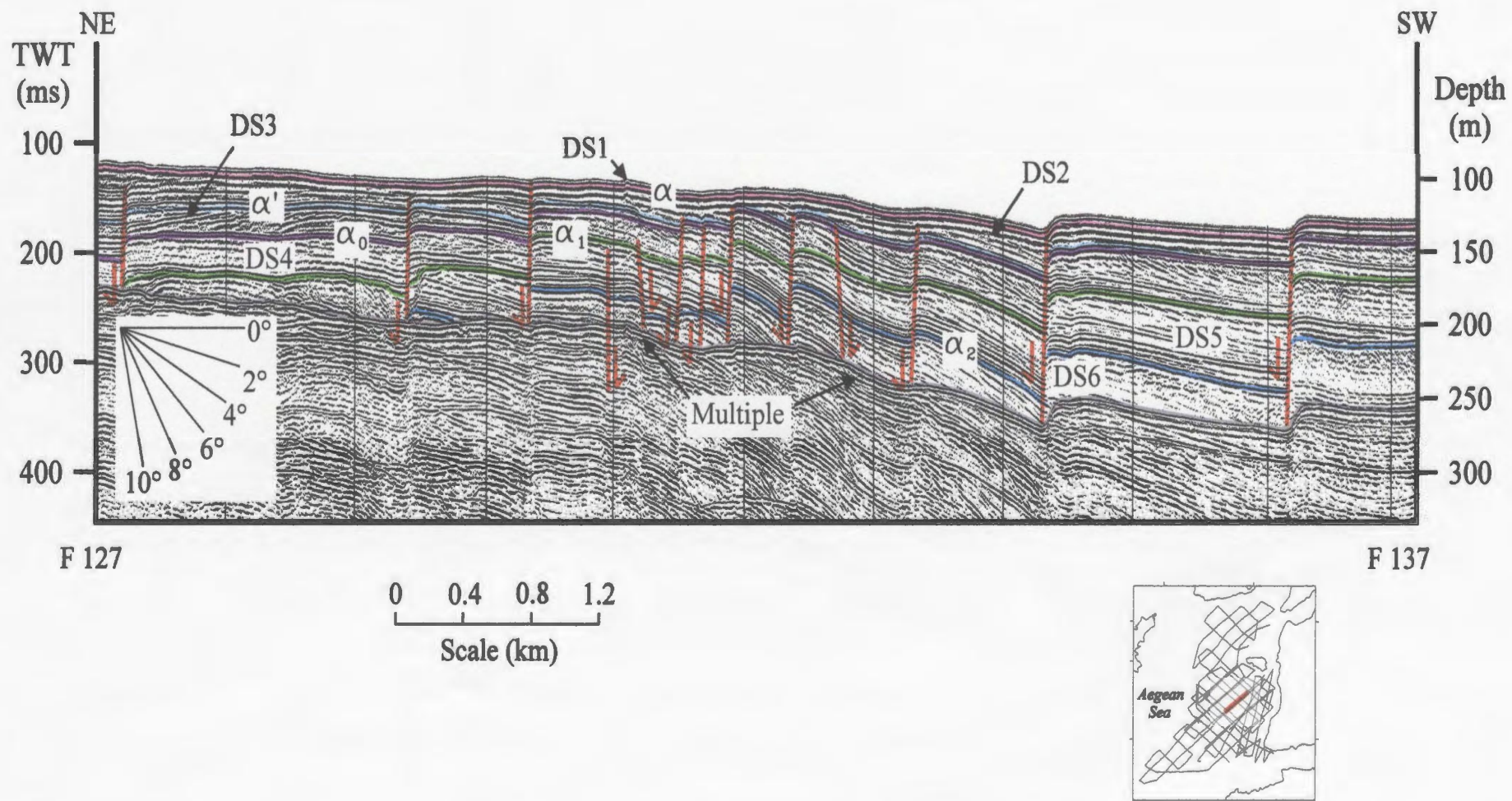
Figure. 3.21. Seismic section along the axis of basin B2 showing the relations between the recognized depositional sequences.

above and below the unconformity display angular contacts with the unconformity. In the southern part of basin B1, α is a disconformity.

Unconformity α'

Unconformity α' is a high amplitude, laterally continuous reflection that separates depositional sequence 2 from 3 (Fig. 3.21). It appears as a local unconformity that is observed only within the northern portions of basin B4. It merges with the underlying unconformity α_0 when traced toward the south. Where imaged, α' mimics the basin morphology and has the shape of an asymmetrical trough (Fig. 3.13). It shows gradual and rapid increase in elevation towards both ridges R1 and R2, but is truncated by the overlying unconformity α across the crestal regions of the ridges.

Unconformity α_0

Unconformity α_0 is a high–moderate amplitude, locally fragmented but mostly laterally continuous reflection which displays a smooth surface throughout the study area. In basins B1, B2 and B3, the unconformity is characterized by a hard reflection where the units above and below show downlap and toplap termination or erosion. However, when traced basinward, it passes into a conformable succession within the central and southern portions of basin B1 (Fig. 3.10). It extends southward beyond the study area.

Unconformity α_1

Unconformity α_1 is a high amplitude, locally fragmented, laterally traceable reflection which separates depositional sequences 4 and 5 (Figs. 3.6, 3.16 and 3.17). It is mainly delineated by toplap terminations within depositional sequence 5. It exhibits a

relatively undisturbed topography and mimics the basin morphology throughout the study area.

In basin B1, unconformity α_1 forms an asymmetric trough-shaped surface within the northern portions. The α_1 trough plunges southward and ranges from 230 ms below sea level in the north to 280 ms in the south along the trough center. Traced southeastward, it extends as a correlative conformity (Fig. 3.10).

In basin B2, unconformity α_1 defines a gently south-plunging, trough-shaped surface. Along its axis, the depth to the unconformity changes from 220 ms below sea level in the north to 260 ms below sea levelin the central portion and reaches to a maximum depth of 280 ms in the southern portion of the basin. Unconformity α_1 climbs gradually toward ridge R1 and terminates updip below unconformity α (Fig. 3.16). However, along the edge of B2, unconformity α_1 is a steeply to gently inclined surface that either terminates updip below unconformity α or abuts ridge R2. At the southernmost extension of R2, α_1 oversteps the ridge and extends farther west (Fig. 3.15). In basin B3, unconformity α_1 gradually climbs toward ridge R2 and terminates below unconformity α.

Unconformity α_2

Unconformity α_2 is a high amplitude, locally fragmented but nevertheless laterally continuous reflection situated between depositional sequences 5 and 6 (Fig. 3.21). It exhibits a generally smooth to locally irregular topography throughout the study area. Units above and below the unconformity display onlap and toplap terminations,

respectively (Figs. 3.6, 3.14). In the southeastern portion of the study area, α_2 becomes conformable with units above and below.

In northern part of basin B1, unconformity α_2 is an asymmetric, south-plunging, trough-shaped (Fig. 3.13). Along the trough center, it ranges in depth below the sea surface from 250 ms to 380 ms. Within central and southern portions of basin B1, the unconformity mostly appears as a gently undulating, nearly horizontal surface which extends beyond the study area (Figs. 3.6 and 3.10).

In basin B2, unconformity α_2 also appears as a south-plunging, trough-shaped surface (Figs. 3.15 and 3.16). Along its axis, the depth to the unconformity ranges from 264 ms below sea level in the north to 320 ms in the central portion and reaches a maximum depth of 460 ms below sea level in the southern portion of the basin. Unconformity α_2 generally rises consistently along the eastern flank of the basin where it merges with the underlying unconformity α_3 (Fig. 3.15). It terminates updip below unconformity α near the crestal region of ridge R1. Along the western flank of basin B2, the α_2 surface shows rapid to gradual convergence with overlying reflections toward ridge R2 (depending on local basin morphology) and terminates updip below unconformity α in the northern and central portions of the basin. However, traced southward, the unconformity drapes over ridge R2 and extends farther west (Fig. 3.15).

Within basin B3, unconformity α_2 appears as an inclined surface that gradually rises in elevation toward ridge R2.

Unconformities α_{3-5}

These unconformities are characterized by high amplitude continuous reflections which are locally recognized by the toplap terminations of the underlying units. However, they are mostly masked by the first multiple where they are shallowest; they are not clearly imaged within deeper portions of seismic profiles because of signal attenuation. Where imaged, they mimic the morphology of the basins and mostly appear as trough-shaped surfaces (Figs. 3.10 and 3.14).

Seismic basement

Seismic basement is characterized by generally high amplitude, folded to inclined and locally chaotic reflections which become predominantly chaotic at depth. Where imaged, it defines the base of the recognized depositional sequences throughout the study area. The top of the seismic basement is either overlain by one of the shelf-crossing unconformities or it constitutes the seafloor. The vertical thickness of the seismic basement cannot be measured because acoustic penetration is limited to its upper part.

3.5. Depositional Sequences in the Study Area

Based on reflection configurations and internal relationships, the seismic profiles are divided into nine stacked depositional sequences (Figs. 3.6, 3.10). Depositional sequences are separated from one another by prominent shelf-crossing unconformities which are recognized in seismic profiles by toplap terminations of obliquely prograded reflectors at or near the unconformities.

On the basis of reflection configuration and stratigraphic architecture depositional

sequences 4–8 are divided into lower and upper subunits (Figs. 3.6 and 3.14). In each depositional sequence, the lower and upper subunits are separated from one another by a local unconformity, recognized by downlap and toplap terminations of both the overlying and underlying reflections of the subunits, respectively. These local unconformities are highlighted by dashed lines in the seismic profiles. Traced seaward, these unconformities pass into correlative conformities (Fig. 3.10). The upper subunit is characterized by oblique-prograded clinoforms, whereas the lower subunit is characterized by parallel–subparallel reflectors which display significant lateral continuity, but eventually gently downlap either against an underlying reflector or onto the major unconformity at the base of the depositional sequence (Fig. 3.6).

Depositional sequence 1 (DS1)

Depositional sequence 1 is the uppermost succession in seismic reflection profiles (Figs. 3.14 and 3.15). It is composed of relatively strong, continuous parallel reflectors and forms a thin (<20 ms) veneer blanketing all the morphological features throughout the study area. Depositional sequence 1 is everywhere marked at its base by the shelf-crossing unconformity α.

Depositional sequence 2 (DS2)

Depositional sequence 2 is a 10–70 ms-thick seismic unit composed of acoustically reflective, relatively continuous, oblique-prograded clinoforms (Figs. 3.6, 3.13). It is bounded at its top and base by shelf-crossing unconformities, α and α_0, respectively, or is underlain by the local unconformity α' (Fig. 3.21). In the northern

portions of basin B2, depositional sequence 2 is underlain by the regional unconformity α' which merges into the prominent unconformity α_0 within the central portions of basin B2. Oblique-prograded clinoforms dip in a southeasterly direction 3–8°, and display apparent downlap terminations onto the underlying unconformities (α_0 or α'; (Fig. 3.21).

In the southern portion of the study area, depositional sequence 2 predominantly occurs within two isolated regions (Fig. 3.22). Thickest accumulations occur within the northern part of basin B2 and in the western portion of basin B1 with thicknesses reaching up to >60 ms and >70 ms, respectively. Depositional sequence 2 occupies an area of ~ 355 km^2 with a total volume of ~ 20.3 km^3.

Depositional sequence 3 (DS3)

Depositional sequence 3 is a 10–80 ms-thick succession bounded at its top and base by the local unconformity α', and by the shelf-crossing unconformity α_0, respectively (Fig. 3.6). It is composed mainly of acoustically weak to locally strong chaotic–parallel reflectors and moderately strong reflectors arranged as oblique-prograded clinoforms. Depositional sequence 3 is identified only in basin B4, within the northeastern portions of the study area (Fig. 3.23). Clinoforms dip in a northwest direction at 4° to 7°, and pass downdip into chaotic–parallel reflectors, particularly in the northernmost profiles (Fig. 3.24). Depositional sequence 3 has total volume of ~ 11.5 km^3.

Depositional sequence 4 (DS4)

Depositional sequence 4 is a 10–60 ms-thick seismic unit which consists of an upper subunit (S4a) formed of acoustically reflective oblique to oblique-parallel
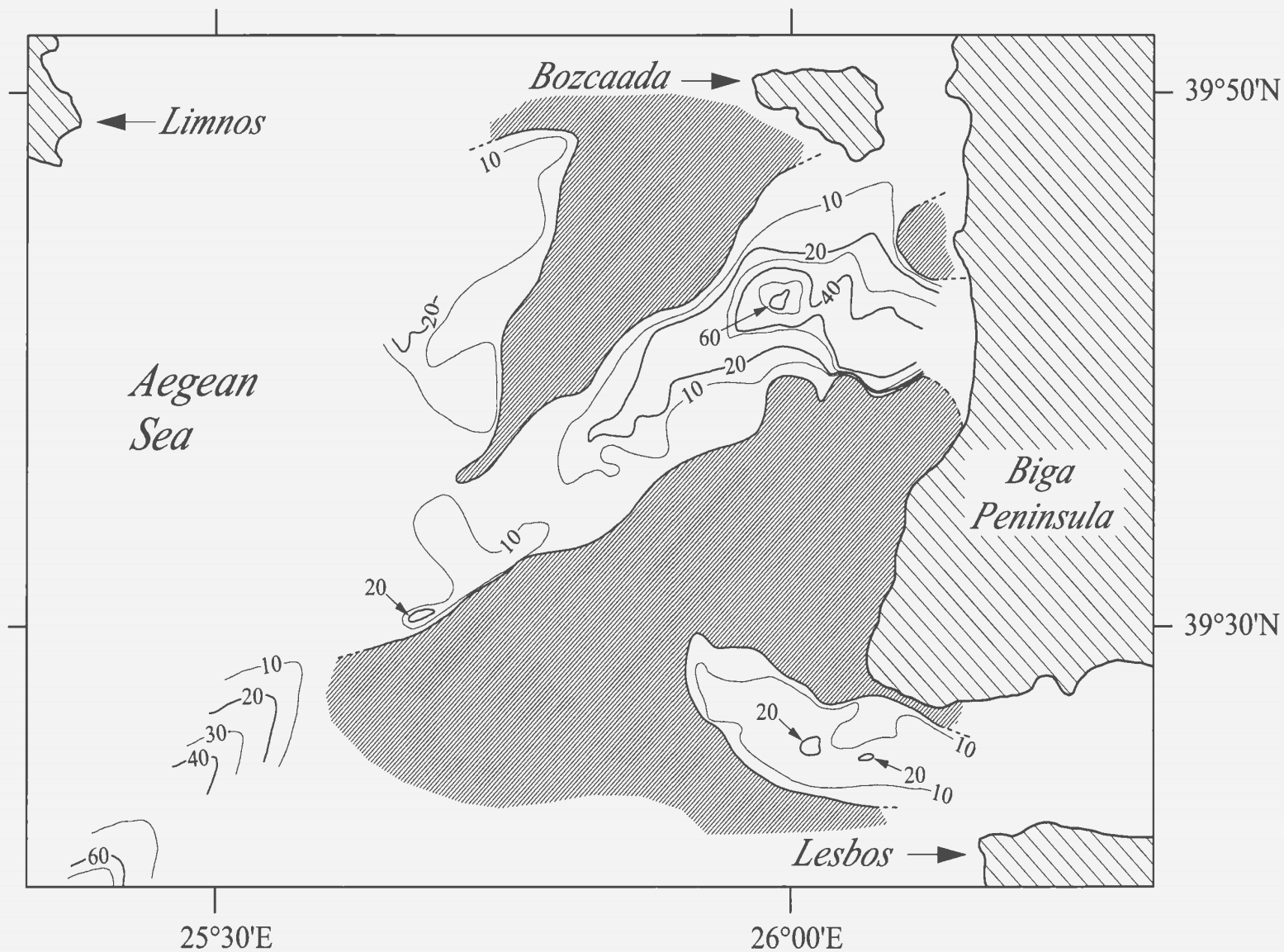
Figure 3.22. Isopach map of depositional sequence 2 showing sediment thicknesses in two-way-travel time (in milliseconds). Densely hatched areas represent regions where depositional sequence 2 is eroded or was not deposited.
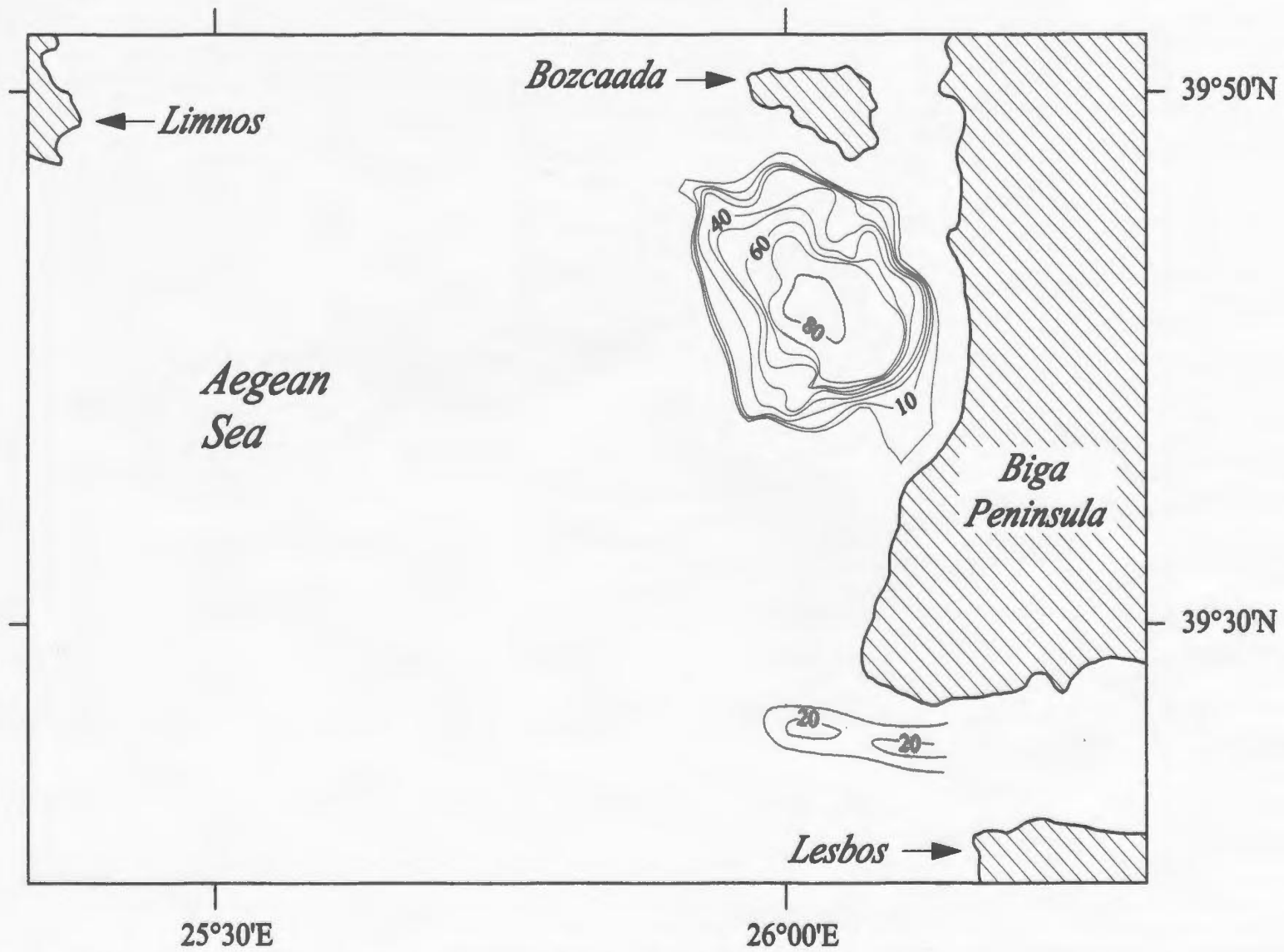
Figure 3.23. Isopach map of depositional sequence 3 showing sediment thicknesses in two-way-travel time (in milliseconds).

Page 83

<u>NOT</u> IN

BOOK

clinoforms, and a lower subunit (S4b) characterized by strong and relatively continuous parallel reflectors (Fig. 3.6). It is bounded at its top and base by the shelf-crossing unconformities α_0 and α_1, respectively. In basin B2, depositional sequence 4 is thickest (~ 40 ms) along the axis of the basin and displays an elongate, basin-fill-like external geometry (Fig. 3.14, 3.25). In basin B2, the oblique clinoforms of Subunit 4a dip 4° and 8° in directions changing from west in the north, to southwest and south-southwest in the south (Fig. 3.24). Subunit 4a is mostly absent in basin B1, particularly within the deeper portions of the basin. Accordingly, within most of the deeper portions of basin B1, the overlying α_0 is a correlative conformity downdip from the clinoforms. The parallel reflections of subunit 4b mostly retain their high-amplitude character throughout the seismic profiles. In the deeper portions of basin B1, Subunit 4b progressively thins toward the south and shows lapout with rare downlap terminations.

Depositional sequence 5 (DS5)

Depositional sequence 5 is a 30–120 ms-thick seismic unit which is bounded at its top and base by the shelf-crossing unconformities α_1 and α_2, respectively (Fig. 3.6, 3.16). Generally, it is composed of an upper 40–100 ms-thick Subunit 5a and a lower 10–40 ms-thick Subunit 5b. Subunit 5a is characterized by acoustically strong, steeply dipping (6°–12°) oblique-prograded clinoforms. Foreset strata of the clinoforms either exhibit abrupt downdip terminations by downlap against older reflectors or extend well downdip as they gradually decrease in angle, then terminate gently by downlap against the underlying reflectors. The dip directions of the oblique-prograded clinoforms of Subunit
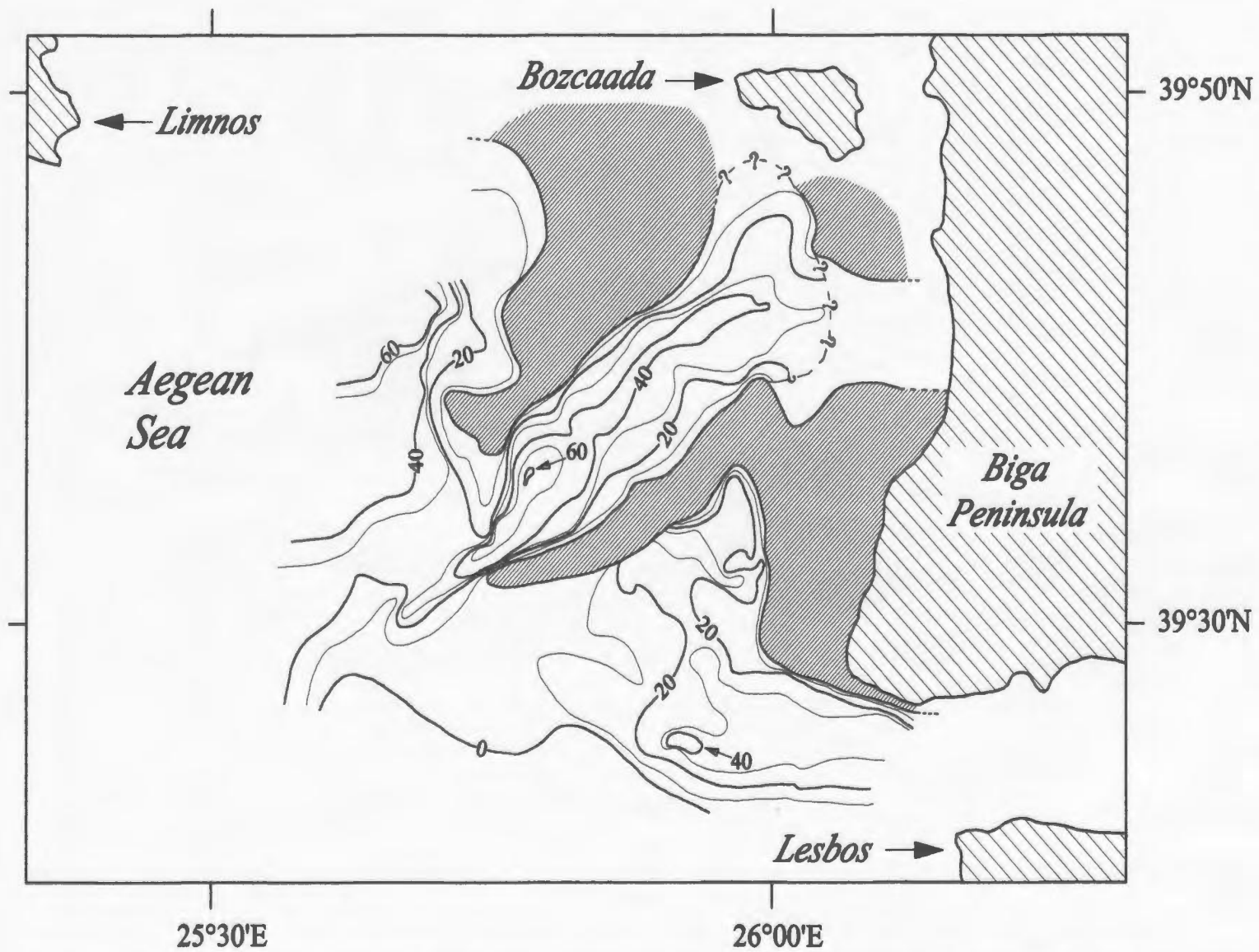
Figure 3.25. Isopach map of depositional sequence 4 showing sediment thicknesses in two-way-travel time (in milliseconds). Densely hatched areas represent regions where depositional sequence 4 is eroded or was not deposited.

5a change from west-southwest in basin B2, to east-southeast in basin B1; dips range from 6 – 8° (Fig. 3.24). Subunit 5b is composed of relatively strong and continuous parallel–subparallel reflections. Within Subunit 5b, subparallel reflectors display limited lateral continuity where they gently downlap against underlying reflectors within the upper portion of the subunit. However, in the lowermost part of the subunit, the reflectors mostly parallel the unconformity α_2, and extend for significant distances before they gently terminate by downlap onto α_2. Particularly within basin B1, Subunit 5b occurs immediately below Subunit 4b, and cannot be readily distinguished from the overlying Subunit 4b because of their similar seismic reflection configurations. Depositional sequence 5 is thickest within basin B1. (Fig. 3.26).

In basin B2, the topset-to-foreset transition of the youngest clinoforms occurs ~ 400 ms below present sea level. Depositional sequence 5 has a volume of 38.2 km^3.

Depositional sequence 6 (DS6)

Depositional sequence 6 is a 10–100 ms-thick seismic unit. It is bounded at its top and base by shelf-crossing unconformities α_2 and α_3, respectively (Fig. 3.6, 3.14). The upper 30–95 ms-thick Subunit 6a consists of acoustically strong, locally diffractive, steeply to gently dipping, oblique-prograded clinoforms. Within the southern portion of the study area in basin B1, the clinoforms dip in directions changing from south-southwest to south-southeast (Fig. 3.24). The lower 10–55 ms-thick Subunit 6b is characterized by strong subparallel to dominantly parallel reflectors. Within Subunit 6a, the gently-dipping clinoforms extend for long distances with angles <4° and gently
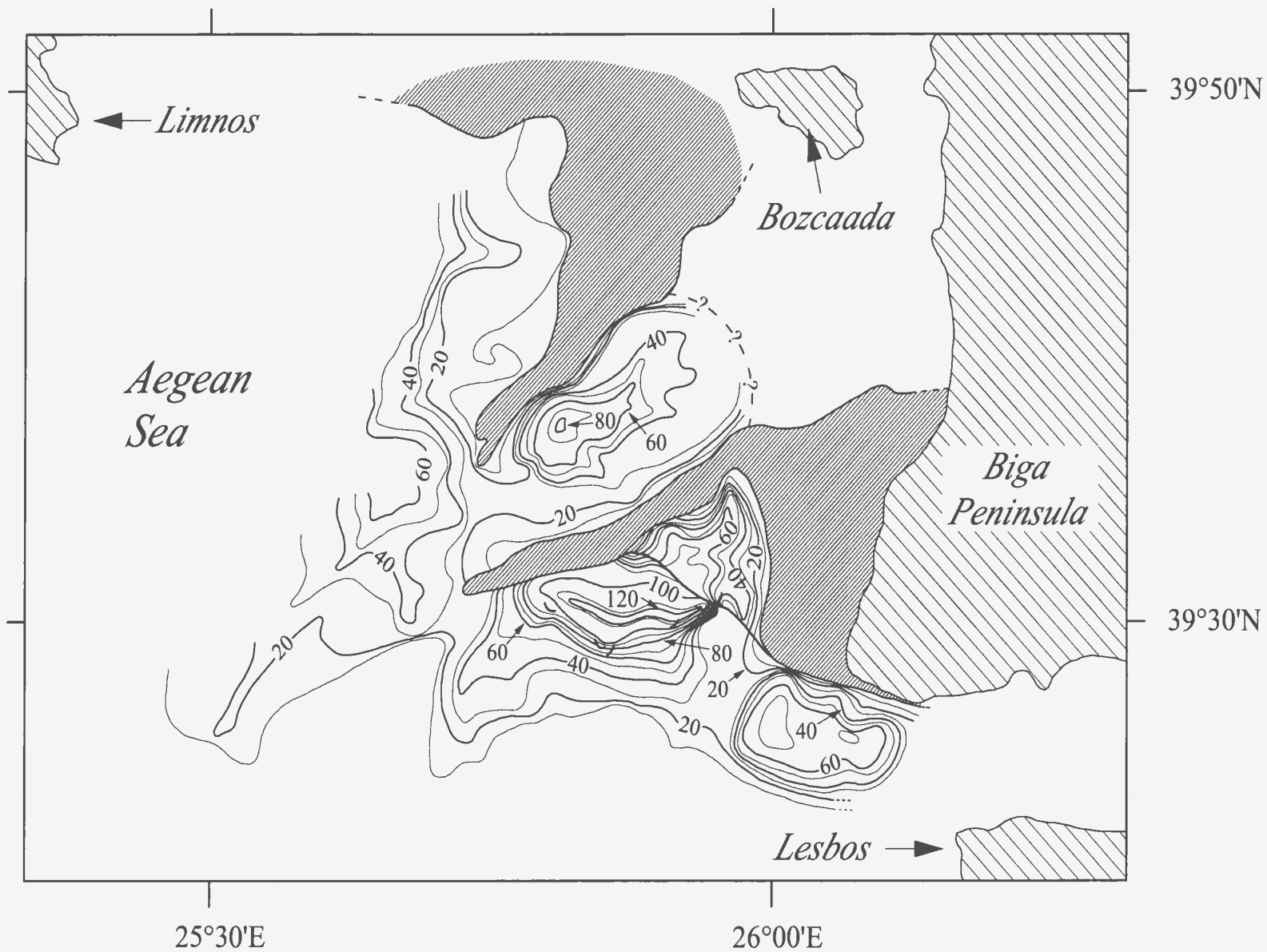
Figure 3.26. Isopach map of depositional sequence 5 showing sediment thicknesses in two-way-travel time (in milliseconds). Densely hatched areas represent regions where depositional sequence 5 is eroded or was not deposited.

downlap against the underlying strata of Subunit 6b. In a south to southwest direction (i.e. along strike) these gently-dipping clinoforms generally change their character laterally and become acoustically weak, steeply dipping reflections with angles ranging between 4° and 12°. The foreset strata of these steeply dipping clinoforms either terminate abruptly by downlap or pass into low-angle (<2°) bottomset strata that extend for considerable distances before they gently terminate against α_3 by downlap. The reflections that form Subunit 6b mainly retain their high amplitude character. They mostly parallel the unconformity α_3 except where rare downlap terminations can be recognized. Depositional sequence 6 displays a lobe-like external geometry especially in basin B1 (Fig. 3.27).

Depositional sequence 7 (DS7)

Depositional sequence 7 is composed of two subunits with thicknesses of 10–50 ms (Subunit 7a) and 10–180 ms (Subunit 7b) (Fig. 3.10). The upper Subunit 7a is characterized by relatively strong, steeply dipping, oblique-prograded clinoforms and is bounded at its top by the shelf-crossing unconformity α_3. The dip angles of the clinoforms range from 8°–14°, dipping toward southeast in the northern part of basin B1(Fig. 3.24). The lower Subunit 7b consists of acoustically strong parallel reflectors. Subunit 7b is considerably thicker than Subunit 7a. It is also thicker than the lower subunit of any younger depositional sequences (i.e., subunits 4b, 5b, 6b). The unconformity α_4 at the base of Subunit 7b is mostly obscured by the first multiple. Therefore, it is generally not possible to measure an accurate thickness and prepare an
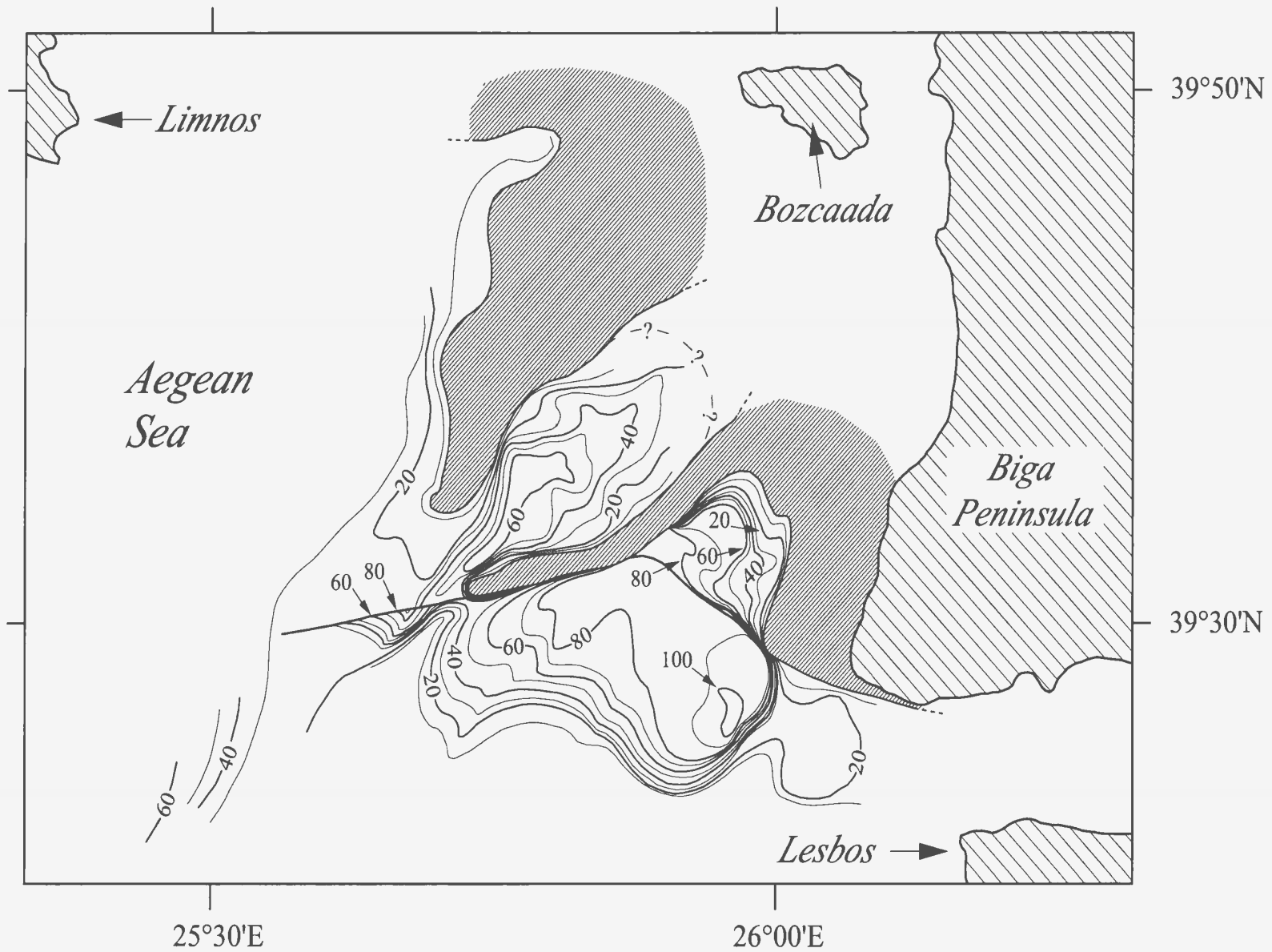
Figure 3.27. Isopach map of depositional sequence 6 showing sediment thicknesses in two-way-travel time (in milliseconds). Densely hatched areas represent regions where depositional sequence 6 is eroded or was never deposited.

isopach map of Subunit 7b.

Depositional sequences 8 and 9

Depositional sequences 8 and 9 are each composed of two subunits characterized by oblique-prograded clinoforms and parallel reflectors that constitute their upper and lower portions, respectively. However, the penetration depth of the seismic source and the strong first multiple do not allow detailed mapping of these packages.

CHAPTER 4

4. Structural framework

The Quaternary architecture of the northeastern Aegean Sea between the islands of Bozcaada, Lesbos and Limnos is characterized by a series of broadly northeast–southwest-trending to east–west-trending faults (Fig. 4.1). On the basis of the fault locations throughout the study area, the positions of the tip lines of these faults, and the amounts of displacement of the stratigraphic successions created across the fault planes, the study area faults are categorized into three assemblages: (i) a group of extensional and/or transtensional faults in the southern half of the study area (basin group faults), (ii) second group of extensional and/or transtensional faults exclusively found in the northernmost portion of the study area (shelf group faults; Fig. 4.1). Where possible, holistic descriptions of structures and structural associations are given throughout the study area; however, faults with very large vertical separations and zones showing intense deformation are described separately.

4.1 Basin group faults

The basin group faults consist of several west-northwest-trending and southeast-trending, either south- or north-dipping, curvilinear and planar faults. A dense grid of seismic reflection profiles allows tracing of faults between adjacent seismic profiles. For example, three prominent faults, designated as δ_2, δ_3 and δ_7, occur along the southern segment of the shelf, north of the shelf-slope break (Figs.
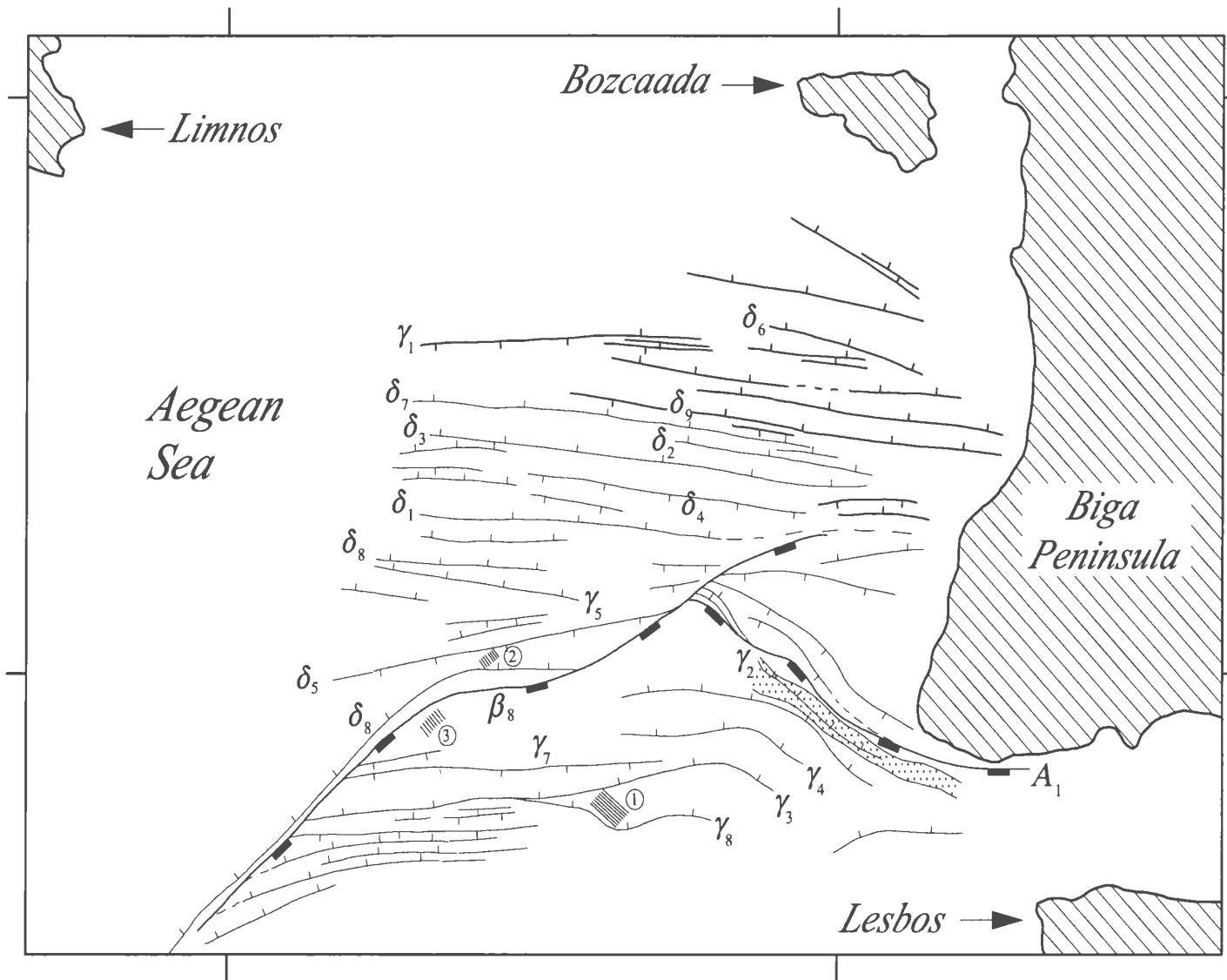
Figure. 4.1. The basin and shelf fault groups within the study area (bolder faults belong to the shelf group faults). The dotted band represents a highly deformed zone south of fault A_1. Circled numbers 1-3 indicate the narrowly spaced fault assemblages.

4.2, 4.3). These faults display steeply to moderately (70–50°) north-dipping fault surfaces, prominently displace depositional sequences 2, 3 and 4, and form mild steps at the seafloor. The faults can be clearly correlated in adjacent seismic profiles, even for seismic data collected in different years using different acquisition systems (compare Figs. 4.2 and 4.3). This exercise reveals that faults δ_3, δ_2 and δ_7 display a clear west-northwest (~281°) strike. Close spacing of seismic profiles allows the fault correlations to be carried across the study area. Limited side-scan sonar images on the shelf portion of the study area verify the orientation of the fault traces. For example, a side-scan sonar profile from the southern shelf region shows a prominent northeast-southwest-trending fault (Fig. 4.4). A high-resolution seismic reflection profile collected concurrently with the side-scan sonar profile shows that this fault is the northern continuation of fault β_8 (Fig. 4.4). The fault trend observed in the side-scan sonar profile has an 87°-267° orientation, almost perfectly matching the strike of the map trace of fault β_8 (Figs. 4.1, 4.4). Another example can be given from the central portion of the study area (Fig. 4.5), where a side-scan sonar profile shows two west–northwest- to east–southeast-trending faults with 113-293° orientation. This direction fairly matches the strikes of the map traces in that area (Fig. 4.1).

In seismic reflection profiles, the basin group faults display moderate to high dips, ranging from 40° to 60°. Correlation of marker reflectors and shelf crossing unconformities across these faults indicate a normal component of throw (Fig. 4.3). High-resolution profiles allow the delineation of fault plane geometries. For instance, many footwall and hangingwall cutoffs of marker reflectors and shelf-crossing
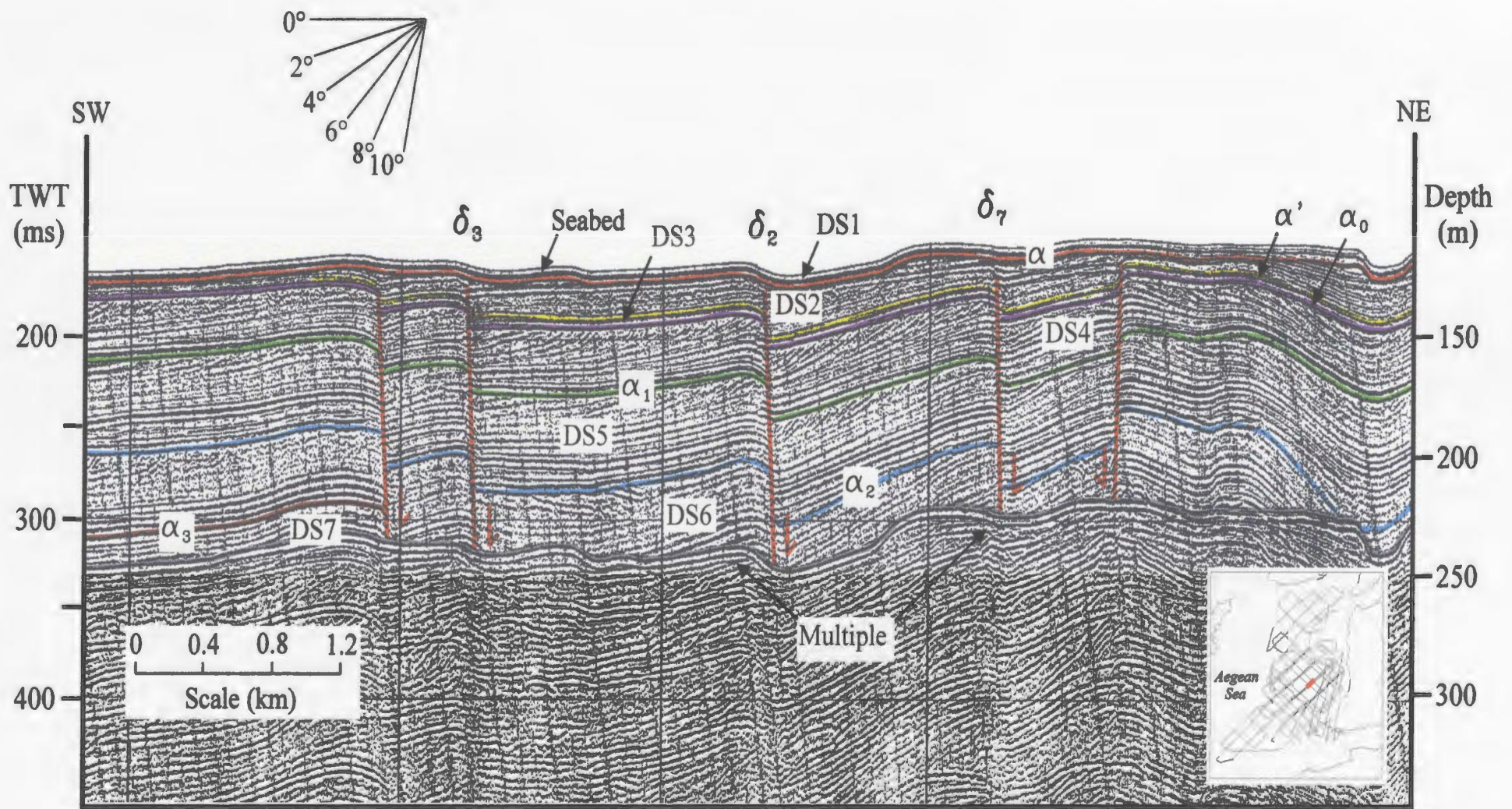
Figure 4.2. Seismic reflection profile showing prominent faults, including δ_2, δ_3, and δ_7. Note greater thicknesses of the depositional sequences on the hanging wall of each fault.
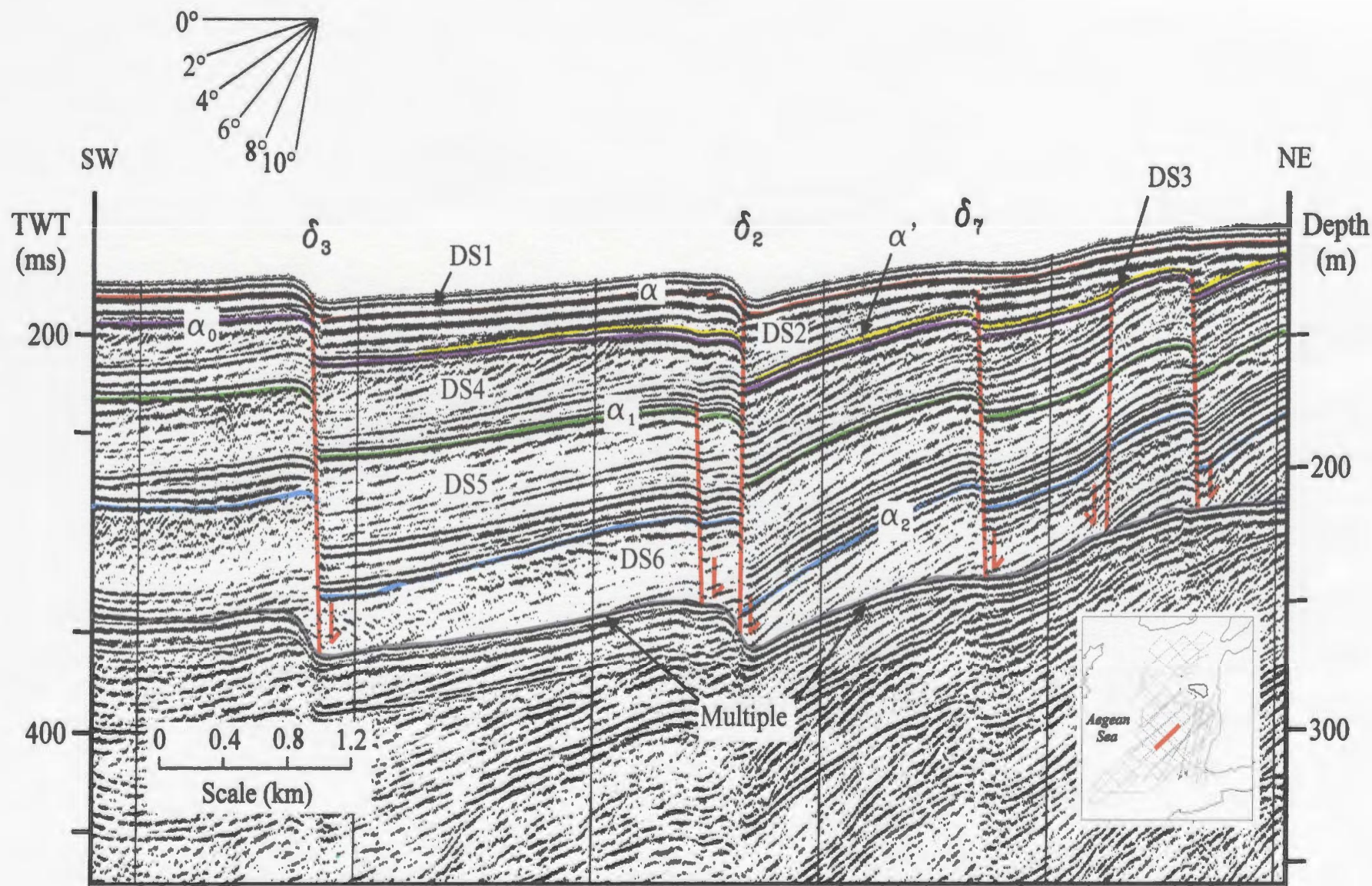
Figure 4.3. Seismic reflection profile showing prominent faults, including δ_2, δ_3, and δ_7 (discussed in text). Note greater thicknesses of depositional sequences on hanging wall of each fault.
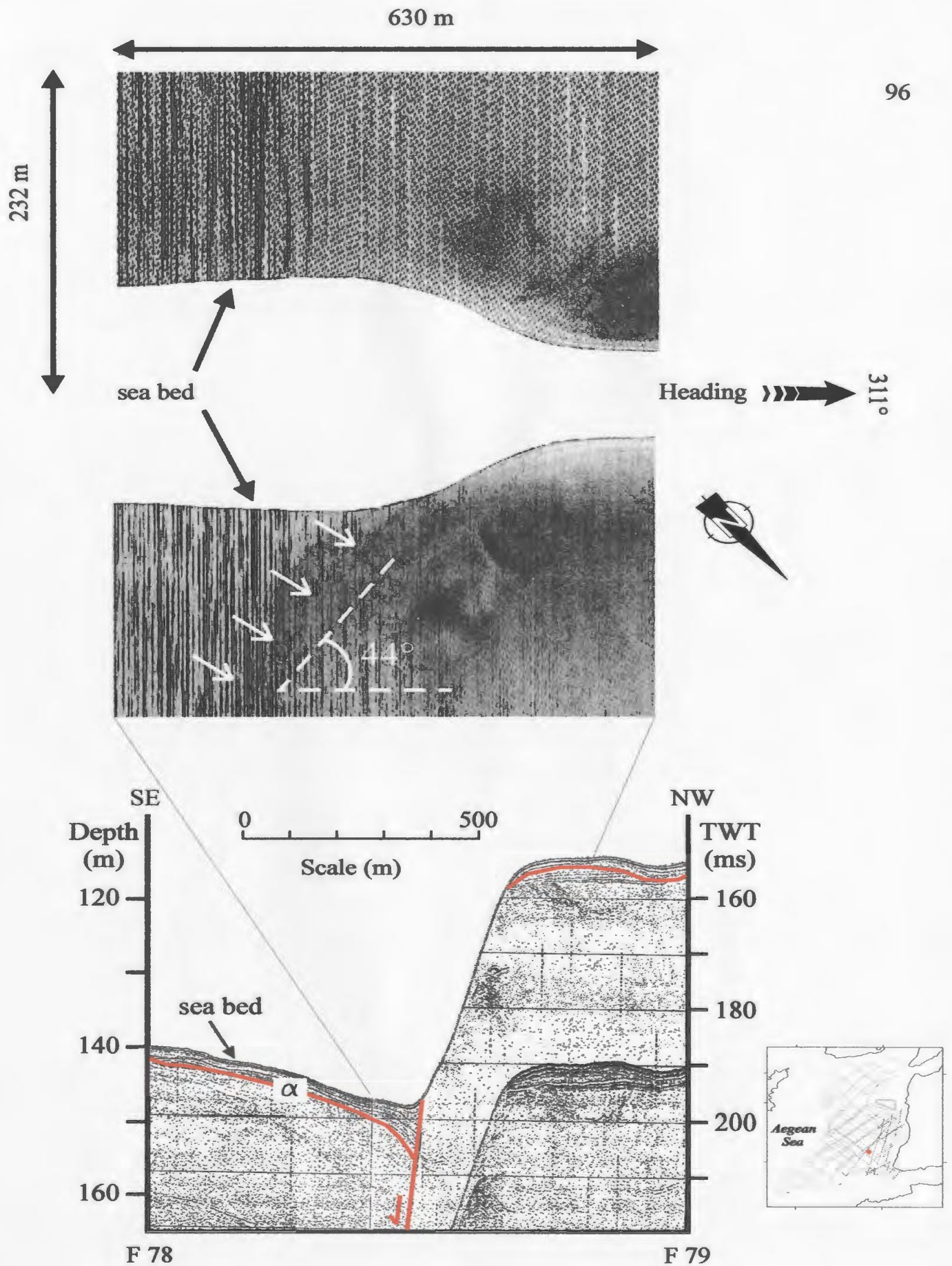
Figure 4.4. Side scan sonar profile (top) and simultaneously acquired Huntec DTS profile (bottom) showing the 267° orientation of fault β_s.

630 m

232 m

sea bed

Heading >>>> 52°

61°

SW   0   500   NE

Depth   sea bed   TWT
(m)   Scale (m)   (ms)   — 110

150 —

120 —   — 160

— 180

140 —

F 129   F 130

Aegean
Sea
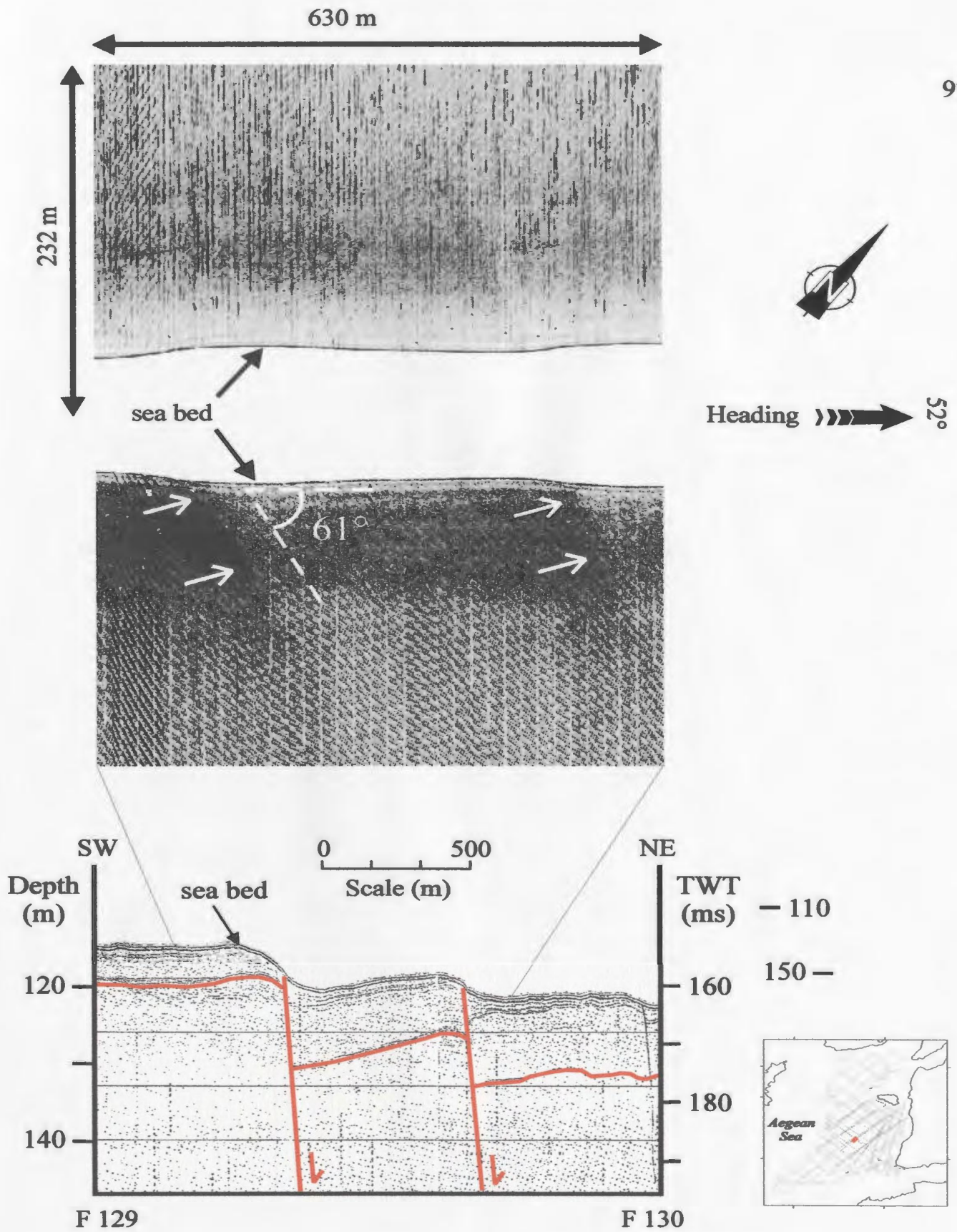
Figure 4.5. Side scan sonar profile (top) and coincident Huntec DTS profile (bottom) showing the orientation of two faults within the central portion of the study area.

unconformities are notably horizontally separated, confirming the extensional or transtensional nature of these faults (Fig. 4.2).

The tip lines of many faults in this group extend to the seafloor, where they create notable morphological steps, ranging in elevation from 2 to >200 m. Correlation of marker reflectors across the faults shows that the depositional sequences are invariably thicker in the hangingwalls of many faults in this group (e.g. Figs. 4.3), forming with prominent sedimentary wedges that thicken toward each fault plane. This architecture can be explained by either protracted syn-sedimentary extensional growth faulting or lateral movement along fault planes resulting in consistent thickness contrasts of the same depositional sequence on either side of the fault (strike-slip or oblique-slip faulting). Considering the overall southward thinning of the depositional sequences in basin B2 and the thickening of strata in the downthrown blocks, it is plausible to suggest that movement along the postulated strike-slip or oblique-slip faults is dextral. In many profiles, the prominent west-northwest-trending, south-dipping faults are paired with similar-trending, north-dipping minor antithetic faults, creating small graben structures (e.g. Fig. 4.2).

The basin group faults can be readily traced across the shelf toward the Biga Peninsula (Fig. 4.1). As the water depth becomes shallower toward the shore, the first multiple rises very close to the sediment surface, making the identification of faults very difficult.

4.1.1 Prominent basin group faults

Fault A$_1$

One of the prominent faults of the basin group is A$_1$, a southeast- and east-striking (90°-115°), southwest-dipping normal fault (Figs. 4.1, 4.6-4.11). At the eastern end of the study area, the fault runs east–west and parallels the southern shores of the Biga Peninsula (Fig. 4.1). Traced westward, fault A$_1$ swings toward the northwest immediately south of the Baba Burnu promontory and eventually merges with another prominent northeast-striking fault β$_8$ at its westernmost extension (Fig. 4.1). Fault A$_1$ gives the appearance of a through-going master fault as it transects basin B1 with a relatively straight map trace (Fig. 4.1).

Fault A$_1$ creates a remarkable scarp on the seafloor, with vertical separations ranging between 45 and >200 m (Figs. 4.1, 4.6-4.11). Several seismic lines, cutting across the strike of the fault almost perpendicularly, demonstrate that fault A$_1$ shows varying amounts of vertical separation along its length. The highest vertical offsets of the seabed (170–203 m) occur along its eastern and central segments; however, in the west, the offsets progressively diminish to <45 m at its westernmost extension. The offset variations along the length of the fault can also be recognized in the three-dimensional bathymetric map of the seabed (Fig. 3.8). Fault A$_1$ delimits the shelf-slope break along the southeastern portion of the study area in basin B1. The sedimentary successions in the footwall and hangingwall of the fault exhibit remarkable differences. For example, subunit 4a, composed of oblique-prograded clinoforms, is absent in the hangingwall of fault A$_1$ (cf. Figs. 3.6, 4.11). Assuming conditions of constant sediment input rate, the absence of oblique-prograded
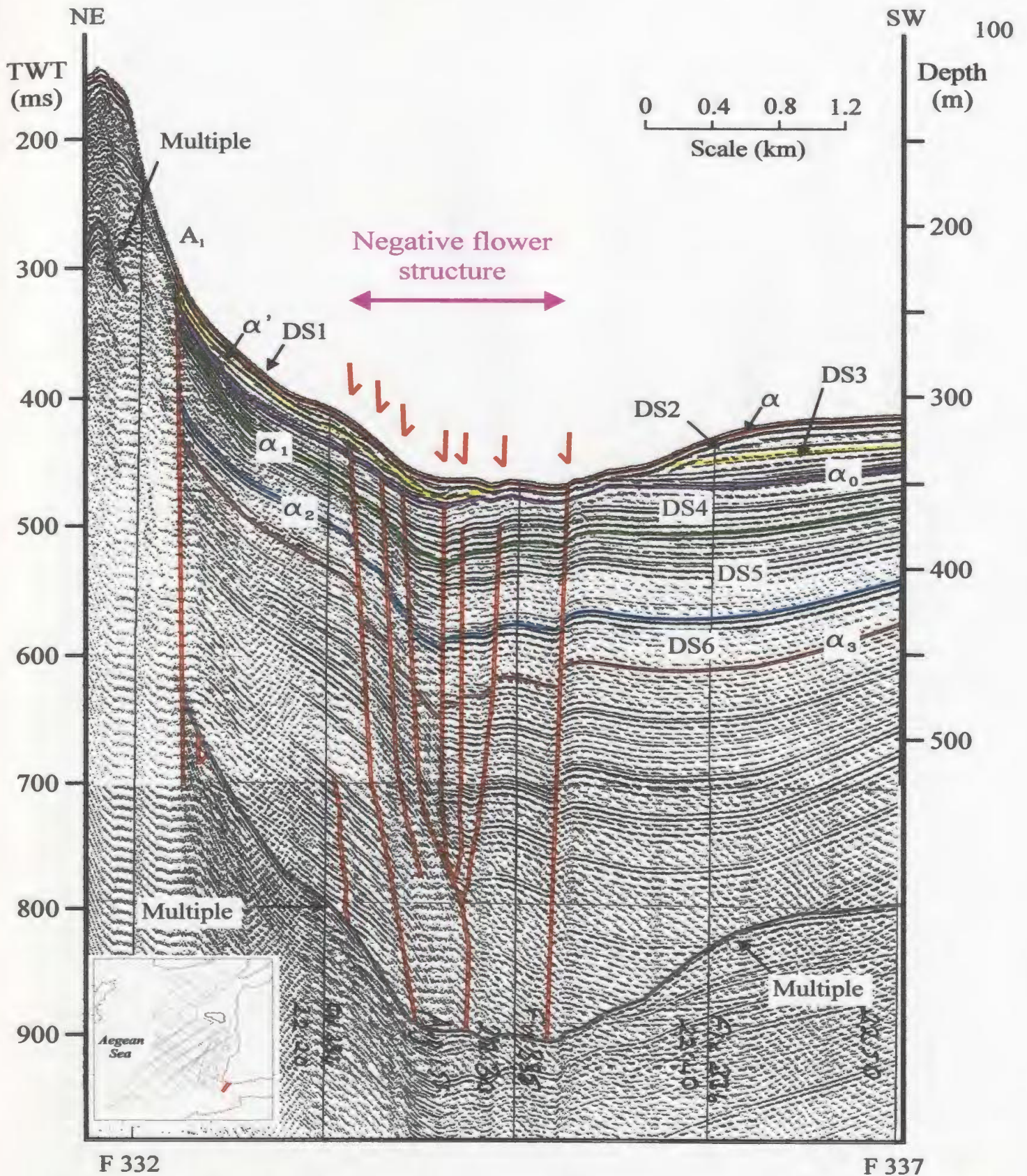
Figure 4.6. Seismic reflection profile showing the prominent fault A₁ and a negative flower structure.
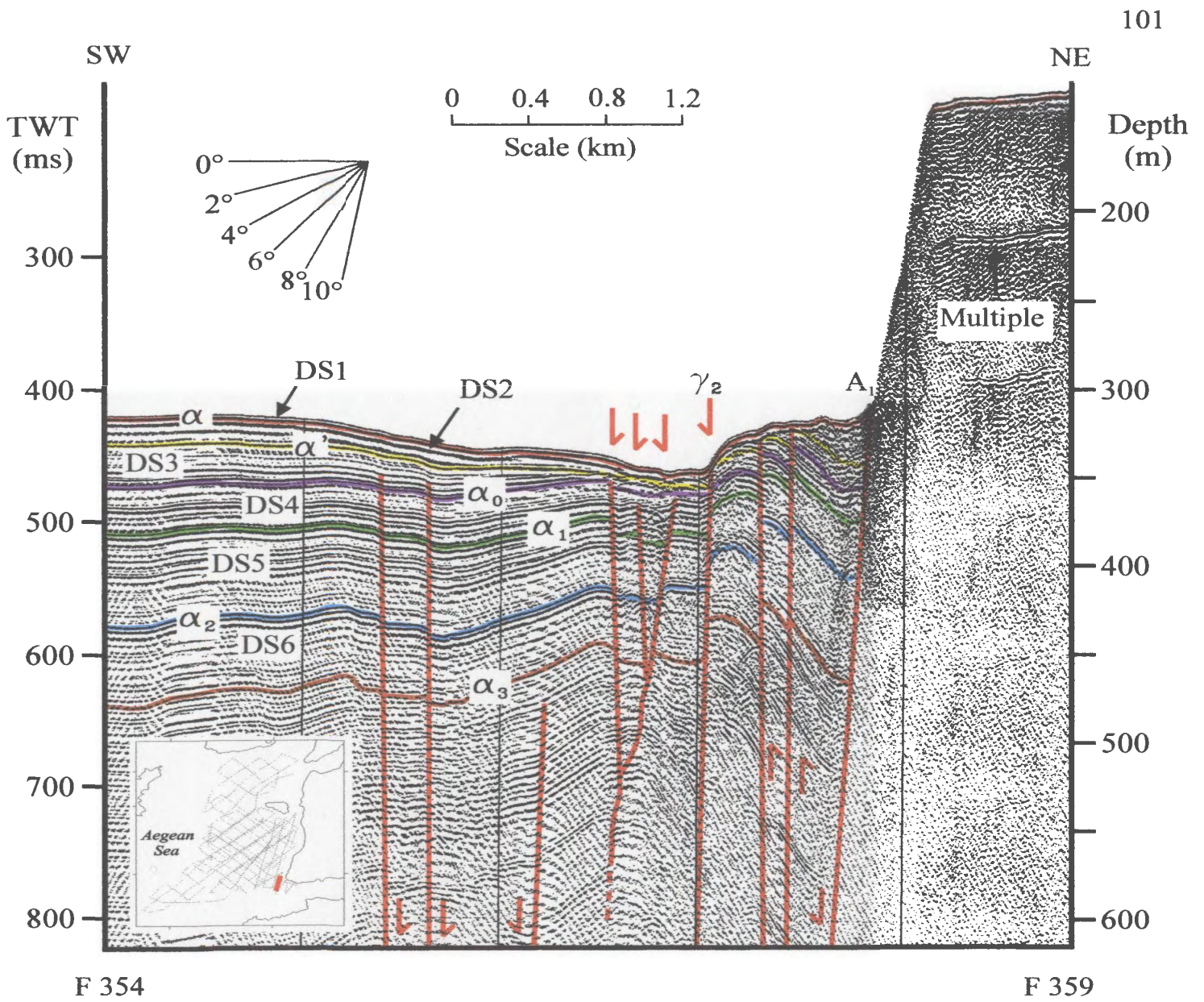
Figure 4.7. Seismic reflection profile showing the prominent fault A_1 and a negative flower structure within the linear belt near the fault.
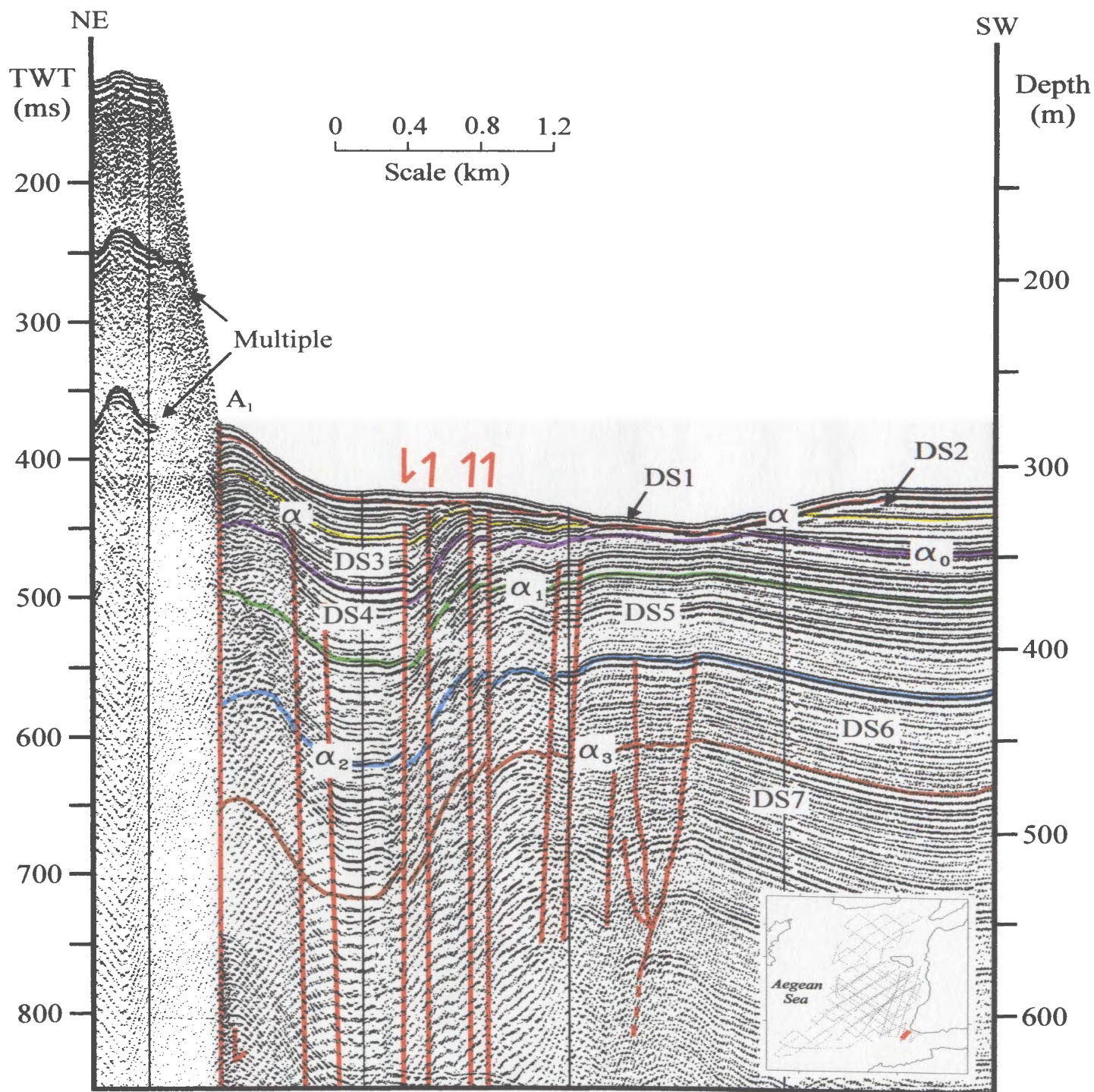
Figure 4.8. Seismic reflection profile showing the prominent fault A_1 and the linear belt with a negative flower structure.
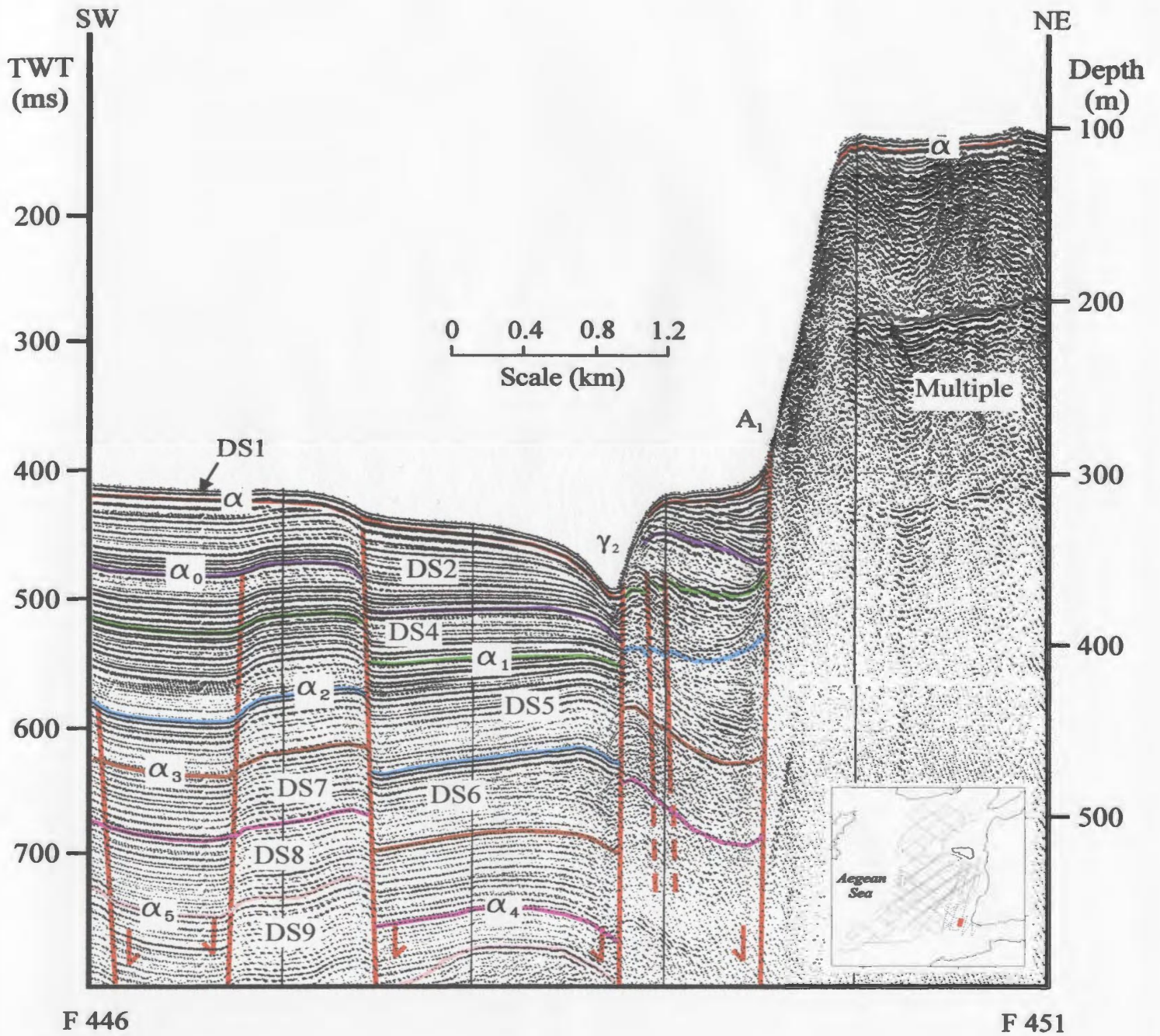
Figure 4.9. Seismic reflection profile showing the prominent fault A_1 and other faults within the same zone.
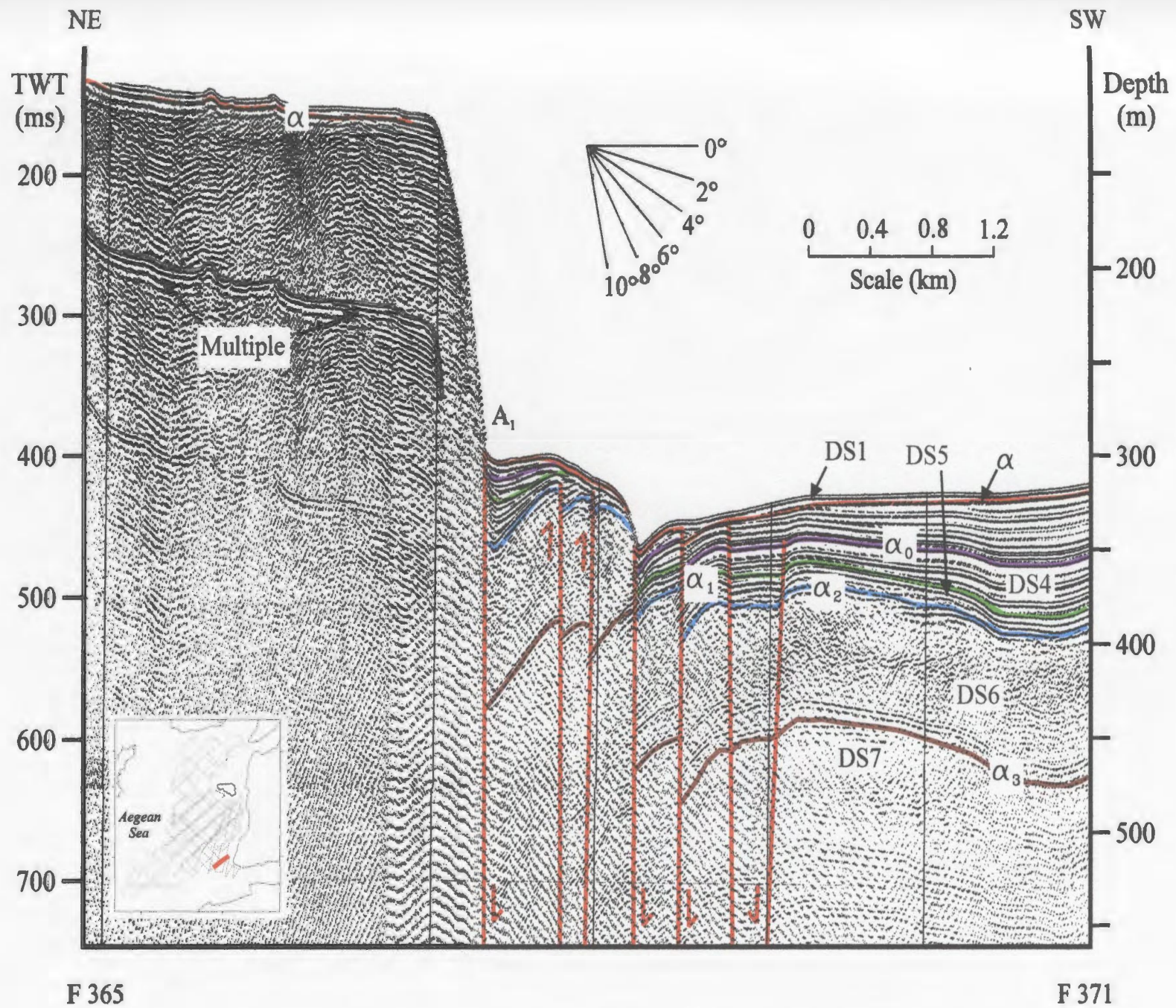
Figure 4.10. Seismic reflection profile showing prominent fault A_1 and the linear belt basinward of A_1.
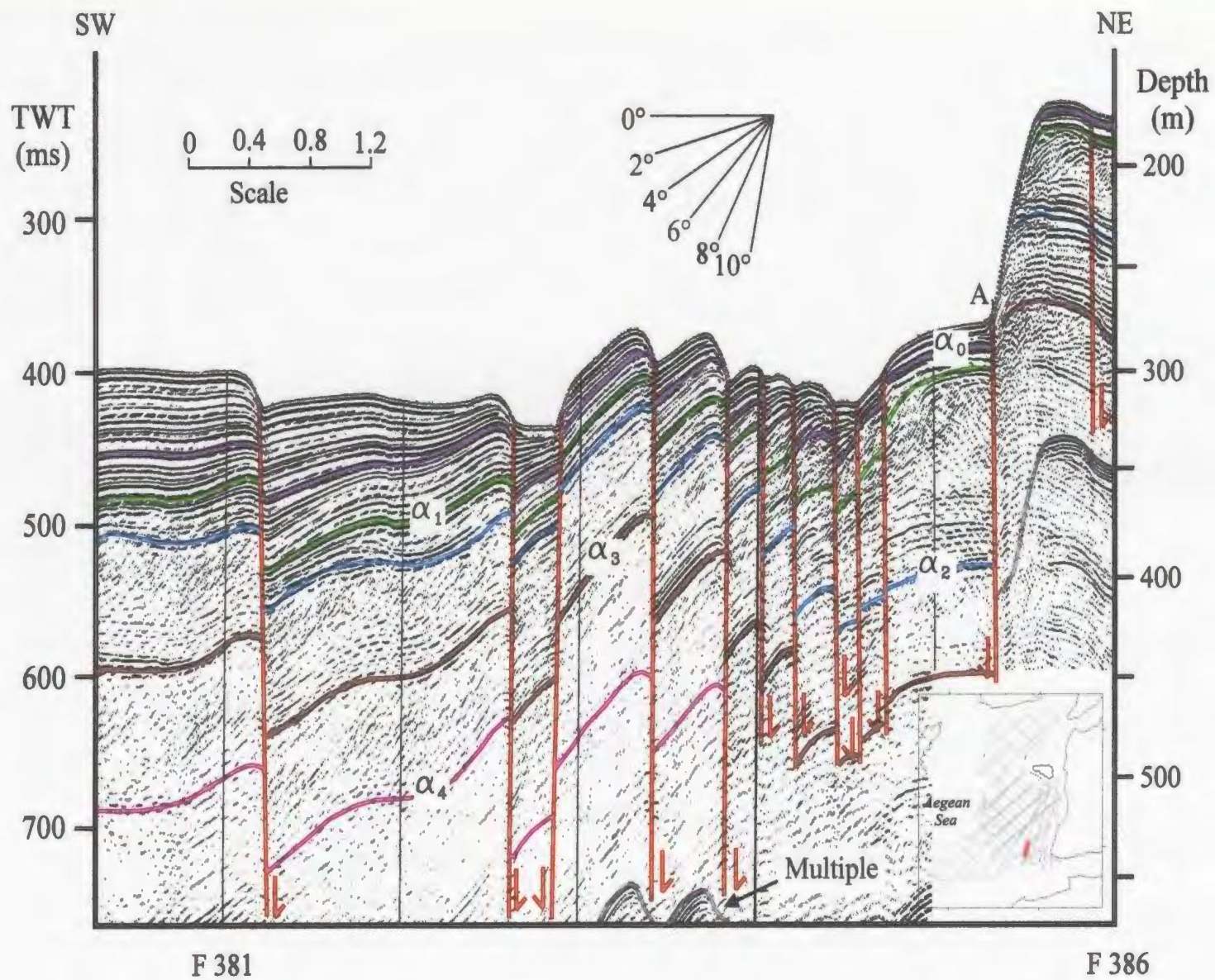
Figure 4.11. Seismic section showing the prominent fault A_1 and the subvertical normal faults within the adjacent linear belt.

clinoforms suggests that during the time of development of depositional sequence 4 noticeably higher rates of subsidence prevailed on the hangingwall block. The higher rates of subsidence created extensive accommodation space which was unsuitable for sediment deposition as clinoforms. Another recognizable difference is that the sedimentary successions in the footwall of fault A_1 are comparatively less disturbed while those in the hanging wall are extensively deformed within a narrow zone close to the master fault (Figs. 3.6, 4.11). This highly disturbed zone will be fully described in section 4.1.3.

Fault β_8

Fault β_8 is another major, broadly northeast- and east-northeast-striking (45°-80°), southeast-dipping normal fault (Figs. 4.1, 4.12). It cuts across the study area in an oblique fashion and creates a curvilinear map trace. Fault β_8 generally behaves as a basin-bounding fault, delimiting the northwestern boundary of basin B1 (Fig. 4.13). The fault creates a prominent bathymetric step on the sea floor with apparent dip-slip amounts changing from 15 m in the northeast to as much as 127 m in the southwest. Fault β_8 retains its character as a basin-bounding fault with high amounts of vertical displacement beyond the southwestern limit of the study area. However, at its northeastern end, the fault cuts across basin B1 and creates a 45 m-step on the seabed (Fig. 3.13). Here, the correlation of the footwall and hangingwall cutoffs of the shelf-crossing unconformities shows that the depositional sequences are thicker on the downthrown block implying either syn-sedimentary extensional or oblique-slip faulting. The thickening of the stacked depositional sequences is intensified by the
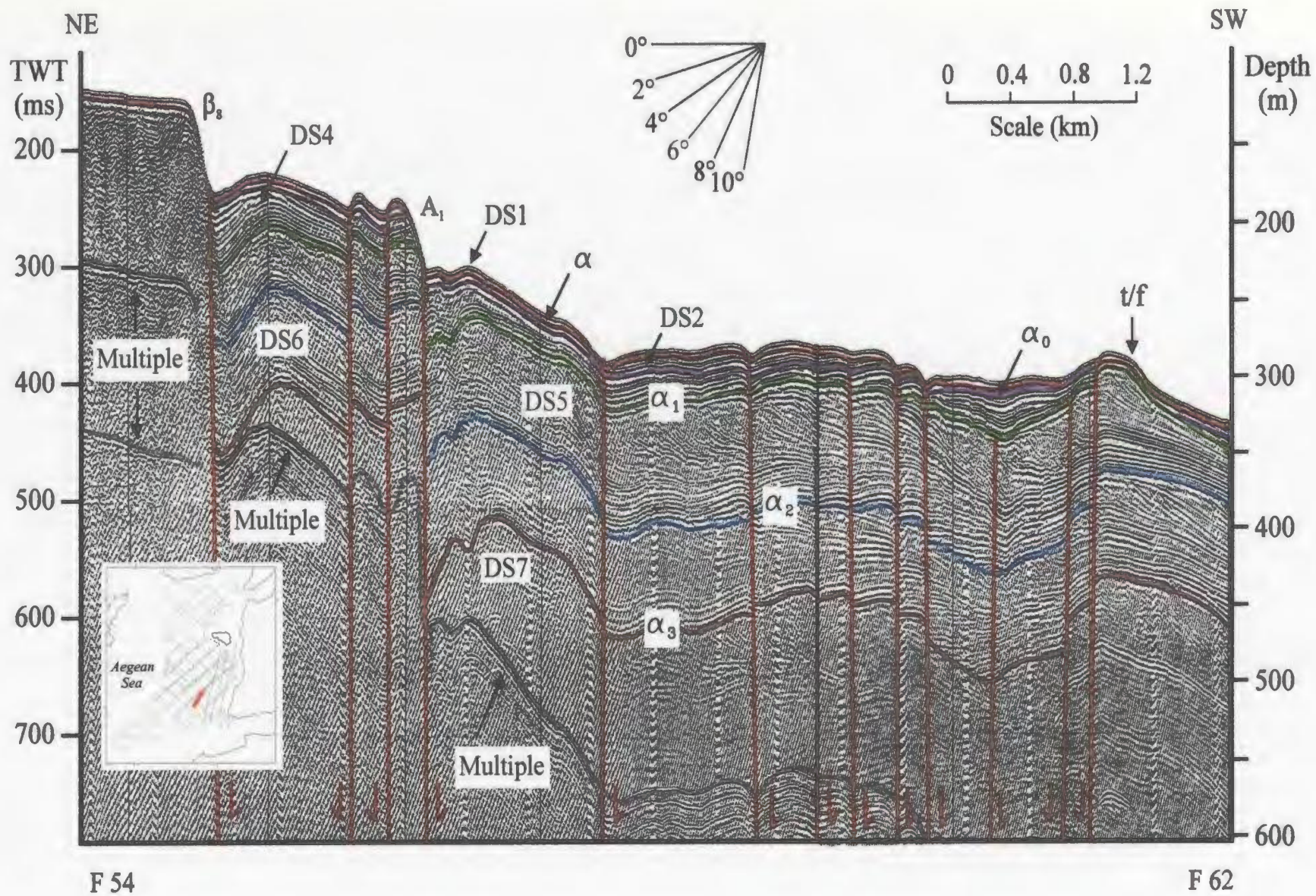
Figure 4.12. Northeast-southwest-trending seismic reflection profile from the deeper portions of basin B1 showing the prominent faults β_8 and A_1.
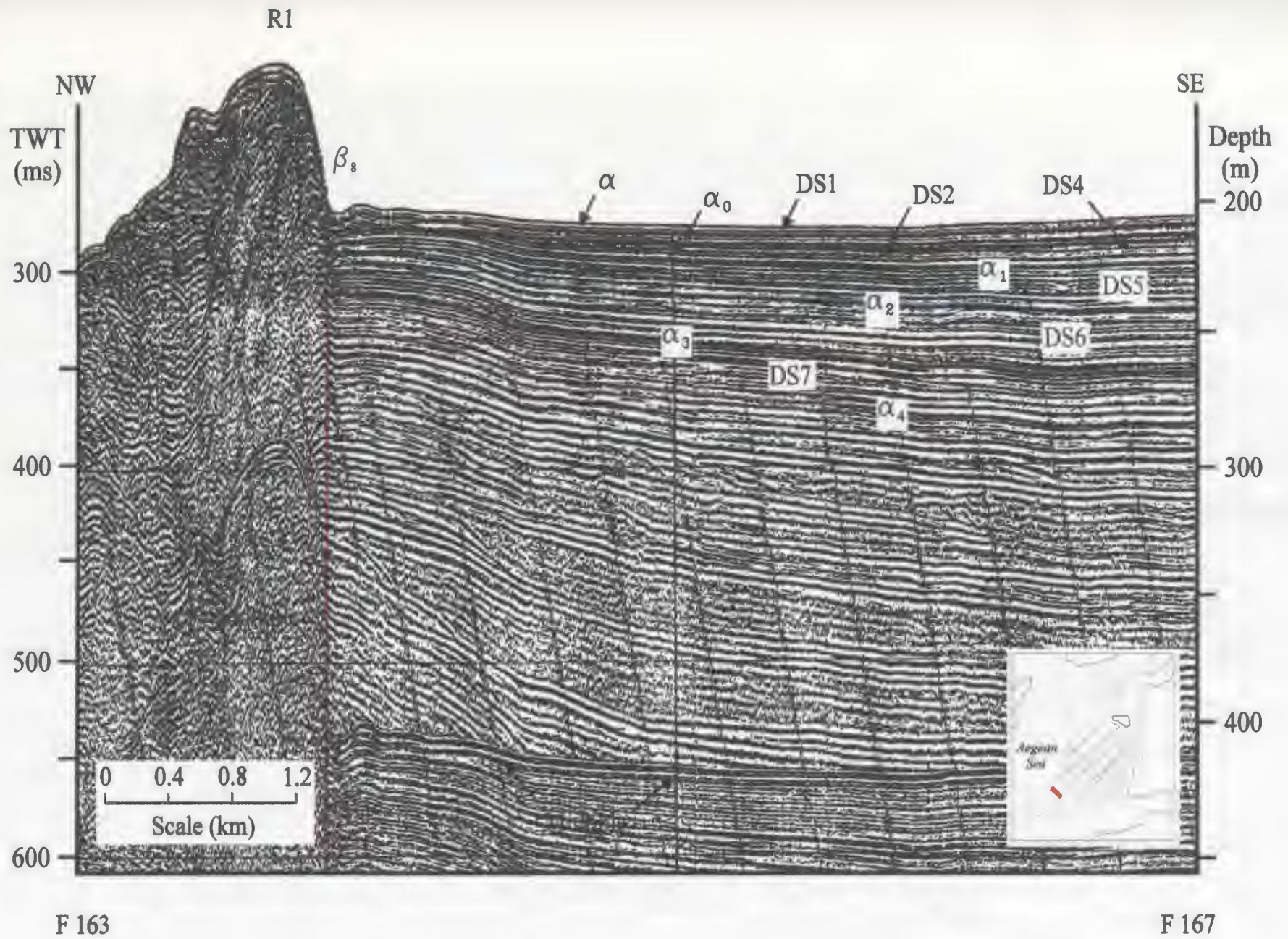
Figure 4.13. Seismic reflection profile showing the prominent basin-bounding fault β_8.

divergent character of the reflectors toward the fault plane as they, collectively, create remarkable sedimentary wedges (Fig. 3.13). When traced farther northeast, the vertical offsets of fault β_8 progressively diminish to ~4 m, the fault loses its bathymetric expression and eventually becomes indistinguishable from any of the minor faults mapped in the study area (Fig. 4.1). Along the southern portion of fault β_8, the sedimentary succession is locally folded proximal to the fault, perhaps because of resistance to slip along the fault (Fig. 4.14). The fold extends parallel to the prominent fault β_8 and is more than 10 km in length. In the south, it has a half-wavelength of ~1.5 km and an amplitude of ~150 ms. These dimensions progressively diminish to a half-wavelength of ~1 km and an amplitude of ~100 ms in the north.

4.1.2 *En échelon* faults

Three distinct, narrowly-spaced clusters of faults are recognized throughout the study area (Fig. 4.1). They are composed of vertical–subvertical, relatively short faults displaying apparent normal- and reverse-sense dip-slip separations. On the basis of their cross-sectional geometries, their proximity to the major faults β_8, δ_5, and γ_3, and their inferred oblique trends relative to the major faults, these faults are interpreted as *en échelon* faults. The term "*en échelon*" refers to the arrangement of relatively short structural elements along a linear zone that are approximately parallel to each other but oblique to the strike of the zone (Wilcox et al., 1973; Christie-Blick and Biddle, 1985).
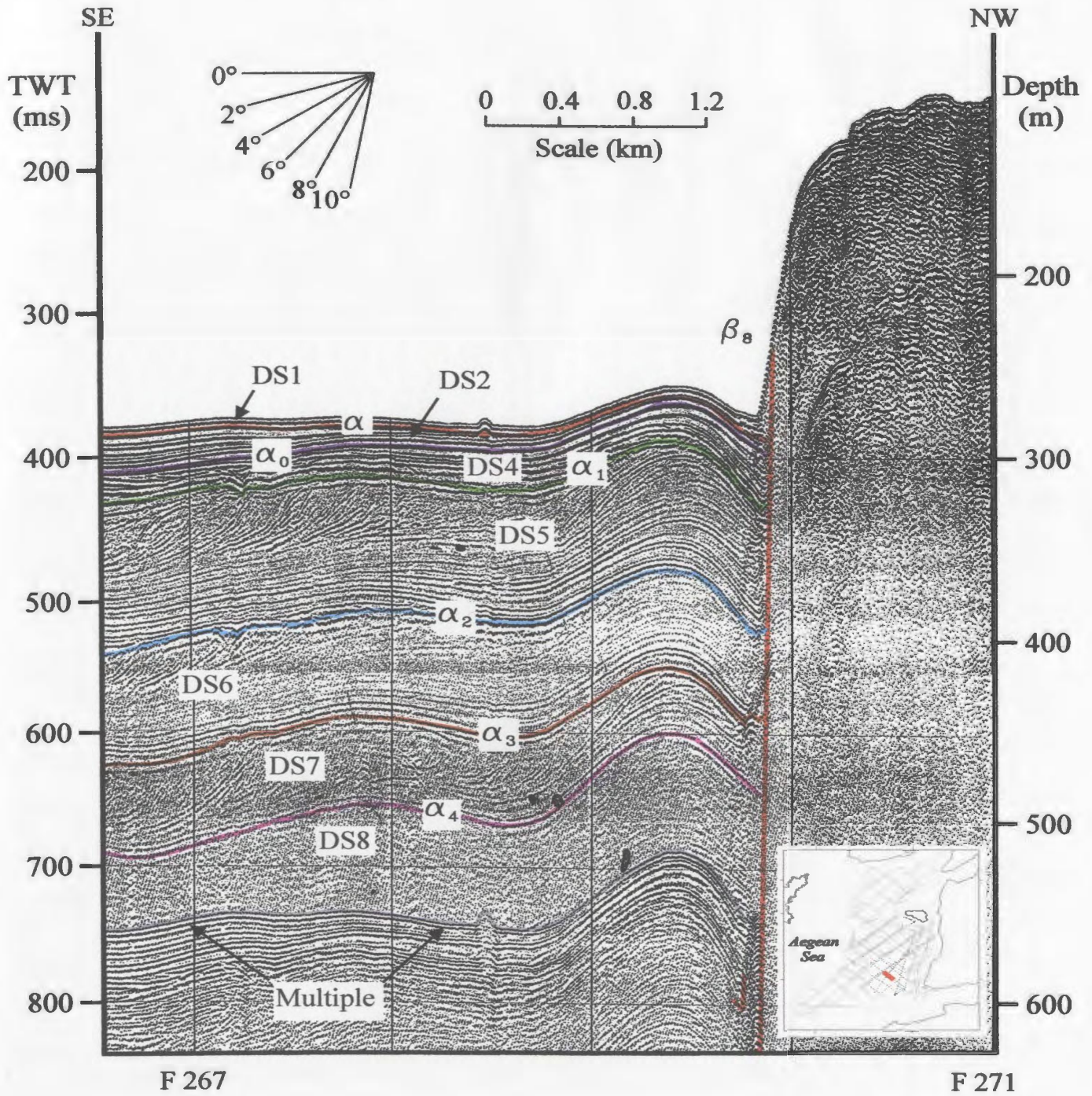
Figure 4.14. Seismic reflection profile showing the prominent fault β_8 and associated folded sedimentary strata.

In the southeastern portion of the study area, a narrowly-spaced fault cluster is recognized (Fig. 4.1). The cluster consists of 10 subvertical, northeast- and southwest-dipping, northwest-trending faults exhibiting apparent normal-sense separations (Fig. 4.15). The faults extend to the seafloor. Faults with the largest vertical separations offset the seabed as much as 5 m, while those with minor vertical separations are expressed on the seabed as minor flexures and undulations (Fig. 4.15). Detailed examination of the footwall and hangingwall cutoffs of marker reflections clearly shows that the vertical separations across the fault planes increase progressively downsection. The sedimentary strata within fault blocks are folded and/or tilted. The faults can be traced to adjacent seismic profiles (Fig. 4.1); however, their closely spaced pattern and the distribution of the seismic profiles in this area do not allow the correlation of individual faults. Nevertheless, the correlation of the fault 'bundle' to the adjacent seismic profile suggests that the constituent faults trend oblique to faults γ_3 and γ_8, confirming an *en échelon* pattern (Fig. 4.1).

The second fault bundle is recognized within the central eastern part of the study area, confined between faults δ_5 and δ_8 (Fig. 4.1). This cluster is composed of eight subvertical, northeast- and southwest-dipping faults (Fig. 4.16). Detailed examination of the positions of the footwall and hangingwall cutoffs of marker reflections across the fault planes shows that three out of eight of the faults have a reverse sense of slip while the rest exhibit normal dip-slip separations. The tip lines of the faults lie near or at the seabed and the amounts of vertical separation estimated from seabed steps range between 15 m and <3 m. The internal architecture of the
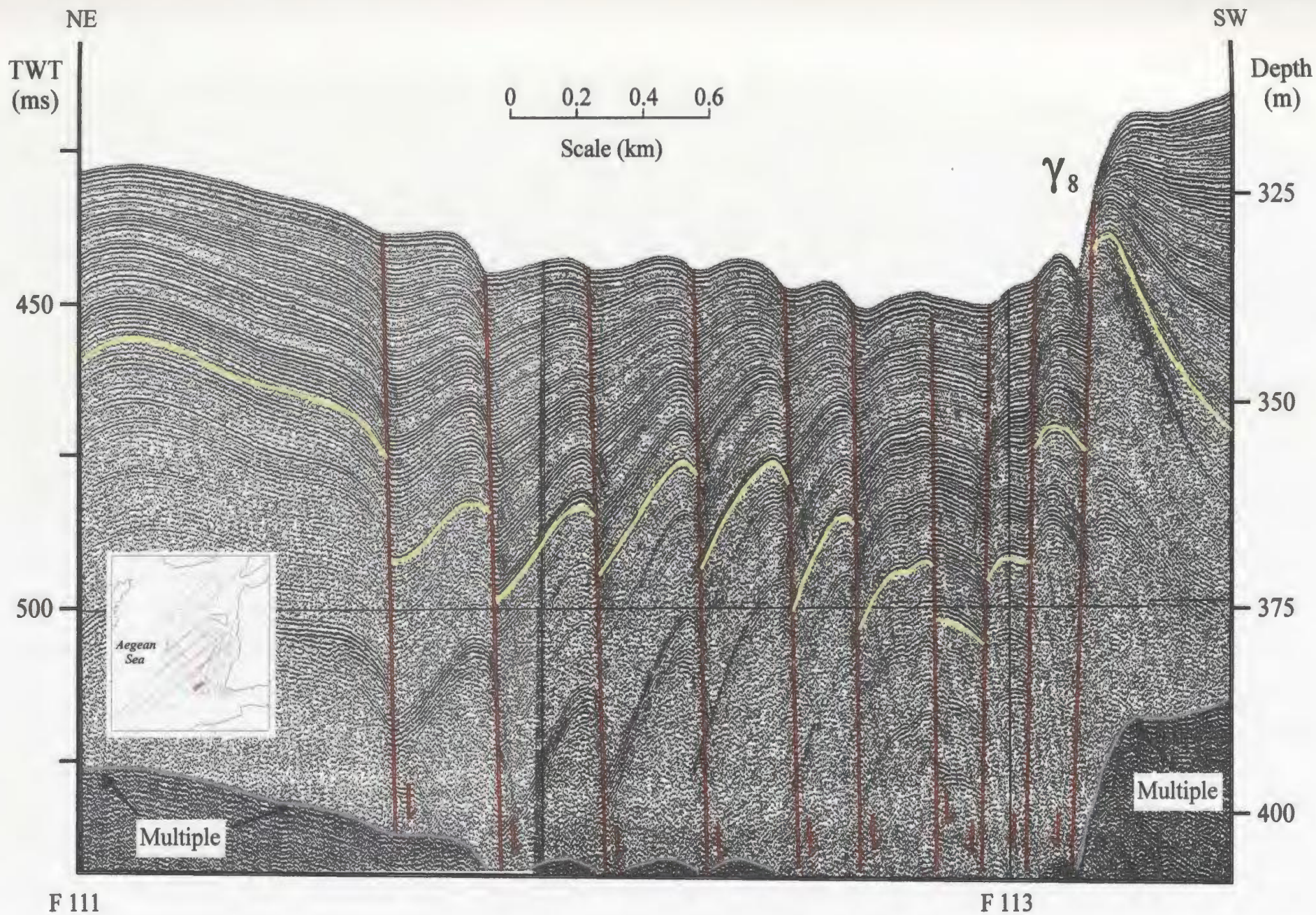
Figure 4.15. Huntec DTS seismic reflection profile showing subvertical normal *en échelon* faults within the first fault cluster.
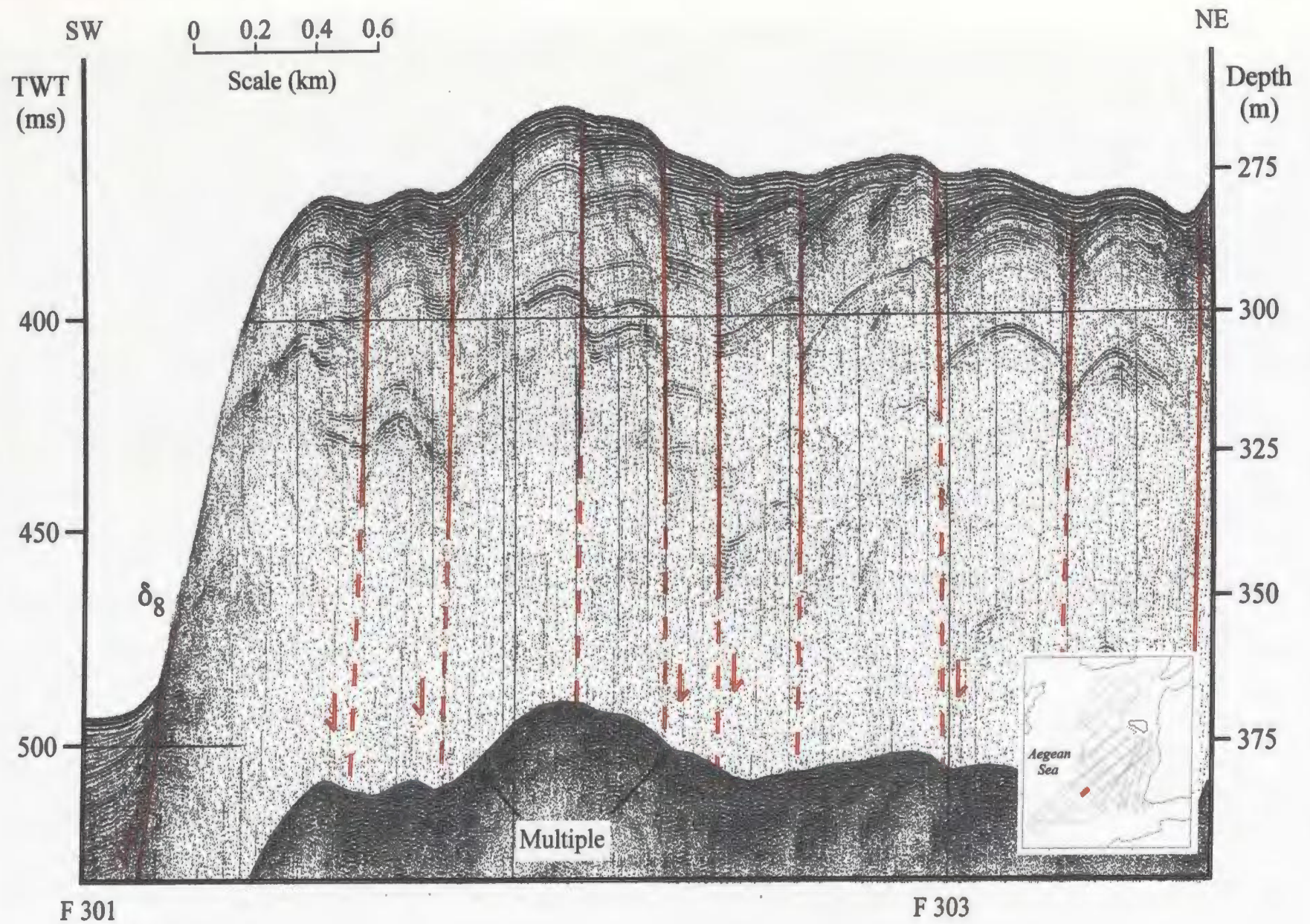
Figure 4.16. Huntec DTS seismic reflection profile showing the subvertical *en échelon* faults of the fault cluster.

sedimentary strata within the upthrown and downthrown fault blocks differs remarkably (Fig. 4.16). For example, the sedimentary strata within one fault block can be relatively undisturbed while those within the adjacent fault blocks are folded and/or tilted. In addition, minor faults within folded fault blocks and local forced folds are also recognized. The trends of the faults cannot be determined because they are not imaged within the nearby northeast–southwest and northwest–southeast-striking seismic lines. Although the faults are not traceable, the directions of the fault trends are constrained by the absence of the faults on the nearby seismic profiles indicating that the only possible direction is northwest–southeast. Thus, it is plausible to suggest that the faults in this cluster trend in an oblique fashion to the faults δ_5 and δ_8, which would be an *en échelon* arrangement.

The third fault cluster is situated within the south central portion of the study area south of the second fault cluster. It is imaged on the seismic line that runs parallel to the prominent fault β_8 (Fig. 4.1). Detailed examination of the footwall and hangingwall cutoffs of the strong reflections to either side of the fault planes shows that this cluster is composed of several subvertical normal and less common reverse faults (Fig. 4.17). The tip lines of the faults lie at the seabed and create steps ranging in height from 20 m to 2 m. The faults have either created horst/graben structures or a step-like morphology on the seabed. Both the hangingwalls and footwalls of these faults are characterized by either folded or strongly tilted sedimentary strata (Fig.4.17). The fault trends cannot be determined due to the distribution of the seismic lines within this part of the survey area (Fig. 4.1).
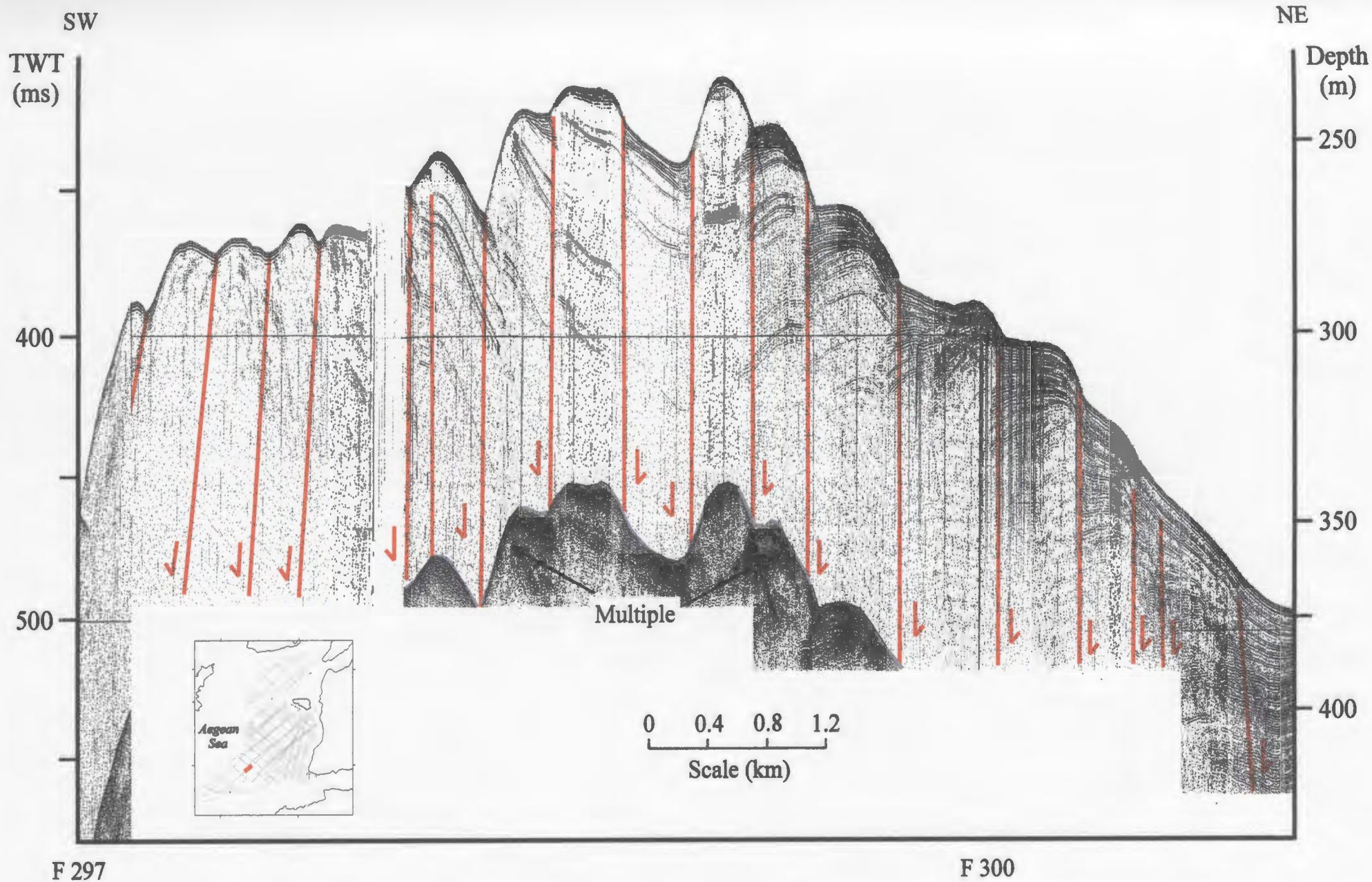
Figure 4.17. Huntec DTS seismic reflection profile showing the subvertical *en échelon* faults of assemblage3.

4.1.3 Highly deformed linear belt

Within the deeper portions of basin B1, near the prominent fault A_1, a distinct narrow zone of concentrated deformation is recognized. The zone is ~20 km long and ~3 km wide and runs parallel to the map trace of fault A_1 (Fig. 4.1). Along the zone, the faults display radical changes on adjacent seismic profiles in terms of intensity, number, sense of slip and fault-plane angle. The tip lines of the faults lie near or at the seabed. Where faults cut the seafloor, they either offset the seabed creating steps of 5–30 m, or create shallow horst and graben structures.

Despite the very dense network of seismic profiles in this region, the correlation of the individual faults between profiles is not always possible. The longest structure that is mapped with confidence is fault γ_2. This fault is ~10 km in length and broadly parallels the map trace of the prominent fault A_1.

In the easternmost part of the zone, five northeast- and southwest-dipping, subvertical and concave-upwards faults with normal sense dip-slip separations are recognized (Fig. 4.6). The dip angles gradually change downsection, where several faults converge, eventually creating a single fault strand. As a whole, this architecture is interpreted as a "negative flower structure". The downward-merging character of the faults is not clearly discernible when traced westward but the slices between faults can be seen to narrow downsection indicating that the faults must converge below the seismic penetration limit. The subvertical extensional faults in this area produce shallow graben structures and intervening horsts (Fig. 4.7). Within the horst block that is uplifted at the seabed, numerous south–southeast-dipping vertical faults have

reverse-sense slips (Fig. 4.7; between γ_2 and A_1). These very narrowly spaced faults result in the chaotic seismic configuration of the reflections. These faults locally change their dip direction and display larger vertical separations.

The central portion of the zone is ~3 km wide and it is composed of five normal and two reverse faults (Fig. 4.10). The tip lines of the faults lie near or at the seabed. Here, the largest extensional fault is labeled as γ_2 and is confidently correlated westward to adjacent seismic profiles. It displays a constant dip direction towards the southwest and offsets the seabed between 55 m and 22 m (Fig. 4.10). Minor extensional faults, situated south of fault γ_2, dip either direction and produce a shallow graben structure. These faults converge downsection, form a single fault strand and collectively produce the architecture of a negative flower structure. The reverse faults dip in a northeast direction toward the prominent fault A_1. The equivalent sedimentary strata within the fault blocks are vertically separated by as much as 13 m. However, these offsets are not reflected on the seabed. The faults display constant dip directions and are correlatable to the adjacent seismic profiles toward the west (Fig. 4.9). The sedimentary strata within the blocks are tilted.

At its western continuation, the zone widens to ~ 4 km (Fig. 4.11). It is composed of ten normal faults displaying subvertical and concave cross-sectional geometries (Fig. 4.11). The faults dip either toward the north–northeast or the south–southwest and cut the sea floor. They create an undulating morphology of the seabed with steps in elevation of 3–55 m. Antithetic pairs form graben structures. Four of these antithetic faults, situated at the western end of the zone, appear to

converge within the deeper section and exhibit an upward-branching cross-sectional geometry which is interpreted as a negative flower structure. The sedimentary strata within the upthrown and downthrown blocks are predominantly tilted.

4.1.4. Evidence for strike-slip movement

Strike-slip deformation occurs where one block moves laterally with respect to an adjacent block (Harding, 1985). One of the prominent features of many strike-slip faults is the occurrence of "en echelon" faults and folds within and adjacent to the principal displacement zone (Christie-Blick and Biddle, 1985). Idealized angular relationships are reproduced in experimental models (Riedel, 1929; Tchalenko, 1970; Tchalenko and Ambraseys, 1970; Wilcox, 1973; Bartlett et al., 1981). Five sets of fractures are commonly observed (Fig. 4.18): (1) synthetic strike-slip faults or Riedel (R) shears; (2) antithetic strike-slip faults or conjugate Riedel (R') shears; (3) secondary synthetic faults or P shears; (4) extension or tension fractures; and (5) faults parallel to the principal displacement zone, or y shears of Bartlett et al. (1981) (Fig. 4.18).

Another decisive feature for the identification of strike-slip faults is the occurrence of flower structures which define narrow, laterally persistent antiforms or synforms which lie within vertical to steeply dipping fault slices, bounded by downward-merging faults with reverse or normal separation, respectively (Harding, 1985; Fig. 4.19).

In addition to these two most reliable features, strike-slip fault zones exhibit
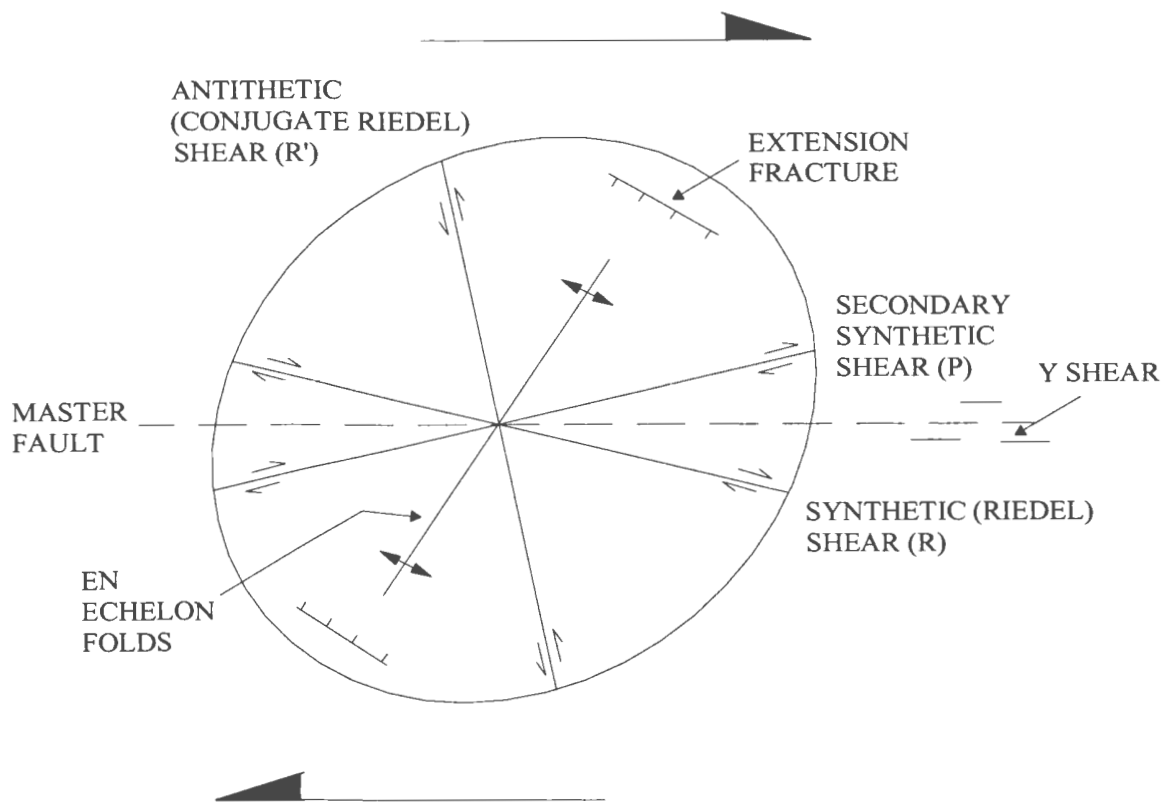
Figure 4.18. The angular relations between structures that tend to form in right-lateral simple shear under ideal conditions (Wilcox et al., 1973).

Negative Flower Structure
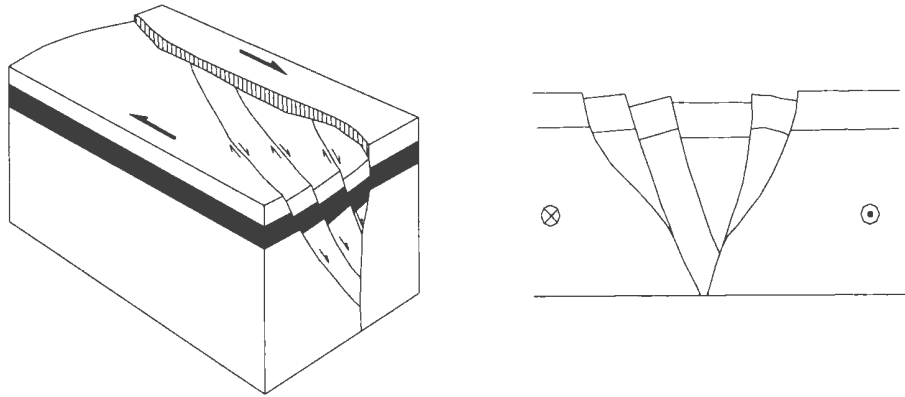
Positive Flower Structure
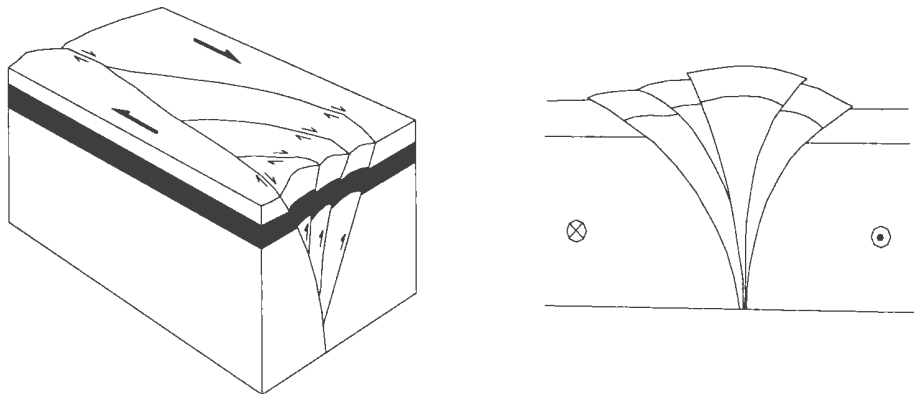
Figure 4.19. Schematic block diagrams and cross-sections showing the geometry of negative and positive flower structures.

several characteristics, such as: (1) the presence, in a given profile across the principal displacement zone, of both normal- and reverse-separation faults, (2) juxtaposed dissimilar sedimentary thickness, facies, or stratigraphic successions in which the dissimilarities do not appear to be a product of simple low-side growth or dip-slip displacements (Harding, 1990), (3) the tendency in successive profiles for a given fault to dip alternately in one direction and then in the opposite direction (Christie-Blick and Biddle, 1985), (4) incomplete fold segments, juxtaposed across a high-angle master fault, that are incompatible with conventional fold geometries (Harding, 1990).

The similarity of the mapped pattern of structural trends within the study area (Fig. 4.1) to fault arrangements predicted from a shear strain ellipse (Fig. 4.18) would have provided strong evidence for strike-slip tectonism. However, natural geological examples tend to be more complicated than experiments and it should not be surprising if the orientation and geometry of the observed structures do not necessarily conform to those predicted by idealized strain-ellipse summaries (Wilcox et al., 1973; Bartlett et al., 1981; Richard, 1991). This is because the deforming rocks and sedimentary cover are seldom homogeneous, because structures develop sequentially rather than instantaneously, and because early-formed structures tend to be rotated during protracted deformation (Christie-Blick and Biddle, 1985). Moreover, the idealized arrangement and the development of structures predicted by experimental models are created under pure shear stress whereas most "strike-slip" faults accommodate oblique displacements along some segments or during part of the

time they are active; and most are associated with an assemblage of related structures including both normal and reverse faults (Christie-Blick and Biddle, 1985). As a result, the character of the strike-slip fault (divergent or convergent) and the ratio of strike-slip to dip-slip movements plays a crucial role in controlling the development and trends of the structures. For example, the reason for the abundant occurrence of normal faults and lesser development of reverse faults and associated folds throughout the study area is most likely the divergent character of strike-slip tectonism. The idealized *en échelon* arrangement of faults is directly related by the ratio of strike-slip to dip-slip movements: the faults tend to be straighter and longer initially and become more and more *en échelon* with an increasing strike-slip component (Richard et al., 1995).

Many aspects of the cross-sectional structural patterns identified within the study area are characteristic of strike-slip deformation. The observed cross-sectional features commonly considered evidence of strike-slip faulting include the following: (1) a steeply dipping solitary master fault that displaces all the observed sedimentary cover and exhibits a through-going, curvilinear map trace (A_1 and β_8; Fig. 4.1); (2) upward splaying subvertical faults defining negative flower structures (Figs. 4.6, 4.8); (3) zones of intense deformation isolated between comparatively undeformed areas; (4) simultaneous development of both extensional and contractional structures in individual transverse profiles within the same local area (e.g., reverse faults adjacent to normal-slip faults and negative flower structure; Figs. 4.6, 4.8); (5) *en échelon* arrangement of the faults (Figs. 4.15-17); (6) along-strike changes in the dip direction

of the faults (Figs. 4.7, 4.8); (7) juxtaposed sedimentary thickness contrasts of the same depositional sequences in the hangingwalls and footwalls of the faults (Figs. 4.2, 4.3).

The absence of some diagnostic criteria for the recognition of strike-slip faults might weaken the case for strike-slip tectonism. However, considering the arrangements of faults and the structural interactions between faults and fault blocks, it is difficult to reconcile the observed structures with any style of deformation other than strike-slip faulting.

4.2. Shelf group faults

The shelf group faults are composed of several west–northwest-trending, northeast- and southwest-dipping planar faults (Fig. 4.1). In seismic reflection profiles, they display moderate- to high-angle dips ranging between 50° and 60°. In this group, most of the major faults have tip lines lying immediately below unconformity α (Fig. 4.20) while the others terminate against the upper boundary of the lowermost depositional sequence seen in Figure 4.20. The shelf group faults are overprinted on, and obliquely transect the broadly northeast-trending basins and ridges (Fig. 4.1).

Detailed examination along the fault planes clearly shows that the footwall and hangingwall cutoffs of marker reflectors and shelf-crossing unconformities are both vertically and horizontally displaced, implying an extensional and/or transtensional mechanism for these faults. Vertical offsets range from <1 to ~10 m.
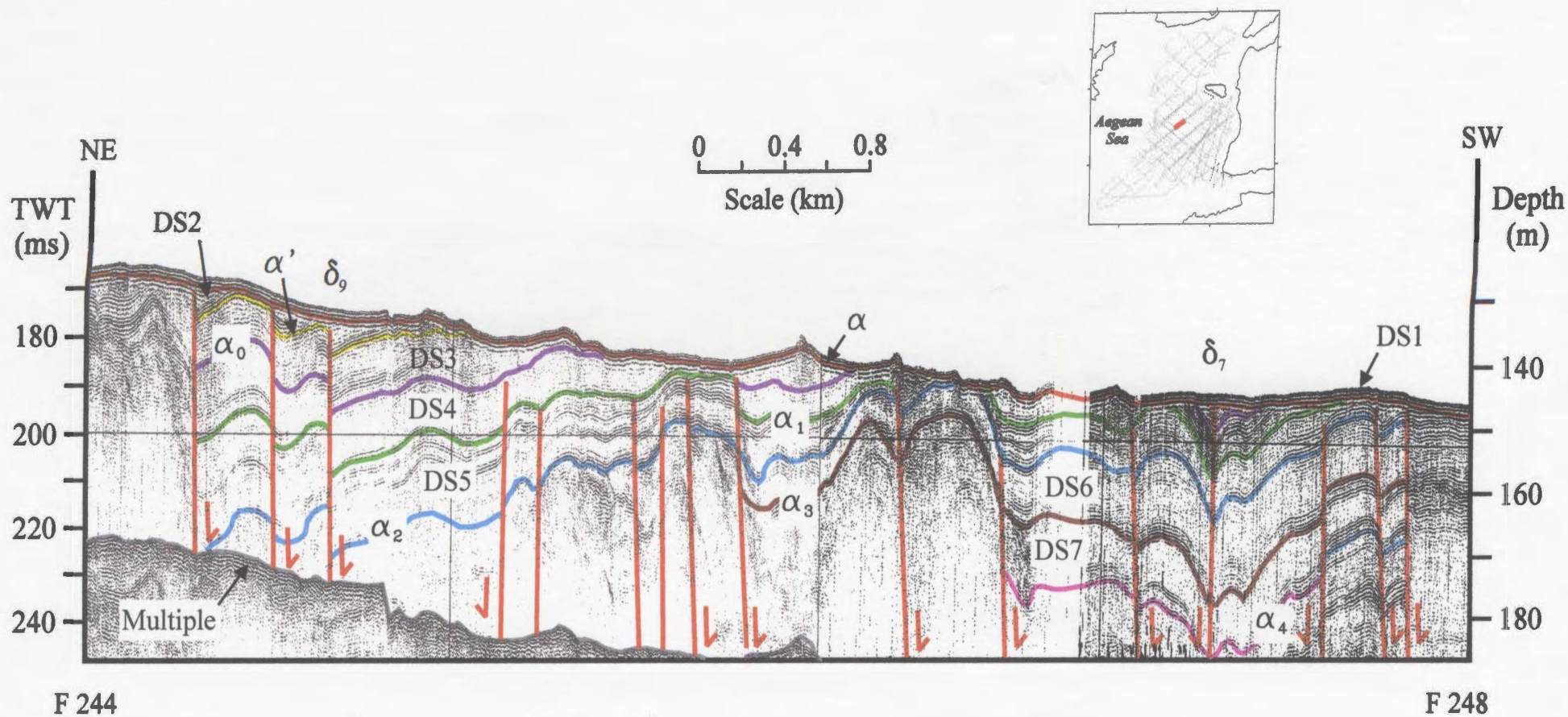
Figure 4.20. Seismic reflection profile from the northern portion of the study area showing the faults of the shelf group and their tip-point positions.

A dense grid of seismic reflection profiles allows reliable correlations of the major faults in adjacent seismic profiles. However, in shallow portions of the study area, the highly corrugated internal architecture of the basement and the elevated position of the first multiple make it difficult to carry the correlations across the study area. For minor faults situated within the basement, correlations cannot be performed due to the high complexity of the basement.

Along the fault planes, the footwall and hangingwall cutoffs of marker reflectors do not show any increase in the amounts of vertical separation downsection, implying that the faulting entirely postdated deposition.

CHAPTER 5

5. Chronology and correlations with global sea-level curves

5.1. Sea-level variations

Following the pioneer work of Emiliani and Epstein (1953) and Emiliani (1955a, 1966), variations in oxygen-isotopic composition of marine organisms from deep-sea sediments are widely used as a proxy for Quaternary global sea-level variations (Imbrie et al., 1984, Chappell and Shackleton, 1986, Shackleton, 1987, Skene et al., 1988). Experimental studies demonstrate that the fixation of oxygen isotopes in biogenic carbonate is controlled by (i) the oxygen-isotopic composition of the seawater in which the organism lives, (ii) the average seawater temperature in which shell or test secretion takes place, and (iii) the species-dependent fractionation of the oxygen isotopes, known as the vital effect (Urey 1947; McCrea, 1950; Epstein et al., 1951, 1953). As a consequence, the variations in the oxygen-isotope ratio contained in calcium-carbonate tests of foraminifera are closely linked to the volume of glacial ice stored on the continents and the ocean water temperature in which test secretion took place (Chappell and Shackleton, 1986). Benthic foraminiferal assemblage data clearly show that the water temperature in deep ocean basins remained remarkably constant throughout the Quaternary (e.g., Shackleton, 1987). Thus, oxygen-isotopic data from benthic foraminifera are best suited for the determination of global ice-volume variations,

because the potential contribution from temperature-dependent fractionation to the $\delta^{18}O$ signal can be considered constant. Benthic foraminifera exhibit large species-dependent oxygen isotopic fractionation (Duplessy et al., 1970). This can be eliminated by using a single species of benthic foraminifera throughout a core (e.g., *Uvigerina* spp.; Shackleton, 1987). When this is done, the variations in the oxygen-isotopic composition of benthic foraminifera provide a good proxy for variations in global bottom-water salinities. Because it is generally accepted that the mixing time of the oceans is $\sim$ 1500 years, a strong positive correlation exists between changing ice volume, the $\delta^{18}O$ composition, and the salinity of average ocean water. First-order salinity variations in Quaternary oceans are controlled by the amount of ice stored in polar regions. The $\delta^{18}O$ record in foraminiferal carbonate shells can be used to approximate variations in continental ice volume and, accordingly, glacio-eustatic sea-level changes.

Coral reefs are sensitive recorders of past sea-level changes (Camoin et al., 2001). Their accurate dating using the ^{14}C and $^{230}Th/^{234}U$ methods is of prime importance for the determination of the timing of deglaciation events and the driving mechanisms for glacial-interglacial cycles. During a glacio-eustatic rise of sea level (e.g., onset of an interglacial period far away from regions which experienced ice loading), reefs build upward and seaward over their own forereef sediments. The most expanded reef crests coincide approximately with the peaks of each transgression (Bloom et al., 1974; Chappell and Shackleton, 1986). The age of each section of a reef can be determined using ^{14}C and $^{230}Th/^{234}U$ methods; thus, sea-level changes relative to the stable ocean floor

can be calculated if the local rate of emergence or subsidence is known (Chappell and Shackleton, 1986). The most useful records of past sea-level changes have come from coral reef terraces exposed on the Huon Peninsula, New Guinea (Broecker et al., 1968; Chappell, 1974; Bloom et al., 1974; Chappell and Veeh, 1978; Chappell and Shackleton, 1986; Stein et al., 1993; Chappell et al., 1996), Barbados (Mesolella et al., 1969; Bard et al., 1990; Gallup et al., 1994), Haiti (Dodge et al., 1983) and Sumba (Pirazzoli et al., 1993; Bard et al., 1996b). The timing and amplitude of the sea-level curves obtained from raised marine terraces and their coral reefs are generally in good agreement with those inferred from oxygen-isotope stratigraphy of deep-sea cores (Camoin et al., 2001).

During the glacial-interglacial cycles of the Quaternary, the Mediterranean Sea must have oscillated in synchroneity with the Atlantic Ocean, because the depth of the Strait of Gibraltar (~300 m) always remained below the minimum Quaternary lowstands of sea level. The oxygen isotopic data from several western and eastern Mediterranean Sea cores have revealed $\delta^{18}O$ records similar to those obtained in cores from the Caribbean and the equatorial Pacific (Emiliani, 1966 ; Broecker and van Donk, 1970; Shackleton and Opdyke, 1976; Cita et al., 1977). Aksu et al. (1995a) suggested that the level of the Aegean Sea also oscillated in synchroneity with the Mediterranean Sea. During the peak of glacial maxima (e.g., glacial isotopic stage 2) the level of the Aegean Sea dropped to ~ −120 m, when continental shelves and many shallow banks were subaerially exposed, and several islands became connected forming arcuate land bridges (Fig. 5.1). For example, during the last glacial maximum, the Cyclades Plateau, including
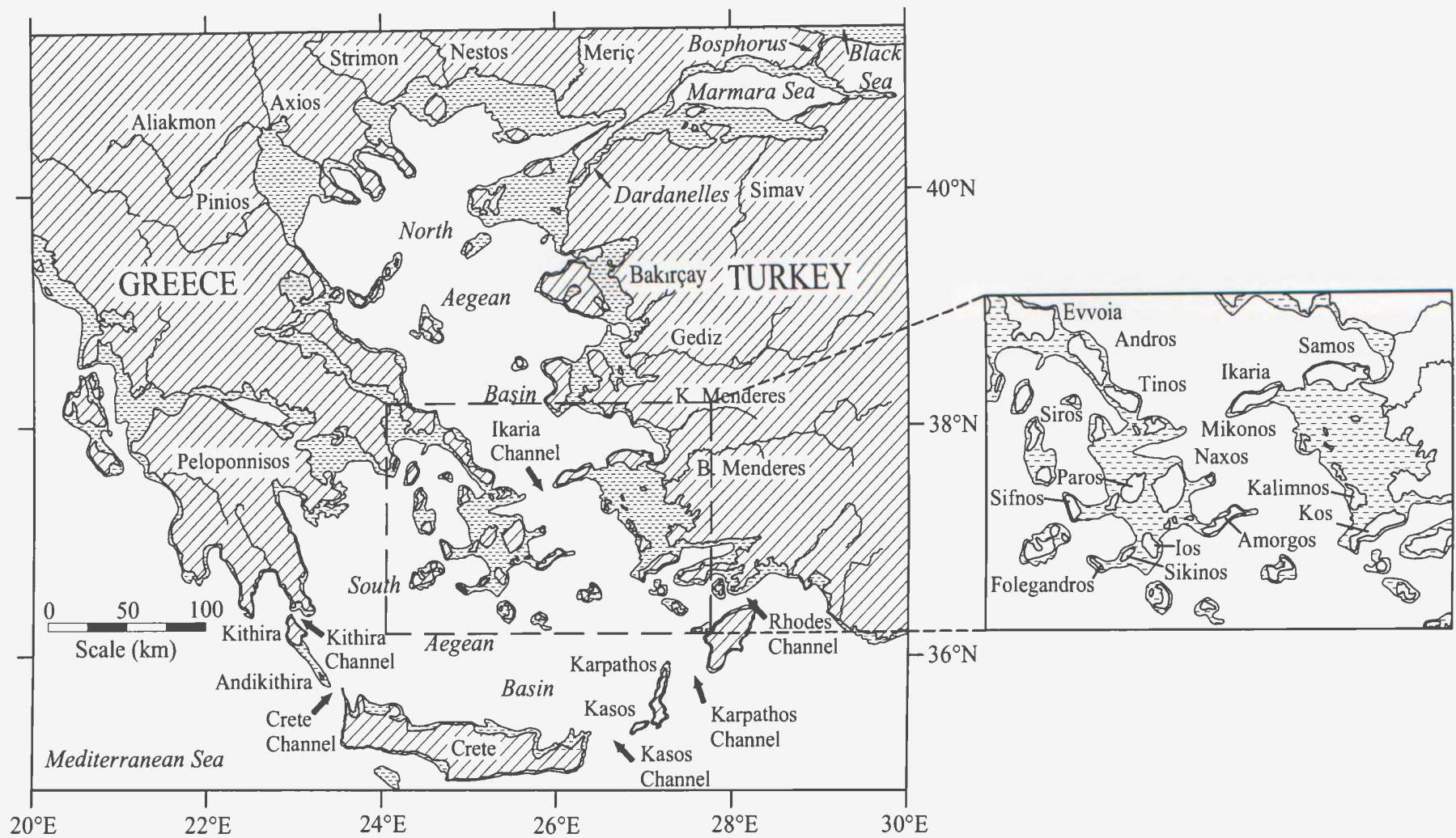
Figure 5.1. Map showing the position of the shoreline in the Aegean Sea during the last glacial maximum when the sea level stood ~ 120 m below present level (dashed hachure). Also shown is the present-day coastline and major rivers draining into the Aegean Sea.

the Islands of Andros, Mikonos, Siros, Naxos, Paros, Amorgos, Ios, Sikinos, Folegandros

and Sifnos, became exposed and extended northwest to join Evvoia Island, forming a

broadly southeast-trending land mass (Fig. 5.1). Farther to the east, the broad continental

shelf between the Islands of Ikaria and Samos in the north and the Islands of Kalimnos

and Kos in the south also became exposed, leaving the narrow and shallow Ikaria

Channel as the only link between the northern and southern Aegean basins (Fig. 5.1).

Another bridge developed in the southern Aegean Sea when the shallow bank between

the Islands of Kithira and Andikithira became exposed leaving two narrow channels

between the Peloponnisos and the Island of Crete: the Kithira and Crete channels (Fig.

5.1). To the east, the bank between the Islands of Karpathos and Kasos became exposed,

limiting the watermass exchange between the southern Aegean Sea and the

Mediterranean Sea east of Crete to the Kasos, Karpathos and Rhodes Channels.

The Quaternary stratigraphic architecture of a shelf situated seaward of a major

river is controlled by the accommodation space created by subsidence and the ability of

the sediment carried by the river to fill this space. In a sufficiently rapidly subsiding shelf

environment, the stratigraphy will be characterized by a number of vertically stacked

prograded depositional sequences (Fig. 5.2a). In this scenario, seaward-prograded

depositional sequences would develop during periods of relative sea-level lowering

associated with transitions from interglacial to glacial stages, whereas shelf-crossing

unconformities would develop by the process of ravinement (shoreface erosion; swift,

1968) during periods of sea-level rises, associated with the transition from glacial to
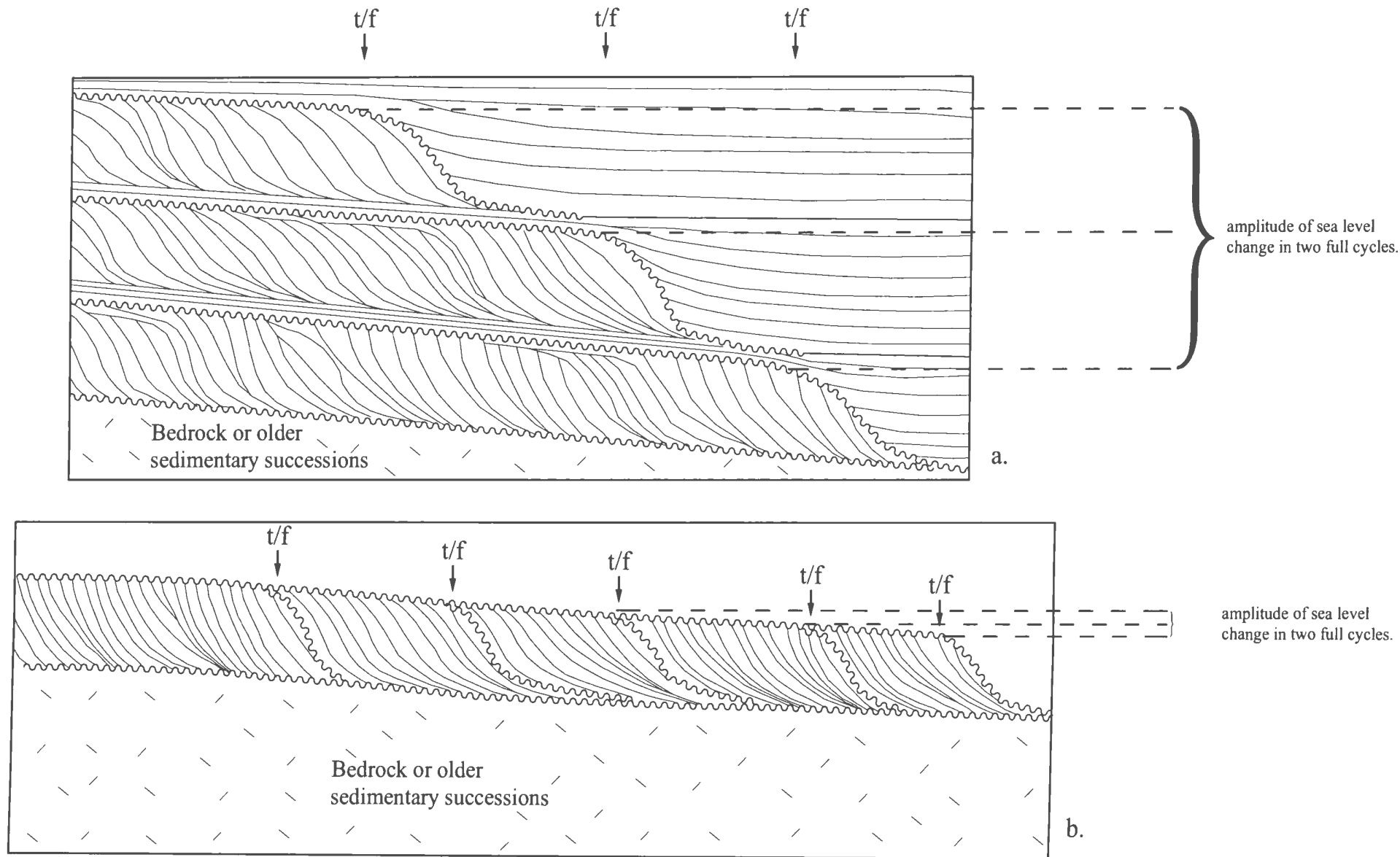
Figure 5.2. Schematic cross-sections showing stratigraphic architecture of a subsiding (a) and stable (b) shelf environment off the mouth of a major river. t/f = topset-to-foreset transition. Wavy lines are unconformities.

interglacial periods. During the peak of an interglacial period, the entire shelf would be below sea level and would receive predominantly hemiplegic sediments or distal terrigenous muds, creating a parallel-bedded seismic architecture (Fig. 5.2a). In the regions very proximal to a river, this seismic unit would pass landward into the prograding deltaic succession. Thus, the parallel bedded seismic unit must also include the variable, but seaward thinning bottomset beds of the delta. As the delta begins its rapid seaward progradation associated with the sea-level lowering during a transition into a glacial period, the delta progrades over the parallel-bedded unit, including its bottomset beds. In such an environment, the seaward extent of the deltaic progradation will depend on the rate of creation of accommodation space, the rate of sediment supply and the rate and amplitude of the eustatic sea-level fall. The depth of the topset–foreset transition depends on local hydrography. Hence, the topset–foreset transition in a depositional sequence can be used to track the position of the sea level during the deposition of the delta, once corrected for the depth of water over the topset–foreset transition during active delta growth. This depth is known for modern deltas in the Aegean Sea (~15 m) and this depth is used as a guide in the thesis, based on the assumption that the intensity of waves and currents has not varied significantly through the late Quaternary. At its maximum seaward extent, the topset–foreset transition would record the position of sea level during the last phase of delta progradation, prior to the subsequent sea-level rise, after correction for any later subsidence or uplift.

In a shelf environment where there is no subsidence, the stratigraphic architecture

will be characterized by a number of laterally shingled seaward-prograded depositional sequences which were deposited during consecutive phases of sea-level lowering during the transitions from interglacial to glacial stages (Figs. 5.2b). Assuming that the sea-level falls were of similar magnitude, the depositional sequences would be deposited on nearly the same datum. This type of deposition would result in seaward progradation of the shelf edge. The seaward-prograded depositional sequences would be separated by shelf-crossing unconformities that developed as ravinement surfaces during successive sea-level rises associated with the transitions from glacial to interglacial stages. During the periods of sea-level highstand, low-energy conditions would prevail and the whole shelf area would receive predominantly hemiplegic sediments or fine-grained terrigenous muds, creating parallel-bedded seismic units. However, during the successive fall and lowstand phases of sea level, the entire shelf would be subaerially exposed and would be subjected to intense erosion. Accordingly, the parallel-bedded seismic sequence and the uppermost segment of the seaward-prograded depositional sequence would be truncated, which, in turn, would result in a characteristic oblique-prograded internal seismic configuration (Fig. 5.2b). The position of the topset–foreset transitions would show the amount of maximum seaward progradation of a depositional sequence in one cycle and the changes in the rate of sediment input during deposition.

5.2. Chronology

The chronology of the depositional sequences observed in the study area is

constrained by seven radiocarbon and two U/Th dates on *in situ* shell samples extracted from five cores which were collected from critical sites throughout the study area (Table 5.1). Core locations were selected using a dense grid of high-resolution seismic reflection profiles with the specific aim to sample as many depositional sequences as possible (i.e., Figs. 5.3–5.9). Therefore, many core sites are in areas where several depositional sequences are either absent or very thin (Figs. 5.6, 5.8, 5.9).

Core MAR98-16 was collected in the northeastern part of the study area with the aim to sample the thin veneer of depositional sequence 1 (Figs. 5.3, 5.4). It recovered only 30 cm of sediments, and bottomed ~ 87 cm above the unconformity α (Fig. 5.4). The age of the depositional sequence 1 is constrained by an *in situ Turritella* spp. shell, which was extracted from a subbottom depth of 23 cm. Correlations with the available seismic data suggest that the *Turritella* shell is situated within the upper portion of the depositional sequence. The radiocarbon age of 9630±70 yr BP (Table 5.1) suggests that depositional sequence 1 is of Holocene age. Because in this region depositional sequences exhibits large thickness variations (e.g., Fig. 5.4), no attempt is made to estimate the age of unconformity α by extrapolation.

The age of depositional sequence 2 is constrained by two radiocarbon ages obtained on shell fragments from core MAR02-113P (Table 5.1; Figs. 5.3, 5.5). The core penetrated depositional sequences 1 and 2 and the intervening unconformity α, which is picked at a depth of 370 cm (Fig. 5.5). There is no physical evidence for a discontinuity at this level, so α might be a correlative conformity at this core site. *Pecten* sp. fragments

Core code	Coordinates	Water depth (m)	Sample	Subbottom depth (cm)	Laboratory Number	Sample Weight	Age
MAR98-16	39° 40 760' N 25° 44 191' E	−126	*Turritella* spp.	23	TO-7793	160 mgr	9,630±70 yr BP
MAR02-113	39° 24 184' N 26° 04 121' E	−298	*Pecten* sp fragments	400	TO-11151	137 mgr	16,930±140 yr BP
MAR02-113	39° 24 184' N 26° 04 121' E	−298	echinoderm fragments; worm tubes	672	TO-11152	439 mgr	26,100±250 yr BP
MAR02-114	39° 32 401' N 25° 55 005' E	−189	fragment of algal bioherm; worm tubes	283	TO-11153	494 mgr	42,490±1020 yr BP
MAR02-114	39° 32 401' N 25° 55 005' E	−189	*Trisidos* sp.	431	TO-11154	320 mgr	42,990±1160 yr BP
MAR02-138	39° 31 312' N 25° 58 000' E	−147	fragment of algal bioherm	45	TO-11155	408 mgr	35,960±560 yr BP
MAR02-138	39° 31 312' N 25° 58 000' E	−147	fragment of algal bioherm	297	TO-11156	497 mgr	43,810±930 yr BP
MAR03-48	39° 28 351' N 25° 51 723' E	−311	Ostrea sp.	44	UQAM	4.4322 gr	118,927 cal yr BP (+6,193/-5,852)
MAR03-49	39° 28 102' N 25° 51 436' E	−321	Ostrea sp.	270	UQAM	3.2369 gr	133,218 cal yr BP (+7,318/-6,814)

Table 5.1. Table showing the details of the cores and the samples. UQAM = U/Th date from Université du Québec à Montréal. TO = ^{14}C Isotrace Laboratories, University of Toronto, presented as uncalibrated .
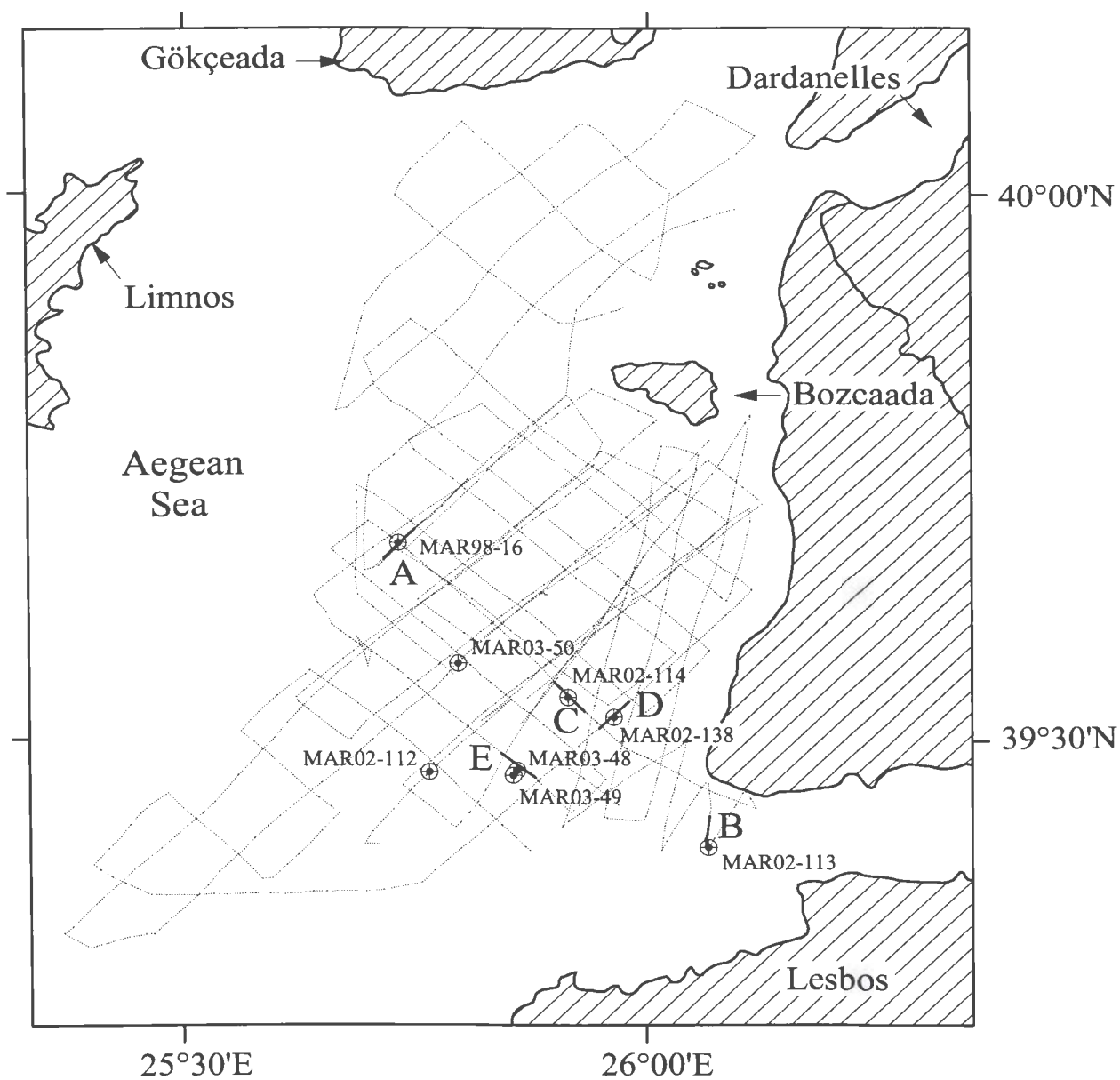
Figure 5.3. Figure showing the core locations in the study area. See Table 5.1 for coordinates and water depths. A, B, C, D, E are seismic reflection profiles illustrated in Figures 5.4-5.9.
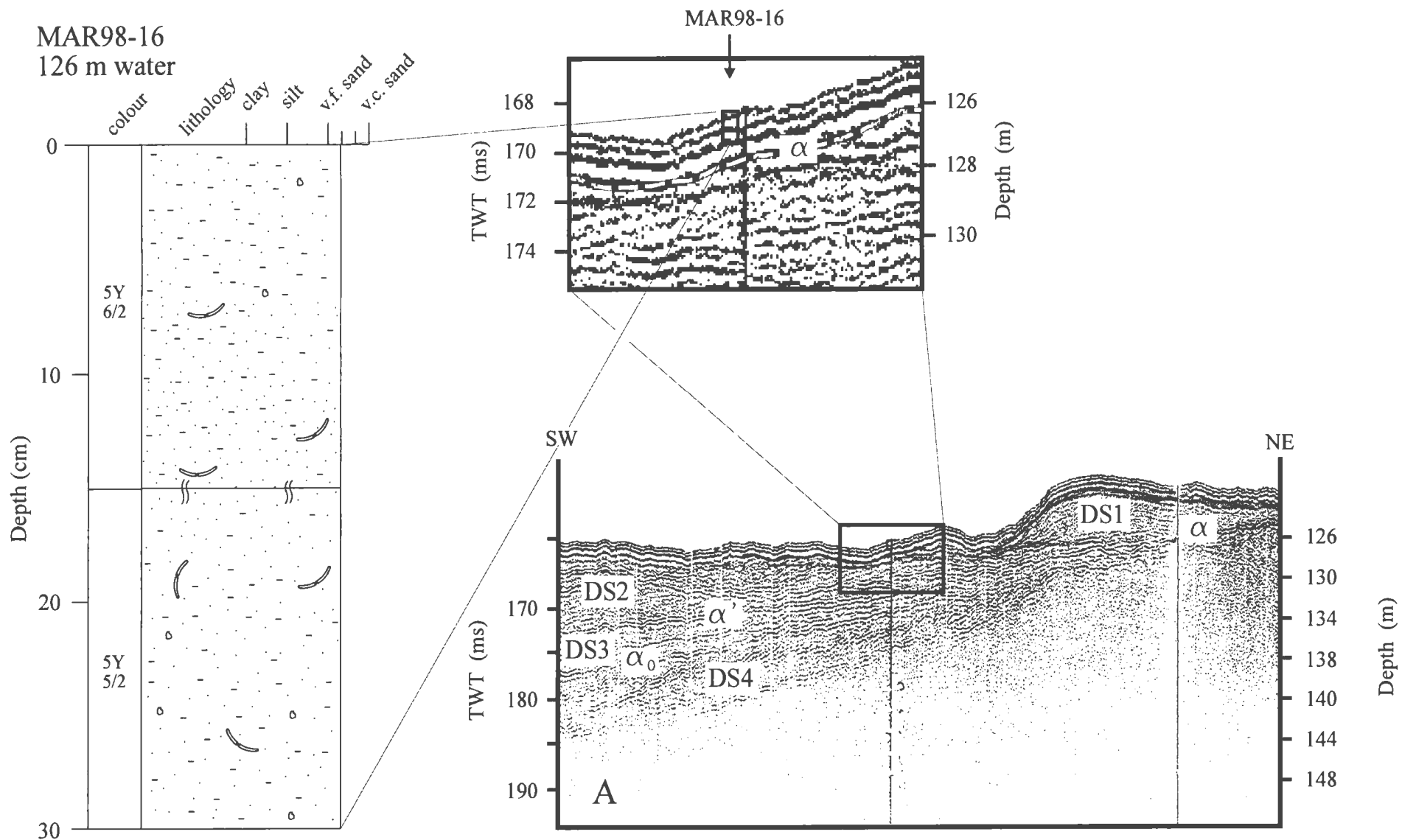
Figure 5.4. Huntec DTS profile showing the position of core MAR98-16. Also shown is the lithostratigraphic column of core MAR98-16. See Figure 5.2 for location. Colour designations are from Geological Society of America Rock Colour Chart.
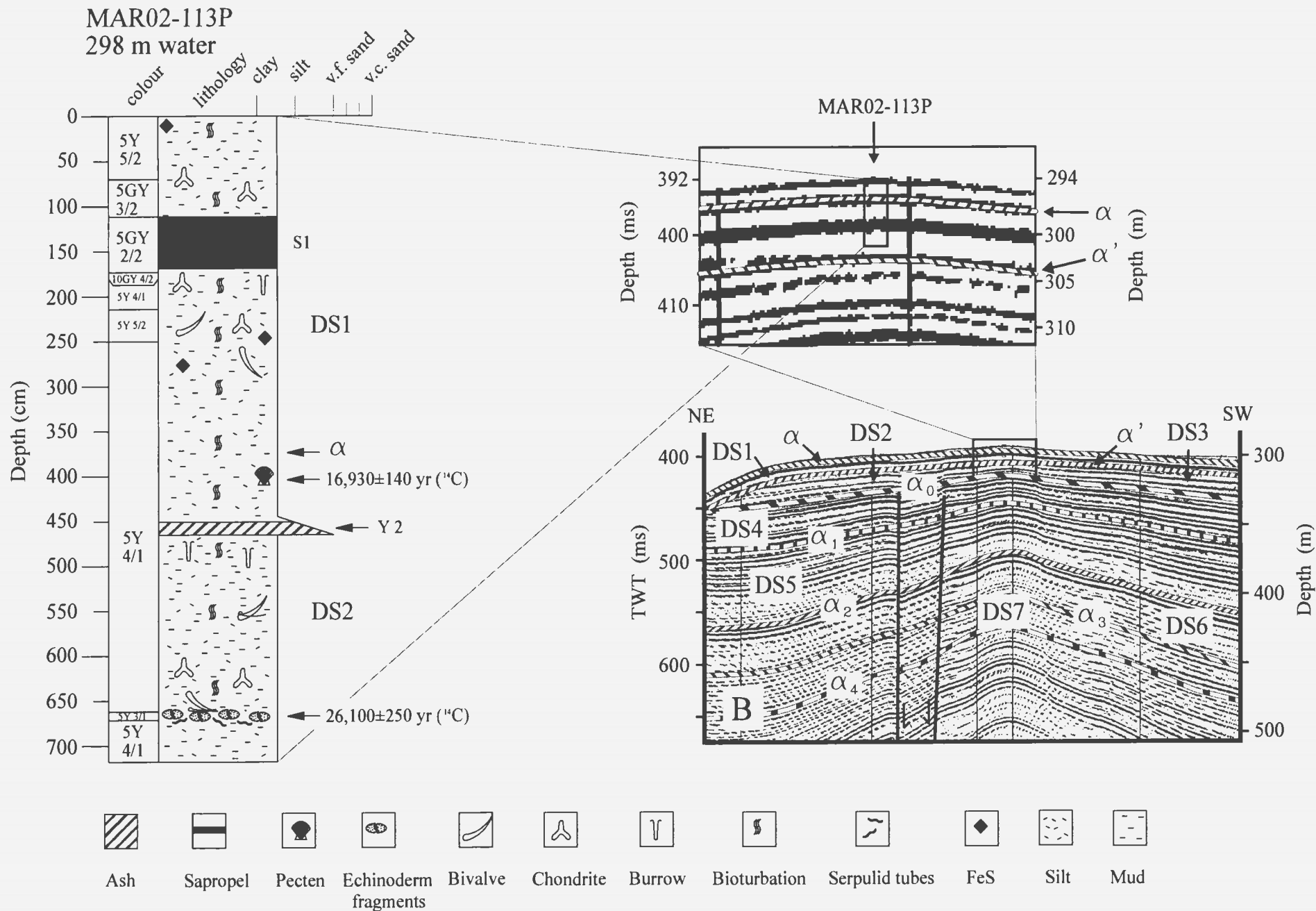
Figure 5.5. Sleevegun seismic reflection profile B showing the location of core MAR02-113P, the correlative conformities and the detailed lithostratigraphic column of the core. See Figure 5.2 for location. Colour designations are from Geological Society of America Colour Rock Chart.
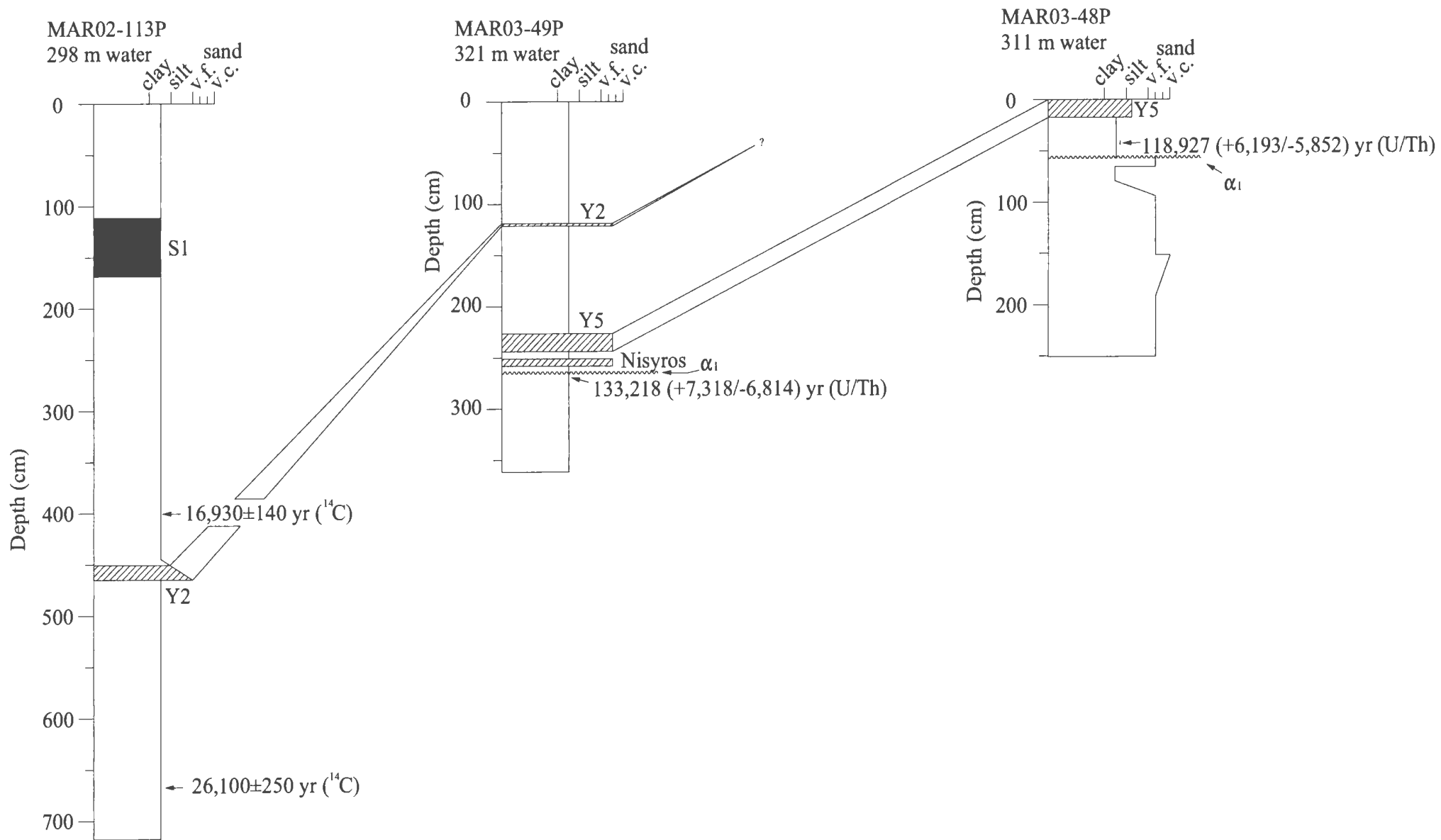
Figure 5.6. Simplified core logs showing the stratigraphic positions of the sapropelic layer, dated shell fragments and the correlations between the identified tephra layers.

Figure 5.7. SiO$_2$ vs. Al$_2$O$_3$ diagram showing the three distinct clusters of the analyzed samples.
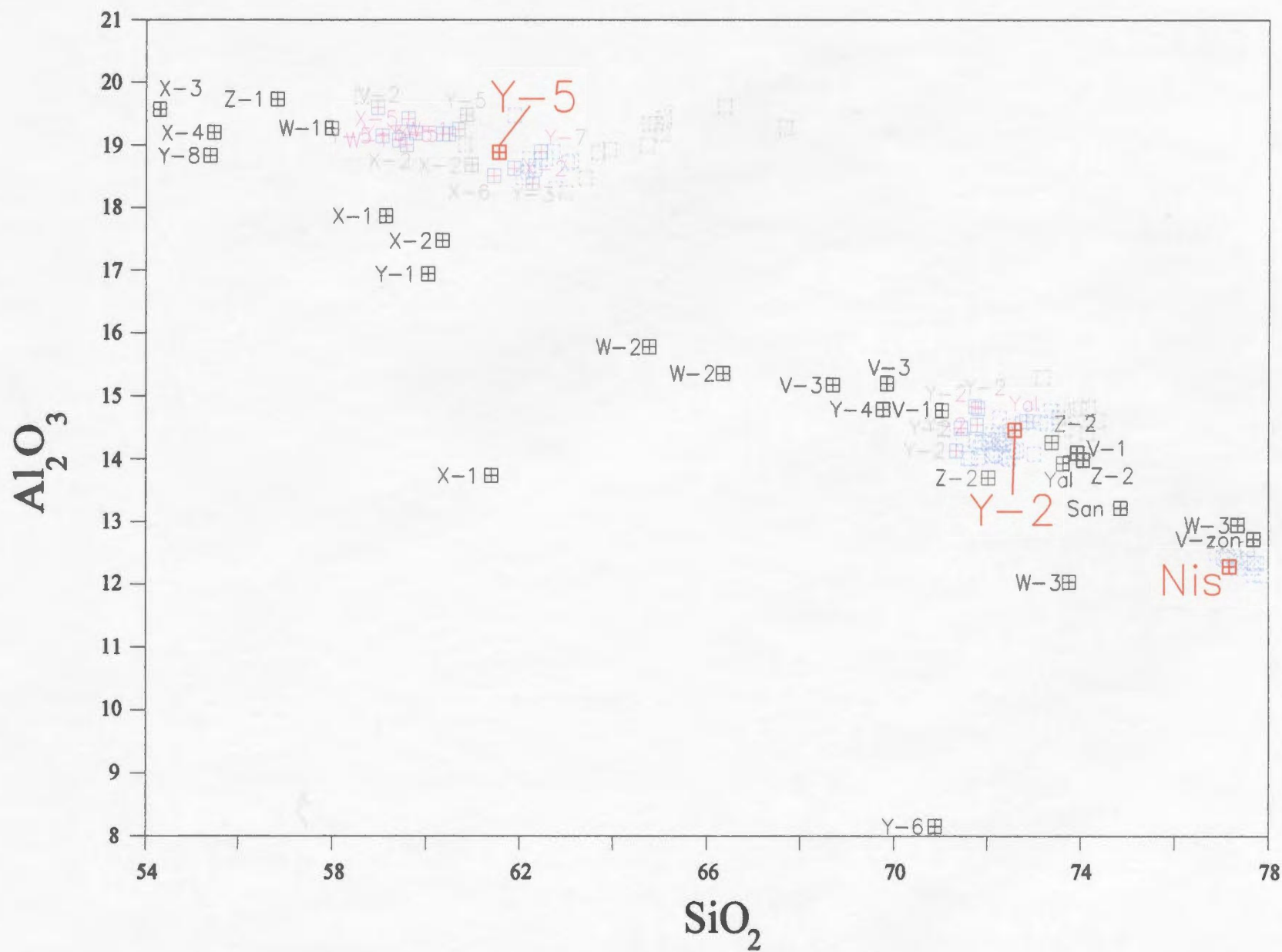
Figure 5.8. The comparison of the potential sources and the analyzed samples which shows the most likely source for each cluster.

Figure 5.9. Slevegun seismic reflection profile showing the location of core MAR02-114P. Also shown is the detailed lithostratigraphic column of core MAR02-114P. See Figure 5.2 for location. Colour designations are from Geological Society of America Rock Colour Chart.

extracted from a subbottom depth of 400 cm subbottom gave a ^{14}C date of 16,930±140 yr

BP, while echinoderm fragments and worm tubes extracted from 672 cm subbottom gave

an age of 26,100±250 yrBP (Table 5.1). The vertical distance between these two dated

intervals is 272 cm and the age difference is 9,170 years, which yields a sedimentation

rate of ~30 cm kyr^{-1} depositional sequence 2 below α. A radiocarbon date of 9630 yr BP

on an *in situ Turritella* spp. shell in core MAR98-16 (Table 5.1) constrains the age of

depositional sequence 1 as Holocene (Fig. 5.4). The age of depositional sequence 2 is

constrained by two radiocarbon ages for shell fragments from core MAR02-113P (Fig.

5.5; Table 5.1). *Pecten* spp. fragments from 400 cm depth give an age of 16,930 yr BP,

while echinoderm fragments and worm tubes from 672 cm depth give an age of 26,100

yrBP (Fig. 5.5; Table 5.1). The vertical distance between these two dated intervals is 272

cm and the age difference is 9,170 years, which yields a sedimentation rate of ~30 cm kyr^{-1}

$^{-1}$ for depositional sequence 2 below α. Extrapolation upward to 370 cm depth provides an

estimate of 16,033 yrBP for α. A check on this age is provided by the presence of

sapropel S1 from 112-173 cm depth in core MAR02-113P. The base of S1 is dated as

9,600 yrBP elsewhere in the Aegean Sea (Aksu et al., 1995 a,b). The depth difference

between the base of sapropel S1 and α is 197 cm. The muds in this interval are

lithologically similar to those seen in depositional sequence 2, thus are provisionally

assumed to share a 30 cm kyr^{-1} sedimentation rate. Using this rate, 197 cm represent

6570 yr of deposition, and α can be estimated to have an age of 9600 + 6570= 16170

yrBP. This is little different from the estimate obtained using radiocarbon dates in

depositional sequence 2 (below α), and confirms a date of ~16,000 yrBP for the correlative conformity to the sequence boundary unconformity. This independent check also validates the use of an accumulation rate of ~30 cm kyr^{-1} for the muds of the lower subunits of the Aegean Sea depositional sequences.

Tephra layers in marine sediments are important stratigraphic markers which can be used for dating and correlating sedimentary sequences (Wulf et al., 2002). Five tephra layers were recognized in cores MAR02-113P, MAR03-48P and MAR03-49P during optical observations on washed and sieved samples (Fig. 5.6). Glass shards were collected from these tephra layers and mounted on an epoxy resin. Major and minor elemental composition of the shards are determined using a Cameca SX50 electron microprobe. Because sodium and to a lesser extent potassium is known to be lost in volcanic glass during electron microprobe analysis, Na was counted first, and the beam was defocussed to ~10μm in diameter to reduce the alkali loss. The results are given in Table 5.2. The comparison of the chemical ratios of the analyzed samples contributes in recognizing any possible relation between the samples. The SiO_2 versus Al_2O_3 diagram defines three distinct clusters. Each cluster has a very narrow compositional range so is interpreted to have originated from the same source (Figs. 5.7). This classification allows us to make reliable correlations between cores MAR02-113P, MAR03-48P and MAR03-49P (Figs. 5.6, 5.7). Furthermore, the origins of these tephra layers can be determined by taking into account their stratigraphic positions within the cores and comparisons with potential sources. Figure 5.8 shows that the most likely sources that match the

				Normalized oxides										
n	Stub	Sample	Na_2O	MgO	Al_2O_3	SiO2	P_2O_5	K_2O	CaO	TiO_2	Cr_2O_3	MnO	FeO	TOT
1	N10-1	M02-113-463 cm	3.25	0.46	14.77	73.62	0.00	2.55	1.81	0.42	0.00	0.09	3.03	100.00
2	N10-2	M02-113-463 cm	3.48	0.42	15.30	73.17	0.00	2.16	1.75	0.46	0.01	0.08	3.18	100.00
3	N10-3	M02-113-463 cm	3.15	0.44	14.48	73.66	0.08	2.76	1.77	0.42	0.00	0.11	3.13	100.00
4	N10-4	M02-113-463 cm	3.26	0.43	14.61	73.14	0.08	2.49	1.82	0.48	0.02	0.09	3.59	100.00
5	3	M02-113-463 cm	4.64	0.48	14.32	72.05	0.08	2.88	1.80	0.47	0.00	0.04	3.26	100.00
6	3	M02-113-463 cm	4.97	0.44	14.02	71.63	0.11	2.95	1.88	0.44	0.00	0.14	3.42	100.00
7	3	M02-113-463 cm	4.69	0.46	14.15	72.13	0.11	2.86	1.90	0.47	0.06	0.06	3.11	100.00
8	3	M02-113-463 cm	4.67	0.42	14.08	72.10	0.12	2.88	1.80	0.46	0.09	0.13	3.26	100.00
9	3	M02-113-463 cm	4.69	0.44	14.06	72.11	0.13	2.99	1.81	0.47	0.04	0.13	3.12	100.00
10	3	M02-113-463 cm	5.02	0.48	14.03	71.79	0.00	2.96	1.81	0.41	0.00	0.06	3.42	100.00
11	3	M02-113-463 cm	4.86	0.38	14.03	72.44	0.11	2.97	1.76	0.43	0.00	0.07	2.96	100.00
12	3	M02-113-463 cm	4.51	0.39	14.25	72.34	0.10	3.10	1.81	0.40	0.03	0.12	2.95	100.00
13	3	M02-113-463 cm	4.77	0.41	14.02	71.57	0.12	3.18	1.83	0.49	0.00	0.07	3.53	100.00
1	N11-1	M02-113-485 cm	3.30	0.47	14.67	73.50	0.08	2.33	1.86	0.44	0.00	0.10	3.24	100.00
2	N11-2	M02-113-485 cm	3.19	0.38	14.82	74.15	0.09	1.58	1.71	0.44	0.00	0.05	3.58	100.00
3	N11-3	M02-113-485 cm	3.37	0.42	14.78	73.33	0.10	2.42	1.80	0.48	0.00	0.07	3.22	100.00
4	N11-4	M02-113-485 cm	2.86	0.45	14.62	74.35	0.11	1.95	1.80	0.47	0.00	0.08	3.30	100.00
5	N11-5	M02-113-485 cm	3.52	0.45	14.57	73.25	0.00	2.63	1.83	0.45	0.05	0.12	3.13	100.00
6	18	M02-113-485 cm	5.10	0.44	14.41	72.10	0.04	2.82	1.58	0.36	0.00	0.11	3.03	100.00
7	18	M02-113-485 cm	5.30	0.47	14.66	72.26	0.08	2.29	1.90	0.42	0.00	0.10	2.53	100.00
8	18	M02-113-485 cm	5.26	0.44	14.39	72.22	0.07	2.83	1.58	0.37	0.02	0.12	2.68	100.00
9	18	M02-113-485 cm	4.79	0.44	14.28	72.47	0.03	2.88	1.67	0.37	0.00	0.15	2.92	100.00
10	18	M02-113-485 cm	4.70	0.44	14.15	72.63	0.07	2.85	1.68	0.40	0.00	0.10	2.98	100.00
11	18	M02-113-485 cm	4.85	0.52	14.28	71.88	0.14	2.84	1.73	0.45	0.00	0.07	3.23	100.00
12	18	M02-113-485 cm	4.88	0.46	14.28	71.93	0.02	2.76	1.73	0.39	0.06	0.13	3.36	100.00
13	18	M02-113-485 cm	4.60	0.48	14.31	72.30	0.07	2.79	1.78	0.40	0.04	0.12	3.13	100.00

| | | | Normalized oxides | | | | | | | | | | | |
n	Stub	Sample	Na₂O	MgO	Al₂O₃	SiO2	P₂O₅	K₂O	CaO	TiO₂	Cr₂O₃	MnO	FeO	TOT
14	18	M02-113-485 cm	5.40	0.45	14.26	72.26	0.00	2.78	1.53	0.38	0.00	0.13	2.82	100.00
15	18	M02-113-485 cm	5.12	0.46	14.47	71.06	0.00	2.83	1.76	0.49	0.04	0.11	3.66	100.00
16	18	M02-113-485 cm	5.17	0.41	14.54	72.47	0.05	2.77	1.50	0.39	0.08	0.10	2.54	100.00
17	18	M02-113-485 cm	4.77	0.43	14.42	72.40	0.08	2.80	1.58	0.46	0.00	0.10	2.96	100.00
18	18	M02-113-485 cm	4.26	0.46	14.58	72.74	0.15	2.49	1.79	0.37	0.00	0.11	3.05	100.00
1	N12-2	M03-49-120 cm	2.95	0.45	14.41	74.12	0.12	2.28	1.83	0.46	0.04	0.07	3.28	100.00
2	N12-3	M03-49-120 cm	2.98	0.43	14.80	73.97	0.02	2.48	1.85	0.40	0.00	0.07	2.99	100.00
3	N12-4	M03-49-120 cm	3.36	0.40	14.66	73.51	0.11	2.42	1.82	0.46	0.00	0.06	3.21	100.00
4	N12-5	M03-49-120 cm	3.33	0.44	14.70	72.95	0.16	2.59	1.75	0.50	0.09	0.05	3.43	100.00
5	10	M03-49-120 cm	4.87	0.45	14.13	72.54	0.00	2.75	1.70	0.40	0.00	0.14	3.02	100.00
6	10	M03-49-120 cm	5.00	0.42	14.10	72.17	0.06	2.82	1.78	0.39	0.00	0.09	3.18	100.00
7	10	M03-49-120 cm	5.09	0.48	14.30	71.75	0.09	2.95	1.79	0.45	0.00	0.10	3.00	100.00
8	10	M03-49-120 cm	4.71	0.46	14.01	72.46	0.00	3.05	1.83	0.42	0.00	0.11	2.96	100.00
9	10	M03-49-120 cm	4.84	0.40	14.19	71.83	0.07	2.96	1.80	0.49	0.07	0.11	3.23	100.00
10	10	M03-49-120 cm	5.03	0.45	14.32	71.47	0.11	2.89	1.85	0.45	0.00	0.10	3.31	100.00
11	10	M03-49-120 cm	4.93	0.45	14.25	72.03	0.08	2.95	1.72	0.41	0.00	0.15	3.04	100.00
12	10	M03-49-120 cm	4.90	0.42	14.33	72.25	0.08	2.82	1.73	0.43	0.02	0.08	2.93	100.00
13	10	M03-49-120 cm	4.56	0.42	14.09	72.99	0.03	2.88	1.67	0.47	0.00	0.07	2.80	100.00
14	10	M03-49-120 cm	4.85	0.39	14.05	72.29	0.06	2.90	1.72	0.41	0.06	0.14	3.13	100.00
1	N13-1	M03-49-233 cm	5.26	0.30	19.34	64.75	0.07	4.69	1.82	0.44	0.00	0.26	3.07	100.00
2	N13-2	M03-49-233 cm	5.05	0.41	19.34	64.90	0.04	4.75	1.94	0.42	0.00	0.26	2.89	100.00
3	N13-3	M03-49-233 cm	5.06	0.30	19.18	65.03	0.07	4.56	1.88	0.46	0.00	0.24	3.23	100.00
4	N13-4	M03-49-233 cm	4.91	0.31	19.45	65.08	0.08	4.71	1.84	0.43	0.04	0.22	2.93	100.00
5	N13-5	M03-49-233 cm	4.04	0.53	19.00	64.72	0.00	5.93	2.16	0.34	0.00	0.12	3.16	100.00
6	1	M03-49-233 cm	6.13	0.35	18.58	62.16	0.04	7.53	1.68	0.38	0.00	0.16	2.97	100.00
7	1	M03-49-233 cm	5.94	0.39	18.77	62.43	0.08	7.19	1.83	0.42	0.02	0.19	2.74	100.00

							Normalized oxides						
n	Stub	Sample	Na₂O	MgO	Al₂O₃	SiO2	P₂O₅	K₂O	CaO	TiO₂	Cr₂O₃	MnO	FeO	TOT
8	1	M03-49-233 cm	5.92	0.38	18.79	62.54	0.04	7.24	1.76	0.41	0.00	0.17	2.73	100.00
9	1	M03-49-233 cm	6.19	0.35	18.68	62.32	0.04	7.04	1.81	0.44	0.00	0.17	2.95	100.00
10	1	M03-49-233 cm	4.86	0.49	18.25	62.97	0.08	7.93	2.02	0.35	0.00	0.14	2.90	100.00
11	1	M03-49-233 cm	5.66	0.41	19.02	60.82	0.02	8.18	2.07	0.41	0.00	0.23	3.18	100.00
12	1	M03-49-233 cm	6.44	0.33	18.68	62.19	0.11	6.93	1.65	0.44	0.00	0.21	3.02	100.00
13	1	M03-49-233 cm	5.94	0.34	18.79	62.19	0.05	7.13	1.73	0.46	0.00	0.25	3.12	100.00
14	1	M03-49-233 cm	4.96	0.45	18.32	62.75	0.11	8.09	1.97	0.34	0.00	0.13	2.88	100.00
15	1	M03-49-233 cm	5.78	0.35	18.90	62.70	0.05	7.11	1.81	0.37	0.00	0.27	2.66	100.00
16	1	M03-49-233 cm	5.99	0.31	18.50	62.06	0.13	7.36	1.79	0.42	0.00	0.22	3.22	100.00
17	1	M03-49-233 cm	6.13	0.36	18.63	62.30	0.06	7.04	1.78	0.40	0.05	0.22	3.02	100.00
1	N14-1	M03-49-256 cm	2.17	0.20	12.77	79.94	0.00	2.37	1.07	0.23	0.00	0.06	1.19	100.00
2	N14-2	M03-49-256 cm	2.35	0.17	12.46	80.16	0.00	2.39	0.93	0.20	0.00	0.04	1.29	100.00
3	N14-5	M03-49-256 cm	2.24	0.15	12.78	80.01	0.00	2.42	0.96	0.25	0.00	0.00	1.19	100.00
4	N14-6	M03-49-256 cm	2.18	0.19	12.66	79.93	0.00	2.43	1.09	0.21	0.02	0.08	1.22	100.00
5	N14-7	M03-49-256 cm	2.08	0.17	12.55	80.19	0.04	2.26	1.00	0.24	0.04	0.02	1.40	100.00
6	25	M03-49-256 cm	3.34	0.20	12.35	77.76	0.00	4.09	0.92	0.17	0.00	0.09	1.08	100.00
7	25	M03-49-256 cm	3.30	0.19	12.40	77.42	0.05	4.17	0.95	0.22	0.00	0.00	1.30	100.00
8	25	M03-49-256 cm	3.45	0.21	12.27	77.35	0.03	4.20	1.00	0.20	0.07	0.14	1.08	100.00
9	25	M03-49-256 cm	3.37	0.15	12.44	77.58	0.06	4.06	0.94	0.19	0.04	0.02	1.15	100.00
10	25	M03-49-256 cm	3.52	0.16	12.45	77.04	0.01	4.21	0.95	0.22	0.00	0.02	1.43	100.00
11	25	M03-49-256 cm	3.44	0.19	12.29	77.66	0.00	3.91	0.99	0.19	0.00	0.05	1.28	100.00
12	25	M03-49-256 cm	3.28	0.22	12.17	77.69	0.03	4.20	0.90	0.22	0.00	0.01	1.27	100.00
13	25	M03-49-256 cm	3.37	0.22	12.35	77.70	0.01	3.95	0.98	0.23	0.02	0.06	1.11	100.00
14	25	M03-49-256 cm	3.57	0.19	12.47	77.13	0.04	4.32	0.91	0.21	0.04	0.03	1.08	100.00
15	25	M03-49-256 cm	3.22	0.21	12.58	77.56	0.00	4.04	0.84	0.20	0.00	0.07	1.27	100.00
16	25	M03-49-256 cm	3.51	0.18	12.45	77.28	0.02	3.94	0.94	0.23	0.00	0.06	1.38	100.00

							Normalized oxides							
n	Stub	Sample	Na_2O	MgO	Al_2O_3	SiO2	P_2O_5	K_2O	CaO	TiO_2	Cr_2O_3	MnO	FeO	TOT
17	25	M03-49-256 cm	3.33	0.19	12.51	76.90	0.01	4.19	1.05	0.19	0.00	0.03	1.60	100.00
18	25	M03-49-256 cm	3.40	0.23	12.42	77.09	0.00	4.31	0.97	0.22	0.01	0.00	1.35	100.00
19	25	M03-49-256 cm	3.21	0.18	12.36	77.47	0.02	4.34	0.92	0.21	0.00	0.03	1.26	100.00
20	25	M03-49-256 cm	3.32	0.19	12.16	77.86	0.00	4.06	0.90	0.24	0.00	0.01	1.25	100.00
1	G1-1	M03-48-8 cm	5.00	0.40	19.62	66.37	0.03	4.81	1.63	0.34	0.04	0.13	1.63	100.00
2	21	M03-48-8 cm	6.32	0.51	19.48	61.88	0.06	7.16	1.72	0.43	0.01	0.18	2.24	100.00
3	21	M03-48-8 cm	6.72	0.41	18.73	63.01	0.04	6.79	1.60	0.34	0.00	0.17	2.17	100.00
4	21	M03-48-8 cm	5.72	0.54	18.76	63.10	0.06	7.12	1.72	0.27	0.06	0.18	2.48	100.00
5	21	M03-48-8 cm	6.96	0.37	18.88	63.67	0.04	5.87	1.41	0.28	0.04	0.15	2.34	100.00
6	21	M03-48-8 cm	6.12	0.31	18.94	63.91	0.02	6.07	1.62	0.39	0.00	0.08	2.56	100.00
7	21	M03-48-8 cm	6.69	0.32	18.48	63.39	0.02	6.55	1.33	0.22	0.10	0.17	2.72	100.00
8	21	M03-48-8 cm	4.75	0.12	19.29	67.67	0.07	5.87	1.04	0.05	0.01	0.00	1.13	100.00
9	21	M03-48-8 cm	3.74	0.97	19.77	58.61	0.13	10.40	2.72	0.33	0.01	0.15	3.16	100.00

Table 5.2. Electron microprobe analyses of glass shards from several potential sources and from the tephra layers recognized within cores MAR02-113P, MAR03-48P and MAR03-49P. Analyses are recalculated to 100% and exclude elements with atomic weights < Na and more minor and trace elements, including Cl.

composition of tephra groups A, B and C. These are tephra layers Y5, Y2 and Nisyros tephras, respectively. No other known tephras in the Aegean Sea area match these compositions, particularly when all oxides are considered.

Y5 represents the most widespread tephra of the Mediterranean area. The estimate of the age of tephra layer has changed with time, ranging from 25–40 kyr (Ninkovich and Heezen, 1967; Vergnaud-Grazzini and Rosenberg, 1969; Olausson, 1971; Keller and Ninkovich, 1972; Di Girolamo et al., 1972; Cita et al., 1977; Thunell et al., 1979). Thunell et al.(1979) have reported an age of 38,000 yrBP, estimated by sedimentation rates derived from oxygen isotope stratigraphy. They correlated the Y-5 layer with the Campanian Ignimbrite formation. The Campanian Ignimbrite has been recently dated to 36±0.4 kyrBP (Deino et al., 1992) which is in good agreement with the extrapolated age of 38,000 yrBP.

On the basis of physical, mineralogical and geochemical properties, layer Y-2 has been attributed to Santorini activity and in particular to the 18,000 yrBP old Akrotiri ignimbrite (Federman and Carey, 1980). This age can be used to confirm the validity of the calculated sedimentation rate in core MAR02-113P. The vertical difference from the 16,930 yr-dated shell fragment to the tephra layer is 45 cm. Linear extrapolation assuming a constant sedimentation rate suggests an age of 18,430 yrBP for the tephra layer which supports the validity of the calculated sedimentation rate of 30 cm kyr^{-1}.

On the basis of strong correlation of the elemental analyses in the core, tightly clustering around the shards from the Nisyros eruption, the tephra layer below the Y-5

tephra is correlated with the Nisyros tephra (Figs. 5.6, 5.8). However, The Nisyros ash has a very limited distribution within the Eastern Mediterranean abyssal sediments and occurs between the Y-4 and Y-2 layers and it is thought to have originated from the Nisyros strato-volcano (Vinci, 1983, 1985; Narcisi and Vezzoli, 1999).

Assuming a constant sedimentation rate of 30 cm kyr^{-1}, ages of the older shelf-crossing unconformities and depositional sequences can also be determined at the MAR02-113P core site using their stratigraphic positions. As imaged in the crossing seismic reflection profile, the underlying unconformities α', α_0, α_1, α_2, α_3 and α_4 lie at ~10.2, 17.7, 38.2, 75.1, 101.9 and 126.4 meters below the seabed, respectively (Fig. 5.5). Linear extrapolations using constant sedimentation rate suggests that the unconformities α', α_0, α_1, α_2, α_3 and α_4 have ages of ~33.8, 63.7, 127.3, 250.3, 339.5 and 421.3 kyr, respectively. The estimated age of α_1 is in perfect agreement with available U/Th dates (Fig. 5.6).

Cores MAR02-114P and MAR02-138P were collected from the shelf area in basin B1 (Figs. 5.3, 5.9, and 5.10). Both cores penetrated down to the lower portions of depositional sequence 3, but did not penetrate the unconformity α_0. Algal bioherm and *Trisidos* sp. valves collected from core MAR02-114P, at subbottom depths of 283 cm and 431 cm, have radiocarbon ages of 42,490±1020 yrBP and 42,990±1160 yrBP, respectively (Fig. 5.9; Table 5.1). Two algal bioherm samples extracted from core MAR02-138P at subbottom depths of 45 cm and 297 cm yielded radiocarbon dates of 35,960±560 yrBP and 43,810±930 yrBP, respectively (Fig. 5.10; Table 5.1). Taking into
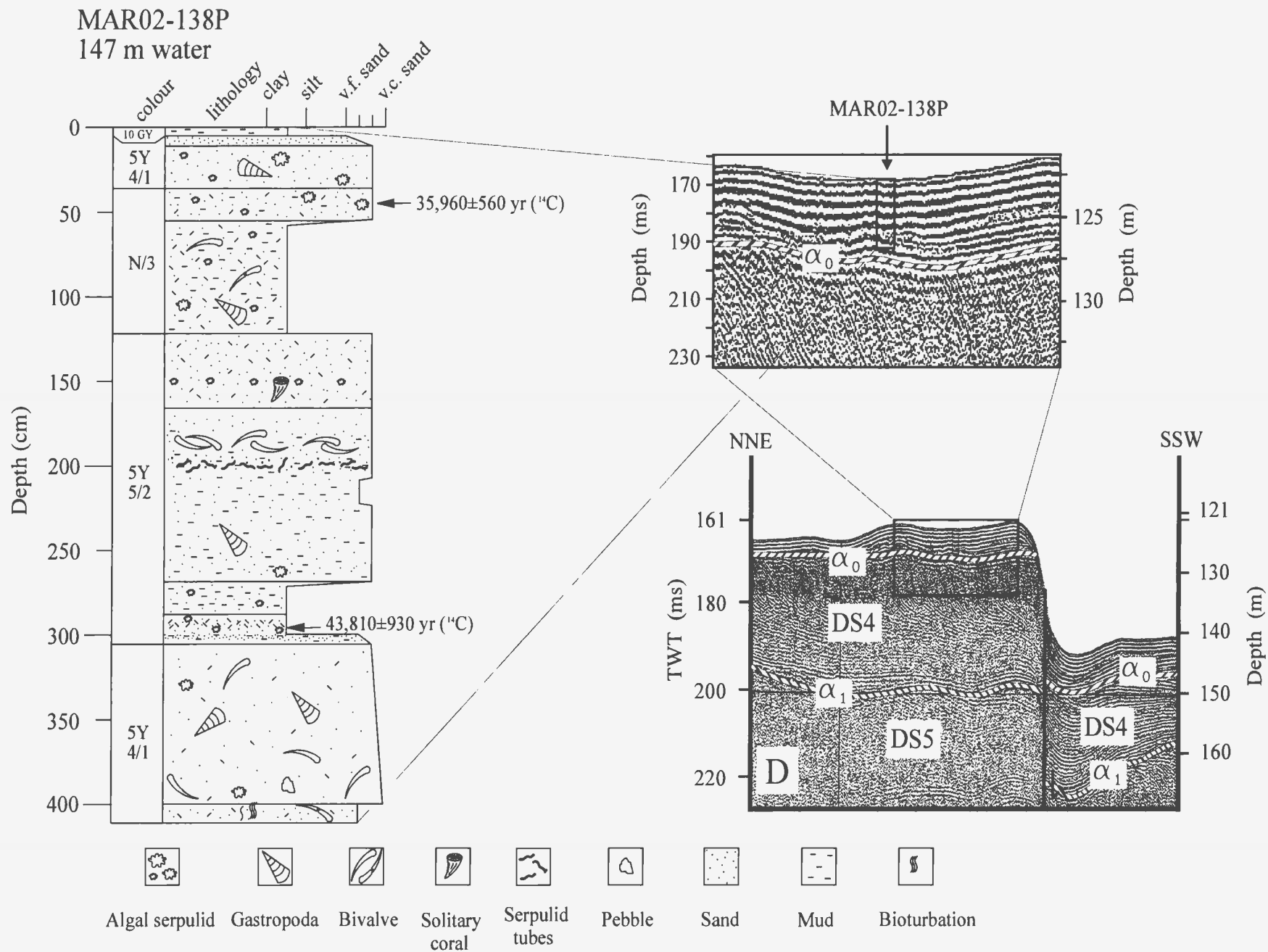
Figure 5.10. Huntec DTS seismic reflection profile showing the location of core MAR-02138P. Also shown is the detailed lithostratigraphic column of core MAR02-138P. See Figure 5.2 for location. Colour designations are from the Geological Society of America Rock Colour Chart.

consideration the large standard deviations of the derived ages, linear extrapolations assuming constant sedimentation rates between dated intervals yield significantly variable amounts. For example, at the MAR02-114P core site, if we ignore the standard deviations of the derived ages, the extrapolated sedimentation rate would be 296 cm kyr^{-1}. Whereas, including the standard deviations, linear extrapolations yield sedimentation rates ranging from 55 to as high as 411 cm kyr^{-1}. Same calculations at the MAR02-138P core site, however, reveal a comparatively narrow range of sedimentation rate changing between 27 and 40 cm kyr^{-1}. This considerable difference in sedimentation rates implies that differential amounts of deposition and/or winnowing effect prevailed the shelf area during the development of shelf sequences. These sedimentation rates suggest ages ranging from 224,000 and 16,000 yr for the unconformity α_0, which is not in keeping with the age of 63,733 years for the same unconformity based on extrapolation at the MAR02-113P core site (Figs. 5.9 and 5.10). Also, U/Th dating of the deeper α_1 to 130 kyr (Fig. 5.6) requires that α_0 be significantly younger than this. This inconsistency may be related to different depositional conditions that dominated the shelf area and the deeper portions separately. The fact that three of the four C-14 dates cluster around 42,000–43,000 yrBP raises another possibility that most, if not all of the carbon is dead carbon. If so, these ages and sedimentation rates calculated from them are suspect. The ages would then be as minimum possible ages, and the rates would have no validity.

The U/Th measurements on two *in situ Ostrea* shells extracted from cores MAR03-48P and MAR03-49P gave ages of 118,927 (+6,193/-5,852) yrBP and 133,218

(+7,318/-6,814) yrBP, respectively (Figs. 5.3, 5.11, 5.12; Table 5.1). Both cores were taken from the deeper portions of the eastern basin, just seaward of the topset–foreset transition of depositional sequence 5, where the overlying shelf-crossing unconformity α_1 is situated near the seabed (Figs. 5.3, 5.11 and 5.12). Seismic stratigraphic correlations (Fig. 5.6) suggest that these ages bracket the age of α_1. This result supports the estimates derived by extrapolation below core site MAR02-113P.

5.3. Correlations with the oxygen isotope stages and sea-level curves

Emiliani (1955a) subdivided the oxygen isotopic record of deep-sea cores into isotopically heavy and light stages (Fig. 5.13). He numbered the stages consecutively from the top of the record downward, with the odd numbered stages (1, 3, 5, 7, 9...) and even numbered stages (2, 4, 6, 8, 10...) representing interglacial and glacial intervals, respectively. The global oxygen isotopic record exhibits a saw-tooth pattern with slow oscillatory transition into glacial periods reflecting progressive glaciation and concomitant ice buildup in polar regions, but sharp rapid transitions into interglacial periods, generally occurring in less than 10^4 years, and primarily reflecting ice-volume decrease and meltwater injection into the global ocean (Vergnaud-Grazzini, 1985).

Sea-level curves constructed using oxygen isotopic data from deep-sea cores (e.g., Shackleton, 1987), and raised marine terraces with coral reefs, have similar 'saw-tooth' patterns as in the $\delta^{18}O$ curves (Fig. 5.13). The curves indicate that, during Quaternary glacial- interglacial cycles, global sea level varied markedly from +7 m during isotopic

MAR03-48P
311 m water

colour lithology clay silt v.f. sand v.c. sand

Depth (cm)

0

5Y4/1

5Y 3/1

118,927 yr (U/Th)

50

5Y 4/1

5GY 4/1

5Y 3/2

5GY 4/1

100

5Y 3/2

150

? ∿∿∿∿∿ α_1

5Y
2/1

200

250

MAR03-48P

Depth (ms)

397

410

420

Depth (m)

298

305

310

α_1

NW   SE

TWT (ms)

400

α_1

DS5

500

α_2

DS6

α_3

600

E   DS7

Depth (m)

300

400

Unconformity   Ash   Shell   Gastropoda   Pecten   Pebble   Sand   Mud   Bioturbation
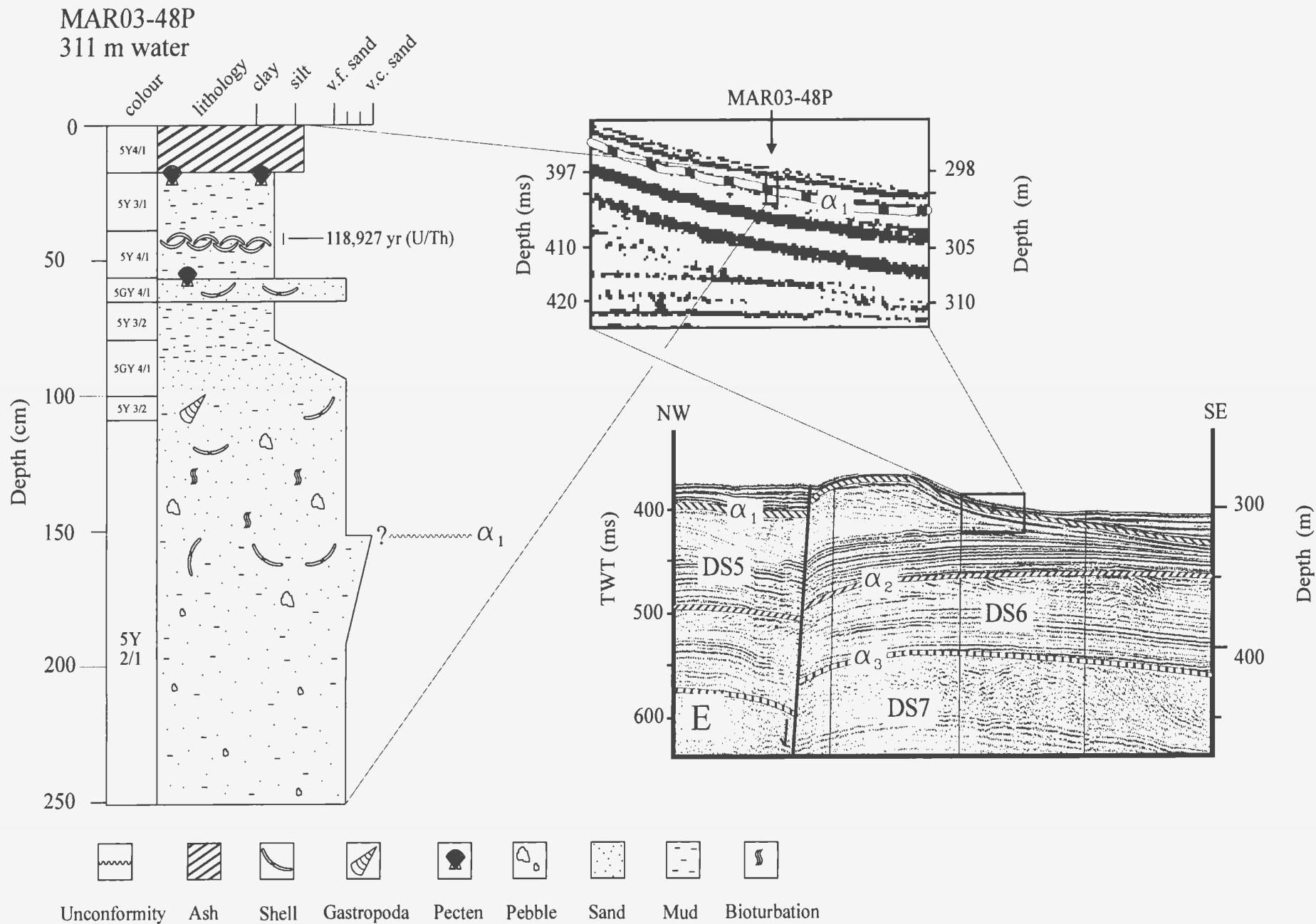
Figure 5.11. Sleeve gun seismic reflection profile showing the location of core MAR03-48P. Also shown is the detailed lithostratigraphic column of core MAR03-48P. See Figure 5.2 for location. Colour designations are from the Geological Society of America Rock Colour Chart.
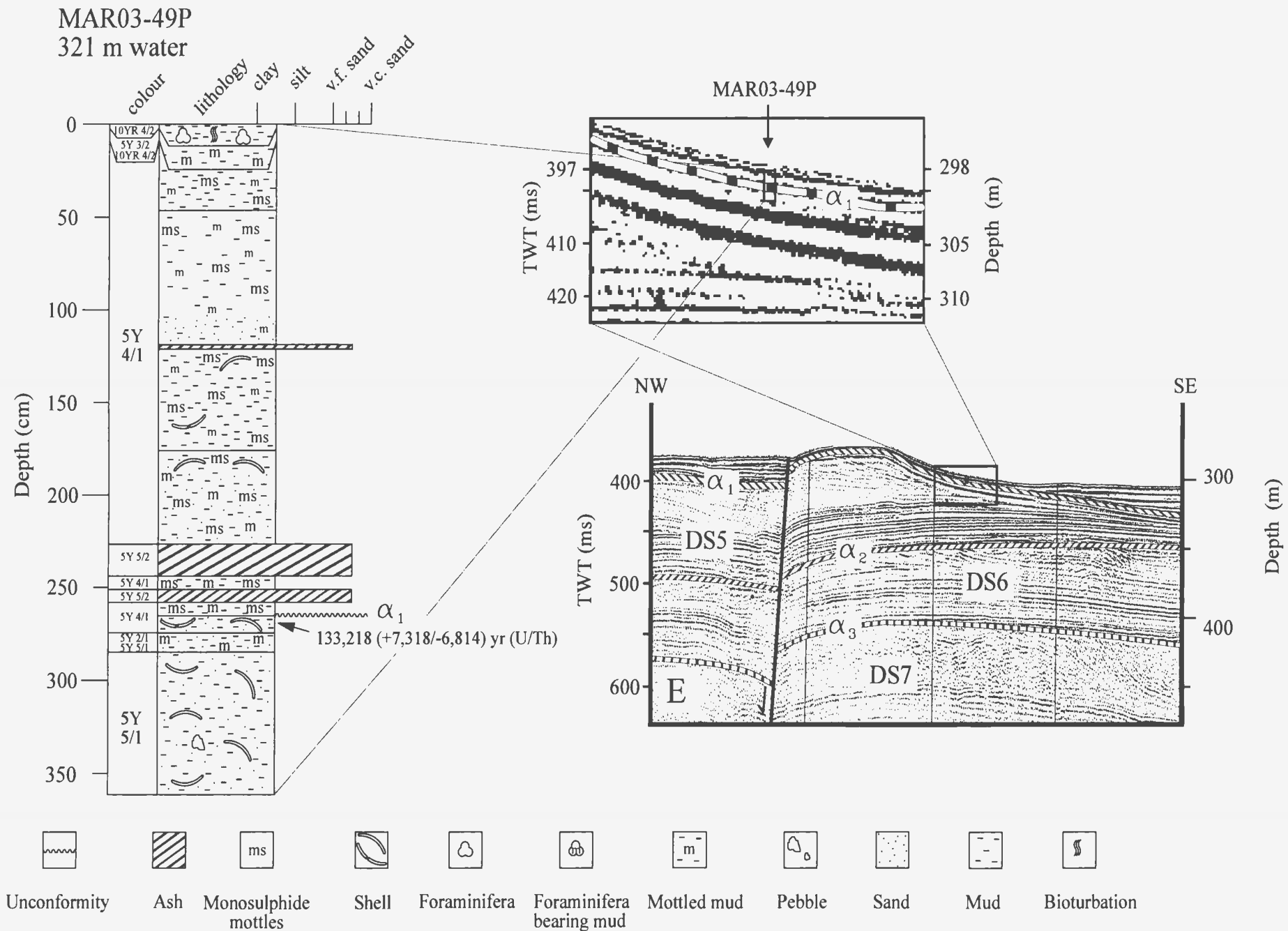
Figure 5.12. Sleeve gun seismic reflection profile showing the location of core MAR03-49P. Also shown is the detailed lithostratigraphic column of core MAR03-49P. See Figure 5.2 for location. Colour designations are from the Geological Society of America Rock Colour Chart.
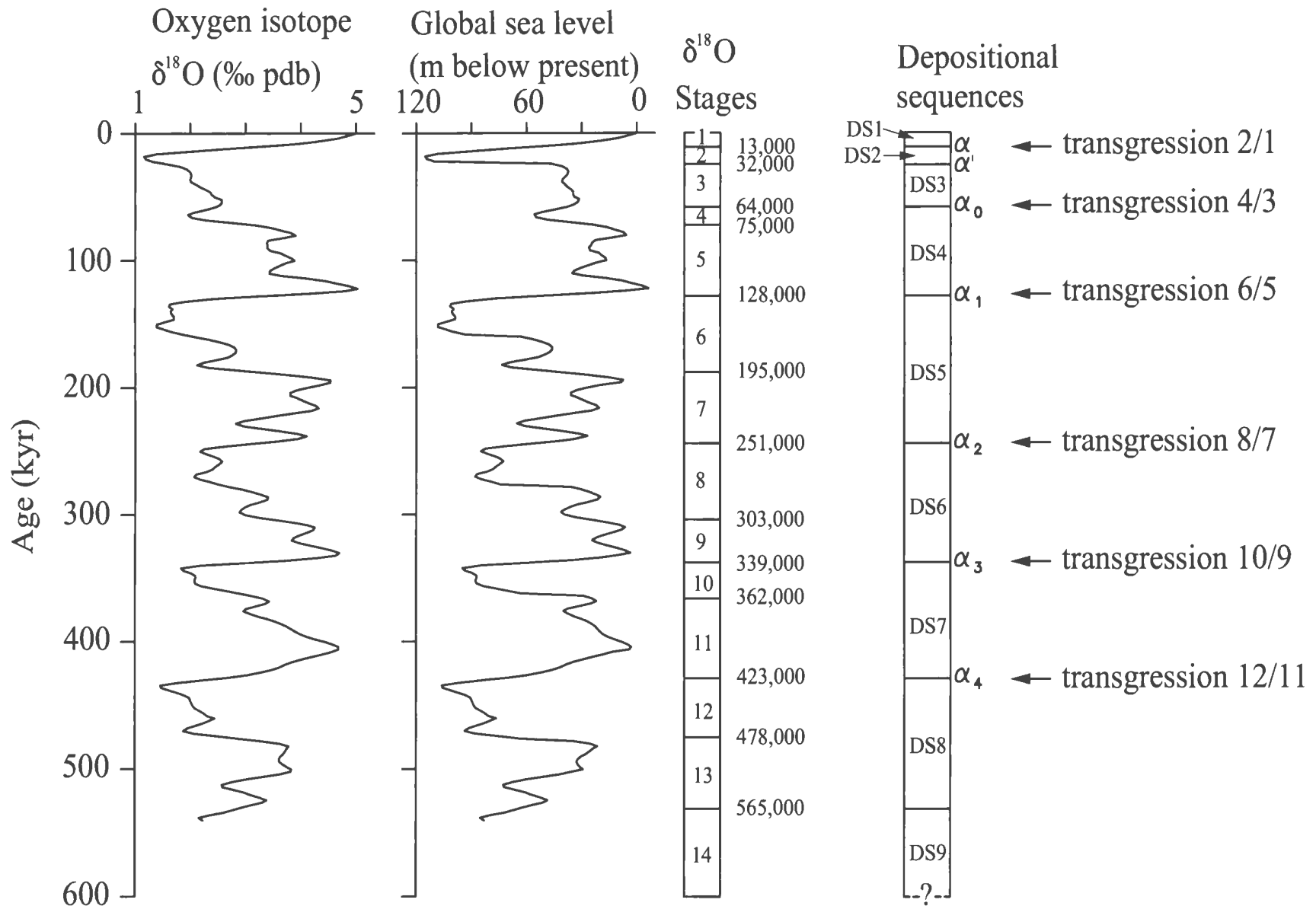
Figure 5.13. Figure showing the correlations of the depositional sequences and the unconformities with the stacked and smoothed global oxygen isotope curve (Imbrie et al., 1984) and the global sea-level curve Skene et al., 1988). Ages of isotopic stage boundaries are from Shackleton and Opdyke (1976). The unconformities and the depositional sequences are discussed in the text.

stage 5e to $-120 - 150$ m during the peak of isotopic stages 12, 6 and 2 (Bloom et al., 1974; Imbrie et al.,1984; Chappell and Shackleton, 1986; Skene et al., 1998; Fig. 5.13). The shifts in sea-level curves indicate sea-level fluctuations. Rapid rises in sea level correspond to oxygen isotope stage boundaries (Shackleton and Opdyke, 1976). Sea-level rises during the transitions from lowstands to highstands generally occurred within $\sim 10^4$ years at rates of 4.7 to 11.5 m kyr^{-1}. As also indicated in the sea-level curve, the successive interglacial periods span comparatively much longer time intervals than the glacial periods (Fig. 5.13). Sea-level lowering and the following rapid sea-level rises are clearly imaged in seismic reflection profiles as oblique-prograded depositional sequences and shelf-crossing unconformities, respectively.

There is no direct chronological control for the interpreted shelf-crossing unconformities within the study area, except unconformities α and α_1. However, ^{14}C and U/Th dated samples extracted from depositional sequences 1, 2 and 3, linear extrapolations below the MAR02-113 core site, and the stratigraphic positions of the unconformities throughout the study area provide a reliable framework to determine the ages of the unconformities and correlate them with the oxygen isotope stages (Fig. 5.13).

Linear extrapolation using a constant sedimentation rate suggests that the onset and the cessation timings of unconformity α are 16,033 and 13,500 years, respectively in core MAR02-113P which agrees with the oxygen isotopic stage boundary 2/1 (13,000 yrBP; Fig. 5.13). In core MAR02-113P, the calculated age of 33,833 years for the underlying unconformity α' favorably matches with the oxygen isotopic stage boundary

3/2 (32,000 yrBP; Fig. 5.13). These extrapolated dates strongly suggest that unconformities α and α' were developed during the transition from isotopic stages 2–1 and 3–2, respectively. The 9,630 yrBP sample extracted from depositional sequence 1 and the 16,930 and 26,100 yrBP samples extracted from depositional sequence 2 suggest that the depositional sequences 1 and 2 developed mostly during the last interglacial stage 1 (0–13,000 yr) and glacial stage 2 (13,000–32,000 yr), respectively. The global sea-level curve shows that approximately 32,000 years ago sea level dropped from –38 to –115 m at a comparatively rapid rate of 4.1 m kyr^{-1}. Depositional sequence 2, comprising oblique-prograded clinoforms, was developed during this sea-level fall. The samples extracted from depositional sequence 3 from cores MAR02-114P and MAR02-138P clearly suggest that unconformity α_0 is older than the ages obtained from the samples (Table 5.1). The extrapolated age of unconformity α_0 (63,733 years) in core MAR02-113P suggests that it formed during the transition from glacial stage 4 to interglacial stage 3, ~ 64,000 years ago (Figs. 5.13, 5.14). The global sea-level curve shows that, during interglacial stage 3, the sea level was situated at –31 to –38 m (Fig. 5.13). Linear extrapolation using a constant sedimentation rate for strata below the MAR02-113P core site (Fig. 5.5) and the two U/Th-dated shell samples extracted from cores MAR03-48P and MAR03-49P clearly suggest that the unconformity α_1 underlying depositional sequence 4 formed during the transition from glacial to interglacial isotopic stages 6–5 at ~128,000 yrBP (Fig. 5.13). The global sea-level curve shows that during interglacial stage 5e, sea level stood 5–7 meters above the present sea level but dropped to –35 meters
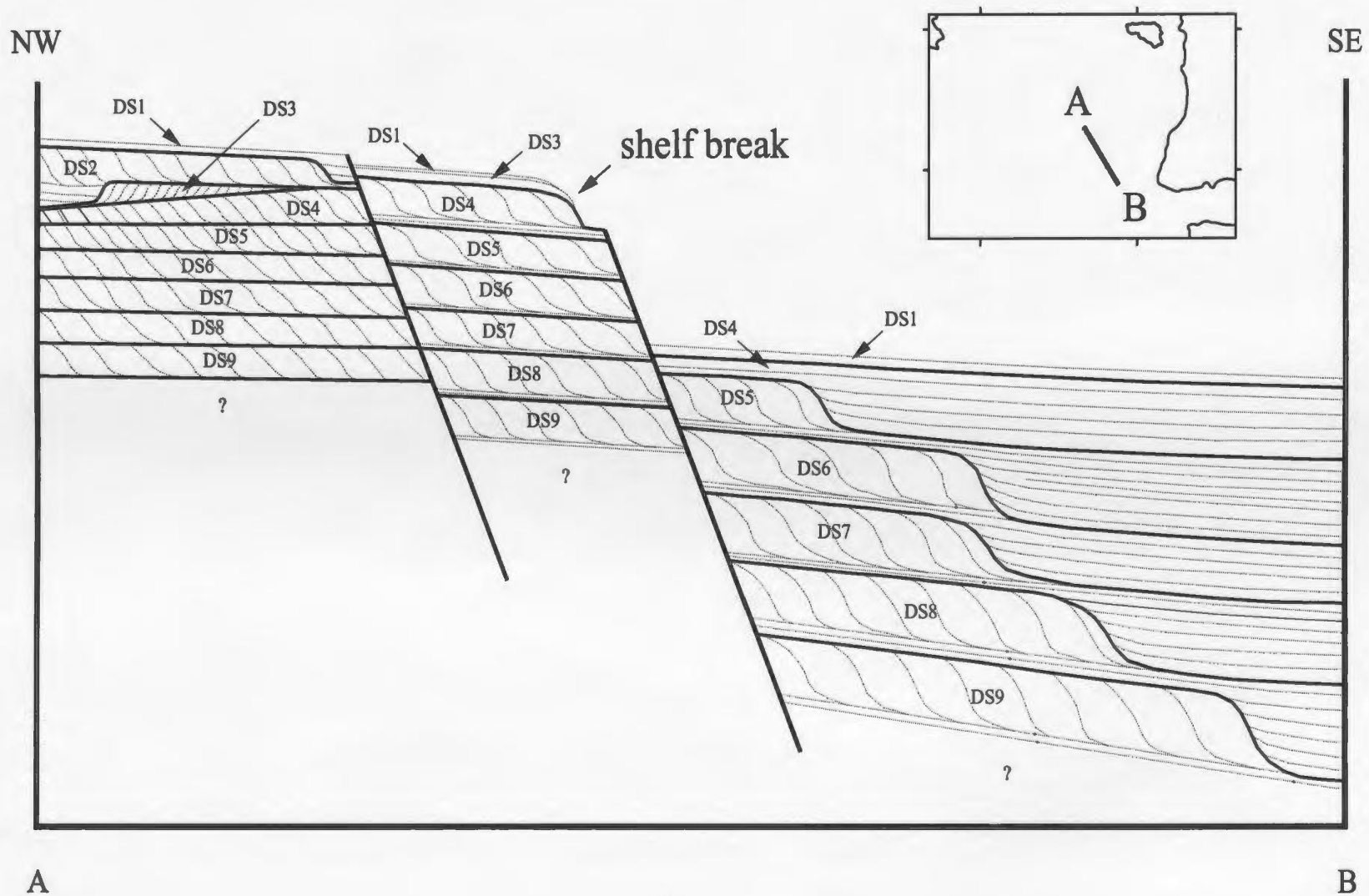
Figure 5.14. Schematic cross-section along A-B showing the stacked architecture of the depositional sequences and their maximum seaward extensions. The descending topset-foreset transitions indicate clinoform develoment during times of falling sea level.

some 110,000 years ago (Fig. 5.13). Subunit 4b, composed of parallel reflections, accumulated during this sea-level highstand (interglacial stage 5) which span 57,000 years, whereas Subunit 4a developed in about 12,000 years during the glacial isotopic stage 4. The global sea-level curve shows that sea level dropped from −5 meters at ~78,000 yrBP to −56 meters at 66,000 yrBP. This continuous sea-level drop resulted in the oblique-prograded configurations of Subunit 4a (Fig. 5.13). The rate of this monotonic sea-level fall averages 0.5 cm yr^{-1} which is consistently higher than the calculated tectonic subsidence rates throughout the study area (0.003–0.11 cm yr^{-1}; see section 5.4.). As a result, the top of Subunit 4a was subaerially eroded throughout the study area and the topsets are absent. Linear extrapolation using a constant sedimentation rate suggests that depositional sequence 5 developed during the transition between isotopic stages 7–6 (Fig. 5.13). During this transition, the global sea-level curve shows that there had been a noticeable amount of sea-level fall from −7 meters at 200,000 yrBP to ~ −109 meters at 150,000 yrBP (Fig. 5.13). This ~102 m fall was responsible for the oblique-prograded seismic configuration of Subunit 5a. The average rate of fall was 0.6 cm yr^{-1} (Fig. 3.8) which is considerably higher than the rate of tectonic subsidence on the shelf area (0.003–0.005 cm yr^{-1}; Fig. 5.15; see section 5.4) and in the deeper portions of the eastern basin (0.11–0.13 cm yr^{-1}; Fig. 5.15; see section 5.4.). Accordingly, sufficient accommodation space for the development of topset beds was not created and Subunit 5a has an eroded top. Bypass association with this erosion caused sediments to be deposited basinward as prograded foreset beds. In the eastern basin, the local presence of topset
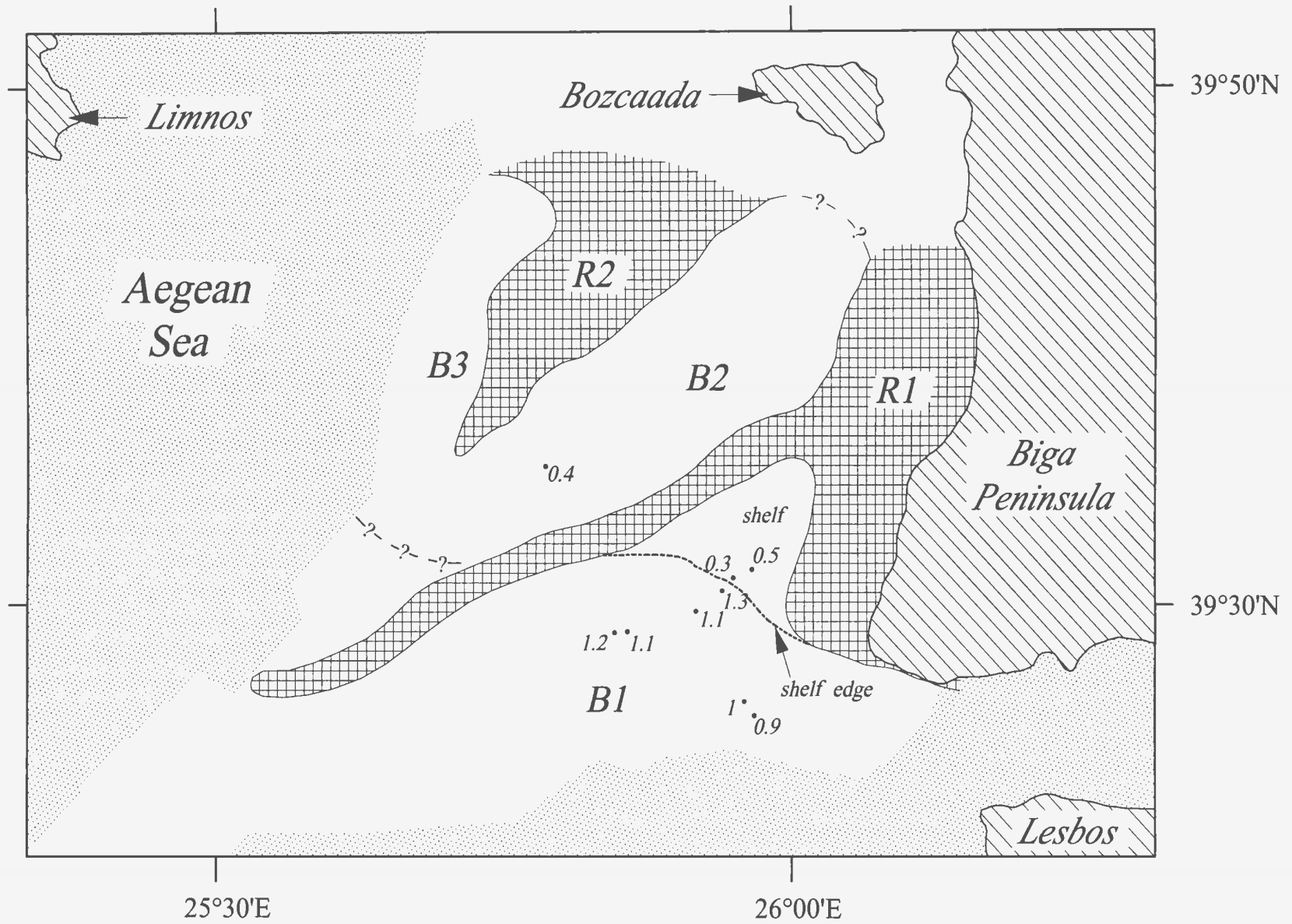
Figure 5.15. Map showing the calculated subsidence rates (m/kyr) for the corresponding locations within the study area. Dotted segment represents the no-data region.

beds might be attributed to an ephemeral sea-level rise which took place between ca.

182,700 and 169,230 yrBP (Fig. 5.13). Subunit 5b formed during interglacial oxygen

isotopic stage 7 where sea level fluctuated but remained higher than that during glacial

stage 6. Taking into account the aforementioned successive development of shelf-

crossing unconformities α to α_1 and the calculated sedimentation rate from core MAR02-

113, shelf-crossing unconformities α_2, α_3 and α_4 are assigned to oxygen isotopic stage

boundaries 8/7, 10/9 and 12/11, respectively (Fig. 5.13).

The calculated ages of the unconformities, intervening depositional sequences and

the overall stacked stratigraphic architecture suggest that depositional sequences 1 to 7

represent distinct phases of delta progradation during the last 423,000 years (Figs. 5.13,

5.14).

5.4. Basin subsidence

Glacio-eustatic sea-level fluctuations, sea-level variations caused by tectonic

movements (emergence and subsidence) and style of sedimentation are the principal

factors that controlled the Quaternary-Recent stratigraphic architecture observed in the

study area. In the seismic reflection profiles, the vertically stacked and seaward-

prograded delta lobes clearly reflect the presence of tectonic subsidence. If there was no

subsidence, each depositional sequence that developed during a phase of sea-level

lowering and the subsequent lowest stand of sea-level would have accumulated in front of

the previously deposited depositional sequence, resulting in a seaward-prograded shelf

break (Aksu et al., 1992b).

The amount of tectonic subsidence can be calculated by measuring the vertical elevation difference of the topset to foreset transitions of two successive depositional sequences provided that the age of the topset–foreset transitions and the elevations of the sea level during these times are accurately known. The ages of the topset–foreset transitions are constrained by radiocarbon and U/Th dates from the samples extracted from cores that penetrated these sediments. The topset–foreset transitions of modern Aegean deltas occur at water depths of ~ 15–20 m (Aksu and Piper, 1983; Aksu et al., 1987; Aksu et al., 1992a).

In basins B2 and B3, most of the topset–foreset transitions below depositional sequences 2 and 3 cannot be imaged due to the limited seismic line coverage and the presence of seafloor multiples that mask the lower portions of the seismic profiles. In basin B1, the topset to foreset transitions in depositional sequences 4 to 7 are imaged, while in basin B2 only the transition for depositional sequence 7 is observed.

The topset to foreset transition in depositional sequence 4 is best imaged in basin B1. It occurs at 168 ms (126 m) below the present sea level and delineates the shelf break. Depositional sequence 4 developed during the interglacial isotopic stage 5 (i.e., Subunit 4b) and the subsequent glacial isotopic stage 4 (i.e., Subunit 4a). The topset to foreset transition represents the last phase of delta progradation during the peak of the glacial maximum prior to the subsequent sea-level rise some 64,000 yr ago. During that time the sea level stood at ~ –90 m. Accordingly, a topset to foreset transition at 20 m

below the paleo sea level suggests a 25 cm kyr^{-1} subsidence rate and a total of 31 m of subsidence for the last 64,000 years for the shelf area (Fig. 5.15).

In depositional sequence 5, the topset to foreset transition is observed on the shelf area and in the deeper portions of basin B1. On the shelf, this transition occurs at 230 ms (173 m), while in the deeper portions it occurs at depths ranging between 371 ms (278 m) and 410 ms (308 m) below present sea level. Depositional sequence 5 developed during interglacial isotopic stage 7 (i.e., Subunit 5b) and the subsequent glacial stage 6 (i.e., Subunit 5a). The last phase of delta progradation took place at the end of glacial oxygen isotopic stage 6, some 128,000 yr BP, when the sea level stood at −120 m. This paleo sea level implies that since the initiation of interglacial oxygen isotopic stage 5, the shelf area has subsided ~ 33 m while the deeper portions of basin B1 experienced subsidence ranging between 138 and 168 m, suggesting subsidence rates of 0.3 m kyr^{-1} and 1.1–1.3 m kyr^{-1} for the shelf area and the deeper portions of basin B1, respectively (Fig. 5.15).

Depositional sequence 6 developed during the interglacial and glacial stages 9 and 8, respectively and spans a time interval of ~ 88,000 yr. The youngest topset to foreset transition was developed during the final stages of the maximum sea-level lowstand prior to the onset of the major transgression at ~ 251,000 yr BP. The transition is imaged in the southeast portion of basin B1 and lies 480 ms (360 m) below present sea level. During the last phase of progradation the sea level stood at ~ −90 m. The present depth of the topset to foreset transition and the paleo sea-level position suggests that the area has subsided 265 m since ~ 251,000 yr which indicates a subsidence rate of 1 m kyr^{-1} (Fig.

5.15).

Depositional sequence 7 formed during the global isotopic stages 11 and 10 between 423,000 and 339,000 yr BP. Seismic reflection profiles show that the topset to foreset transition in depositional sequence 7 occurs at 574 ms (430 m) in basin B1 and at at 348 ms (261 m) in basin B2. The final phase of delta progradation ceased some 339,000 yr ago before the initiation of the major sea-level rise. During that time the sea level stood at –90 m. Assuming that the topset to foreset transition occurred at ~ 20 m water depth, the data indicate subsidence amounts of 320 m and 151 m for basins B1 and B2, respectively, which correspond to subsidence rates of 0.9 m kyr^{-1} in basin B1 and 0.4 m kyr^{-1} in basin B2 (Fig. 5.15).

The magnitude of the global sea-level variations, the rates of tectonic subsidence (or emergence) and the rate of sediment input constitute the major factors that control the thickness of a depositional sequence. If the sea-level fall was of similar magnitude and the rate of tectonic subsidence was constant, then the depositional sequences that would develop during consecutive glacial-interglacial cycles would have the same thicknesses throughout the study area, provided that the durations of the successive interglacial and glacial isotopic stages were the same. However, seismic reflection profiles show that in basin B1 the thicknesses of the depositional sequences are noticeably higher than those in basins B2 and B3. This considerable amount of thickness difference between basins B2, B3 and basin B1 may be attributed to differential subsidence rates among these basins. For example, the vertical thickness difference of depositional sequence 5 in basins B1 and

B2 is ~ 30 ms (~ 23 m). During the development of depositional sequence 5, basin B2 might have subsided less than basin B1. Consequently, accommodation space created in basin B2 would be less than that in basin B1 which, in turn, resulted in a greater amount of sediment bypass across the shelf area, thus lesser amounts of sediment accumulation in basin B2. The sediments winnowed by waves and longshore currents would have most likely been deposited within the deeper portions of the study area where low-energy conditions prevailed.

The calculated subsidence rates for the shelf area range between 0.3 and 0.5 m kyr^{-1} while deeper portions of basin B1 reveal much higher rates varying from 0.9 to 1.3 m kyr^{-1} (Fig. 5.15). Comparatively, the values for the shelf region are in good agreement with the published values for the central, northern and northwestern Aegean Sea. However, they are lower than values calculated from parts of western Turkey (Table 5.3).

	Subsidence rates
NW Aegean (Lykousis, 1991)	0.95 m kyr^{-1} 1.8 m kyr^{-1}
N Aegean (Piper and Perissoratis, 1991)	0.3–1.5 m kyr^{-1}
Central Aegean (Lykousis et al., 1995)	0.33 m kyr^{-1} 0.57 m kyr^{-1}
İzmir Bay and Çandarlı Basin (Aksu et al., 1987)	0.5–1 m kyr^{-1}
Gulf of Kuşadası (Aksu et al., 1987)	1 m kyr^{-1}
W Turkey (Flemming, 1972)	1–2 m kyr^{-1}
This study	0.25–1.3 m kyr^{-1}

Table 5.3. Calculated subsidence rates from different parts of the Aegean Sea by various authors.

CHAPTER 6

6. Discussion

6.1. Kinematic Analysis

The area situated between the islands of Bozcaada and Lesbos and the Biga Peninsula plays an important role in the delineation of the westward continuations of the central branch of the North Anatolian Fault into the Aegean Sea. The most important structural features in the Biga Peninsula are NE–SW trending faults and NE–ENE-trending mountains and graben. Following the inception of the North Anatolian Transform Fault in the early Miocene, large number of NE–SW-trending dextral faults have formed in the Biga Peninsula (Fig. 6.1; Siyako et al., 1989). During the early and middle Miocene, calc-alkaline volcanism and ~ N–S compression characterized the region (Siyako et al., 1989; Yılmaz and Karacık, 2001). In the late Miocene, the calc-alkaline volcanism largely ceased and the region has since undergone ~ N–S extension, which has produced the Ezine horst and the Etili and Gülpınar graben (Fig. 6.2; Yılmaz and Karacık, 2001). Contemporaneously, the North Anatolian Transform Fault extended westward across the Biga Peninsula. As a result of this intense faulting, the region situated between the Toluklar-Eskiyayla Fault and the Küçükkuyu-Göre Fault was uplifted. As a result of this uplifting, Kazdağ Mountain and Bayramiç depression formed (Figs. 6.1, 6.2; Siyako et al., 1989).
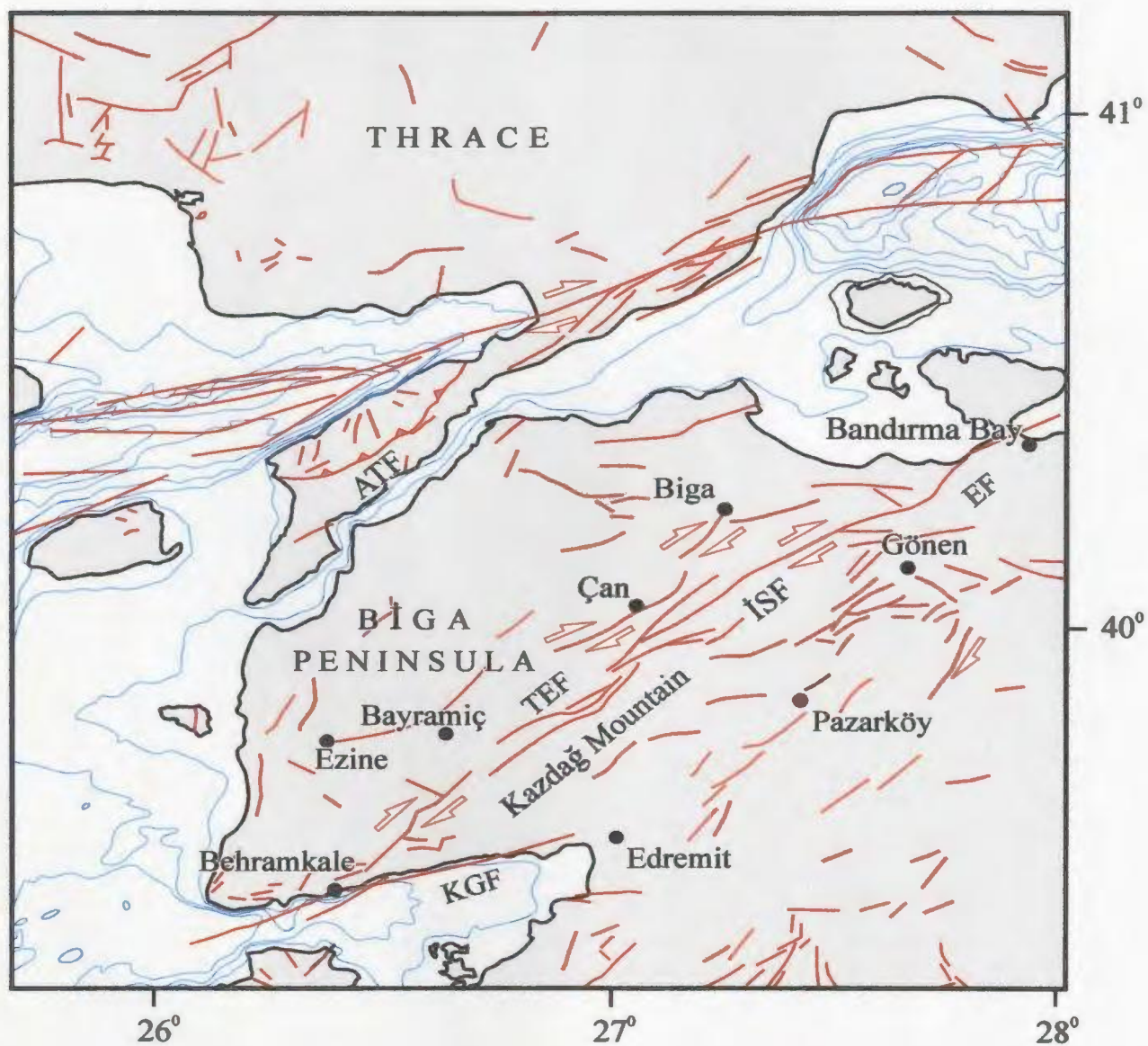
Figure 6.1. Map showing the faults throughout the Biga Peninsula (from Siyako et al., 1989, and Yaltırak, 2003). KGF=Küçükkuyu-Göre Fault; İSF= İnova-Sarıköy Fault; TEF= Toluklar-Eskiyayla Fault; EF= Edincik Fault, ATF= Anafartalar Thrust Fault
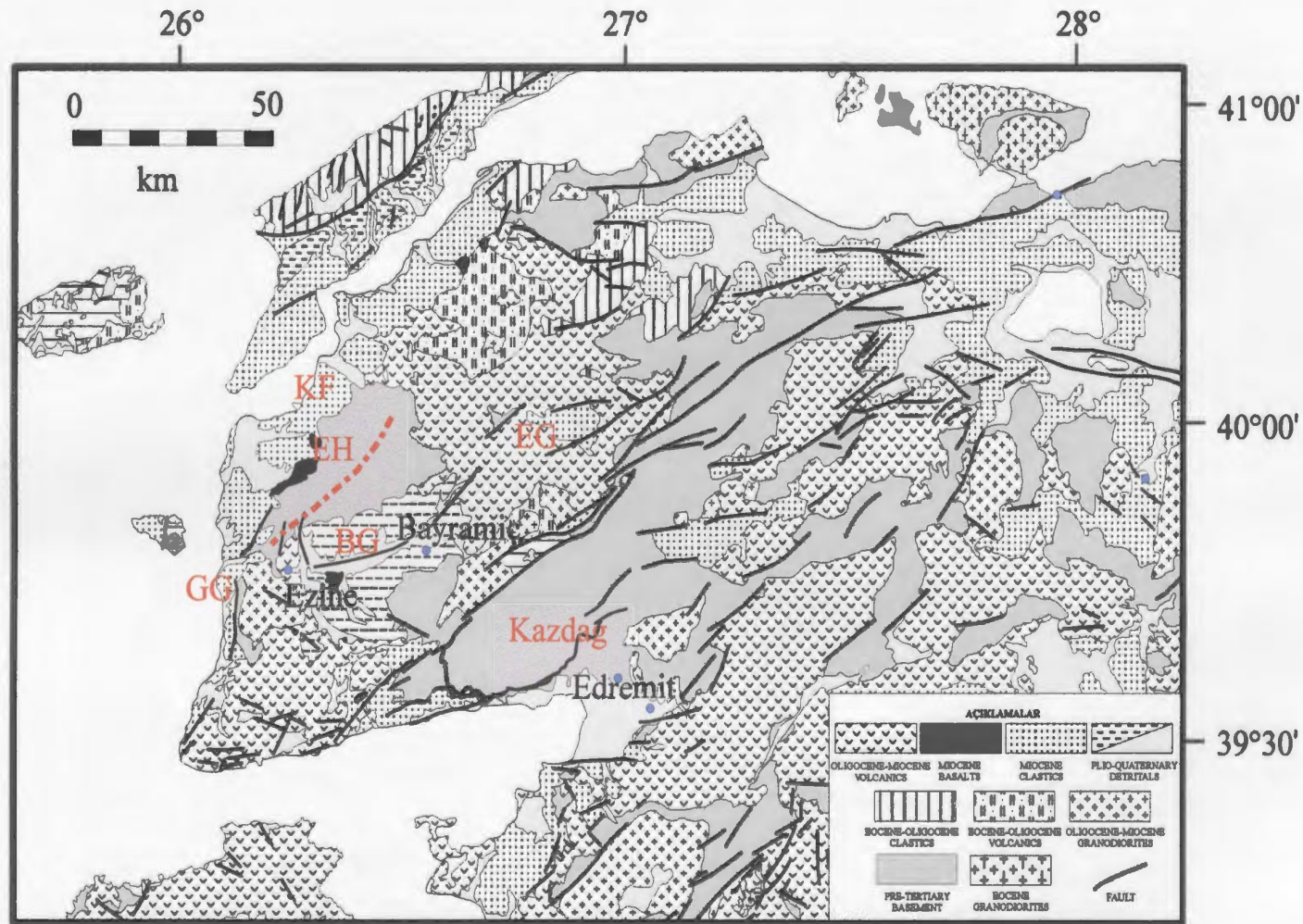
Fig. 6.2. Map showing the major structural features in the Biga Peninsula.
GG: Gülpınar Graben, BG: Bayramiç Graben, EG: Etili Graben, EH: Ezine Horst, KF: Kirazlı Formation
(compiled from Yaltırak, 2002, and Yılmaz and Karacık, 2001).

The most outstanding features observed throughout the marine study area are the NE–SW-trending ridges and their intervening basins (ridges R1 and R2; basins B1, B2, B3), and the major faults, A_1 and β_8, which constitute the main fault system in the study area (Figs. 3.9, 4.1). The NE–SW-trending ridges and their intervening basins constitute the seismic basement in the study area. The origin of the basement rocks cannot be determined due to the lack of well data and limited acoustic penetration. However, Alpar and Doğan (1999) undertook a seismic profiling survey in the area situated between the islands of Bozcaada and Limnos and the Aegean exit of the Strait of Dardanelles and interpreted folded acoustic basement in this area as mainly Miocene formations. Since the study area deposits are composed of upper Pleistocene sediments and taking into account the folded architecture of the ridges, it is plausible to extend this Miocene age to the basement rocks throughout the study area. Alpar and Doğan (1999) further pointed out that this folding occurred during the development phase of the Anafartalar Thrust Fault on the Gelibolu Peninsula (Fig. 6.1).

The sediments are thickest along the axes of basins B1–B3 and thin toward the ridges (Fig. 3.16). The sag along the centerline of each basin is effectively a synclinal fold. The interlimb angle formed by successively younger deposits shows a progressive decrease upsection. For example, in basin B2, the interlimb angle of depositional sequence 6 is as small as 150°, whereas this amount progressively increases upwards to 170° and the deposits become almost flat (180° interlimb angle) within the upper portions of the seismic section (Fig. 3.16). This upward-flattening

architecture of the basin fill indicates that the tectonic regime which created the ridges and basins must still be active. Otherwise, the sediments deposited within the basins would have exhibited horizontal layering onlapping the flanks of the ridges. The upward-flattening architecture of the basin fill might also be ascribed to differential compaction. Hegarty et al. (1988) constructed a lithology-dependent porosity curve used for compaction correction (Fig. 3.11). The curves, particularly for coarse-grained sediments (sandstone), clearly show that the porosity loss due to compaction is very small (4%) for the first 500 m (Fig. 3.11). Throughout the study area, the maximum sediment thickness imaged in seismic profiles is not more than 520 m (Fig. 3.12). Furthermore, in basin B2, the thickness of the imaged depositional sequences does not exceed 150 m (Fig. 3.16). Additionally, each depositional sequence contains noticeably thicker upper subunits developed during global sea-level falls and is, accordingly, composed of coarse-grained sediments. Taking into account these observations, its reasonable to suggest that differential compaction contributed little to the upward-flattening architecture of basin fill. Instead, this architecture must result from syn-sedimentary tectonism.

In the study area, the overall NE–SW-trending ridge R1 ($\sim$ N35°E) can be tentatively correlated with the similar-trending Ezine Horst ($\sim$ N40°E). Alpar and Doğan (1999) also noticed the onland correlation of the ridges and basins off the Biga and Gelibolu peninsulas. Alpar and Doğan (1999) pointed out that most of the main E–W-trending ridges imaged in the area between the islands of Gökçeada and Bozcaada and the Aegean exit of the Strait of Dardanelles have similar-trending axes

to those on the Biga and Gelibolu Peninsulas. Given that the E–W-trending and NE–SW-trending fold axes within the northern and southern parts of the Island of Bozcaada have counterparts on the Biga and Gelibolu Peninsulas, it is reasonable to suggest that compressional forces are important.

Fault β_8, imaged in the southwestern portion of the study area, is a NE–SW-trending, SE-dipping major fault. It extends SW beyond the study area with a progressive increase in its normal-sense offset (Fig. 4.1). Traced to the northeast, the fault rapidly loses its expression. Fault β_8 created significant amounts of offset on the seabed, delineating the western boundary of basin B1. Detailed analysis of seismic reflection profiles along the fault reveals that fault β_8 is an oblique-slip fault (see section 4.1.1).

Taymaz et al. (1991) pointed out that the northeastern portion of the North Skyros Basin is connected to the straight northern coast of the Gulf of Edremit by narrow deep basins striking ENE (Fig. 6.3a). The bathymetric trend as well as the nodal plane obtained from fault plane solutions from the eastern segment of the North Skyros Basin clearly show a deviation from the northeasterly trend at the eastern end of the North Skyros Basin to an east–northeasterly trend toward the Gulf of Edremit (Fig. 6.3a). This overall trend perfectly matches with the N30°E strike and the nature of fault β_8 (cf. Figs. 6.3a and 4.1) and its oblique-slip character can be inferred to apply along the entire lineament. Mascle and Martin (1990) had also suggested that the Edremit trough extends westward north of the Island of Lesbos. They interpreted this trough as a NE–SW-trending asymmetric graben bounded along its southern side
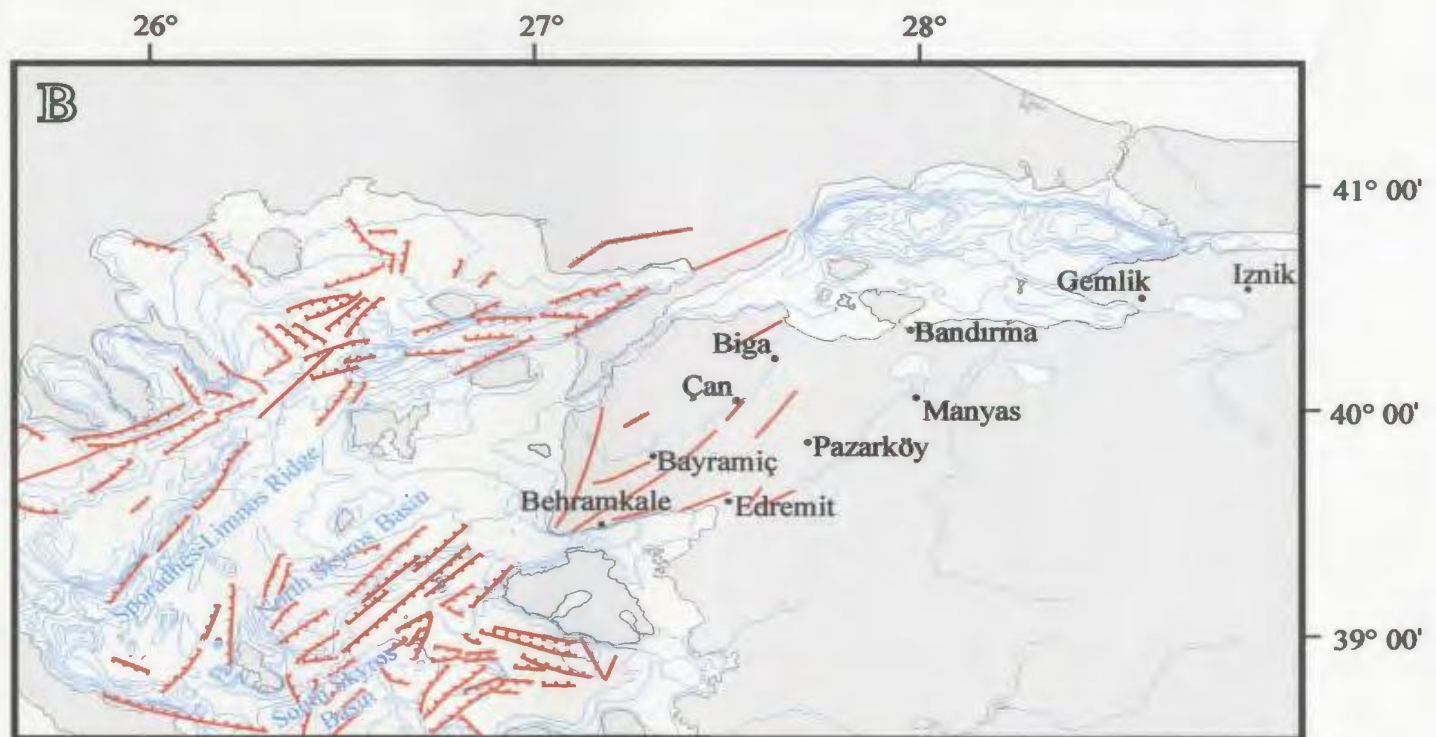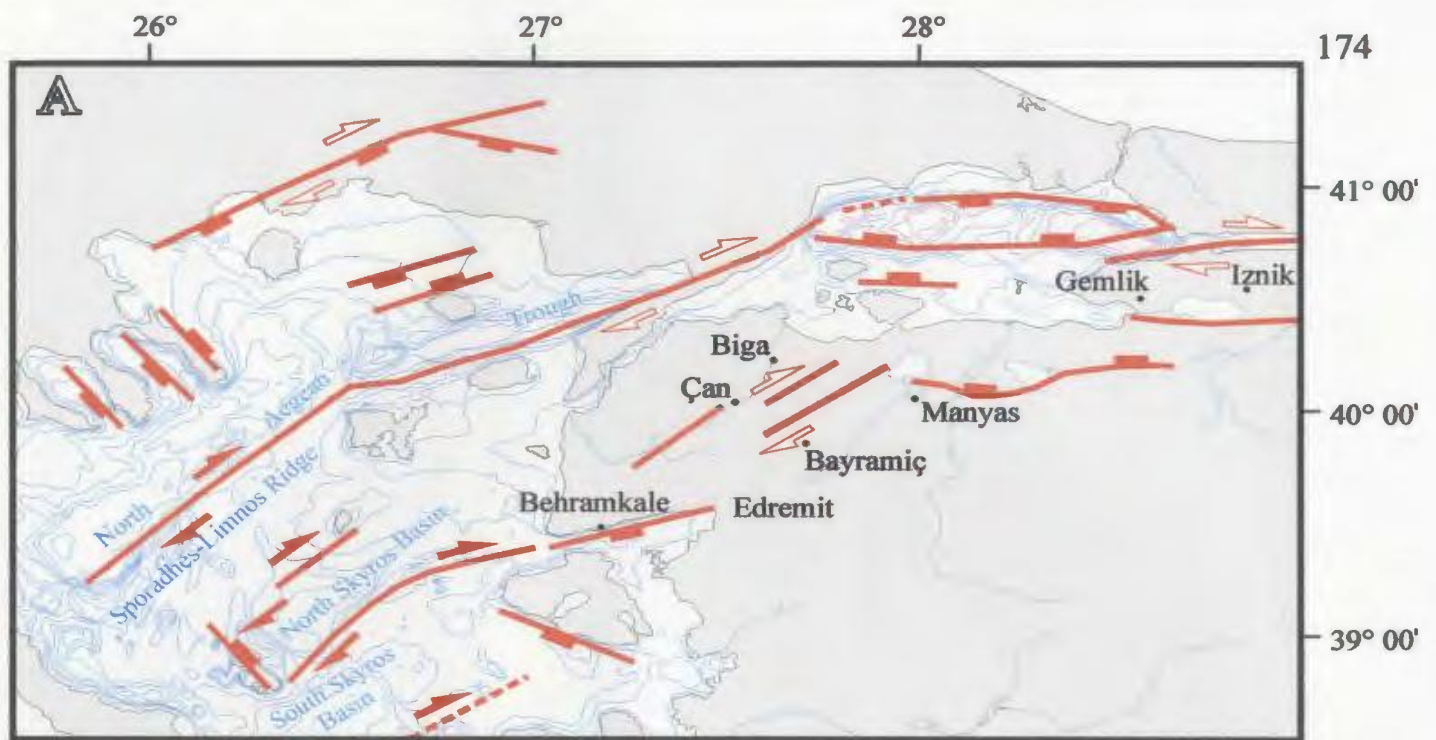
Figure 6.3. Maps showing the tectonic model suggested by Taymaz et al. (1991) (A) and the north and central Aegean Sea faults from Mascle and Martin (1990) (B).

by important normal faults showing strike-slip deformation of the sedimentary cover. The SE-dipping, NE–SW-trending major fault imaged on the north side of this graben by Mascle and Martin (1990) matches perfectly the trend of fault β_8. Moreover, the trends as well as the dip directions of the major faults on the Institute of Geology and Mineral Exploration (IGME) compilation permit the westward correlation of fault β_8. The major fault delimiting the southern edge of the Mansell Bank in that compilation extends from the southeastern end of the North Skyros Basin to the western end of the Gulf of Edremit (Fig. 6.4). The map trace of this major NE–SW-trending, SE-dipping normal fault clearly overlaps with that of fault β_8 which, in turn, allows a confident correlation of these two faults. These correlations clearly suggest that fault β_8 is the northeastward continuation of a major NE–SW-trending oblique-slip fault that extends as far southwest as the North Skyros Basin (Figs. 6.3a,b, 6.4).

The A_1 fault is a major SW-dipping normal fault, which creates a remarkable scarp on the seafloor. In the easternmost part of the study area, the fault extends with an ESE–WNW trend south of the Baba Burnu promontory (Fig. 4.1). It then deviates toward the northwest (N65°W) and finally merges with fault β_8 at its westernmost extremity. Boztepe-Günay et al. (2001) also recognized the same fault designated as A_1 in this study. They interpreted the fault as one of a number of synthetic normal faults related to a major fault seen on shore.

Fault A_1 seems to continue farther east beyond the study area. A lack of seismic data therefore precludes the eastward tracking and/or correlation of fault A_1
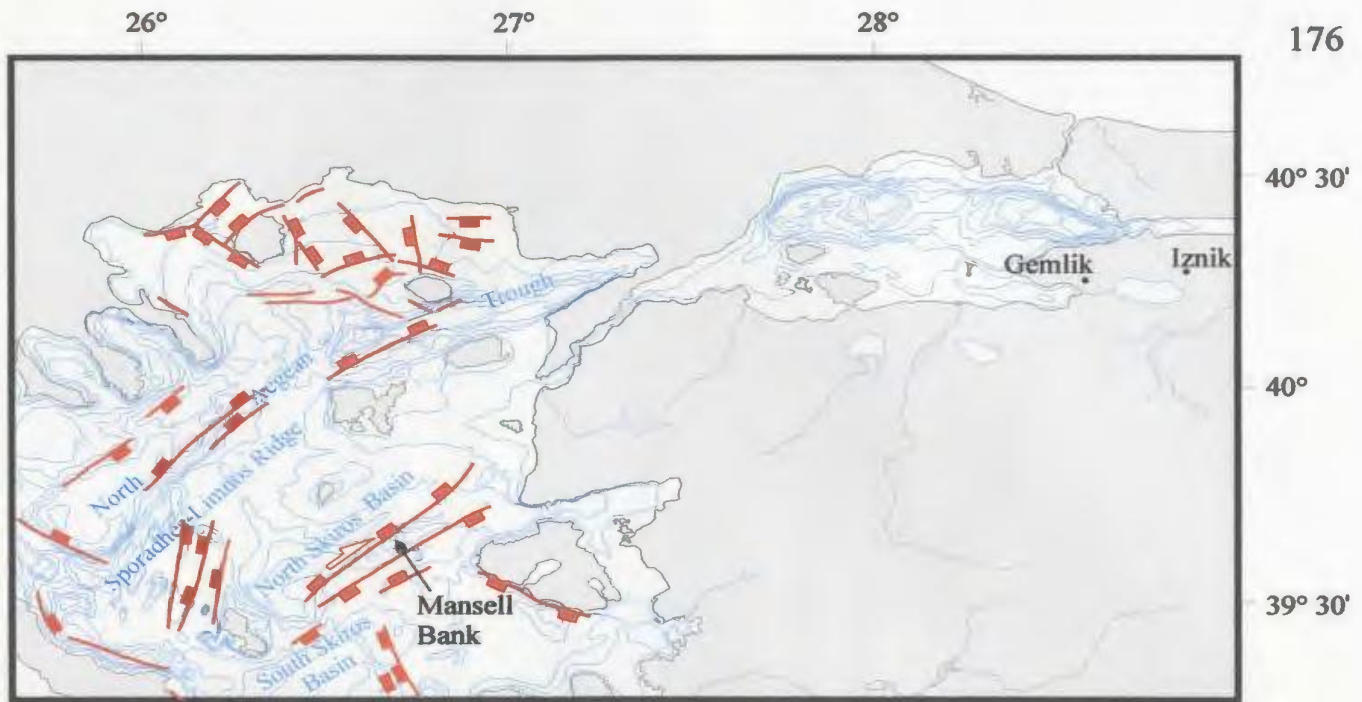
Figure 6.4. Major faults of the Northern Aegean Sea (faults from the Institute of Geology and Mineral Exploration-IGME).
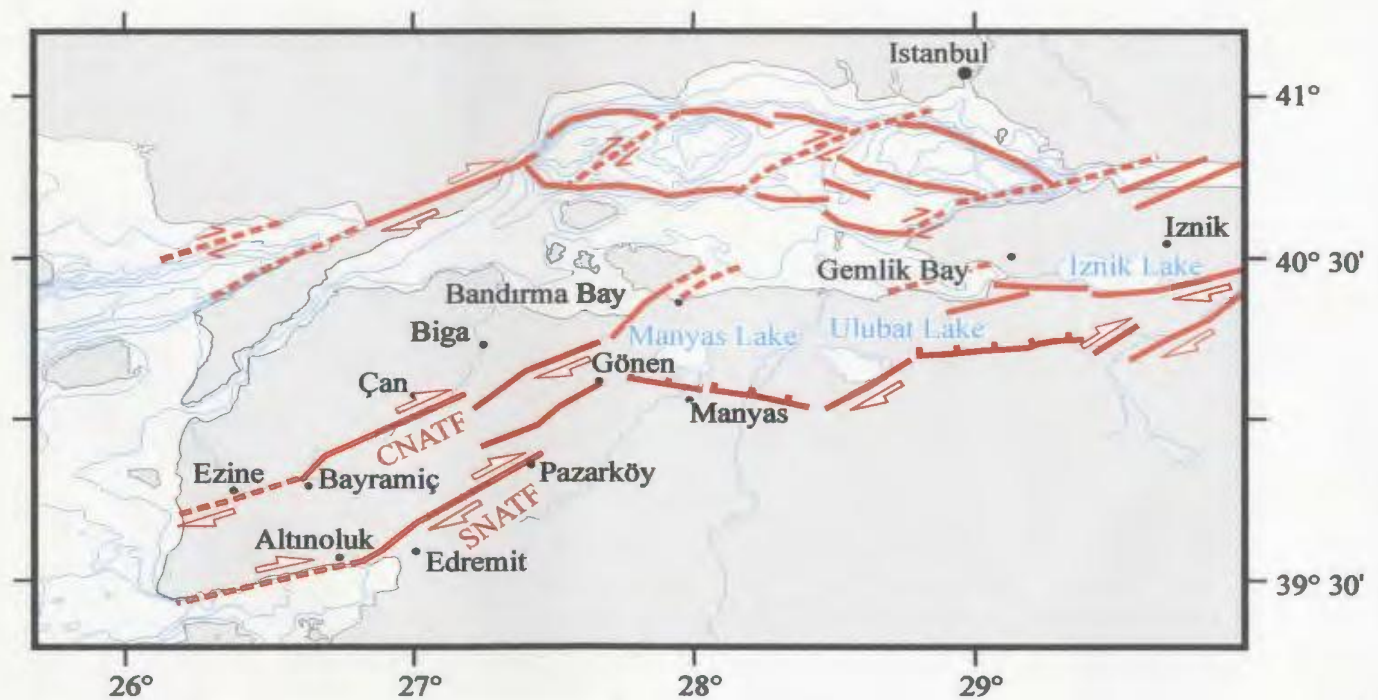
Figure 6.5. Map showing the central (CNATF) and southern (SNATF) branches of the North Anatolian Transform Fault (from Barka and Kadisky-Cade, 1988).

with faults on land. However, some characteristics of fault A_1 suggest its correlation with one of the branches of the North Anatolian Transform Fault in the Biga Peninsula. These include the E–W and NW–SE-striking map trace, significant displacement amounts along the fault, the existence of strike-slip deformation proximal to the fault, and its linkage with the SW-trending major fault β_8. The propagation path of the North Anatolian Transform Fault in the Biga Peninsula has been mapped by several authors. Barka and Kadinsky-Cade (1988) suggested that the North Anatolian Transform Fault bifurcates at Lake İznik. The central strand follows a southwesterly route and reaches the Aegean Sea at Ezine (Fig. 6.5). In the study area, the seismic profiles acquired along the west coast of the Biga Peninsula show no evidence for a major fault system trending E–W or NE–SW from Ezine. Therefore, it is clear that the western continuation of the central strand of the North Anatolian Transform fault does not emerge there as proposed by Barka and Kadinsky-Cade (1988).

The southern strand of the North Anatolian Transform Fault skirts the Ulubat and Manyas lakes, deviates toward the SW at the town of Gönen, continues on the same trend and reaches the Gulf of Edremit near Altınoluk. The fault then deflects toward the west, and delimits the northern coast of the Gulf of Edremit (Fig. 6.5). Yılmaz and Karacık (2001) also noticed this E–W-trending major fault with vertical displacements reaching as much as 500 m. Yılmaz and Karacık (2001) further pointed out a sinistral strike-slip component for this fault and interpreted it to be the northern bounding fault of the Edremit Graben. On the other hand, Yaltırak (2002,

2003) proposed that the central strand of the North Anatolian Transform fault, instead of reaching the Aegean Sea at Ezine, follows the coastline of the Marmara Sea from Gemlik Bay to Bandırma Bay. It then deviates southward into Bandırma Bay. On land, the overall direction of the fault segments extends in an NE–SW direction and propagate toward the Gulf of Edremit: major segments include the Edincik Fault, İnova-Sarıköy Fault, and Toluklar-Eskiyayla Fault (Fig. 6.1). The Toluklar-Eskiyayla Fault delimits the northern side of the Kazdağ Mountain. This fault then continues broadly with the same trend, finally reaching the Gulf of Edremit at Behramkale (Fig. 6.1; Yaltırak, 2003). Because there is no evidence for the seaward continuation at Ezine, it seems more reasonable to conclude that the central branch of the North Anatolian Transform Fault enters the Aegean Sea at the Gulf of Edremit.

The two different localities (Altınoluk versus Behramkale) for the seaward extrusion of the central branch of the North Anatolian Transform Fault bring about the following two possible alternatives which are equally valid.

(i) The central branch of the North Anatolian Transform Fault might deviate toward the west off Behramkale and continue farther westward along fault A_1 (Fig. 6.6A). In this case, the overall trend of the North Anatolian Transform Fault, starting from Behramkale extending as far as the North Skyros Basin, creates an ~ E–W then a NE–SW-trending, throughgoing map trace. The fault changes its direction west of the Baba Burnu promontory by a releasing bend based on its dextral-slip nature. This particular region (designated as Baba Burnu Basin in Figure 6.4) is interpreted as a rhomboidal pull-apart basin. It is well imaged in the seismic reflection profiles,
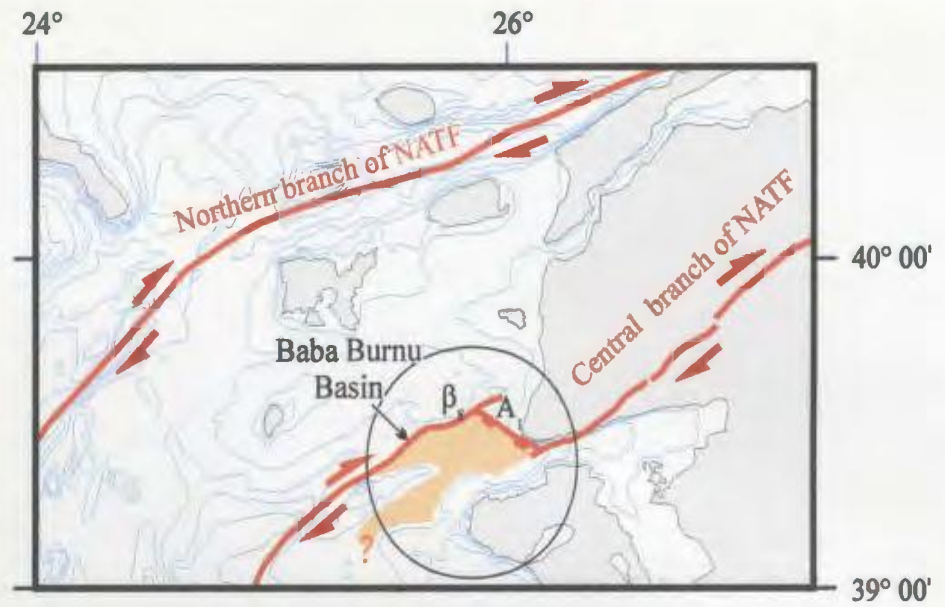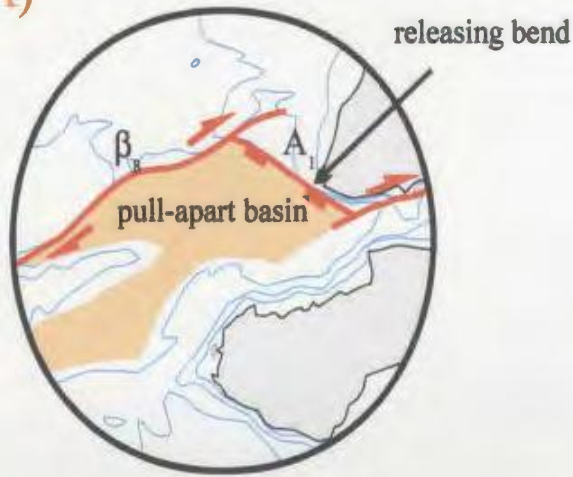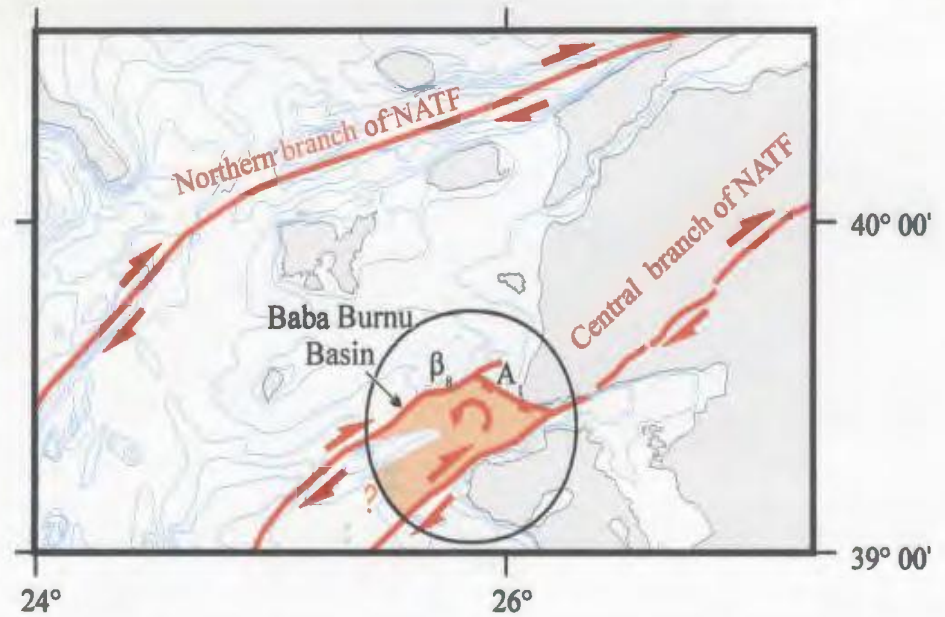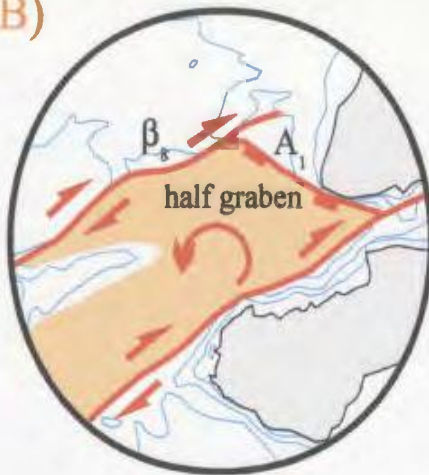
Figure 6.6. Models suggested in this study for the seaward continuation of the central branch of the North Anatolian Transform Fault.

bathymetry and 3D morphologic maps (Figs. 3.7, 3.8, 4.10–12,). However, the suggested geometry of the basin is speculative due to the lack of thesis data at its southern boundary.

(ii) The central branch of the North Anatolian Transform Fault might deflect toward the southwest off Behramkale, north of the Island of Lesbos, and extends farther southwestward beyond the study area (Fig. 6.6B). In that case, the Baba Burnu Basin remains situated between two dextral strike-slip faults, thus would be formed as a rotational half-graben.

It is also important to notice that the trend of the central branch of the North Anatolian Transform Fault is similar in the central Aegean Sea (i.e. North Skyros Basin) to the overall NE-SW trend of the northern branch of the North Anatolian Transform Fault in Saros Bay and North Aegean Trough (Fig.6.6 A, B).

The basin group faults are interpreted to be the consequence of the strike-slip faulting which dominates the region. This group of faults can be further divided into two subgroups depending on their locations. The ones confined to the Baba Burnu Basin are parallel to fault A_1 and their dip directions are mostly towards the major fault. These faults are interpreted to be the antithetic normal to oblique faults generated coeval with the development of the Baba Burnu Basin. The second subgroup of basin group faults are located on the northern and western side of faults A_1 and β_8. They trend obliquely to the major faults A_1 and β_8 and are interpreted to be the splays of these major faults. Detailed mapping shows that they merge with these faults along their strikes. Additionally, most of them exhibit thickness dissimilarities

in the hangingwall and footwall blocks which indicate either syn-sedimentary growth faulting or post-depositional oblique- slip faulting of a tapered wedge of strata (e.g. faults δ_2, δ_3, δ_7 in Figs. 4.2, 4.3).

The shelf group faults, occupying the northernmost portion of the study area, exhibit an overall fan shape map trace that widens progressively from the east toward the west (Fig. 4.1). These faults create negligible amounts of displacement along their fault planes and their tip lines are generally buried. They are oriented obliquely to the axes of the basins and cut the basement. They are interpreted to have been generated by dextral shear stress created by the North Anatolian Transform Fault.

6.2. Stratigraphic evolution

Several vertically stacked, broadly south-southwest-prograded depositional sequences are observed in the NE Aegean Sea, between the islands of Bozcaada and Lesbos and the Biga Peninsula. The successive development of younger depositional sequences atop older depositional sequences is the characteristic architecture of a rapidly subsiding shelf environment off a delta.

Depositional sequences 1–9 are confidently identified in seismic reflection profiles from the deeper portions of basin B1. However, the shallow depth of acoustic penetration and the detrimental position of the multiple where water depths are shallow prevented imaging of all the depositional sequences throughout the study area. Only isopach maps of depositional sequences from 2 to 6 could be constructed.

6.2.1. The determination of source

Possible source(s) for the terrigenous material delivered to the study area can be determined using detailed examination of the distribution and thickness variations of the depositional sequences observed on seismic profiles, paleogeographic maps constructed using the position of the topset-to-foreset transitions in depositional sequences, the global sea-level curve, estimated rates of tectonic subsidence, and the present-day drainage systems in the Biga Peninsula. The absence of a sufficiently large river (or rivers) that could account for the significant amount of terrigenous material contained within the depositional sequences, together with the wide regional distribution of the depositional sequences (extending beyond the study area) present the biggest challenges for the determination of the accountable river(s).

The fact that the depositional sequences were developed within broadly northeast–southwest- and northwest–southeast-trending basins separated by major ridges requires that the terrigenous clastics within each basin were transported independently by different rivers rather than by a single river. Several superimposed cut-and-fill structures created by these paleovalleys are present within basin B2 (Figs. 3.19, 3.20). The true dip-directions of the clinoforms calculated from different depositional sequences, and the trends of paleovalleys identified off the Biga Peninsula further support the idea that the sediments were transported by several rivers. The Tuzla, Karamenderes, and Dümbek Rivers are the most plausible sources for the sediments observed in depositional sequences 9–1. What volumes have these rivers delivered to the sea during the late Quaternary?

Calculation of the amount of sediment eroded from each drainage basin

requires the estimation of the original volume of rock stripped over the drainage area, above the elevation of the present interflueves as well as the volume removed from the incised valleys. Field observations in the Biga Peninsula show that, at present, the Bayramiç Formation is largely restricted to the drainage area of the Karamenderes River. In the most complete sections, and that it has an average thickness ranging between 50 and 150 m (Siyako et al., 1989). This formation is predominantly composed of poorly lithified fluvial sediments, including gravels, sands and silty-muds (Siyako et al., 1989). Limited biostratigraphic data suggest that the youngest age of the formation is earliest Pleistocene, or approximately 1.2 Ma (Siyako et al., 1989; Genç, 1998). Assuming that the original areal distribution of the Bayramiç Formation was also largely restricted to the present day Karamenderes drainage basin (e.g. Siyako et al., 1989; Yılmaz and Karacık, 2001) and that it had a pre-erosion average thickness of ~ 100 m, we can calculate the original volume of sediment that was present over this area, prior to exhumation and erosion in the Quaternary–Recent. The Karamenderes drainage basin covers an area of 1897 km^2 which would yield a total volume of 190 km^3. Assuming that the rate of erosion remained approximately constant for the last 1.2 Ma, the volume of sediment removed across this region during the last 330,000 years can be estimated. This volume, which excludes the volume associated with valley incision, is approximately 52.3 km^3. The Bayramiç Formation has its base near the tops of the present fluvial valleys. The valleys themselves are almost excessively carved into Oligo-Miocene rocks. The volume of the terrigenous material eroded during valley incision of these

older strata was calculated from digitized contour lines using 1:100000-scale topographic maps. A 3-D topographic image of the area was generated by using DTM (Digital Terrain Modelling) and GIS (Geographic Information System). From this detailed 3-D topographic image, the Karamenderes drainage divide was delineated. Then, using ERDAS software, the volume of the rock that must have been excavated from the river valley system was calculated. This calculation shows that the volume supplied by the Karamenderes River incision during the last 330,000 years was an additional 57.5 km^3, bringing the total sediment supply to 110 km^3.

Similar calculations reveal that the amounts of bedrock eroded since 330,000 yrBP from the drainage area, including river incision are 48 km^3 and 9.5 km^3 for the Tuzla and Dümbek drainage basins, respectively. Recall that the total volume of sediments needed to account for the material contained within the depositional sequences in basins B1, B2, B3 and B4 are 50.5 km^3, 51.2 km^3, 19.5 km^3, and 11.5 km^3, respectively (Table 3.1). The total estimated erosional contribution since 330,000 yrBP is 110+48+9.5 = 167.5 km^3. The total amount of detrital (excluding porosity) in the four basins is 50.5+51.2+19.5+11.5 = 132.7 km^3. The above first-order calculations clearly show that the late Quaternary yields of the Karamenderes, Tuzla and Dümbek rivers were more than adequate to deliver the required quantity of detrital material to the basins.

Today, the Karamenderes and Tuzla rivers are the two largest rivers that occupy the Biga Peninsula. The present Dümbek River is a tributary to the Karamenderes River (Fig. 6.7). However, tectonic studies in northwestern Turkey
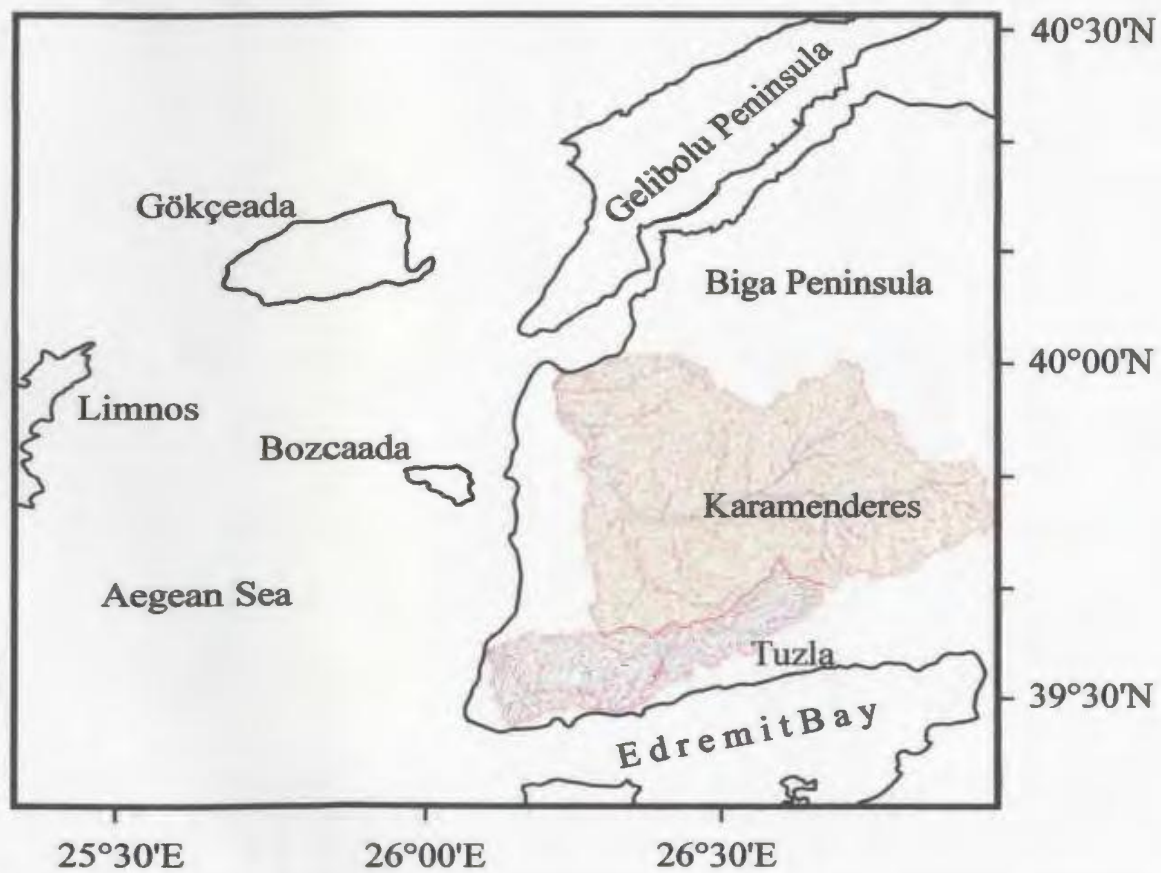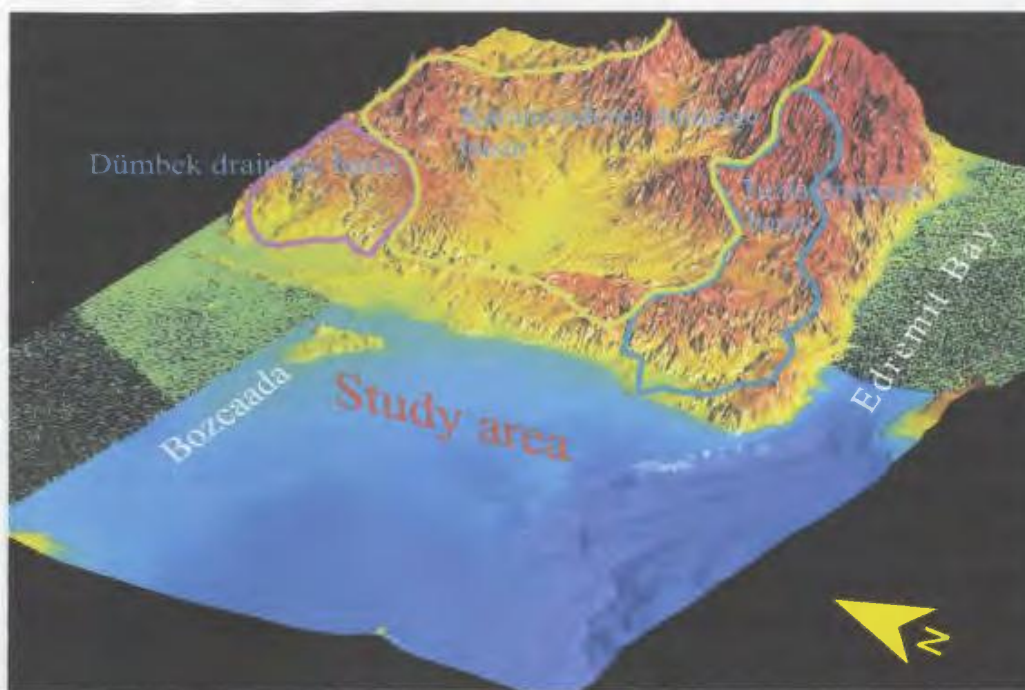
Figure 6.7. Map showing the 3D present-day topography and the drainage systems of the Biga Peninsula.

suggest that the paleoflow patterns of the Karamenderes and Dümbek rivers were different during the early-middle Quaternary than they are today: protracted tectonic uplift along the major NE–SW- trending fault in this region controlled the course of the rivers in their lower reaches. In contrast, the Tuzla River is situated away from the region of sustained tectonic uplift, and thus has not been affected by this tectonic activity and has presumably maintained its earlier paleoflow path until today.

The Tuzla River occupies the northern coast of Edremit Bay (Fig. 6.7). Today, it drains an elongate basin of ~504 km^2 (~52 km long and 12 to 8 km wide). The drainage basin is composed of nine fourth order and numerous third order drainage basins. In its upper and middle reaches, the Tuzla River follows a relatively smooth course and the channel gradient is about 1:54 and 1:166, respectively. Along the coastal plain, the lower 9 km of the river is meandering with a channel gradient of 1:420.

The Karamenderes River possesses the largest drainage basin in the region and occupies the majority of the Biga Peninsula (Fig. 6.7). Excluding the Dümbek tributary, it drains a basin of ~1897 km^2 (~73 km long, 36 to 6 km wide). Throughout the drainage basin, eight fourth order drainage basins feed the Karamenderes River. In its upper and middle reaches, the channel gradients are 1:51 and 1:200, respectively and the river is braided. Along its lower segment the Karamenderes River is meandering with a channel gradient of 1:340.

The Dümbek River has the smallest drainage basin among these three rivers and occupies the northwest portion of the Biga Peninsula (Fig. 6.7). The drainage

basin covers an area of ~ 238 km^2 (~31 km long and 14 to 5 km wide). The Dümbek River is braided in its upper reaches with a channel gradient of 1:67. In its middle reaches and along the coastal plain the channel gradients are 1:124 and 1:354, respectively and the river is meandering.

The characteristics of the Karamenderes, Tuzla and Dümbek rivers are given for the present drainage systems and topography of the region. However, since 330 kyr BP, there must have been some modifications in the riverine processes and the topography in response to palaeoenvironmental changes, such as regional tectonism, global eustasy and climate changes (pluvial/arid conditions). In some respects, climate and tectonism (e.g., uplifting) were probably the most influential of all the processes that affected the fluvial and delta systems in that it controlled the amount and variation in sediment supply.

Through the intervals of delta progradation during the successive eustatic sea-level falls associated with glacial oxygen-isotopic stages, there might have been a terrigenous influx to the study area through the Dardanelles. It has long been accepted that the Marmara Sea was periodically isolated from the Aegean Sea during glacial stages and became reconnected through the Dardanelles during interglacial (English, 1904; Pfannenstiel, 1944; Erol, 1987; Aksu et al., 1999). However, Yaltırak et al. (2002) used paleogeographic maps constructed using tectonic uplift rates deduced from U/Th dates of *in situ* shells from four localities along the coast of the Dardanelles to reveal that there has been a more complicated history of communication between the Aegean Sea and the Marmara Sea. Yaltırak et al. (2002)

postulated that, prior to glacial oxygen isotopic stage 8, the Marmara Sea was never isolated from the Aegean Sea, even when global sea level was low, because the floor of the Dardanelles was too deep early in its uplift history.

6.2.2. Delta progradation history and Paleogeography

Within the following pages, a comprehensive depositional history of the identified depositional sequences from 6-2 (since ~ 330 kyr BP) is described. The events are depicted with schematic cross-sections and paleogeographic maps showing the positions of the paleoshoreline and the flow patterns of the rivers during the successive glacial/interglacial cycles.

6.2.2.1. The transition from $\delta^{18}O$ stage 10 to stage 9 (342–330 kyr BP)

At ~ 340 kyr BP, sea level reached a lowstand of -94 m associated with glacial isotopic stage 10 (Imbrie et al., 1984). During this time, the shallow shelves, including floodplains of the rivers in the study area were subjected to intense subaerial erosion which contributed to the development of the shelf-crossing unconformity α_3 (Fig. 6.8b). The sea level started to rise at ~ 342 kyr BP ending the progradation of Subunit 7a of depositional sequence 7, and finalizing the development of u_3 as a transgressive ravinement surface (Fig. 6.8a).

During the transition from glacial isotopic stage 10 to interglacial isotopic stage 9 the global sea level rose from - 94 to - 3 m between 342 and 330 kyr at a rapid
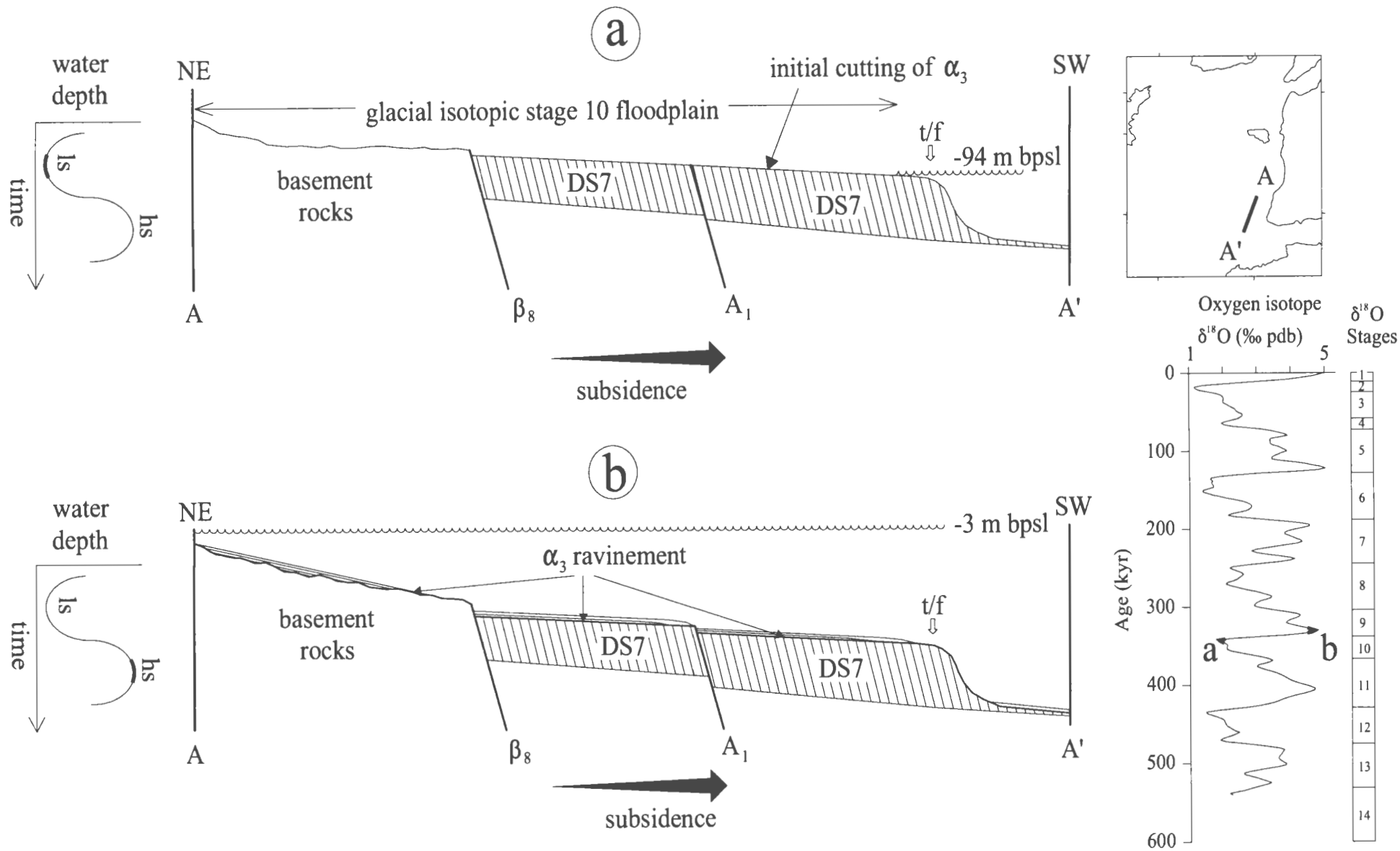
Figure 6.8. Schematic cross-sections from the eastern part of the study area showing the position of the paleo-sea level and shelf-crossing unconformity α3 during lowstand (ls) and highstand (hs) intervals ca. 342 and 330 kyr BP, respectively. bpsl=below present sea level, t/f=topset to foreset transition. A1 and β8 are the major faults discussed in Chapter 4.

rate of ~ 7.6 m/kyr. The nearshore currents and waves further eroded the shelf during this transgressive phase leading to the final development of the major shelf-crossing unconformity α_3. Delta progradation ceased during this time, and the coarser sediments carried by the river(s) as well as those eroded during the development of the ravinement were redistributed on the shelf by currents and waves, whereas the fines were dispersed into deeper basins in the northern Aegean Sea.

6.2.2.2. Isotopic stages 9 and 8 (330–250 kyr BP)

During the peak of interglacial isotopic stage 9 at ~ 330 kyr BP the sea level reached its highest level of - 3 m (Skene et al., 1988). Tectonic subsidence in the region (~ 0.9 m/kyr) together with the global sea-level rise, created a considerable amount of accommodation space. Isolation from the shoreline led to the deposition of a veneer of sediments originating from the distant active delta and from reworking of formerly deposited Subunit 7a deposits (Fig. 6.8b). This blanket of sediments probably filled the topographic lows (i.e., former incised valleys) created during the previous erosional stage. Figure 6.9 clearly shows that during the highstand interval, the paleo-shoreline migrated well into landward and a considerable part of the islands of Limnos, Bozcaada and Gökçeada, and the low lying regions of the Gelibolu and Biga Peninsulas were flooded.

The global sea-level curve shows that, during interglacial isotopic stage 9, the sea level experienced a 20 m drop from -3 m to -23 m and a subsequent rise from -23 m to -7 m between 330–320 kyr BP and 320–310 kyr BP, respectively (Fig. 5.13;

Figure 6.9. Map showing the position of the paleoshoreline (bold brown line) in the northern Aegean Sea and the Dardanelles during the maximum highstand of sea-level at ~ 310 kyr BP, when the sea level stood -7 m below its present level. Also shown is the present-day coastline (dot-dash lines). Isobaths in metres. The map is constructed using published topographic and bathymetric maps, corrected for subsequent uplift along the Dardanelles (e.g. Yaltırak et al., 2002) and subsidence along the shelf south of the Island of Bozcaada. The red and green dashed lines show the areas that are currently uplifting and subsiding, respectively (Cenk Yaltırak, pers. comm., 2005). Double-dotted yellow dashed line and '+', '-' signs show the Quaternary–Present boundary (pivot) between regional uplift and subsidence for the study area.

Skene et al., 1988). During these times, the Karamenderes, Tuzla and Dümbek Rivers had already retreated to their minimum extent and must have started to prograde seaward during the minor sea-level fluctuations (stadial and interstadial stages) of interglacial isotopic stage 9.

Through the interglacial stage 9 highstand, the Karamenderes, Tuzla and Dümbek rivers must have re-established a dynamic equilibrium with the environment landward of the present day shoreline. However, none of the reflection profiles show the presence of a highstand delta with its diagnostic sigmoidal- to complex oblique-sigmoidal internal seismic architecture typically observed at the mouths of moderate-size rivers along the Aegean coastline (Aksu et al., 1987). In contrast, deposits of the lower subunit of depositional sequence 6 are characterized by nearly flat-lying to gently seaward-dipping parallel reflectors which constitute Subunit 6b (Fig. 6.10a). The absence in the marine survey area of sigmoid prograded clinoforms implies that either these deposits are only preserved near the present-day shoreline (or as raised deposits) or they were subjected to intense subaerial erosion during the subsequent sea-level fall and were completely stripped away, being used for foreset progradation of the upper subunit, Subunit 6a, of depositional sequence 6.

Across the transition from the interglacial isotopic stage 9 to glacial isotopic stage 8, the Karamenderes, Tuzla and Dümbek rivers started to prograde farther seaward contemporaneous with the initiation of the global sea-level fall. The global sea-level started to fall from its highest level of -7 m to a low of ~ -88 m, but experienced two short intervals of sea-level rise (Figs. 6.10a,b; Skene et al., 1988).
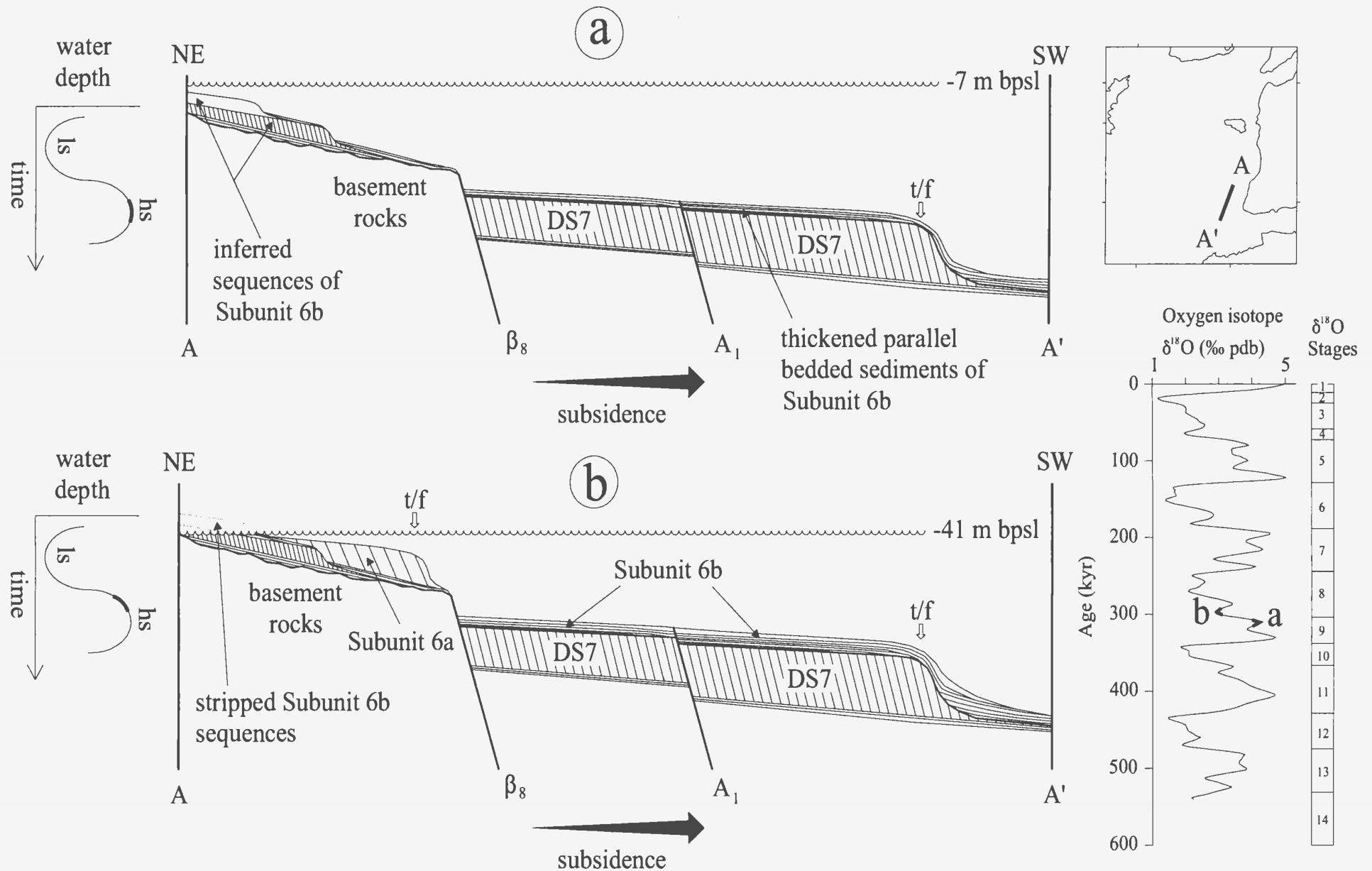
Figure 6.10. Schematic cross-sections from the eastern part of the study area showing the inferred squences of Subunit 6b and the early stages of Subunit 6a during highstand (hs) and lowstand (ls) of sea level ~ 310 and ~ 296 kyr BP, respectively. bpsl=below present sea level, t/f=topset to foreset transition. A1 and β8 are the major faults discussed in Chapter 4.

Between 310 and 296 kyr BP, the sea level displayed a continuous fall from -7 m to -41 m at a rate of 2.6 m/kyr (Fig. 6.10b). Through this period, the Tuzla River immediately swung toward the southwest into basin B1. Concurrently, the Karamenderes and the Dümbek rivers took a southwesterly course, passing southeast of the Island of Bozcaada and between the islands of Tavşan and Bozcaada, respectively. The rate of sea-level fall far exceeded the rate of subsidence; thus, no accommodation space was created on the former shelf during this period, and the Karamenderes, Tuzla and Dümbek deltas prograded as sediment largely bypassed the topset area, creating the well-imaged oblique-prograded foreset deposits. The progressive subaerial exposure of the former deltas must have created some erosion of the previously deposited sediments, providing more sediment for progradation (Fig. 6.10b).

The global sea-level curve shows that the sea level rose ~ 21 m between 296 and 286 kyr BP (Fig. 5.13; Skene et al., 1988). The rapidly rising sea level (1.75 m/kyr; Skene et al., 1988) was accompanied by subsidence of 0.9 m/kyr. The stability of the delta fronts in such a dynamic environment was controlled by an interplay between the rate of sediment discharge and the rate of addition of accommodation space created by the rising sea level and tectonic subsidence. Assuming that the rate of sediment discharge remained constant, the excess accommodation space created might have been completely filled by the deltaic sediments, in which case the deltas would show vertical aggravation. Alternatively, the deltas might have prograded seaward if the sediment discharge exceeded the accommodation space, but in this case

the topset-to-foreset transitions would rise seaward. A third possibility is that the delta would lose its dynamic equilibrium and the shoreline would retrograde. In this case, the sediments would be dispersed by longshore currents and waves, and accumulate as a thin veneer. The seismic reflection profiles show no evidence of topset beds generated during this ephemeral sea-level rise, suggesting that they were either never deposited or were stripped away and used for delta progradation during the subsequent sea-level fall from -20 m to -88 m between 285 and 270 kyr BP. During this regression, the high rate of sea-level fall (i.e., 4.1 m/kyr) surely created topset bypass and the prominent oblique-prograded clinoform architecture observed in Subunit 6a. During the lowstand between 270 and 250 kyr BP, the Gulf of Edremit and the region between the islands of Limnos, Gökçeada and the Baba Burnu Peninsula were all subaerially exposed (Fig. 6.11). The progradation of the Karamenderes, Tuzla, and Dümbek deltas must have decelerated and possibly halted during the 16 m sea-level rise that took place between 270 and 260 kyr BP. However, during the final stage of the sea-level fall, the deltas must have re-established a dynamic equilibrium with the environment and started to prograde. The youngest Subunit 6a foreset development occurred at -83 m below the present sea level at ~ 250 kyr BP, during the transition from glacial isotopic stage 8 to interglacial isotopic stage 7 (Fig. 6.12a). At this time of maximum lowstand, the Karamenderes, Tuzla and Dümbek rivers reached their maximum extent and prograded well into basins B1, B2, and B3, respectively (Fig. 6.11).

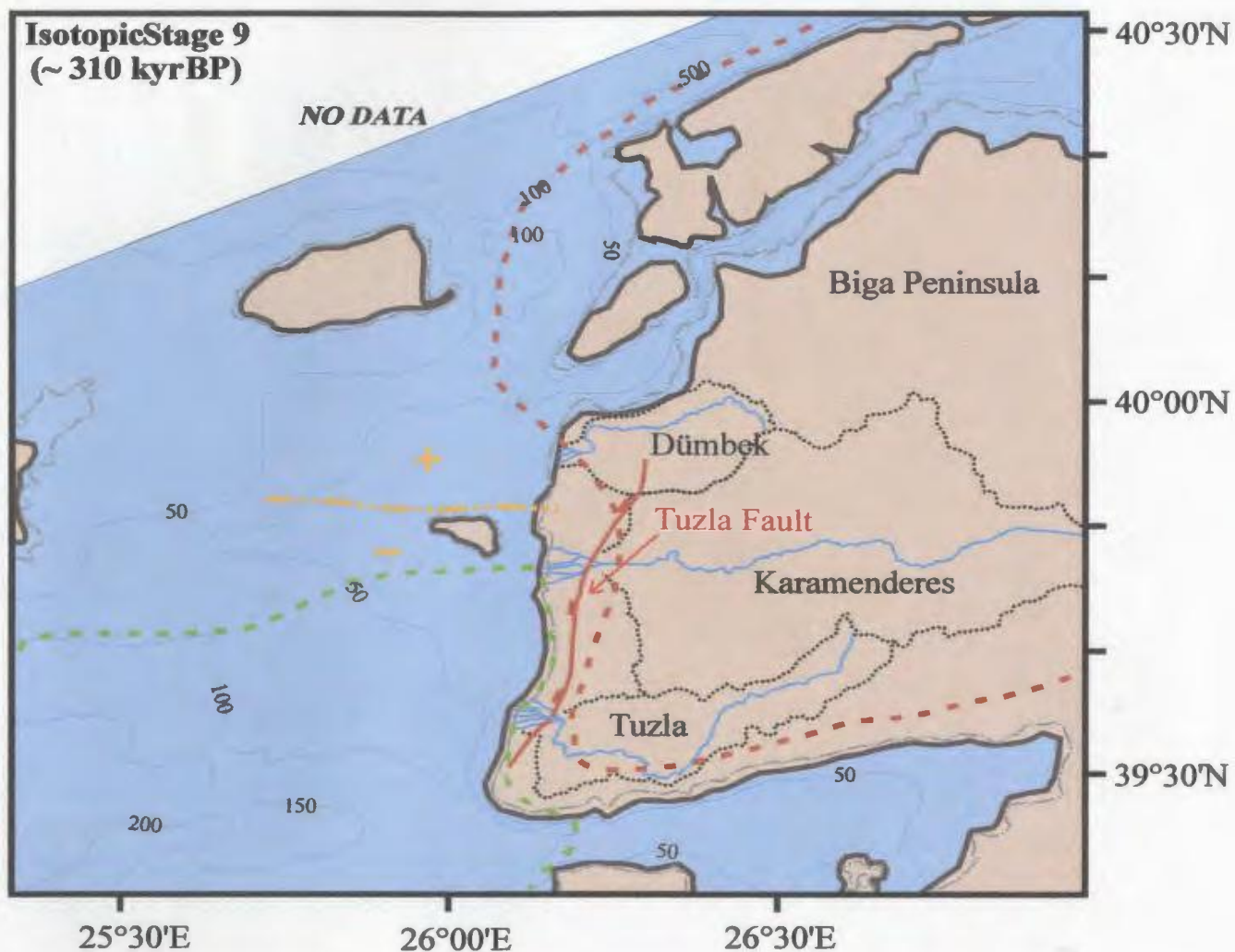**6.2.2.3. The transition from $\delta^{18}O$ stage 8 to stage 7 (250–238 kyr BP)**
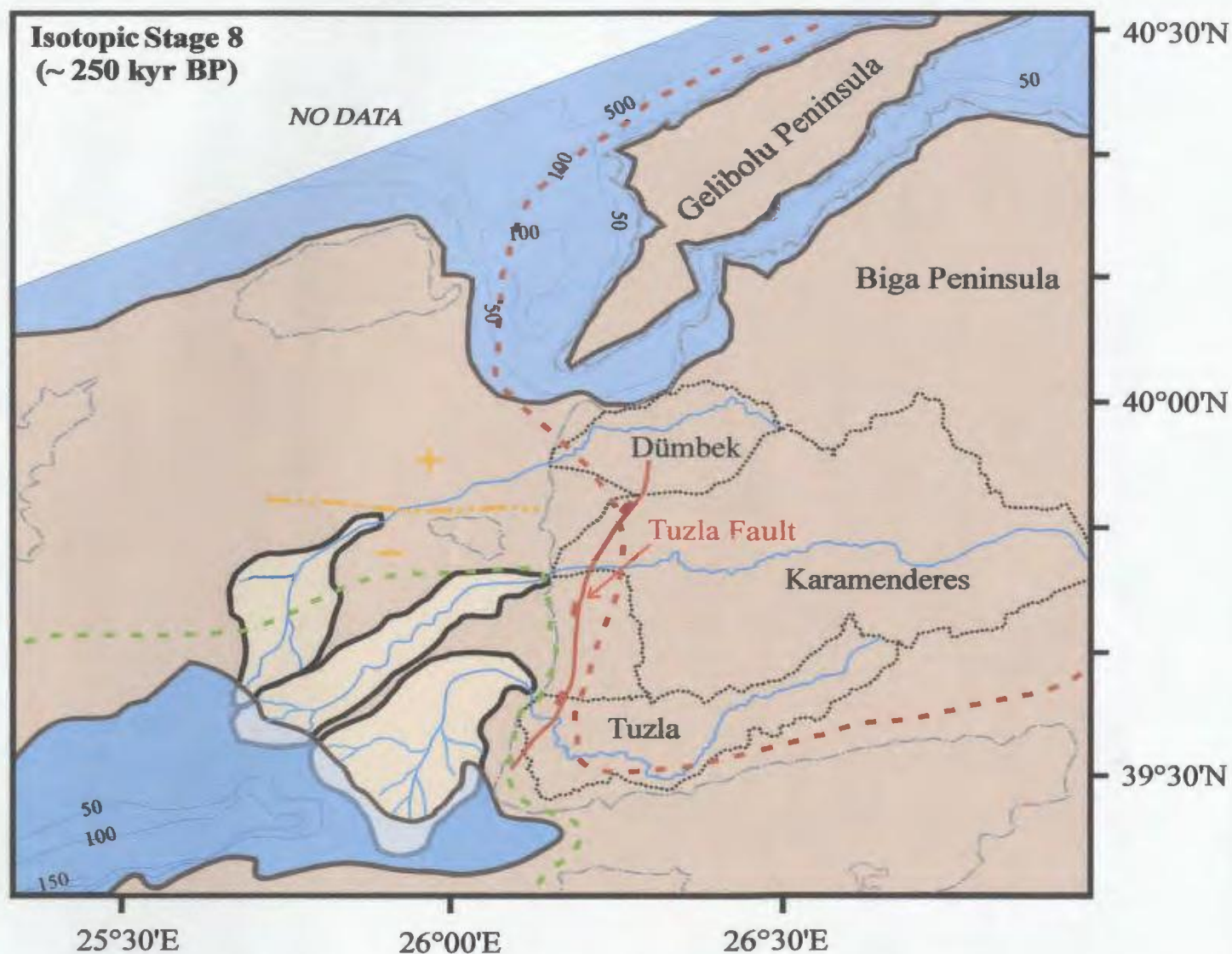
Figure 6.11. Map showing the position of the paleoshoreline (bold brown line)in the northern Aegean Sea and the Dardanelles during the maximum lowstand of sea-level ~ 250 kyr BP when the sea level stood ~ - 85 m below the present level. Also shown is the present-day coastline (dot-dash lines), isobaths in meters. The map is constructed using published topographic and bathymetric maps, corrected for subsequent uplift along the Dardanelles (e.g. Yaltırak et al., 2002) and subsidence along the shelf south of the Island of Bozcaada. The red and green dashed lines show the areas that are currently uplifting and subsiding, respectively (Cenk Yaltırak, pers. comm., 2005). Double-dotted yellow dashed line and '+', '-' signs show the Quaternary–Present boundary (pivot) between the regional uplift and subsidence for the study area.
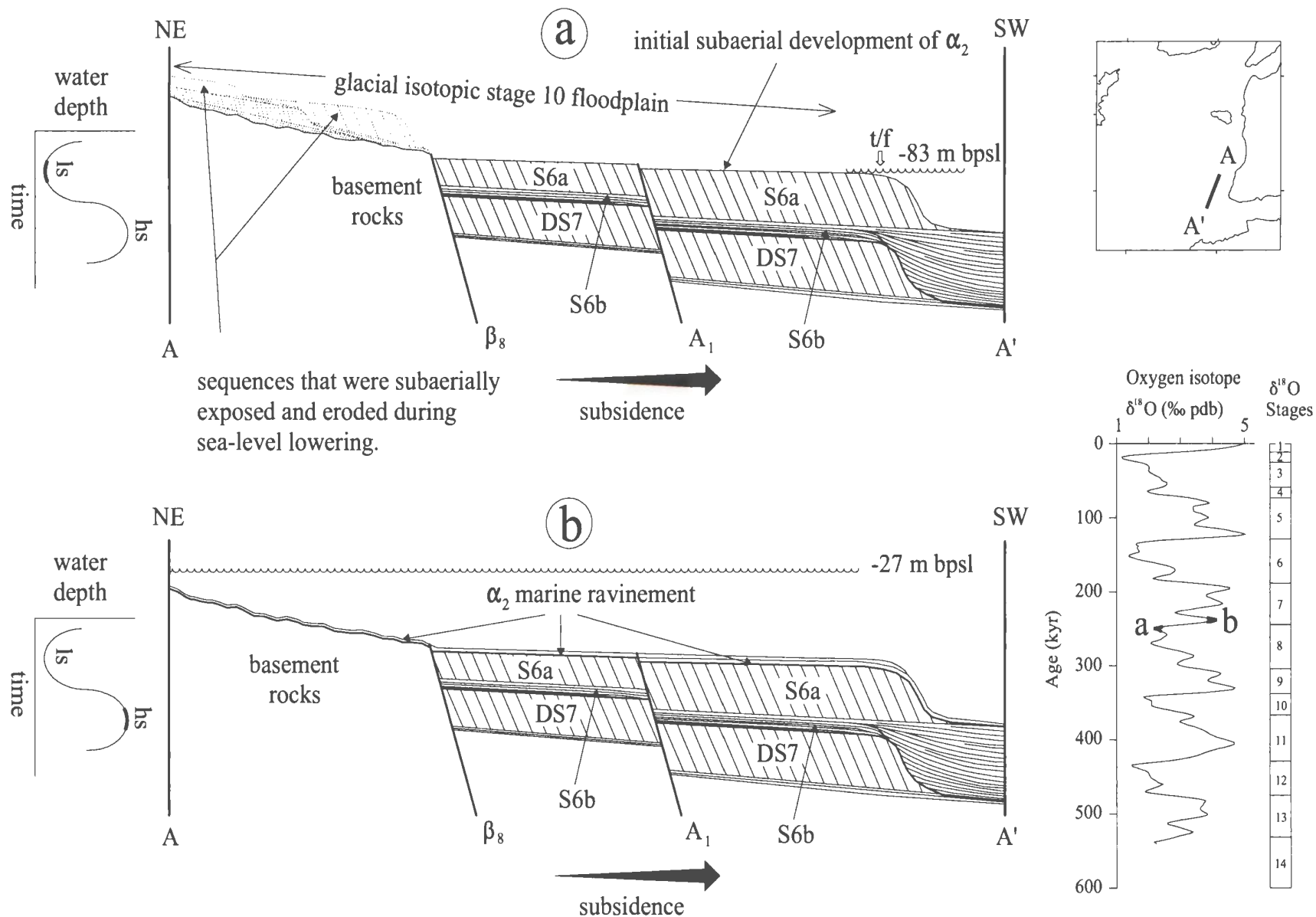
Figure 6.12. Schematic cross-sections from the eastern part of the study area showing the final stages of depositional sequence 6 and the development of the shelf-crossing unconformity α2 during maximum lowstand (ls, ~ 250 kyr BP) and highstand (hs, ~ 238 kyr BP) intervals, respectively. bpsl=below present sea level, t/f=topset to foreset transition. A1 and β8 are the major faults discussed in Chapter 4.

The global sea-level curve shows that during the transition from glacial isotopic stage 8 to interglacial isotopic stage 7 (i.e., between 250 and 238 kyr BP), the sea level rose from - 83 m to - 27 m at a rate of ~ 4.7 m/kyr (Fig. 6.11b; Skene et al., 1988). As the shoreline migrated landward, the Karamenderes, Tuzla and Dümbek rivers must have lost their equilibrium: the high rate of the sea-level rise, augmented by subsidence of ~ 1.1 m/kyr (Fig. 5.15; Table 5.3), far exceeded sediment discharge as indicated by the complete absence of any retrogradational and/or aggradational sequences in seismic reflection profiles. Hence, delta progradation initially slowed down and eventually stopped shortly after the onset of the sea-level rise. The coastal systems then rapidly withdrew landward. Through this transgressive phase, the former glacial isotopic stage 8 floodplain underwent substantial submarine erosion (i.e., ravinement; Fig. 6.12a). Sediments delivered from the source and those stripped from the upper portion of Subunit 6a were reworked by currents and waves and spread across the shelf to form a thin sheet of coarse sediment. By the end of the transgressive phase, the shelf-crossing unconformity α_2 was formed and the reworked sediments had accumulated as a thin blanket over the unconformity (Fig. 6.12b). During the subsequent highstand of sea-level, a large part of the islands of Limnos, Gökçeada and Bozcaada, as well as the low lying regions of the Gelibolu and Biga Peninsulas, were flooded (Fig. 6.13). Through this highstand sea-level period, the rivers must have re-established a dynamic equilibrium with the environment and started to prograde seaward depending on the rate of sediment input.

6.2.2.4. Isotopic stages 7 and 6 (238–135 kyr BP)
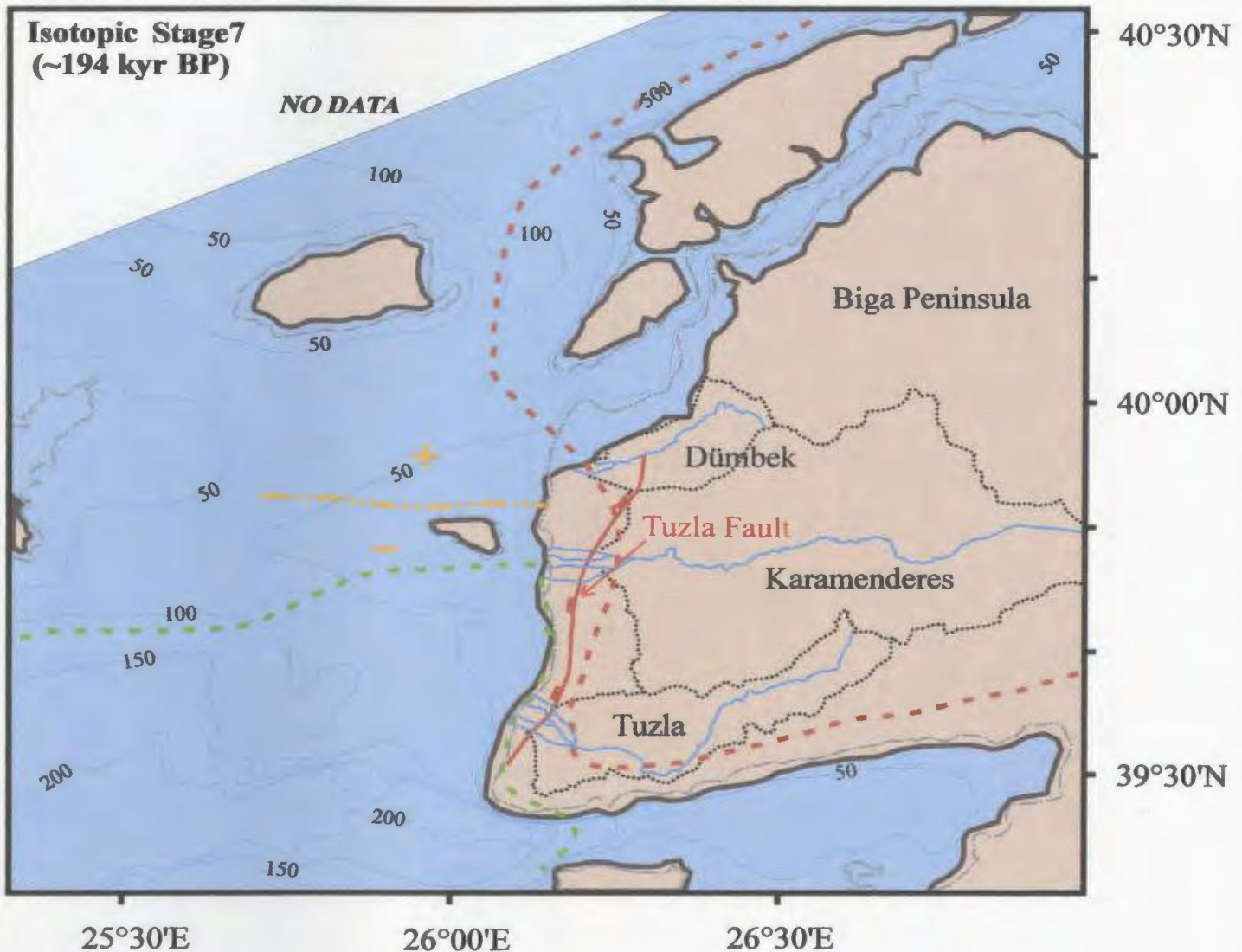
Figure 6.13. Map showing the position of the paleoshoreline (bold brown line) in the northern Aegean Sea and the Strait of Dardanelles during the maximum highstand of sea-level ~ 194 kyr BP when the sea level stood ~ - 7 m below present level. Also shown is the present-day coastline (dot-dash lines). Isobaths in metres. The map is constructed using published topographic and bathymetric maps, corrected for subsequent uplift along the Strait of Dardanelles (e.g. Yaltırak et al., 2002) and subsidence along the shelf south of the Island of Bozcaada. The red and green dashed lines show the areas that are currently uplifting and subsiding, respectively (Cenk Yaltırak, pers. com., 2005). Double-dotted yellow dashed line and '+', '-' signs show the Quaternary–Present boundary (pivot) between regional uplift and subsidence for the study area.

The global sea-level curve indicates large-scale fluctuations during interglacial isotopic stage 7, which are attributable to waxing and waning of ice stored on land (Chappell and Shackleton, 1986). During the early interglacial isotopic stage 7 between 238 and 228 kyr BP, the sea level dropped from -27 m to -65 m at a rate of 3.8 m/kyr (Fig. 6.8a). During this sea-level lowering, basinward advance of the Karamenderes, Tuzla, and Dümbek deltas accelerated. Because the rates of subsidence (0.4–1.1 m/kyr; Fig. 5.15; Table 5.3) were considerably lower than the rates of eustatic sea-level fall, river load most likely bypassed the delta plains and was deposited along the delta slopes. Hence, it is plausible to suggest that the older part of Subunit 5b was deposited downslope from a set of oblique- prograded clinoforms (Fig. 6.14a). During the subsequent sea-level rise between 228 and 216 kyr BP, any delta that had formed was subjected to intense wave-base erosion, and the sediments were distributed over a larger area of the shelf as a thin transgressive veneer (Fig. 6.14b). Between 216 and 194 kyr BP, the sea level initially dropped ~ 16 m but subsequently rose ~ 29 m. The Karamenderes, Tuzla, and Dümbek deltas possibly responded to these sea-level fluctuations, but apparently in minor ways. Depending on the rates of sediment input and relative sea-level rise (subsidence), the consequent deposits would be oblique and/or sigmoid prograded clinoforms, and thin veneers of hemipelagic or terrigenous muds accumulated during sea-level falls and rises, respectively (Fig. 6.14b). However, there is no evidence for these fluctuations in the seismic reflection profiles.

The only preserved sediments deposited during interglacial isotopic stage 7
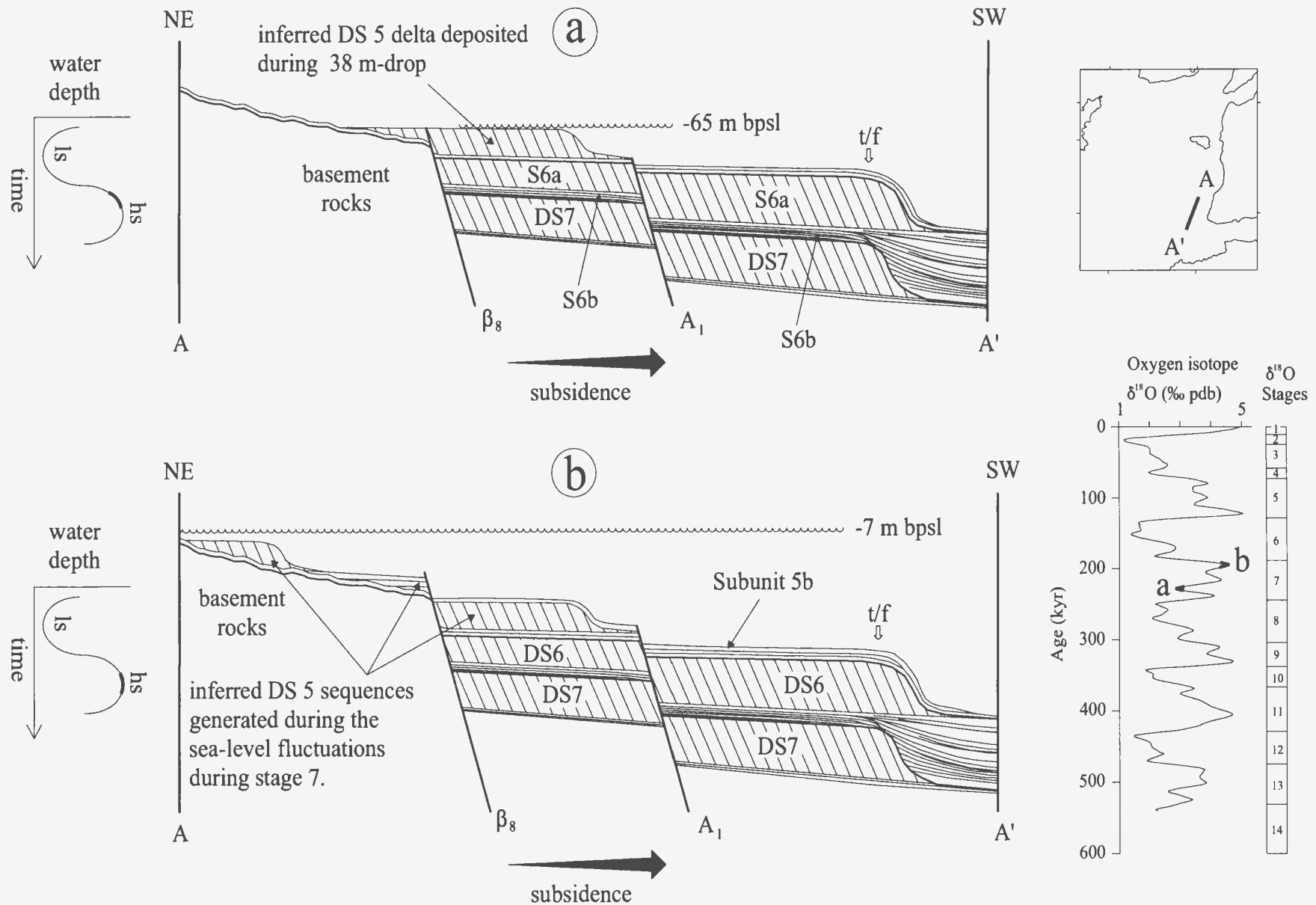
Figure 6.14. Schematic cross-sections from the eastern part of the study area showing the sequences formed during interglacial isotopic stage 7 between 228 and 194 kyr BP. bpsl=below present sea level, t/f=topset to foreset transition, ls=lowstand, hs=highstand. A1 and β8 are the major faults discussed in Chapter 4.

belong to Subunit 5b (Fig. 6.14). It is possible that any contemporaneous oblique-prograded deposits which formed during the short regressive intervals of isotopic stage 7 might have been mistakenly mapped as part of Subunit 5a, which mostly developed during the subsequent glacial isotopic stage 6. Otherwise, it is a reasonable assumption that they were just ephemeral features that were eroded during multiple fluctuations of sea level. The transition from interglacial isotopic stage 7 into glacial isotopic stage 6 at ~ 195 kyr BP is marked by a pronounced sea-level drop (Figs 6.14b, 6.15a; Skene et al., 1988). In fact ~ 66 m of sea-level fall (i.e., from -7 m to -73 m) is recorded in the global sea-level curve between 195 and 182 kyr BP, with an average rate of fall of 5.8 m/kyr. During this period, the Karamenderes, Tuzla, and Dümbek deltas rapidly shifted seaward. Throughout this interval of base-level fall, sediments bypassed the topsets of the deltas and accumulated as foresets, creating the observed oblique-prograded clinoform pattern of Subunit 5a (Figs. 6.14b, 6.15a).

The global sea-level curve shows that between 182 and 170 kyr BP, the sea level rose from -73 m to -46 m (Fig. 6.15b; Skene et al., 1988). During initial stages of this 2.1 m/kyr sea-level rise, delta progradation first slowed down and then stopped. In accordance with the rapid creation of the accommodation space, which was accompanied by subsidence, sediments were distributed over a larger area and were mostly deposited under low energy conditions as the shoreline retreated (Fig. 6.15b).

Between 152 and 135 kyr BP, sea level again fell and the shoreline reached its minimum isotopic stage 6 level of ~-100 m (Skene et al., 1988). During this lowstand
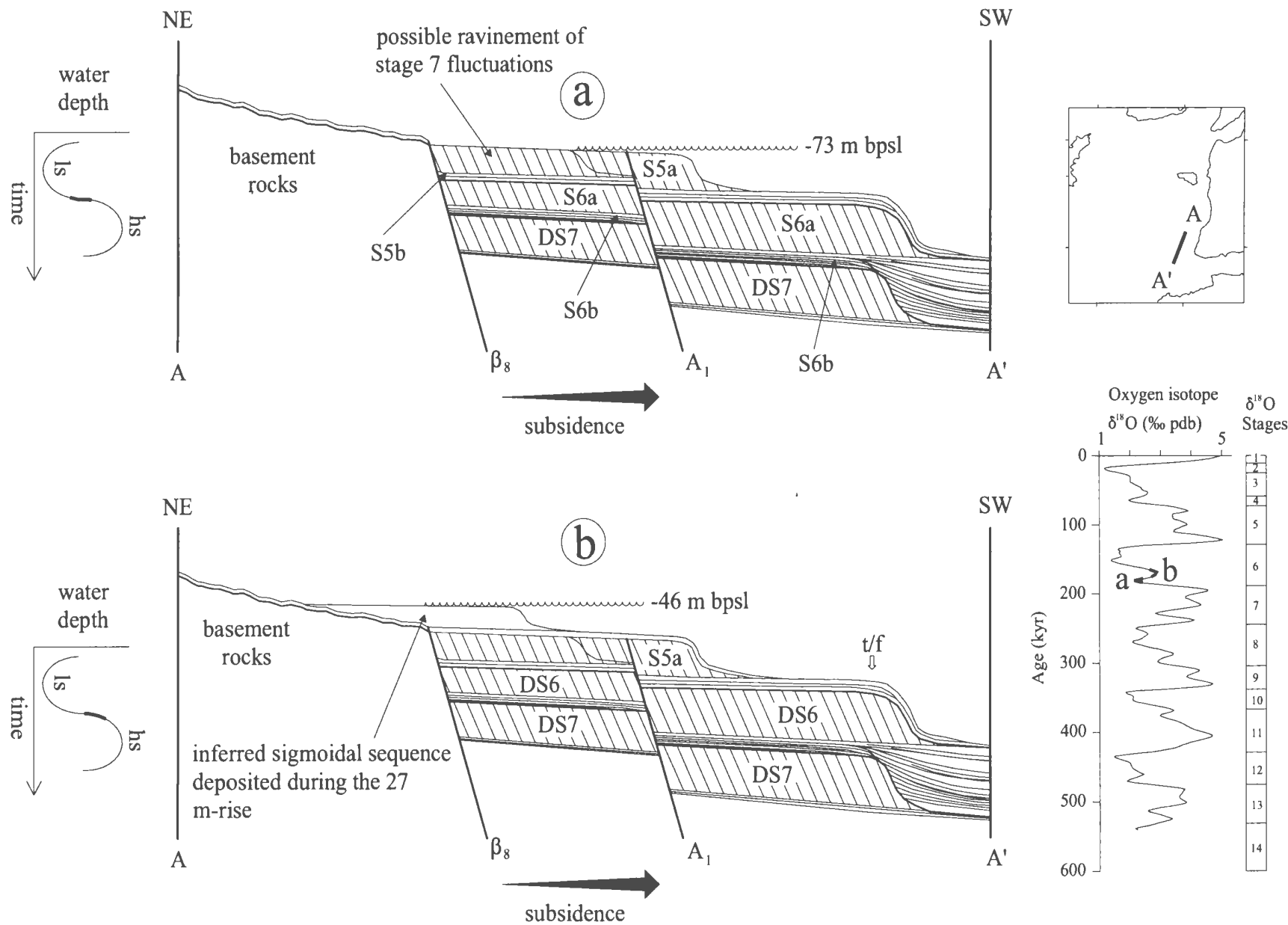
Figure 6.15. Schematic cross-sections from the eastern part of the study area showing the sequences developed during the early stages of the major regression, and the subsequent ephemeral sea-level rise between 182 and 169 kyr BP. bpsl=below present sea level, t/f=topset to foreset transition, ls=lowstand, hs=highstand. A1 and β8 are the major faults discussed in Chapter 4.

the Karamenderes, Tuzla, and Dümbek rivers were at a maximum extent. Their delta

plains including most of the shelf area were subaerially exposed (Fig. 6.16). The

youngest foreset beds in Subunit 5a of depositional sequence 5 were formed at ~135

kyr BP, immediately before the onset of the major transgressive phase associated with

the transition from isotopic stages 6 to 5 (Fig. 6.17a). The global sea-level curve

shows a lower lowstand for stage 6 than for stage 8 (Skene et al., 1988). Accordingly,

the maximum progradation limit of Subunit 5a is expected to be farther seaward than

that of Subunit 6a. However, seismic reflection profiles (e.g., Figure 5.14) clearly

show that the topset-to-foreset transition of Subunit 6a is situated farther seaward.

This inconsistency can be explained by different amounts of relative sea-level rise

caused by subsidence. The subsidence rate during the development of depositional

sequence 6 must have been greater than during the development of depositional

sequence 5. Higher subsidence rates, creating more accommodation space over a

protracted period of time, allowed the deltas to prograde farther seaward.

6.2.2.5. The transition from $\delta^{18}O$ stage 6 to stage 5 (135–122 kyr BP)

The global sea-level curve shows that during the transition from glacial

isotopic stage 6 to interglacial isotopic stage 5 (i.e., between 135 and 122 kyr BP), the

sea level rose from -102 m to +7 m at a rate of 7.3 m/kyr in response to waning of ice

stored on land (Figs. 6.17a, 6.17b; Skene et al., 1988). The sea-level rise, augmented

by subsidence of 1.1 m/kyr (Fig. 5.15; Table 5.3), ensured that the Karamenderes,
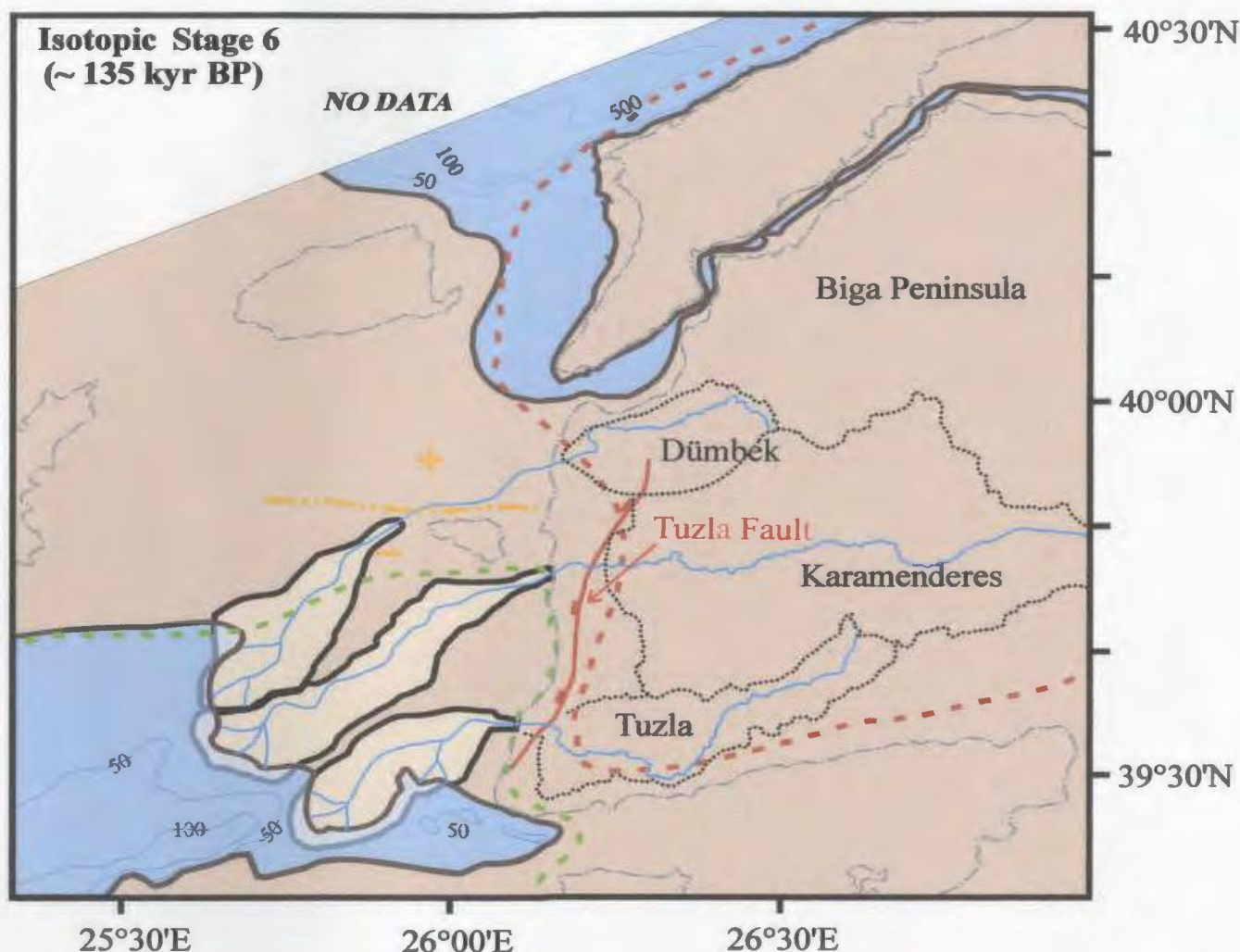
Figure 6.16. Map showing the position of the paleoshoreline (bold brown hachure) in the northern Aegean Sea and the Dardanelles during the maximum lowstand of sea-level ~ 135 kyr BP when the sea level stood ~ - 102 m below present level . Also shown is the present-day coastline (dotted dash lines). Isobaths in metres. The map is constructed using published topographic and bathymetric maps, corrected for subsequent uplift along the Dardanelles (e.g. Yaltırak et al., 2002) and subsidence along the shelf south of the Island of Bozcaada. The red and green dashed lines show the areas that are currently uplifting and subsiding, respectively (Cenk Yaltırak, pers. comm., 2005). Double-dotted yellow dashed line and '+', '-' signs show the Quaternary–Present boundary (pivot) between regional uplift and subsidence for the study area.
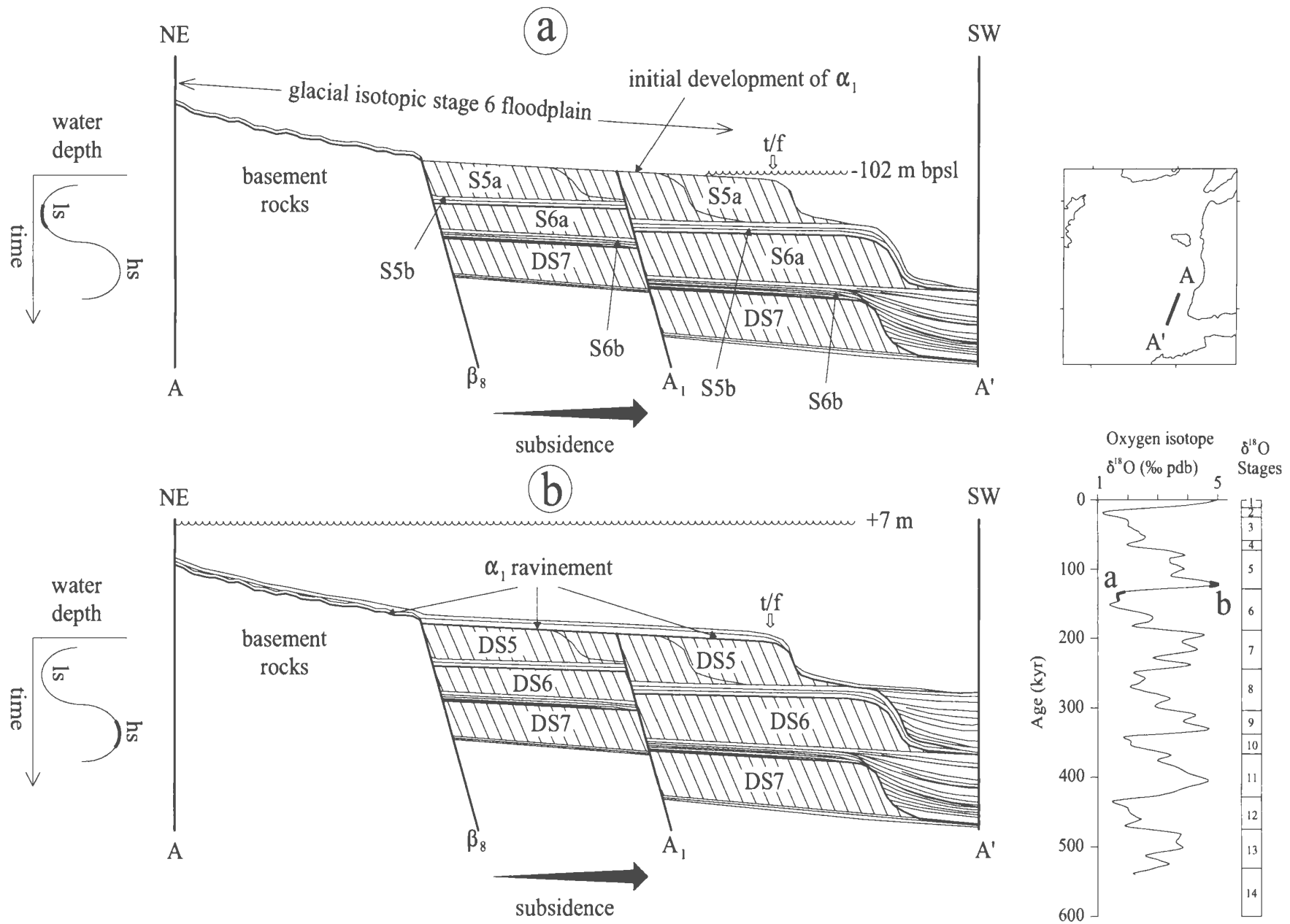
Figure 6.17. Schematic cross-sections from the eastern part of the study area showing the development of depositional sequence 5 and the shelf-crossing unconformity α1 during maximum lowstand (ls) and highstand (hs) sea-levels at 135 and 122 kyr BP, respectively. bpsl=below present sea level, t/f=topset to foreset transition. A1 and β8 are the major faults discussed in Chapter 4.

206

Tuzla, and Dümbek deltas could not track the rapid landward migration of the shoreline. Thus, delta progradation stopped and river ,mouths stepped rapidly landward. Prior to this transgressive phase, the majority of the shelf area was subaerially exposed and was subjected to significant subaerial erosion, initiating the development unconformity α_1 (Figs. 6.17a, 6.18). During the transgression, intense ravinement completed the development of the shelf-crossing unconformity α_1 (Fig. 6.17b).

6.2.2.6. Isotopic stages 5 and 4 (122–63 kyr BP)

The global sea-level curve shows that during interglacial isotopic stage 5, the sea level fluctuated significantly, but generally remained near its present level at the peak of the interstadial stages (Fig. 6.19; Skene et el., 1988). Between 122 and 110 kyr BP, the sea level dropped from its highest stand of +7 m (stage 5e) to -35 m (stage 5d), at a rate of 2.3 m/kyr (Fig. 6.20a). As the coastline started to migrate seaward, the Karamenderes, Tuzla, and Dümbek deltas re-established a dynamic equilibrium with the environment and started to prograde. The rate of sea-level lowering was higher than the rate of subsidence (0.4 m/kyr; Fig. 5.15; Table 5.3), so sediments bypassed the topset-to-foreset transitions of the deltas and accumulated along the delta slopes as foresets. The limited accommodation space created during this minor regression might have been suitable for the deposition of topset beds; thus, the deltas likely produced sigmoid prograded clinoforms near the present-day shoreline (Fig. 6.20a). During the following phases of sea-level rise/fall (stages 5a–c), the

Figure 6.18. Map showing the position of the paleoshoreline (bold brown line) in the northern Aegean Sea and the Dardanelles during the maximum highstand of sea-level ~ 122 kyr BP when the sea level stood ~ +7 m above the present level. Also shown is the present-day coastline (dotted dash lines). Isobaths in metres. The map is constructed using published topographic and bathymetric maps, corrected for subsequent uplift along the Dardanelles (e.g. Yaltırak et al., 2002) and subsidence along the shelf south of the Island of Bozcaada. The red and green dashed lines show the areas that are currently uplifting and subsiding, respectively (Cenk Yaltırak, pers. comm., 2005). Double-dotted yellow dashed line and '+', '-' signs show the Quaternary–Present boundary (pivot) between regional uplift and subsidence for the study area.
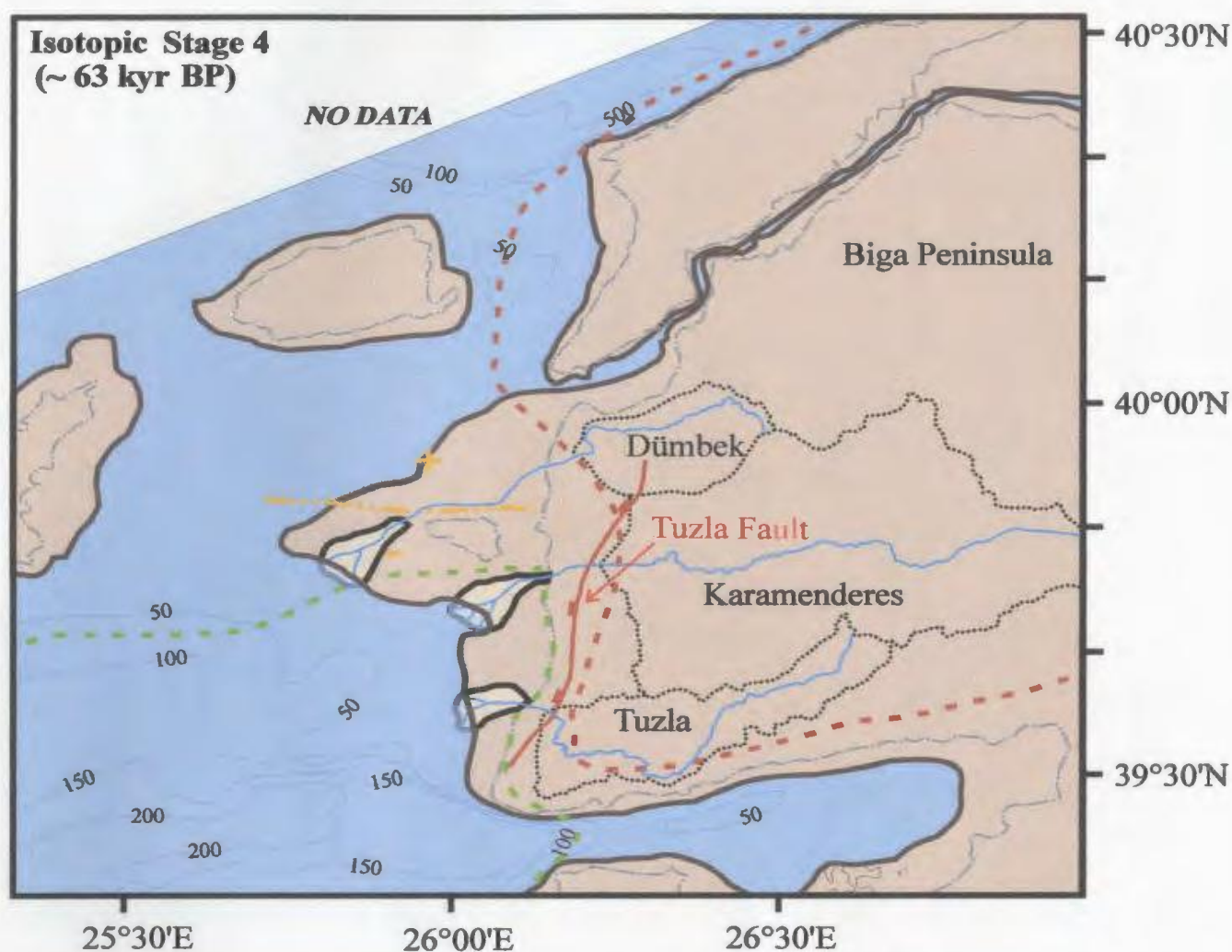
Figure 6.19. Map showing the position of the paleoshoreline (bold brown line) in the northern Aegean Sea and the Dardanelles during the maximum lowstand of sea-level ca. 63 kyr BP when the sea level stood ~ - 56 m below the present level . Also shown is the present-day coastline (dotted dash lines). Isobaths in metres. The map is constructed using published topographic and bathymetric maps, corrected for subsequent uplift along the Dardanelles (e.g. Yaltırak et al., 2002) and subsidence along the shelf south of the Island of Bozcaada. The red and green dashed lines show the areas that are currently uplifting and subsiding, respectively (Cenk Yaltırak, pers. comm., 2005). Double-dotted yellow dashed line and '+', '-' signs show theQuaternary–Present boundary (pivot) between regional uplift and subsidence for the study area.
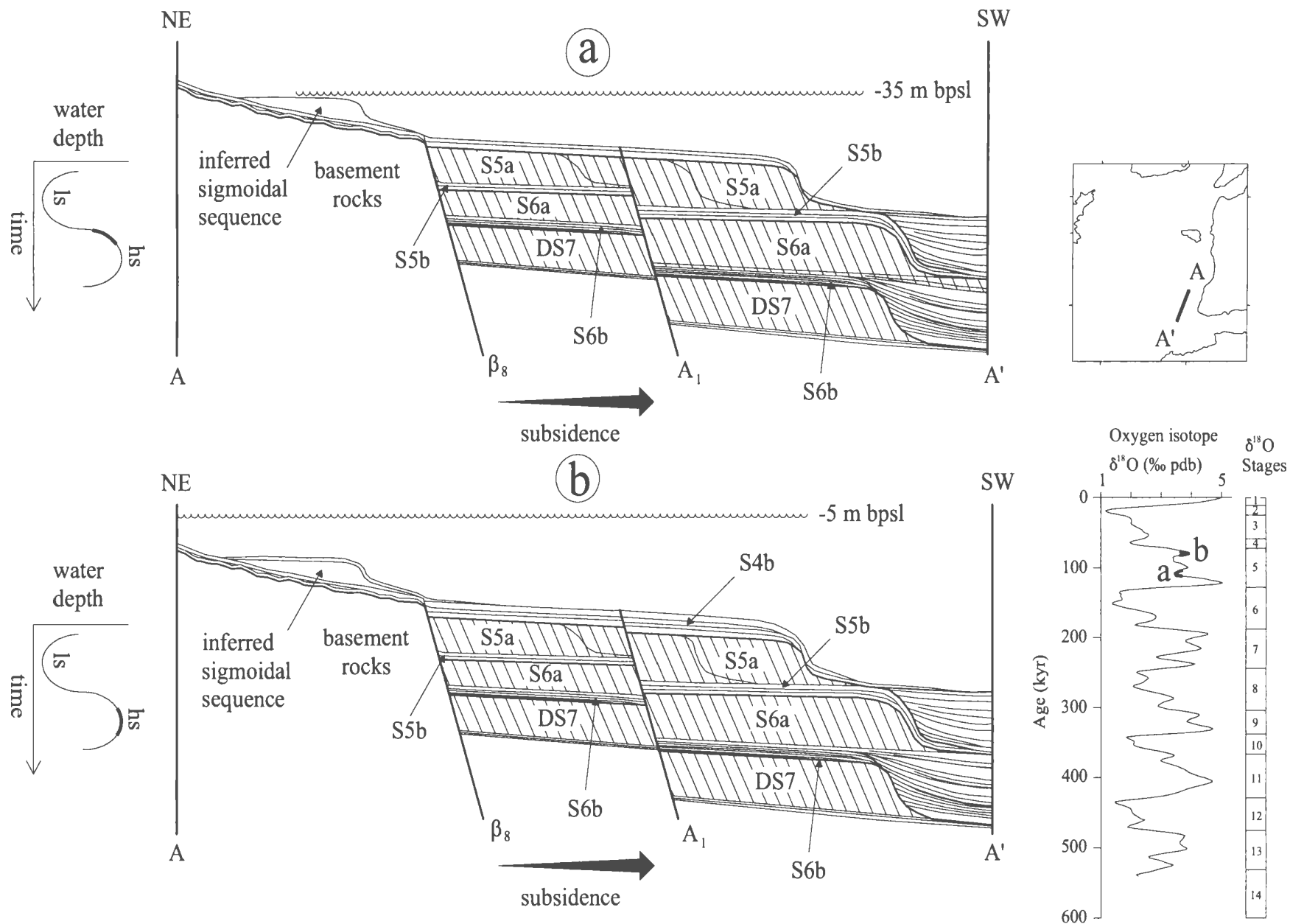
Figure 6.20. Schematic cross-sections from the eastern part of the study area showing the retrogressive sequence and the parallel bedded sediments deposited during the highstand of sea level between 110 and 80 kyr BP. bpsl=below present sea level, ls=lowstand, hs=highstand

Karamenderes, Tuzla, and Dümbek deltas likely reacted to these fluctuations in minor ways. Depending on the rates of terrigenous influx and relative sea-level change the resulting deposits would be oblique- and/or sigmoid- prograded clinoforms and thin veneers of prodelta sediments formed during sea-level drops and rises respectively (Fig. 6.20b). Sediments deposited during interglacial isotopic stage 5 are represented by Subunit 4b. Contemporaneous clinoforms have not been recognized in the study area.

The transition from interglacial isotopic stage 5 to glacial isotopic stage 4 began at ~ 74 kyr BP. The global sea-level curve shows that sea level experienced a continuous drop from -5 m to -56 m between 74 and 63 kyr BP at a rate of 3 m/kyr (Figs. 6.20b, 6.21a). The Karamenderes, Tuzla, and Dümbek deltas started to rapidly shift seaward to follow the receding shoreline. Because subsidence rates were small (0.3–0.4 m/kyr), accommodation space was lost and topsets could not form. Sediments delivered to the shoreline by the river largely bypassed the delta plain and were used entirely for foreset development, forming the oblique-prograded clinoforms of Subunit 4a. The youngest foreset bed was generated 56 m below the present sea level at ~ 65 kyr BP, immediately prior to the transgressive phase associated with the transition from glacial isotopic stage 4 to interstadial isotopic stage 3.

6.2.2.7. The transition from $\delta^{18}O$ stage 4 to stage 3 (63–52 kyr BP)

The global sea-level curve shows that sea level rose from -56 m to -32 m between 63 and 52 kyr BP (Figs. 6.21a, 6.21b; Skene et al., 1988). With this sea-level

Figure 6.21. Schematic cross-sections from the eastern part of the study area showing the final stages of the development of depositional sequence 4 and the shelf-crossing unconformity α0 at 63 and 52 kyr BP, respectively. bpsl=below present sea level, ls=lowsatnd, hs=highstand, t/f=topset to foreset transition. A1 and β8 are the major faults discussed in Chapter 4.

rise, the progradation of the Karamenderes, Tuzla, and Dümbek deltas gradually decelerated and terminated. The shoreline experienced a rapid landward migration. Accordingly, sediments were distributed over a much larger area by currents and waves. During the lowstand and through the following transgressive phase, the glacial isotopic stage 4 floodplain was subjected to significant subaerial/submarine erosion which resulted in the development of shelf-crossing unconformity α_0 (Figs. 6.20a; 6.21b).

6.2.2.8. Isotopic stage 3 (52–28 kyr BP)

During the interstadial isotopic stage 3, the Karamenderes and Dümbek rivers changed their courses due to tectonic activity along the major NE–SW-trending, west-dipping normal Tuzla Fault (Yaltırak, 2003; pers. comm., 2005; Fig. 6.22). The displacement along the fault prevented the rivers from maintaining their previous courses along their lower reaches. Tilting of the footwall fault block obliged the Karamenderes and Dümbek rivers to deviate toward the northwest. After this alteration in course, the rivers most likely started to follow their present-day flow patterns where the Dümbek River became one of several tributaries of the Karamenderes River (Figs. 6.7, 6.22). Whenever sea level was sufficiently low, the Karamenderes River has drained into the Aegean exit of the Strait of Dardanelles, then along a NW and then a NNE flow path and eventually into the Gulf of Saros (Alpar and Doğan, 1999). The Tuzla River, on the other hand, did not change its course on land, but as global sea level started to fall, it followed a NW-oriented flow
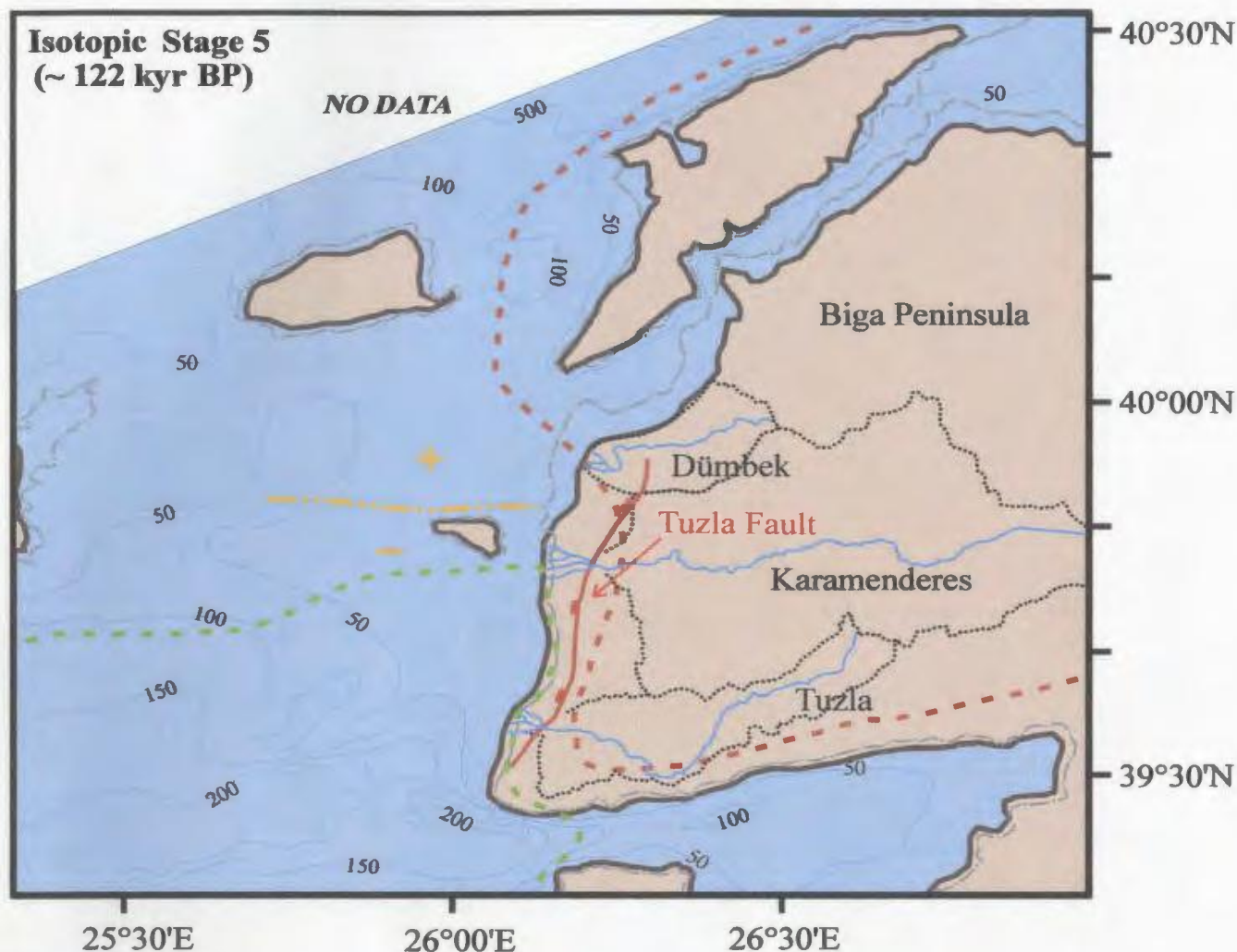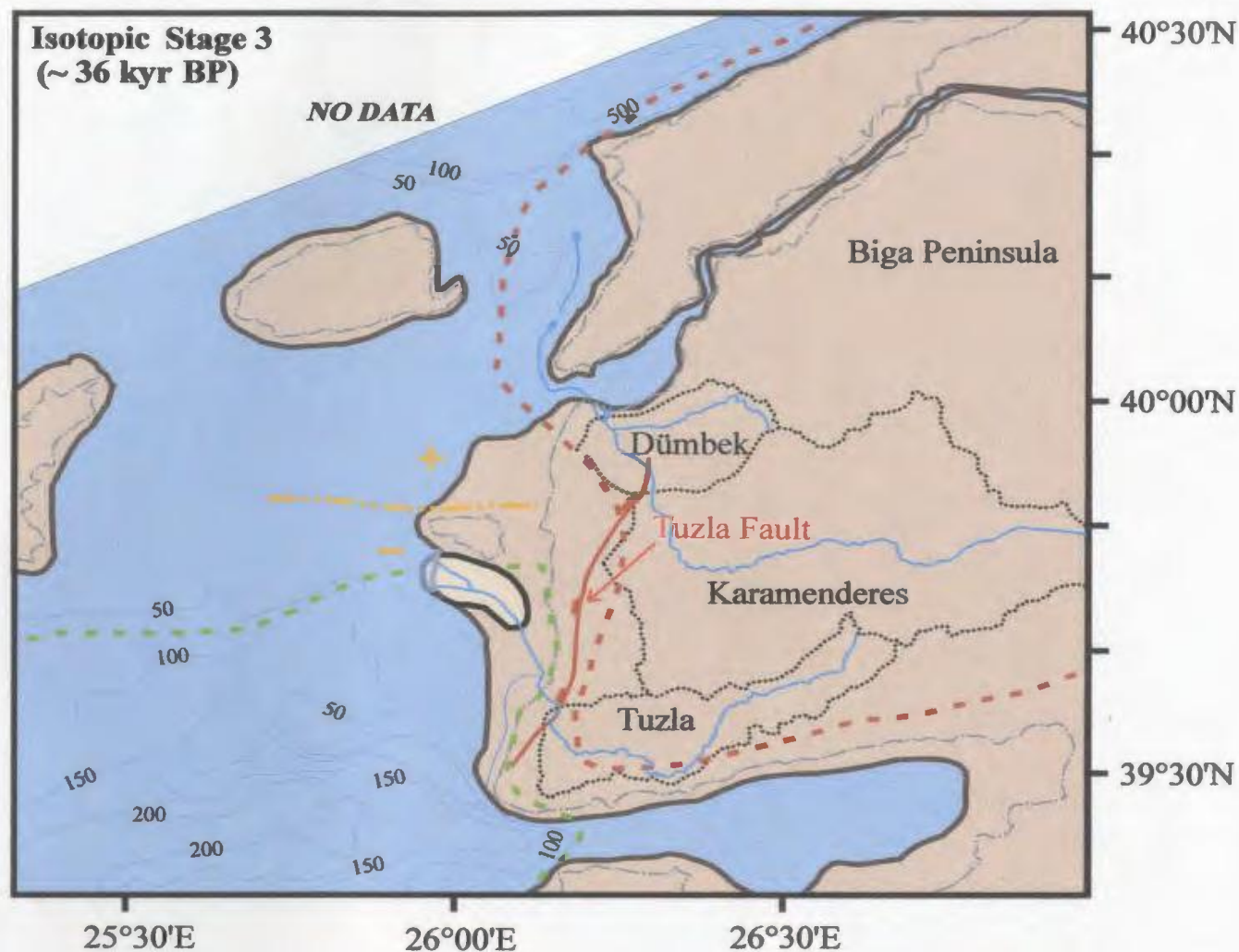
Figure 6.22. Map showing the position of the paleoshoreline (bold brown line) in the northern Aegean Sea and the Dardanelles during the maximum lowstand of sea-level ca. 36 kyr BP when the sea level stood ~ - 41 m below the present level. Also shown is the present-day coastline (dotted dash lines). Isobaths in metres. The map is constructed using published topographic and bathymetric maps, corrected for subsequent uplift along the Dardanelles (e.g. Yaltırak et al., 2002) and subsidence along the shelf south of the Island of Bozcaada. The red and green dashed lines show the areas that are currently uplifting and subsiding, respectively (Cenk Yaltırak, pers. comm., 2005). Double-dotted yellow dashed line and '+', '-' signs show the Quaternary–Present boundary (pivot) between regional uplift and subsidence for the study area.

path west of the fault, which is different to its previous SW-oriented courses (cf. Figs. 6.19 and 6.22). Evidences for these changes in course are noticed from the seismic profiles acquired along the western coast of the Biga Peninsula and from the isopach maps of depositional sequences 3 and 2.

During interstadial isotopic stage 3, sea level did not show any notable fluctuation and displayed a constant descent from -32 m to -41 m between 52 and 36 kyr BP (Figs. 6.21b, 6.23a; Skene et al., 1988). With the onset of this minor sea-level lowering, the Tuzla delta became dynamically balanced with the environment and started to prograde toward the northwest, carrying terrigenous material to basin B4 and constructing depositional sequence 3 (Fig. 6.22). Due to the moderate rate of sea-level lowering and assuming a constant subsidence, topset bed deposition along the Tuzla delta plain was possible.

The isopach map (Fig. 3.23) and seismic reflection profiles show that depositional sequence 3 was deposited within two isolated areas with different internal architectures. Within basin B4, depositional sequence 3 is composed entirely of oblique-prograded clinoforms, while in basin B1 it consists of parallel reflections. The reason for these different internal signatures and isolated deposition might be attributed to bifurcation of the Tuzla River and different subsidence rates in the two basins. While the Tuzla River was flowing toward the northwest and transporting most of its sediment load to basin B4, one of its distributaries must have been flowing toward the southwest with a smaller carrying capacity; thus, the sedimentary record in basin B1 is composed mostly of finer-grained detrital material resulting in the parallel
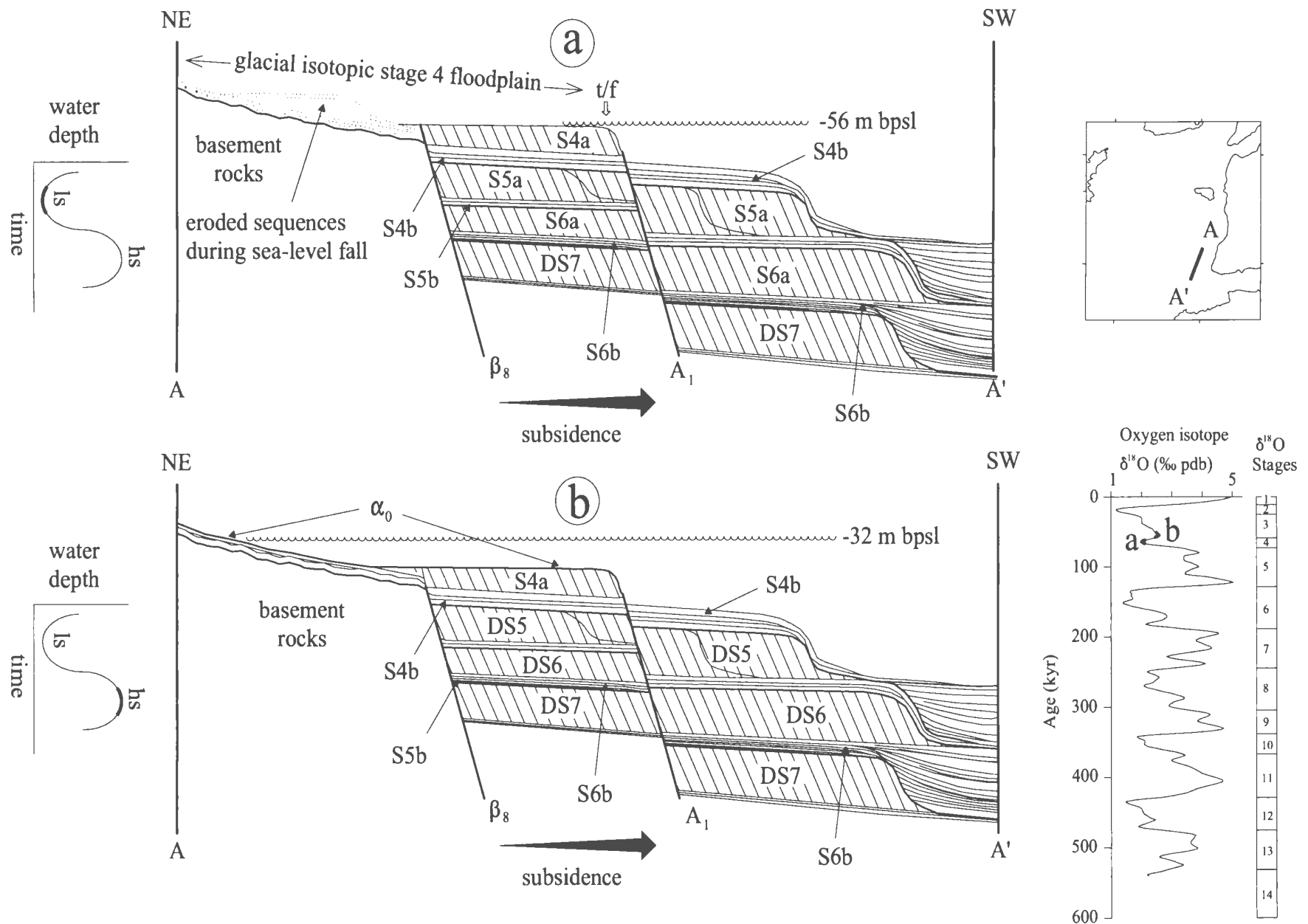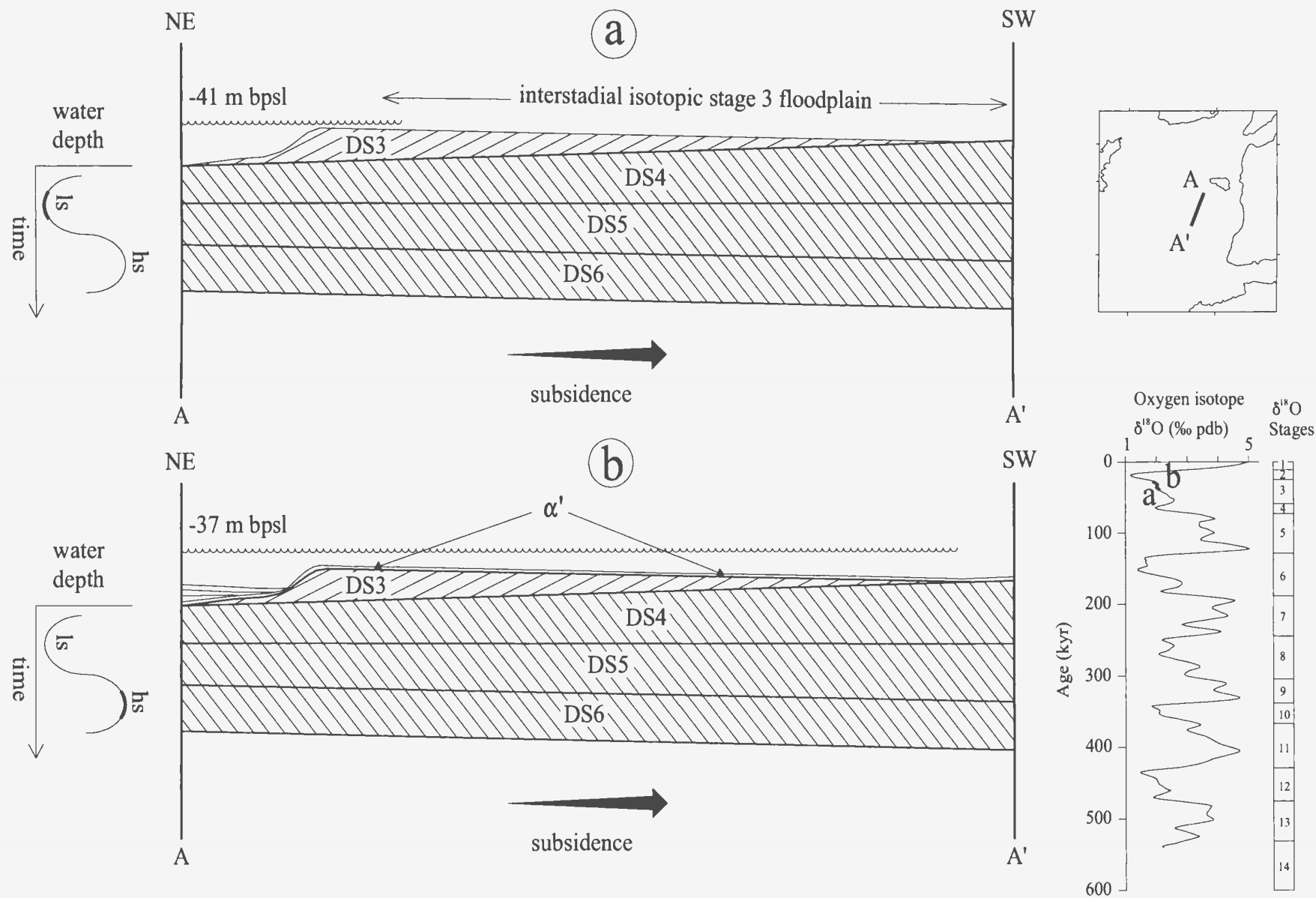
Figure 6.23. Schematic cross-sections from the central part of the study area showing the locally developed depositional sequence 3 and unconformity α' at 36 and 28 kyr BP. bpsl=below present sea level, ls=lowstand, hs=highstand. Depositional sequence 3 clinoforms are at a high angle to early progradation directions (Fig. 3.24), so are shown to have an opposing direction of advance.

bedded seismic configuration. Moreover, it is reasonable to suggest that the subsidence rate within basin B4 must have been less than in basin B1. Slow subsidence rate in basin B4 created a suitable environment for the development of oblique prograded clinoforms, while in basin B1 a comparatively higher subsidence rate together with the fine-grained sediments resulted in the deposition of parallel stratified thin layers rather than clinoforms.

Between 38 and 30 kyr BP, the sea level rose slightly from -41 m to -37 m (Figs. 6.23a, 6.23b). During this short-lived transgressive phase, local unconformity α' was developed by shoreface erosion (Fig. 6.23b). In basin B4, it is defined by the toplap reflection terminations of the underlying oblique-prograded clinoforms of Subunit 3a. However in basin B1, α' is mapped as a correlative conformity within a parallel-bedded succession.

6.2.2.9. Isotopic stage 2 (28–18 kyr BP)

During the transition from isotopic stage 3 to 2 between 30 and 18 kyr BP, global sea-level dropped sharply from -37 m to -115 m. During this period depositional sequence 2 was deposited (Fig. 6.24a). The Tuzla River re-established a dynamic equilibrium with the environment shortly after the onset of sea-level lowering and started to rapidly prograde along a northwest-oriented path within the early stages of progradation. The isopach map (Fig. 3.12) shows that the main deposition within the study area occurred along the axis of basin B2. The sediments which accumulated within basins B1 and B3 were likely carried by distributary
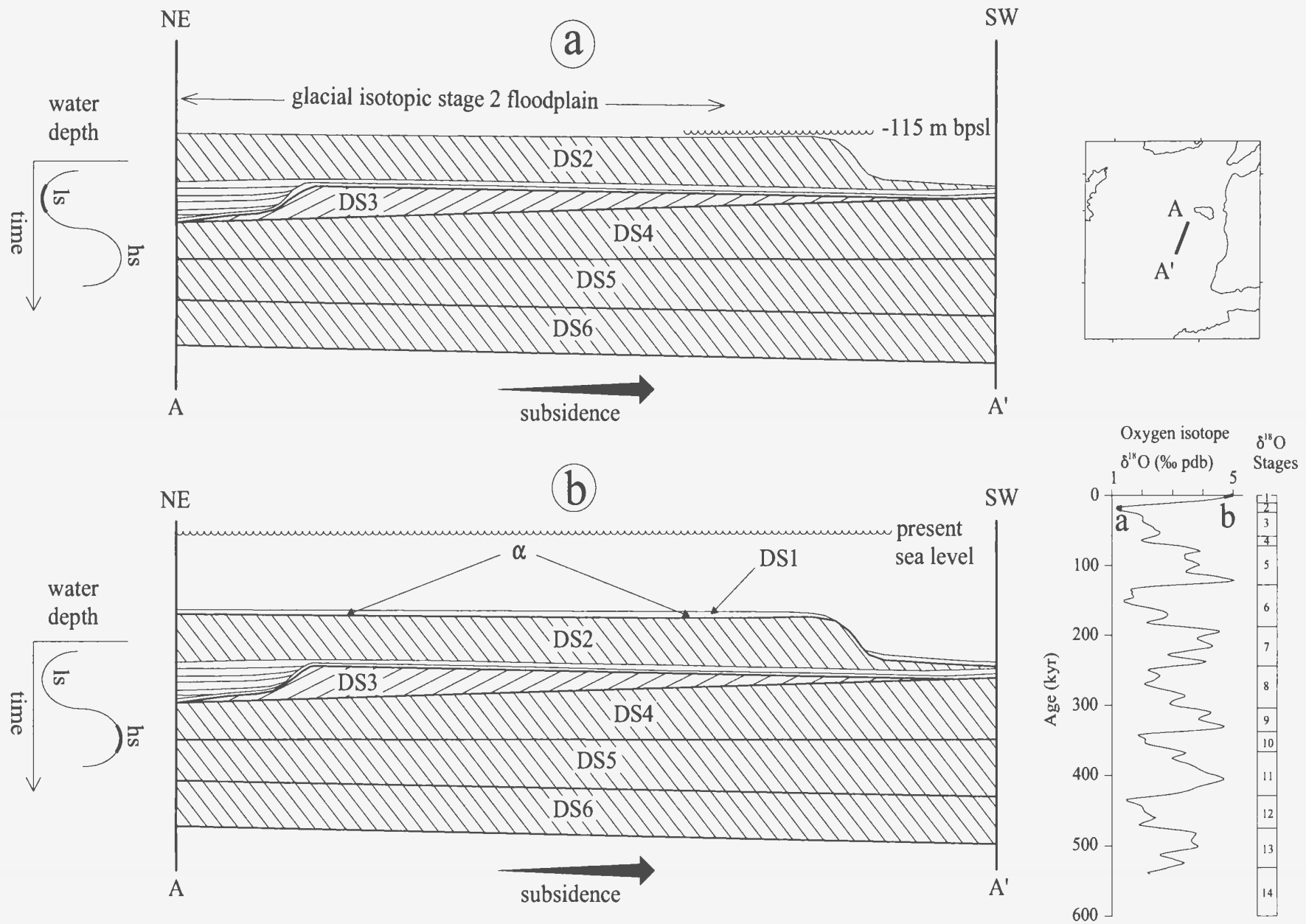
Figure 6.24. Schematic cross-sections from the central part of the study area showing depositional sequence 2 and unconformity α developed during the last major regression and the Holocene transgression, respectively from 18 kyr BP to Present. bpsl=below present sea level, ls=lowstand, hs=highstand. Depositional sequence 3 clinoforms are at a high angle to early progradation directions (Fig. 3.24), so are shown to have an opposing direction of advance.

channels with lower sediment load and transporting capacity. As the global sea level continued to fall, the Tuzla River is believed to have turned toward the northwest into basin B2. The seismic reflection profiles show that depositional sequence 2 is composed predominantly of oblique- prograded clinoforms within basin B2. This internal architecture suggests that constant sediment supply and relative sea-level fall dominated the area during the development of depositional sequence 2. No accommodation space became available for topset bed deposition. The youngest foreset bed development occurred 115 m below the present sea level at ~18 kyr BP. At this time, the area between the islands of Limnos and Gökçeada, and the Baba Burnu Peninsula was subaerially exposed (Fig. 6.25). As the sea level started its final ascent, the Tuzla River lost its equilibrium and delta progradation terminated. Since that time ~ 18 kyr BP and to the Present, the Tuzla River mouth rapidly retreated with the landward-migrating coastline. Only in the last few thousand years, at the present highstand, has the Tuzla Delta stabilized. During interglacial isotopic stage 2, floodplain was subjected to intense subaerial then submarine (transgressive) erosion, which resulted in the development of shelf-crossing unconformity α (Fig. 6.24b).

Page 220 not in bound thesis

CHAPTER 7

Conclusions

Detailed interpretation of ~ 1600 km of single-channel airgun, Huntec deep

tow system seismic reflection profiles, side-scan sonar profiles and radiometric ages

from five piston/gravity cores collected from the northeastern Aegean Sea between

the islands of Bozcaada and Lesbos and the Biga Peninsula revealed the following

salient conclusions.

- The acoustic basement in the study area defines two prominent NE–SW-

trending ridges (R1 and R2) and three intervening basins (B1, B2 and B3). First order

correlations suggest that these ridges and basins can be linked with similar trending

horsts and graben on the Biga Peninsula.

- The Quaternary successions in the region are largely confined to basins B1,

B2 and B3. The stratigraphic architecture of the Quaternary successions is

characterized by several vertically-stacked depositional sequences. Each depositional

sequence consists of a lower package of predominantly horizontal-lying reflectors

overlain with a mild unconformity by an upper oblique to complex sigmoid-oblique

prograded reflectors. Depositional sequences are separated from one another by

major shelf-crossing unconformities.

- The ages of the depositional sequences, including the shelf-crossing

unconformities are established using nine radiometric dates in *in situ* shells extracted

from five sediment cores. The chronostratigraphic framework of the Quaternary

sequences observed in the seismic profiles is established using linear extrapolation of ages obtained in the cores, and by correlations with the oxygen isotopic stratigraphy and global sea-level curve.

• Radiometric ages and the present-day elevation of the topset-to-foreset transitions of the stacked delta successions revealed that the NE Aegean Sea shelf has been subsiding at a rate ranging from 0.3 m/kyr to 1.3 m/kyr.

• Linear extrapolations using the available radiometric ages reveal bulk sedimentation rates ranging between 19 cm/kyr and 30 cm/kyr for the deep basinal successions.

• Correlations of the stacked delta successions with the global oxygen isotopic curve showed that the observed architecture characterized by prograded depositional sequences separated by shelf-crossing unconformities developed in response to rise and fall of the sea level associated with the glacial/interglacial cycles of the Quaternary.

• Sediment budget calculations and the paleocurrent directions suggest that the terrigenous material contained with the depositional sequences was delivered by the Tuzla, Karamenderes and Dümbek rivers. Between 423 and 52 kyr, the Tuzla, Karamenderes and Dümbek rivers follow a southwest-oriented flow path and fed the three basins simultaneously. Approximately 52kyr BP, the tectonic activity of the Tuzla Fault resulted in tilting along the coast of the Biga Peninsula which, in turn, forced the Karamenderes and Dümbek Rivers to change their courses from southwest to northwest. At the time of the maximum lowstand intervals, associated with glacial

maxima, the rivers extended as far seaward as 65 km off the Biga Peninsula. During these stages, the Edremit Bay and the area situated between the Biga Peninsula and the Island of Limnos became land and were occupied by the surrounding rivers.

• With the initiation of the subsequent global sea-level rises, associated with the transitions from glacial to interglacial isotopic stages, the formerly subaerially exposed areas were reflooded by the landward-migrating coastline. By the end of the transgressive phases and throughout the interglacial periods, the position of the paleoshoreline was more or less the same with the present-day coastline.

• Detailed mapping of the fault traces reveal two possible kinematic model for the evolution of the Baba Burnu Basin, and the westward continuation of the central strand of the North Anatolian Transform Fault. (i) the major A_1 and β_8 faults represent the seaward continuations of the southern strand of the North Anatolian Fault. It extends westward along the fault A_1 and deflects toward SW by forming a releasing bend. It then continues farther southwest along fault β_8 as far as the Skyros Basin. (ii) the southern strand of the North Anatolian Transform Fault extends in an ENE-WSW direction in the Gulf of Edremit. It deviates toward NE-SW off the Island of Lesbos and continues further seaward in an NE-SW direction parallel to fault β_8. The central strand of the North Anatolian Transform Fault does not emerge at Ezine as proposed by Barka and Kadinsky-Cade (1988).

References

Aksu A. E. and Piper, D. J. W., 1983. Progradation of the late Quaternary Gediz delta, Turkey. Marine Geology, v. 154, no. 1-2, pp. 1–25.

Aksu, A. E., Piper, D. J. W. and Konuk, T., 1987. Late Quaternary tectonic and sedimentary history of outer İzmir and Çandarlı Bays, western Turkey. Marine Geology, 76, 89–104.

Aksu, A. E., Uluğ, A., Piper, D. J. W., Konuk, Y. T. and Turgut, S., 1992a. Quaternary sedimentary history of Adana, Cilicia and Iskenderun basins; Northeast Mediterranean Sea. Marine Geology, v. 104, no. 1-4, pp. 55–71.

Aksu A. E., Calon, T. J., Piper, D. J. W., Turgut, S. and İzdar, E., 1992b. Architecture of late orogenic Quaternary basins in northeastern Mediterranean Sea. Tectonophysics, v. 210, no. 3-4, pp. 191–213.

Aksu, A. E., Yaşar, D., Mudie, P. J., Gillespie, H., 1995a. Late glacial to Holocene paleoclimatic and paleoceanographic evolution of the Aegean Sea: micropaleontological and stable isotopic evidence. Mar. Micropaleontol., 25: 000–000.

Aksu, A. E., Yaşar, D. and Mudie, P. J., 1995b. Paleoclimatic and paleoceanographic conditions leading to the development of Sapropel layer S1 in the Aegean sea. Palaeogeography, Palaeoclimatology, Palaeoecology, v. 116, no. 1-2, pp. 71–101.

Aksu, A. E., Hiscott, R. N., Yaşar, D., 1999. Oscillating Quaternary water levels of the Marmara Sea and vigorous outflow into the Aegean Sea from the Marmara

Sea-Black Sea drainage corridor. Marine Geology, 153, 275–302.

Aksu, A. E., Calon, T. J., Hiscott, R. N., Yaşar, D., 2000. Anatomy of the North Anatolian Fault Zone in the Marmara Sea, Western Turkey: Extensional Basins Above a Continental Transform. Geological Society of America, v. 10, no. 6, p. 3–7.

Aksu, A. E., Hiscott, R. N., Kaminski, M. A., Mudie, P. J., Gillespie, H., Abrajano, T., Yaşar, D., 2002. Late glacial–Holocene paleoceanography of the Black Sea and Marmara Sea: stable isotopic, foraminiferal ana coccolith evidence. Marine Geology, 190, 119–151.

Allen, C. R., 1975. Geological criteria for evaluating seismicity. Geological Society of America Bulletin, 86, 1041.

Alpar, B. and Doğan, E., 1999. The Miocene Sill at the aegean prolongation of the strait of Çanakkale. Turkish Journal of Marine Sciences 5(1): 3–16.

Altunel, E., 1998. Geological and geomorphological observations in relation to the 20 September 1899 Menderes earthquake, Western Turkey. J. Geol. Soc., London, 156, 241–246.

Ambraseys, N. N., 1970. Some characteristic features of the Anatolian Fault zone. Tectonophysics, 9, 143–165.

Ambraseys, N. N. and Finkel, C. F., 1987. Seismicity of the Northeast Mediterranean region during early 20th century. Annal. Geophys., 5B, 701–726.

Ambraseys, N. N., 1988. Engineering seismology. Earthq. Engineer. Struct. Dynm., 17, 1–105.

Armijo, R., Meyer, B., Hubert, A. and Barka, A. A., 1999. Westward propagation of the North Anatolian Fault into the northern Aegean: Timing and kinematics. Geology, 27, 3, 267–270.

Bard, E., Hamelin, B. and Fairbanks, R. G., 1990. U-Th ages obtained by mass spectrometry in corals from Barbados: sea level during the last 130,000 years. Nature (London), v. 346, no. 6283, pp. 456–458.

Bard, E., Hamelin B., Arnold, M., Montaggioni, L. F., Cabioch, G., Faure, G. and Rougerie, F., 1996. Nature (London), v. 382, no. 6588, pp. 241–244.

Boztepe-Güney, A., Yılmaz, Y., Demirbağ, E., Ecevitoğlu, B., Arzuman, S. and Kuşçu, I., 2001. Reflection seismic study across the continental shelf of Baba Burnu Promontory of Biga Peninsula, Northwest Turkey. Marine Geology, v. 176, pp. 75–85.

Barka, A. A. and Reilinger, R., 1997. Active tectonics of the eastern Mediterranean region: Deduced from GPS, neotectonic, and seismicity data. Ann. Geofis., 40, 587–610.

Barka, A. A., Akyüz, S. H., Cohen, H. A., Watchorn, F., 2000. Tectonic evolution of the Niksar and Taşova-Erbaa pull-apart basins, North Anatolian Fault Zone: their significance for the motion of the Anatolian block. Tectonophysics, 322, 243–264.

Barka, A. A. and Kadinsky-Cade, K., 1988. Strike-slip fault geometry in Turkey and its influence on earthquake activity. Tectonics, 7, 663–684.

Bartlett, W. L., Friedman, M., Logan, J. M., 1981. Experimental folding and faulting

of rocks under confining pressure. Part IX. Wrench faults in limestone layers: Tectonophysics, v. 79, p. 255–277.

Bingöl, E., Akyürek, B., Korkmazer, B., 1975. Biga Yarımadası'nın jeolojisi ve Karakaya Formasyonu'nun bazi özellikleri: Cumhuriyet'in 50. Yılı Yerbilimleri Kongresi Tebliğleri. Maden Tetkik ve Arama Enstitüsü, ankara. 70–77.

Bloom, A. L., Broecker, W. S., Chappell, J., Matthews, R. K. and Mesolella, K. J., 1974. Quaternary sea level fluctuations on a tectonic coast: new (super 230) Th/(super 234)U dates from the Huon Peninsula, New Guinea. Quaternary Research,(New York), v. 4, no. 2, pp. 185–205.

Bozkurt, E. and Koçyiğit, A., 1996. The Kazova basin: an active negative flower structure on the Almus Fault Zone, a splay fault system of the North Fault Zone, Turkey. Tectonopyhsics, 265, 239–254.

Bozkurt, E., 2001. Neotectonics of Turkey—a synthesis. Geodinamica Acta, 14, 3–30.

Broecker, W. S. and Donk, J., 1970. Insolation changes, ice volumes, and the O (super 18) record in deep-sea cores. Reviews of Geophysics and Space Physics, v. 8, no. 1, pp. 169–198.

Broecker, W. S., Thurber, D. L., Goddard, J., Ku, T., Matthews, R. K. Mesolella, K. J., 1968. Milankovitch hypothesis supported by precise dating of coral reefs and deep-sea sediments. Science, v. 159, no. 3812, pp. 297–300.

Brooks, M. and Ferentinos, G., 1980. Structure and evolution of the Sporades basin of

the north Aegean trough, Northern Aegean sea, Tectonophysics, 68, 15–30.

Camion, G. F., Ebren, P., Eisenhauer, A., Bard, E. and Faure, G., 2001. A 300,000 yr coral reef record of sea level changes, Mururoa Atoll (Tuamotu Archipelago, French Polynesia). Palaeogeography, Palaeoclimatology, Palaeoecology, v. 175, no. 1-4, pp. 325–341.

Chappell, J., 1974. Relationships between sealevels, (super 18) O variations and orbital perturbations, during the past 250,00 years. Nature, (London), v. 252, no. 5480, pp. 199–202.

Chappell, J. and Veeh, H. H., 1978. (super 230) Th/ (super 234) U age support of an interstadial sea level of –40 m at 30,000 yr BP. Nature (London), v. 276, no. 5866, pp. 602–604.

Chappell, J. and Shackleton, N. J., 1986. Oxygen isotopes and sea level. Nature, 324, 137–140.

Chappell, J., Omura, A., Esat, T., McCulloch, M, Pandolfi, J., Ota, Y. and Pillans, B., 1996. Reconciliation of the late Quaternary sea levels derived from coral terraces at Huon Peninsula with deep sea oxygen isotope records. Earth and Planetary Science Letters, v.141, no. 1-4, pp. 227–236.

Christie-Blick, N. and Biddle, K., 1985. Deformation and basin formation along strike-slip faults. In: Biddle, K., Christie-Blick, N. (Eds.), Strike-Slip Deformation, Basin Formation, and Sedimentation. Society of Economic Paleontologists and Minerologists Special Publication, vol. 37, pp. 1–34.

Cita, M. B., Vergnaud-Grazzini, C., Robert, C., Chamley, H., Ciaranfi, N. and

d'Onofrio, S., 1977. Paleoclimatic record of a long deep-sea core from the eastern Mediterranean. Quaternary Research (New York), v. 8, no. 2, pp.205–235.

Crampin, S. and Evans, R., 1986. Neotectonics of the Marmara Sea region of Turkey. Journal of the Geological Society, London. 143, 343–348.

Deino, A, Curtis, G. and Rosi, M., 1992. (super 40) Ar/ (super 39) Ar dating of the Campanian Ignimbrite, Campanian region, Italy. International Geological Congress, Abstracts, v. 29, no. 3, pp. 633.

DeMets, C., Gordon, R. G., Argus, D. F., Stein, S., 1990. Current plate motions. Geophys. J. Int., 101, 425–478.

Dewey, J. F., 1976. Seismicity of Northern Anatolia. Bull. Seismol. Soc. Am., 66, 843–868.

Dewey, J. F., Şengör, A. M. C., 1979. Aegean and surrounding regions: complex multiplate and   continuum tectonics in a convergent zone. Bull. Geol. Soc. Am., 90, 84–92.

Dewey, J. F., Hempton, M. R., Kidd, W. S. F., Şaroğlu, F., Şengör, A. M. C., 1986. Shortening of the continental lithosphere: the neotectonics of Eastern Anatolia–a young collision zone, in Collision Tectonics. Special Publication Geological Society of London, 19, 3–36.

Di Girolamo, P., Lirer, L., Porcelli, C. and Stanzione, D., 1972. Correlazioni stratigrafiche fra le principali formazione piroclastiche della Campania (Roccamonfina, Campi Flegrei, Somma-Vesuvio). Stratigraphic correlation of

the principal pyroclastic formations of Campania; Roccamonfina, Phlegraean Fields and Monte Somma-Vesuvius. Rendiconti della Societa Italiana di Mineralogia e Petrologia, v. 28, no.1, pp. 77–123.

Dodge, R. E., Fairbanks, R. G., Benninger, L. K. and Maurrasse, F., 1983. Pleistocene sea levels from raised coral reefs of Haiti. Science, v. 219, no. 4591, pp. 1423–1425.

Duplessy, J. C., Labeyrie, J., Lalou, C. and Nguyen, H. V., 1970. Continental climatic variations between 130,00 and 90,000 years BP. Nature (London), v. 226, no. 5246, pp. 631–633.

Dziewonski, A. M., Chou, T. A., Woodhouse, J. H., 1981. Determination of earthquake source parameters from waveform data for studies of global and regional seismicity. J. Geophys. Res., 86, 2825–2852.

Ekström, G. A. and England, P. C., 1989. Seismic strain rates in regions of distributed continental deformation. J. geophys. Res., 94, 10 231–10 257.

Emiliani, C. and Epstein, S., 1953. Temperature variations in the lower Pleistocene of southern California. Journal of Geology, v. 61, no. 2, pp. 171–181.

Emiliani, C., 1955a. Pleistocene temperatures. Journal of Geology, 63, 538–573.

Emiliani, C., 1966. Paleotemperature analysis of Caribbean Cores P 6304-8 and P 6304-9 and a generalized temperature curve for the last 425,000 years. Journal of Geology, 74, 109–126.

English, T., 1904. Eocene and later formations surrounding the Dardanelles. Q. J. Geol., Geol. Soc. London, 58.

Epstein, S., Buchsbaum, R., Lowenstam, H.A., and Urey, H.C., 1951. Carbonate-water isotopic temperature scale. Geological Society of America Bulletin, 62: 417-426.

Epstein, S., Buchsbaum, R., Lowenstam, H.A., and Urey, H.C., 1953. Revised carbonate-water isotopic temperature scale. Geological Society of America Bulletin, 64: 1315-1325.

Ergin, K., Güçlü, U. and Uz, U., 1967. Türkiye ve Civarının Deprem Kataloğu (1965-1970), Publication no. 28, İstanbul Technical University, İstanbul (in Turkish).

Erol, O., 1987. Quaternary sea level changes in the Dardanelles area, Turkey. Dil, Tarih ve Coğrafya Fakültesi Bull. (University of Ankara), 60th Anniversary Issue, Ankara, pp. 179–187.

Evans, R., Asudeh, I., Crampin, S. and Üçer, S. B., 1985. Tectonics of the Marmara Sea region of Turkey: new evidence from micro–earthquake fault plane solutions. Geophys. J. R. astr. Soc., 83, 47–60.

Eyidoğan, H., 1988. Rates of crustal deformation in western Turkey as deduced from major earthquakes. Tectonophysics, 148, 83–92.

Eyidoğan, H., Utku, Z. Değirmenci, E., 1991. Türkiye Büyük Depremleri Makro-sismik Rehberi. İstanbul Teknik Üniversitesi, Maden Fakültesi Yayını (in Turkish).

Fairbanks, R. G., 1989. A 17,000-year glacio-eustatic sea level record: influence of glacial melting rates on the Younger Dryas event and deep-ocean circulation. Nature, 342, 637–642.

Federman, A. N. and Carey, S. N., 1980. Electron microprobe correlation of tephra

    layers from eastern Mediterranean abyssal sediments and the Island of

    Santorini. Quaternary Research (New York), v. 13, no. 2, pp. 160–171.

Gallup, C. D., Edwards, R. L. and Johnson, r. G., 1994. Thorium-230 dating of

    glacial-interglacial cycles by TIMS: results to date. U. S. Geological Survey

    Circular, Report:C 1107, pp. 108.

Genç, Ş. C., 1998. Evolution of Bayramiç magmatic complex, northwestern Anatolia.

    Jour. of Volcan. And Geoth. Res., v. 85, pp. 233–249.

Gürbüz, C., Aktar, M., Eyidoğan, H., Cisternas, A., Haessler, H., Barka, A., Ergin,

    M., Türkelli, N., Polat, O., Üçer, S. B., Kuleli, S., Barış, S., Kaypak, B.,

    Bekler, T., Zor, E., Biçmen, F. and Yörük, A., 2000. The seismotectonics of

    the Marmara region (Turkey): results from a microseismic experiment.

Harding, T. P., 1985. Seismic characteristics and identification of negative flower

    structures, positive flower structures, and positive structural inversion. AAPG

    Bulletin 69 (4), 582–600.

Harding, T. P., 1990. Identification of wrench faults using subsurface structural data:

    Criteria and pitfalls: AAPG Bulletin, v. 3: AAPG Studies in Geology.

Hegarty, K. A., Weisel, J. K., Mutter, J. C., 1988. Subsidence history of the

    Australia's southern margin: constraints on basin models. Am. Assoc. Pet.

    Geol. Bull. 72, 615–633.

Hiscott, R. N., Aksu, A. E., 2002. Late Quaternary history of the Marmara Sea and

    Black Sea from high-resolution seismic and gravity core studies. Marine

Geology, 190, 261–283.

Imbrie, J., Hays, J. D., Martinson, D. G., McIntyre, A., Mix, A. C., Morley, J. J., Pisias, N. G., Prell, W. L. and Shackleton N. J., 1984. The orbital theory of Pleistocene climate: support from revised chronology of the marine $\delta^{18}O$ record. In: Berger, A. L., Imbrie, J., Hays, J., Kukla, G., Saltzman, B. (Eds.), Milankovitch and Climate, Part I. Reidel, Dordrecht, pp. 269–305.

İnci, U., 1984. Demirci ve Burhaniye bitümlü şeyllerin stratigrafisi ve organik özellikleri. Türkiye Jeoloji Kurumu Bülteni, 5, 27–40.

Institute of Geology and Mineral Exploration (IGME), 1989. 1:500 000 scale Seismotectonic Map Of Greece with Seismological Data, 4 sheets.

Intergovernmental Oceanographic Commission (IOC), 1981. International Bathymetric Chart of the Mediterranean. Published by the Head Department of Navigation and Oceanography, Russia under the authority of IOC, 10 sheets.

Jackson, J. A., 1994. Active tectonics of the Aegean region. Annu. Rev. Earth Planet. Sci., 22, 239–271.

Jackson, J. A. and McKenzie, D., 1984. Active tectonics of the Alpine-Himalayan Belt between western Turkey and Pakistan. Geophysical Journal of the Royal Astronomical Society, v. 77, no. 1, pp. 185–264.

Jackson, J. A. and McKenzie, D., 1988. Rates of active deformation in the Aegean Sea and surrounding areas. Basin Res., 1, 121–128.

Jestin, F., Huchon, P., Gaulier, J. M., 1994. The Somalia Plate and the East African

rift system: Present-day kinematics. Geophys. J. Int., 116, 637–654.

Kalafat, D. and Pınar, A., 1998. August 14, 1996 (Ms = 5.6) Mecitözü– ÇORUM
AND January 22, 1997 (Ms = 5.5) Antakya (Turkey) earthquakes: implication
for inner deformation pattern. Third International Turkish Geology
Symposium, METU-Ankara, Abstracts, p.320.

Keller, J. and Ninkovich, D., 1972. Tephra-Lagen in der Aegaeis. Tephra layers IN
THE Aegean Sea. Zeitschrift der Deutschen Geologischen Gesselschaft, v.
123, Part 2, pp. 579–588.

Ketin, İ., 1968. Relations between general tectonic features and the main earthquake
regions of Turkey. Min. Res. Explor. Inst. Bull., 71, 63–67.

Koçyiğit, A., 1988. Basic geologic characteristics and total offset of the North
Anatolian Fault Zone in Suşehri area, NE Turkey, METU. Pure Appl. Sci., 22,
43–68.

Koçyiğit, A., 1988a. Tectonic setting of the Geyve basin: age and total displacement
of the Geyve fault zone, METU. Pure Appl. Sci., 21, 81–104.

Koçyiğit, A., 1989. Suşehri basin: an active fault-wedge basin on the North Anatolian
Fault Zone, Turkey. Tectonophysics, 167, 13–29.

Koçyiğit, A., 1990. Tectonic setting of the Golova basin, total offset of the North
Anatolian Fault Zone, Eastern Pontide, Turkey. Annales Tecton., 4, 155–170.

Kukal, Z., 1971. Geology of Recent Sediments. Academic press, London, 490 pp.

Latif, M. L., Özsoy, E., Salihoğlu, İ., Gaines, A. F., Baştürk, Ö., Yılmaz, A., Tuğrul,
S., 1992. Monitoring via Direct Measurements of the Modes of Mixing and

Transport of Wastewater Discharges into the Bosphorus Underflow. Middle East Technical University, Institute of Marine Sciences, Technical Report No. 92-2, 98 pp.

Le Pichon, X., Lybéris, N. and Alvarez, F., 1984. Subsidence history of the North Aegean Trough. Geological Society Special Publications, 17, 727–741.

Lybéris, N., 1984. Tectonic evolution of the North Aegean trough, in Geological Evolution of the Eastern Mediterranean. Special Publication Geological Society of London, 17, 709–725.

Martinod, J., Hatzfeld, D., Brun, J. P., Davy, P. and Gauter, P., 2000. Continental collision, gravity spreading, and kinematics of Aegean and Anatolia. Tectonics, 19, 290–299.

Mascle, J. and Martin, L., 1990. Shallow structure and recent evolution of the Aegean sea: a synthesis based on continuous reflection profiles. Marine Geology, 94, 271–299.

Mesolella, K. J., Matthews, R. K., Broecker, W. S. and Thurber, d. L., 1969. The astronomical theory of climatic change-barbados data. Journal of Geology, v. 77, no. 3, pp. 250–274.

McClusky, S., Balassanian, S., Barka, A. A., Demir, C., Ergintav, S., Georgiev, I., Gürkan, O., Hamburger, M., Hurst, K., Kahle, H., Kastens, K., Kekelidze, G., King, R., Kotzev, V., Lenk, O., Mahmoud, S., Mishin, A., Nadariya, M., Ouzounis, A., Paradissis, D., Peter, Y., Prilepin, M., Reilinger, R., Şanlı, I., Seeger, H., Tealeb, A., Toksöz, M. N. and Veis, G., 2000. Global positioning

system constraints on plate kinematics and dynamics in the eastern Mediterranean and Caucasus. Journal of Geophysical Research, 105, B3, 5695–5719.

McCrea, J.M., 1950 On the isotopic chemistry of carbonates and a paleotemperature scale. Journal of Chemical Physics, 18: 849-857.

McKenzie, D. P., 1970. Plate tectonics of the Mediterranean region. Nature, 220, 239–343.

McKenzie, D. P., 1972. Active tectonics of the Mediterranean Region. Geophys. J. R. Astr. Soc., 30, 109.

McKenzie, D. P., 1978. Active tectonics of the Alpine–Himalayan belt: the Aegean Sea and surrounding regions. Geophys. J. R. Astr. Soc., 55, 217–254.

Meulenkamp, J. E., Wortel, W.J. R., Van Wamel, W. A., Spakman, W. and Hoogerduyn Strating, E., 1988. On the Hellenic subduction zone and geodynamic evolution of Crete since the late Middle Miocene. Tectonophysics, 146, 203–215.

Mitchum, M. R., Jr., Vail, P. R. and Sangree, J. B., 1977. Seismic stratigraphy and global changes of sea level, part 6: Stratigraphic interpretation of seismic reflection patterns in depositional sequences. In: C. E. Payton (Editor), Seismic Stratigraphy Applications to Hydrocarbon Exploration. Mem., Am. Assoc. Pet. Geol., 26: 117–135.

Myers, K. J. and Milton, N. J., 1996. Concepts and principles of sequence stratigraphy. In: D. Emery and K. J. Myers (Editors), Sequence Stratigraphy,

11–45.

Nalbant, S. S., Hubert, A., King, G. C. P., 1998. Stress coupling between earthquakes in northwest Turkey and the north Aegean Sea. Journal of Geophysical Research, 103, 24 469–24 486.

Narcisi, B. and Vezzoli,. L., 1999. Quaternary stratigraphy of distal tephra layers in the Mediterranean; an overview. Global and Planetary Change, v. 21, no. 1-3, pp. 31–50.

Ninkovich, D. and Heezen, B. C., 1967. Physical and chemical properties of volcanic glass shards from pozzuolana ash, Thera Island, and from upper and lower ash layers in eastern Mediterranean deep sea sediments. Nature (London), v. 213, no. 5076, pp. 582–584.

Okay, A. İ., Siyako, M., Bürkan, K. A., 1990. Geology and Tectonic Evolution of the Biga Peninsula. TAPG Bulletin, V.2/1, p. 83–121.

Okay, A. İ., Demirbağ, E., Kurt, H., Okay, N. and Kuşçu, İ., 1999. An active, deep marine strike-slip basin along the North Anatolian Fault in Turkey. Tectonics, 18, 1, 129–147.

Olausson, E., 1971. Oceanographic aspects of the Pleistocene of Scandinavia. Geologiska Foereningen i Stockholm Foerhandlingar, v. 93, Part 3, no. 546, pp. 459–475.

Oral, M. B., Reilinger, R. E., Toksöz, M. N., King, R. W., Barka, A. A., Kınık I., 1995. Coherent plate motions in the eastern Mediterranean continental collision zone. Eos. Trans. AGU., 76(2), 9–11.

Özsoy, E., Latif, M. A., Tuğrul, S., Ünlüata, Ü., 1995. Exchanges with the Mediterranean, fluxes and boundary mixing processes in the Black Sea. In: Briand, F. (Ed.), Mediterranean Tributary Seas. Bulletin de l'Institut Ocèanographique, Monaco, Special No. 15, CIESME Science Series 1, 1–25.

Pamir, H. N. and Ketin, İ., 1941. Das Anatolische Erbeden Ende 1939. Geol. Runds., 32, 278–287.

Paréjas, E. and Pamir H. N., 1939. 19/4/1938 Orta Anadolu Yer Depremi. İstanbul University, Faculty of Science Publication IV.

Pfannensteil, M., 1944. Diluviale Geologie des Mittelmeergebietes die diluvialen Entwicklundgstadien und die Urgeschichte von Dardanellen, Marmara Meer und Bosphorus. Geol. Rundsch. v. 34, pp. 334–342.

Philip, H., Cisternas, A., Gvishiani, A. and Gorshkov, A., 1989. The Caucasus: an actual example of the initial stages of continental collision. Tectonophysics, 161, 1–21.

Pirazzoli, P. A., Radtke, U., Hantoro, W. S., Jouannic, C., Hoang, C. T., Causse, C. and Borel, B., 1993. A one million-year-long sequence of marine terraces on Sumba Island, Indonesia

Polat, Ç., Tuğrul, S., 1996. Chemical exchange between the Mediterranean and Black Sea via the Turkish Straits. In: Briand, F. (Ed.), Dynamics of Mediterranean Straits and Channels. Bulletin de l'Institut Ocèanographique, Monaco, Special No. 17, CIESME Science Series 2, pp. 167–186.

Reilinger, R. E., McClusky, S. C., Oral, M. B., King, R. W., Toksöz, M. N., Barka, A.

A., Kınık, I., Lenk, O. and Sanlı, I., 1997. Global Positioning System measurements of the present-day crustal movements in the Arabia-Africa-Eurasia plate collision zone. Journal of Geophysical Reserach, 102, 9983–9999.

Richard, P. A. and Krantz, R. W., 1991. Experiments on fault reactivation in strike-slip mode. Tectonophysics 188, 117–131.

Richard, P. D., Naylor, M. A. and Koopman, A., 1995. Experimental models of strike-slip tectonics: Petroleum Geoscience, v. 1, p. 71–80.

Riedel, W., 1929. Zur Mechanik geologischer Brucherscheinungen: Zentrablatt für Mineralogie, Geologie und Pälaeontologie, v. 1929 B, p. 354–368.

Royden, L. H., 1993. Evolution of retreating subduction boundaries during continental collision. Tectonics, v. 12, no. 3, pp. 629–638.

Saatçılar, R., Ergintav, S., Demirbağ, E. and İnan, S., 1999. Character of active faulting in the North Aegean sea. Marine Geology, 160, 339–353.

Saltık, O., 1974. Şarköy-Mürefte sahaları jeolojisi ve petrol olanakları. TPAO Arama Grubu Rap. No, 877, 30 s.

Seyitoğlu, G. and Scott, B. C., 1992a., The age of the Büyük Menderes graben (west Turkey) and its tectonic implications. Geol. Mag., 29, 239–242.

Shackleton, N. J. and Opdyke, N. D., 1976. Oxygen-isotope and paleomagnetic stratigraphy of Pacific Core V28-239, late Pleistocene to latest Pleistocene. Memoir - Geological Society of America, no. 145, Investigation of late Quaternary paleoceanography and paleoclimatology, pp. 449–464.

Shackleton, N. J., 1987. Oxygen isotopes, ice volume and sea level. Quaternary Science Reviews, v. 6, no. 34, pp. 183–190.

Siyako, M., Bürkan, A. K., Okay, A. İ., 1989. Tertiary Geology and Hydrocarbon Potential of the Biga and Gelibolu Peninsulas. TAPG Bulletin, V.1/3, p 183–199.

Skene, K. I., Piper, D. J. W., Aksu, A. E., Syvitski, J. P. M., 1998. Evaluation of the global oxygen isotope curve as a proxy for Quaternary sea level by modeling of delta progradation. Journal of Sedimentary Research, v. 68, no. 6, pp. 1077–1092.

Stanly, D. J. and Blanpied, C., 1980. Late Quaternary water exchange between the eastern Mediterranean and the Black Sea. Nature, 285, 537–541.

Stein, M., Wasserburg, G. J., Aharon, P., Chen, J. H., Zhu, Z. R., Bloom, A. and Chappell, J., 1993. TIMS U-series dating and stable isotopes of the last interglacial event in Papua New Guinea. Geochimica et Cosmochimica Acta, v. 57, no. 11, pp. 2541–2554.

Straub, C. and Kahle, H., 1994. Global Positioning system (GPS) estimates of crustal deformation in the Marmara Sea region, northwest Anatolia. Earth. Plan. Sci. Lett., 121, 495–502.

Straub, C. and Kahle, H., 1995. Active crustal deformation in the Marmara Sea region, NW Anatolia, inferred from GPS measurements. Geophysical Research Letters, 22, 2533–2536.

Straub, C. and Kahle, H. and Schindler, C., 1997. GPS and geologic estimates of the

tectonic activity in the Marmara Sea region, NW Anatolia. J. Geoph. Res. - Solid Earth, B12, 27587–27601.

Swift, D.J.P., 1968. Coastal erosion and transgressive stratigraphy. Journal of Geology., 76, 444–456.

Şaroğlu, F., Emre, Ö. and Kuşçu, İ., 1992. Active Fault Map of Turkey. 1:1,000,000., General Directorate of Mineral Research and Exploration (MTA) Printing Office, Ankara, Turkey.

Şengör, A. M. C., 1979. The North Anatolian transform fault: its age, offset and tectonic significance. Journal of Geological Society, London, 136, 269–282.

Şengör, A. M. C., Yılmaz, Y., 1981. Tethyan evolution of Turkey: a plate tectonic approach: Tectonophysics, 75, 181–241.

Taymaz, T., Jackson, J. and McKenzie, D., 1991. Active tectonics of the north and central Aegean Sea. Geophys. J. Int., 106, 433–490.

Taymaz, T., 1993. The source parameters of the Cubukdag (W. Turkey) earthquake of October 11, Geophys. J. Inter., 113, 260–267.

Tchalenko, J. C., 1970. Similarities between shear zones of different magnitudes: Geological Society of America Bulletin, v. 81, p. 1625–1640.

Tchalenko, J. C. and Ambraseys, N. N., 1970. Structural analyses of the Dasht-e Bayaz (Iran) earthquake fractures: Geological Society of American Bulletin, v. 81, p. 41–60.

Tchalenko, J. C. and Ambraseys, N. N., 1970. Structural analysis of the Dasht-e Bayaz (Iran) earthquake fractures: GSA Bulletin, v. 81, p. 41–60.

Thunell, R., Federman, A., Sparks, S. and Williams, D., 1979. The age, origin and volcanological significance of the Y-5 layer in the Mediterranean. Quaternary Research (New York), v. 12, no. 2, pp. 241–251.

Tokay, M., 1973. Geological observations on the North Anatolian Fault Zone between Gerede and Ilgaz. in: Proceedings of Symposium on North Anatolian Fault Zone and Earthquake Belt. Min. Res. Expl. Inst. Publ., Ankara., pp. 12–29. (in Turkish with English Abstract).

Tüysüz, O., Barka, A. A., Yiğitbaş, E., 1998. Geology of the Saroz graben and its implications for the evolution of the North Anatolian Fault in the Ganos–Saros region, northwestern Turkey. Tectonophysics, 293, 105–126.

UNESCO, 1981. Bathymetric map of the Mediterranean Sea. UNESCO Int. Comm., sheets 4 and 9.

Urey, H.C., 1947. The thermodynamic properties of isotopic substances. Journal of Chemical Society, 562-581.

Üçer, B. S., Crampin, S., Evans, R., Miller, A. and Kafadar, N., 1985. The Marnet radiolinked seismometer network spanning the Marmara Sea and the seismicity of Western Turkey. Geophys. J. R. astr. Soc., 83, 17–30.

Vergnaud-Grazzini, C. and Rosenberg, H. Y., 1969. Etude paleoclimatique d'une carotte de Mediterranee orientale. Paleoclimatic study of a core sample from the eastern Mediterranean. Revue de Geographie Physique et de Geologie Dynamique, v. 11, no. 3, pp. 279–291.

Vergnaud-Grazzini, C., 1985. Mediterranean late Cenozoic stable isotope record;

stratigraphic and paleoclimatic implications.

Westaway, R., 1993. Neogene evolution of the Denizli region of western Turkey. J. Struct. Geol., 15, 37–53.

Westaway, R., 1994a. Present-day kinematics of the Middle East and eastern Mediterranean. J. Geophys. Res., 99, 12,071–12,090.

Wilcox, R. E., Harding, T. P., Seely, d. R., 1973. Basic wrench tectonics: American Association of Petroleum Geologists Bulletin, v. 57, p. 74–96.

Wright, T., Fielding, E., Parsons, B., England, P. and Haynes, M., 2000. Source parameters of the 17 August 1999 İzmit earthquake from SAR interferometry, in: Barka A. A., Kozacı, O., Akyüz S. H. Altunel E. (Eds), 1999 İzmit and Düzce Earthquakes: Preliminary Results, İstanbul Technical University Publ., İstanbul. pp. 289–293.

Wulf, S., Kraml, M., Kuhn, T., Schwarz, M., Inthorn, M., Keller, J., Kuşçu, İ and Halbach, P., 2002. Marine tephra from the Cape Riva eruption (22 ka) of Santorini in the Sea of Marmara. Marine Geology, v. 183, no. 1-4, pp. 131–141.

Yaltırak, C., 1996. The tectonic history of the Ganos fault system (in Turkish). Türkiye Petrol Jeologları Derneği Bülteni, 8, 137–150.

Yaltırak, C. and Alpar, B., 2002. Kinematics and evolution of the northern branch of the North Anatolian Fault (Ganos Fault) between the Sea of Marmara and the Gulf of Saros. Marine Geology, 190, 351–367.

Yaltırak, C., 2003. Edremit Körfezi ve Kuzeyinin Jeodinamik Evrimi, PhD Thesis

(unpublished).

Yaşar, D., 1994. Late glacial–Holocene evolution of the Aegean Sea. Ph.D. Thesis, Inst. Mar. Sci. Technol., Dokuz Eylül Univ., 329 pp. (Unpubl.)

Yılmaz, Y., Genç, Ş.C., Gürer, F., Bozcu, M., Yılmaz, K., Karacık, Z., Altunkaynak, Ş. and Elmas, A., 2000. When did the western Anatolian grabens begin to develop? In: E. Bozkurt and J.D.A. Piper (Eds.), Tectonics and Magmatism in Turkey and the Surrounding Area. Geological Society, Special Publication, 173: 353–384.

Yılmaz, Y. and Karacık, Z., 2001. Geology of the northern side of the Gulf of Edremit and its tectonic significance for the development of the Aegean grabens. Geodinamica Acta, v. 14, pp. 31–43.

Yüce, H., 1991. Water level variations in the northeastern Aegean Sea. Doğa-Tr. J. of Engineering and Environmental Sciences, TÜBİTAK, 15, 179–187.

Yüce, H., 1992. Deep water characteristics of the Aegean Sea. Doğa-Tr. J. of Engineering and Environmental Sciences, TÜBİTAK, 15, 17–26.

Appendix A

Details of the earthquakes given in Fig. 1.5. Magnitude (Mag) in Richter scale.

No	Date d m y	Time h m s	Location		Mag	Depth (km)	Author
			Lat °N	Long °E			
1	19041938	105917	39.5	33.8	6.6	0	Jackson and McKenzie (1984)
2	26121939	235717	39.7	39.41	8	0	Jackson and McKenzie (1984)
3	13081953	190613	40.07	27.39	7.2	0	McKenzie (1972)
4	16071955	70711.2	37.66	27.19	6.8	6	McKenzie (1972)
5	9071956	.31138.6	36.69	25.81	7.5	0	McKenzie (1972)
6	24041957	191013	36.37	28.61	6.9	5	McKenzie (1972)
7	25041957	22541.9	36.45	28.59	7	0	McKenzie (1972)
8	25041959	2619.5	37.05	28.55	6.1	43	McKenzie (1972)
9	15111959	170841	37.8	20.56	6.6	0	McKenzie (1972)
10	18091963	165813	40.9	29.2	5.2	33	McKenzie (1972)
11	18091963	165813	40.9	29.2	5.2	15±3	Taymaz et al. (1991)
12	14061964	121531	38	38.5	5.5	8	Jackson and McKenzie (1984)
13	6101964	143119	40.3	28.2	6	10	McKenzie (1972)
14	6101964	143123	40.3	28.23	5.9	14±2	Taymaz et al. (1991)
15	9031965	175755	39.34	23.82	5.7	7±2	Taymaz et al. (1991)
16	20081966	115909	39.4	40.9	5.3	12	Jackson and McKenzie (1984)

17	4031967	175809	39.25	24.6	6	10±2	Taymaz et al. (1991)
18	22071967	165653	40.7	30.8	6	4	McKenzie (1972)
19	22071967	165658	40.67	30.69	6	12±2	McKenzie (1972)
20	26071967	185301	39.5	40.4	5.6	33	Jackson and McKenzie (1984)
21	19021968	224542	39.4	24.94	6	15±3	Taymaz et al. (1991)
22	30051968	174024	35.49	27.96	5.3	21	McKenzie (1972)
23	5121968	75211	36.58	26.97	5.5	35	McKenzie (1972)
24	14011969	231208	36.18	29.2	5.5	33	McKenzie (1972)
25	3031969	5910.5	40.12	27.43	5.6	4	McKenzie (1972)
26	3031969	5910.5	40.08	27.5	5.6	5±2	Taymaz et al. (1991)
27	23031969	210843	39.16	28.48	5.6	12	McKenzie (1972)
28	25031969	132132	39.18	28.37	5.6	23	McKenzie (1972)
29	28031969	14830.4	38.59	28.45	6	9	McKenzie (1972)
30	6041969	34933.5	38.5	26.42	5.5	14	McKenzie (1972)
31	16041969	232105	35.34	27.77	5.2	45	McKenzie (1972)
32	30041969	202032	39.16	25.58	5.1	9	McKenzie (1972)
33	8071969	80917.5	37.56	20.28	5.4	33	McKenzie (1972)
34	2831970a	210223	39.2	29.57	6	20	McKenzie (1978)
35	2831970b	231144	39.22	29.52	5.2	37	McKenzie (1978)
36	8041970	135027	38.43	22.66	5.8	17	McKenzie (1978)
37	8041970	135028	38.34	22.86	5.8	9	Taymaz et al. (1991)
38	16041970	104219	39.03	30	5.5	9	McKenzie (1978)
39	19041970	132936	39.06	29.83	5.4	20	McKenzie (1978)
40	23041970	90124.7	39.13	28.7	5.2	18	McKenzie (1978)
41	3011971	231841	34.67	26.34	5.2	32	McKenzie (1978)

42	1251971a	62513	37.59	29.76	5.5	23	McKenzie (1978)
43	1251971b	101037	37.53	29.72	5.5	33	McKenzie (1978)
44	1251971c	125725	37.58	29.6	5.4	33	McKenzie (1978)
45	22051971	164359	38.83	40.52	6	3	Jackson and McKenzie (1984)
46	25051971	54327	39.03	29.74	5.8	24	McKenzie (1978)
47	14031972	140546	39.28	29.42	5.4	33	McKenzie (1978)
48	4051972	214001	35.12	23.61	5.9	46	McKenzie (1978)
49	17091972	140716	38.28	20.34	5.6	33	McKenzie (1978)
50	5011973	54917.5	35.81	21.84	5.3	33	McKenzie (1978)
51	4111973	155212	38.9	20.44	5.8	8	McKenzie (1978)
52	29111973	105743	35.18	23.8	5.7	26	McKenzie (1978)
53	27031975	51507.9	40.45	26.12	6	15±3	Taymaz et al. (1991)
54	30041975	42856.9	36.18	30.77	5.6	56	McKenzie (1978)
55	6091975	92011	38.47	40.72	6.1	10	Jackson and McKenzie (1984)
56	1061977	125449	36.24	31.34	5.2	67	Jackson and McKenzie (1984)
57	5101977	53447	40.96	33.41	5.3	33	Jackson and McKenzie (1984)
58	23051978	233411	40.76	23.27	5.6	10	Ekström and England (1989)
59	19061978	103105	40.75	23.22	5.3	15	Ekström and England (1989)
60	20061978	200322	40.78	23.24	6.1	7	Taymaz et al. (1991)
61	28051979	92732	36.41	31.75	5.9	98	Jackson and McKenzie (1984)
62	14061979	114445	38.79	26.57	5.9	8±2	Taymaz et al. (1991)

63	16061979	184200	38.75	26.63	4.9	15	Ekström and England (1989)
64	18071979	131203	39.67	28.66	5.2	15	Ekström and England (1989)
65	31121979	62134	36.18	31.51	5.3	79	Jackson and McKenzie (1984)
66	9071980	21152.8	39.27	23.04	5.8	10	Taymaz et al. (1991)
67	10071980	193901	39.31	22.92	5.3	15	Ekström and England (1989)
68	11081980	91558.3	39.27	22.66	5.2	15	Ekström and England (1989)
69	19121981	141051	39.22	25.25	6	10±3	Taymaz et al. (1991)
70	27121981	173913	38.91	24.92	5.4	6±1	Taymaz et al. (1991)
71	29121981	80045	38.8	24.77	5	15	Ekström and England (1989)
72	18011982	192725	39.96	24.39	5.8	7±1	Taymazet al. (1991)
73	5071983	120127	40.33	27.23	5.5	15	Ekström and England (1989)
74	6081983	154352	40.14	24.74	6	7±1	Taymaz et al. (1991)
75	10101983	101658	40.27	25.32	4.9	15	Ekström and England (1989)
76	21101983	203449	40.13	29.38	5	15	Ekström and England (1989)
77	6051984	91201.7	38.82	25.66	5	10	Ekström and England (1989)
78	17061984	74802.6	38.86	25.72	5	15	Ekström and England (1989)
79	30041985	181413	39.26	22.81	5.4	11±2	Taymaz et al. (1991)

80	25031986	14134.5	38.36	25.15	5.2	15	Ekström and England (1989)
81	19031989	53702.5	38.61	23.53	5.2	15	PDE
82	5091989	65237.2	40.2	25.1	4.9	15	PDE